



HAL
open science

Transparent ionic conductors and fluorescent materials based on hybrid PEO/PPO siloxanes

Gustavo Palácio

► **To cite this version:**

Gustavo Palácio. Transparent ionic conductors and fluorescent materials based on hybrid PEO/PPO siloxanes. Material chemistry. Université Clermont Auvergne [2017-2020], 2017. English. NNT : 2017CLFAC075 . tel-01795605

HAL Id: tel-01795605

<https://theses.hal.science/tel-01795605>

Submitted on 18 May 2018

HAL is a multi-disciplinary open access archive for the deposit and dissemination of scientific research documents, whether they are published or not. The documents may come from teaching and research institutions in France or abroad, or from public or private research centers.

L'archive ouverte pluridisciplinaire **HAL**, est destinée au dépôt et à la diffusion de documents scientifiques de niveau recherche, publiés ou non, émanant des établissements d'enseignement et de recherche français ou étrangers, des laboratoires publics ou privés.

UNIVERSITE CLERMONT AUVERGNE

ÉCOLE DOCTORALE DES SCIENCES FONDAMENTALES
N°867

THESE

présentée pour obtenir le grade de

DOCTEUR D'UNIVERSITÉ

Spécialité: Chimie, Sciences des Matériaux

Par PALÁCIO Gustavo

**Conducteurs ioniques transparents et Matériaux
Fluorescents à Basé de Mélanges Hybrides PEO/PPO-
Siloxane**

Soutenue publiquement le le 21 septembre 2017 devant la commission d'examen :

- Président:** Silvania LANFREDI, Professeur - Université de l'État de São Paulo, Presidente Prudente, Brésil.
- Rapporteurs:** Michel WONG CHI MAN, Directeur de Recherche CNRS – Institut Charles Gerhardt, Montpellier, France.
Karim DAHMOUCHE, Professeur - Université Nationale de Rio de Janeiro, Rio de Janeiro, Brésil.
- Examineur:** Bérangère TOURY-PIERRE, Maître de Conférences / HDR - Université de Lyon, Lyon, France.
- Directeurs de thèse:** Damien BOYER, Maître de Conférences / HDR – SIGMA Clermont, Aubière, France.
Celso V. SANTILLI, Professeur, Université de l'État de São Paulo, Araraquara, Brésil
- Invité:** Sandrine THERIAS, Directeur de Recherche CNRS, ICCF, Aubière, France.

Gustavo Palácio

Condutores Iônicos Transparentes e Materiais Fluorescentes Baseados em
Blendas Híbridas PEO/PPO – Siloxano

Transparent Ionic Conductors and Fluorescent Materials Based on PEO/PPO –
Siloxane Hybrid Blends

Conducteurs Ioniques Transparents et Matériaux Fluorescents à Basé de
Mélanges Hybrides PEO/PPO – Siloxane

Thesis in Co-title presented to the
Institute of Chemistry, Universidade
Estadual Paulista, and the Université
Clermont Auvergne (UCA) - École
Doctorale de Sciences Fondamentales, to
obtain the degree of Doctor in
Chemistry.

Advisors: (Brazil): Prof. Dr. Celso V. Santilli.
(France): Dr. Damien Boyer.

Araraquara
2017

FICHA CATALOGRÁFICA

P153c	<p>Palácio, Gustavo</p> <p>Condutores iônicos transparentes e materiais fluorescentes baseados em blendas híbridas PEO/PPO – Siloxano / Gustavo Palácio. – Araraquara: [s.n.], 2017 190 f.: il.</p> <p>Tese (doutorado) – Universidade Estadual Paulista, Instituto de Química Orientador: Celso Valentim Santilli Orientador: Damien Boyer</p> <p>1. Processo sol-gel. 2. Fotodegradação. 3. Revestimentos. 4. Fotoluminescência. 5. Polímeros-Propriedades elétricas.</p> <p>I. Título</p>
-------	--

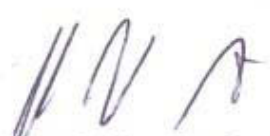
Elaboração: Seção Técnica de Aquisição e Tratamento da Informação
Biblioteca do Instituto de Química, Unesp, câmpus de Araraquara

Gustavo Palácio

Tese de doutorado nos termos da Convenção de Co-Tutela com à Université Clermont Auvergne, apresentada ao Instituto de Química, Universidade Estadual Paulista, como parte dos requisitos para obtenção do título de Doutor em Química.

Araraquara, 21 de Setembro de 2017.

BANCA EXAMINADORA

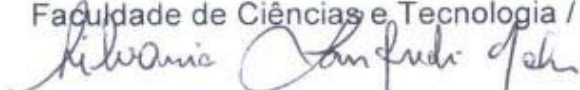


Prof. Dr. Celso Valentim Santilli (Orientador/Brasil)
Instituto de Química / UNESP / Araraquara – SP

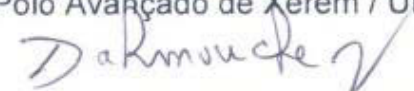
Prof. Dr. Damién Boyer (Orientador/França)
Université Clermont Auvergne / Clermont-Ferrand - França.



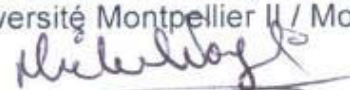
Profª Drª Sílvia Lanfredi Nobre
Faculdade de Ciências e Tecnologia / UNESP – Presidente Prudente - SP



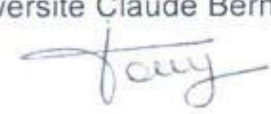
Prof. Dr. Karim Dahmouche
Polo Avançado de Xerém / UFRJ – Xerém - RJ



Prof. Dr. Michel Wong Chi Man
Université Montpellier II / Montpellier - França



Profª Drª Bérangeère Toury
Université Claude Bernard Lyon 1 - Villeurbanne - França.



Curriculum Vitae

Name: Gustavo Palacio

Name in citations: PALACIO, GUSTAVO; PALACIO, G.

Date of birth: January 24, 1988.

Nationality: Brazilian

Professional address:

- (1) Universidade Estadual Paulista “Júlio de Mesquita Filho” – UNESP, Instituto de Química, Departamento de Físico-Química, Grupo de Físico-Química de Materiais (GFQM). Rua Prof. Francisco Degni, 55. Jd. Quitandinha, CEP: 14800-900 – Araraquara – SP. Telefone +55 16 3301 – 9564.
- (2) Université Clermont Auvergne, Institut de Chimie de Clermont-Ferrand UMR 6296 CNRA/UCA/SIGMA, Campus de Cézeaux – AUBIERE 63178 – France. Tel.: +33 (0) 4 73 28 80 00.

e-mail: palacio.gustavo@yahoo.com.br

Academic Graduation/Titles

2006-2010	Degree in Chemistry obtained by the Faculdade de Ciências e Tecnologia - Universidade Estadual Paulista campus of PRESIDENTE PRUDENTE (FCT-UNESP).
2011-2013	Master Degree obtained by the Instituto de Biociências, Letras e Ciências Exatas - Universidade Estadual Paulista campus of SÃO JOSÉ DO RIO PRETO (IBILCE-UNESP). Advisor: Prof ^a Dr ^a Sylvania Lanfredi. Dissertation title: “Efeito da Adição de Níquel nas Propriedades Elétricas de Nanopós de Niobato de Potássio e Estrôncio”. Scholarship: CAPES.
2015/2016	Co-title thesis, from 01/09/15 to 30/07/16, obtained by the Institut de Chimie de Clermont-Ferrand (ICCF), campus Aubière, of the l’Université Clermont Auvergne (UCA), Clermont-Ferrand, Auvergne, França. Advisor: Dr Damien Boyer. Thesis title: Transparent Ionic Conductors and Fluorescent Materials Based on PEO/PPO – Siloxane Hybrid Blends. Scholarship: Ciências sem Fronteiras.
2013-2017	Ph. D. Degree in Chemistry obtained by the Instituto de Química da Universidade Estadual Paulista campus of ARARAQUARA (IQ-UNESP). Advisor: Prof Dr Celso Valentim Santilli. Thesis title: Transparent Ionic Conductors and Fluorescent Materials Based on PEO/PPO – Siloxane Hybrid Blends. Scholarship: CNPq

Bibliographic Productions

- 1) LANFREDI, SILVANIA, **PALACIO, GUSTAVO**, BELLUCCI, FELIPE S, COLIN, CLAIRE V, NOBRE, MARCOS A L ; Thermistor behaviour and electric conduction analysis of Ni-doped niobate ferroelectric: the role of multiple parameters. **Journal of Physics. D, Applied Physics**, v.45, p.435302, 2012.
- 2) LANFREDI, S.; NOBRE, M. A. L.; BESSE M. R. ; LIMA, A. R. F. ; **PALACIO, G. .** Spectral deconvolution as a tool to understanding Curie-temperature shifting and niobium off-centering phenomenon in ferroelectrics of type niobates. **Applied Mathematical Sciences**, v. 9, p. 5839-5869, 2015.

Events: Oral presentation

- Apresentação oral na XIII Reunião Anual da Sociedade Brasileira de Pesquisa em Materiais, SBPMat, do trabalho “ *SAXS study of lithium-loaded Siloxane-Polyether hybrid blend*” na cidade de João Pessoa - PB, no período de 28/09/2014 a 02/10/2014.
- Apresentação oral no 21º Congresso Brasileiro de Engenharia e Ciências dos Materiais, CBECiMat, do trabalho “Nanoestrutura e propriedades de blendas poliméricas híbridas Siloxano-Poliéter” na cidade de Cuiabá - MT, no período de 09/11/2014 a 13/11/2014.
- Apresentação oral na *Journée Sol-Gel et Chimie Liquide Rhône-Alpes Auvergne JSGRAA12*, do trabalho “ *Study of electrical/structural properties for a hybrid blend materials Li⁺ doped based PEO/PPO – siloxanes*” realizada na cidade de Saint-Etienne - França, no dia 24/03/2016.
- Apresentação oral, no European Materials Research Society (E-MRS – Spring), do trabalho “New hybrid materials constituted of PEO and PPO based siloxanes: photostability study and embedding of Li⁺/Eu³⁺ ions”, na cidade de Lille - França, no período de 02/05/2016 a 06/05/2016.
- Apresentação oral no 22º Congresso Brasileiro de Engenharia e Ciências dos Materiais, CBECiMat, do trabalho “Efeito da Photo-Oxidação nas propriedades luminescente de materiais híbridos siloxano-PEO e Siloxano-PPO dopados com Eu³⁺” na cidade de Natal - RN, no período de 06/11/2016 a 10/11/2016.

Languages

Portuguese: Native

	<i>Read</i>	<i>Speak</i>	<i>Write</i>	<i>Listen</i>
English:	Advanced	Advanced	Advanced	Advanced
French:	Advanced	Advanced	Advanced	Advanced
Spanish:	Advanced	Basic	Basic	Basic

Projects using Synchrotron Radiation

SAXS1-20160623: In situ SAXS measurements during programmed temperature change: study of the not irradiated and UV-Vis irradiated Eu³⁺ -doped siloxane hybrid blends. (2017)

Project 20160589, ROCK beamline at SOLEIL, Saint-Aubin, France: Combined Raman-QuickXAFS in situ measurement during programmed temperature change: study of the Eu³⁺ neighborhood in doped siloxane hybrid blends, (2016).

SAXS1 - Transformations affecting the LDH long-range order: from the decomposition to the regenerations, (2015).

SAXS1 - 17952 - Memory effect of semi-crystalline state on the nanostructure of melt siloxane-PEO/siloxane-PPO hybrid blends: an in situ study of glass transition and melting, with and without app (2015)

SAXS1 - 17009 - Nanostructural characterization of multifunctional organic-inorganic hybrids by SAXS measurements (2014)

SAXS1 - 16174 - Study of the nanostructure of new hybrids with antibacterial properties by SAXS measurements (2014)

SAXS1 - 16123 - Acompanhamento da reação de formação de crescimento de nanopartículas de ZnO dopadas com Cu (2014)

Eu dedico este trabalho aos meus pais, Leandro e Elisabete por todo amor e confiança depositados em mim, durante todos estes anos.

Acknowledgments

Aos meus pais Leandro S. Palácio e Elisabete Teruel, pelo amor incondicional que depositaram em mim, sua fé e esperança, mesmo quando eu mesmo não acreditava mais. E pela força doada, todas as vezes que eu pensei em desistir. Obrigado não é suficiente. Eu amo vocês.

Ao Prof. Dr. Celso V. Santilli, pela excelente orientação e pela oportunidade da realização deste trabalho em um grupo com uma equipe tão unida e competente.

Je remercie le Dr. Damien Boyer pour m'accepter dans votre équipe et aussi pour me trop aide pendant mon séjour en France.

To the Thesis Jury Dr. Karim Dahmouche, Dr^a Sylvania Lanfredi, Dr. Michel Wong Chi Man and Dr^a Bérangère Toury, for their disponibility, patience and time to help me and collaborate with this work.

À Prf^a. Dr^a Sandra H. Pulcinelli e ao Dr. Peter Hammer pela atenção e paciência quando precisei de algum conselho ou esclarecimento de alguma dúvida.

Je voudrais faire un remercie spécial à Dr^a. Sandrine Thérias et au groupe de Photo-Chemie pour disponibiliser son temp et ses laboratoires de recherche. Aussi pour sa paciencie avec moi, tous le jours que j'ai la demandé une 'petite' aide avec mes résultats.

Ao grupo de responsáveis da linha SAXS1 do Laboratório Nacional de Luz Síncrotron – LNLS, como parte das instalações do CNPEM, em especial ao Dr. Florian Meneau pela paciência e disposição na explicação do funcionamento dos equipamentos.

À Dr^a. Valérie Brios pour sa impressionnant disposition en travailler sur la ligne ROCK à Synchrotron Soleil, et pour me disponibilé du temps pour les mesures de Raman et EXAFS. Mme Valérie, sa motivation est contagieuse.

Ao meu irmão e melhor amigo Vinicius Palácio, que mesmo sem saber, é responsável direto por este trabalho estar finalizado, onde para mim era inaceitável decepciona-lo.

Aos amigos do Grupo de Físico-Química de Materiais Rodrigo, Rosembergue, Álvaro, Rodolfo, Paula, Fernanda, Aline, Lídia, Douglas, Thiago, Nalva, Danúbia, Marina Bianca, Marlon, Bruno, Eloísa, Wellington, Yane, Celso, Fábio, Ana, Samara, Andressa, Mayte, Jorge, e Laurianne, por toda a ajuda, pela amizade e alegria que tornava o trabalho ainda mais prazeroso.

À tous les amis que j'ai connu en France, pour les moments très agreables en spécial à Mika, Ayoub, Jérémy, Mai e Rafa.

Aos amigos da República Xerém Kiko, Pacato, Godão, Alf, Cepacol, Lixeira, Sinistro, Betão, Nariga, Pinguim, Pirla, Óbito, Caxueira, Mariano, Calabresa, Kelly, Fuminho, Prancheta e Cicrópi, pela amizade verdadeira formada entre nós, e pelo bom convívio ao longo desta etapa de nossas vidas. E claro à Dona Ana, por salvar nossa pele incontáveis vezes.

À FAPESP, CNPq, CAPES/COFECUB e Ciências sem Fronteiras pelo apoio financeiro.

À todos que contribuíram direta ou indiretamente na realização deste trabalho.

“...Verás que um filho teu não foge a luta...”

Joaquim O. D. Estrada

*“Ce n’est pas possible, m’écrivez-vous : cela
n’est pas français.”*

Napoléon Bonaparte

Resumo

Neste trabalho de Tese uma metodologia sol-gel mais verde para a preparação de materiais híbridos orgânico-inorgânicos (OIH) a base de dois poli-éter amina terminal (Jeffamine®), o óxido de poli-etileno (PEO) e o óxido de poli-propileno (PPO), ligados de forma covalente com o agente reticulador ureasil (U) é apresentada. Devido aos diferentes sítios ativos presentes na estrutura do material OIH, uma vasta gama de cátions metálicos pode ser introduzida na matriz híbrida a partir da coordenação com os átomos de oxigênio do tipo éter ou do tipo carbonil. Assim, diferentes matrizes híbridas contendo cátions Eu^{3+} e Li^+ , foram sintetizadas visando avaliar seu potencial como material fotoluminescente ou condutor iônico, respectivamente. O entendimento das características térmicas e estruturais dos OIH contendo cátions Eu^{3+} ou Li^+ , assim como o efeito plastificante do PPO_{2000} na blenda híbrida $\text{U}_x\text{PEO}_{1900}/\text{U}_{1-x}\text{PPO}_{2000}$, (fração de PPO_{2000} na mistura, $x = 0,2, 0,5$ e $0,8$), foram investigadas por DSC e SAXS. Os resultados de DSC revelaram uma única temperatura de transição vítrea (T_g) para todos os materiais estudados. A adição de cátions Eu^{3+} nas matrizes não causou variações nos valores de T_g enquanto a adição de cátions Li^+ causou aumento dos valores de T_g , indicando a existência de interações entre o cátion Li^+ e a fase polimérica do material OIH. As curvas calorimétricas referentes ao U-PEO_{1900} ainda revelaram a presença de um pico endotérmico em 25°C , associado à fusão dos domínios cristalinos do PEO_{1900} . A presença de um segundo máximo nas curvas de espalhamento de raios X a baixo ângulo (SAXS) confirmaram a presença da estrutura semicristalina do PEO_{1900} em uma região de temperatura entre $-100^\circ\text{C} < T < T_f$. Todas as amostras, não dopadas e dopadas com cátions Li^+ e Eu^{3+} , apresentaram um pico de correlação, indicando que a nanoestrutura da matriz híbrida não é afetada pela dopagem com os cátions metálicos. As análises por Espectroscopia no Infravermelho com Transformada de Fourier (FTIR) e por Espectroscopia Raman confirmaram a interação dos cátions Eu^{3+} com o oxigênio tipo carbonil, presente nos grupos ureia da matriz híbrida, e dos cátions Li^+ com o oxigênio tipo éter. A fotodegradação acelerada revelou uma perda da eficiência da fotoluminescência (PL) associada a mudanças na coordenação dos cátions Eu^{3+} com a matriz híbrida. A fotodegradação induz a formação de fotoprodutos provenientes da β -cisão do macroradical formado na fração orgânica da matriz híbrida. A β -cisão pode ser a responsável da diminuição da PL do material devido a queda da eficiência do efeito antena do ligante orgânico para o centro luminescente. A transição no visível da cor de emissão de vermelho \rightarrow azul com a fotodegradação qualifica estes materiais como bons candidatos para aplicação como sensores e marcadores ópticos. A condução iônica das matrizes híbridas dopadas com cátions Li^+ foi investigada por Espectroscopia de Impedância em função da temperatura e os resultados revelaram correlações entre a superestrutura lamelar do PEO_{1900} com o processo de condução. A adição de um plastificante (PPO_{2000}) permitiu aumentar a condutividade iônica em regiões de baixa temperatura, $-100^\circ\text{C} < T < 10^\circ\text{C}$ devido ao aumento da fração da região amorfa utilizada como caminho efetivo de transporte iônico na blenda híbrida polimérica $\text{U}_x\text{PEO}_{1900}/\text{U}_{1-x}\text{PPO}_{2000}$.

Palavras-chaves: híbridos orgânico-inorgânicos; processo sol-gel; fotoluminescência, revestimentos OIH, condutores iônicos sólidos.

Résumé

Ce travail de thèse présente une méthode de synthèse par le procédé sol-gel pour la préparation de matériaux hybrides organiques-inorganiques (OIH) basés sur le mélange de deux polyéthers différents, le poly (oxyde d'éthylène) (PEO) et le poly (oxyde de propylène) (PPO) liées de façon covalente avec l'agent de réticulation ureasil (U). Dû aux différents sites actifs présents dans la structure du matériau OIH, plusieurs cations métalliques peuvent être introduits dans la matrice hybride par complexation soit avec l'oxygène de type éther, soit avec l'oxygène du type carbonyle. Suite à ce constat, différentes matrices hybrides ont été synthétisées en introduisant des ions Eu^{3+} ou Li^+ afin de conférer aux matériaux des propriétés optiques ou électriques. La compréhension des propriétés structurales et thermiques des différents polymères, l'ajout de différents cations $\text{Eu}^{3+}/\text{Li}^+$, et l'effet du plastifiant (PPO₂₀₀₀) dans la mélange hybride $\text{U}_x\text{PEO}_{1900}/\text{U}_{1-x}\text{PPO}_{2000}$ (ratio de PPO₂₀₀₀ dans la mélange, $x = 0.2, 0.5$ et 0.8), ont été étudiés par DSC et SAXS. Les résultats de DSC ont révélé une unique température de transition vitreuse (T_g) pour tous les matériaux étudiés. L'ajout des ions Eu^{3+} dans la matrice n'a pas causé de variations dans les valeurs de T_g tandis que l'insertion de cations Li^+ a provoqué une augmentation dans les valeurs de T_g , indiquant l'existence d'interactions entre les cations Li^+ et la phase polymérique du matériau OIH. Les courbes de calorimétrie de l' U-PEO_{1900} ont aussi révélé la présence d'une pic endothermique à 25 °C, associé à la fusion des domaines cristallins du PEO_{1900} . La présence d'un deuxième maximum dans les courbes de diffusion des rayons X à petits angles (SAXS) a confirmé l'existence de la structure semi-cristalline du PEO_{1900} dans une région de température entre $-100\text{ °C} < T < T_f$. Tous les échantillons, non-dopés et dopés avec les ions Li^+ et Eu^{3+} , ont montré un pic de corrélation indiquant que la nano-structure de la matrice hybride n'est pas affecté par le dopage avec les cations métalliques. Les études par Spectroscopie Infrarouge à Transformée de Fourier (FTIR) et par spectroscopie Raman ont confirmé l'interaction des ions Eu^{3+} avec l'oxygène du type carbonyle présent dans les groupes urées de la matrice hybride, et des ions Li^+ avec l'oxygène du type éther. La photodégradation accélérée a révélé une perte des performances de la photo-luminescence (PL) associée à des changements dans la coordination des ions Eu^{3+} avec la matrice hybride. La photodégradation induit la formation de photo-produits venant de la β -scission du macroradical formé dans la portion organique de la matrice hybride. La β -scission peut-être responsable pour la diminution de la PL du matériau dû la perte de l'efficacité de l'effet antenne du ligand organique pour le centre luminescent. La transition dans la région visible du rouge vers le bleu avec la photodégradation qualifie ces matériaux de bons candidats pour l'application comme capteurs et marqueurs optiques. La conduction ionique des matrices hybrides dopés avec Li^+ a été évaluée par Spectroscopie d'Impédance en fonction de la température et les résultats ont révélé des corrélations entre la superstructure lamellaire du PEO_{1900} et le mécanisme de conduction. L'addition d'un plastifiant, le PPO₂₀₀₀, a permis l'augmentation de la conductivité ionique dans une région de température entre $-100\text{ °C} < T < 10\text{ °C}$ dû à l'augmentation de la portion amorphe utilisée comme chemin de transport ionique efficace dans le mélange polymère hybride $\text{U}_x\text{PEO}_{1900}/\text{U}_{1-x}\text{PPO}_{2000}$.

Mots-clefs: Hybrides organique-inorganique; procédé sol-gel; photoluminescence; revêtements OIH; conducteurs ioniques solides.

Abstract

In this PhD thesis a greener synthesis route via sol-gel reactions aiming to prepare multifunctional organic-inorganic hybrid (OIH) materials based on blending of two polyether amine end chains (i.e., Jeffamine® compounds) Poly(ethylene oxide) (PEO) and Poly(propylene oxide) (PPO) covalently bonded with an ureasil cross-linking agent (U) is reported. Due to the different polar oxygen sites present in this OIH material, several metallic cations can be introduced into the OIH matrix via ether- or carbonyl-type oxygen. So, different OIH matrices containing Eu^{3+} or Li^+ cations were synthesized to evaluate their potential as photoluminescent or ionic conductor material, respectively. The thermal and structural characteristics of the Eu^{3+} or Li^+ – loaded OIH materials, as well as the plasticizer effect of PPO_{2000} at the $\text{U}_x\text{PPO}_{2000}/\text{U}_{1-x}\text{PEO}_{1900}$, (PPO_{2000} fraction $x = 0.2, 0.5$ and 0.8) blends, were carried out by DSC and SAXS. DSC results revealed a unique glass transition temperature (T_g) for all the studied OIH materials. The addition of Eu^{3+} cations do not change the T_g values while the Li^+ cations caused an increase in the values of T_g , due to the Li^+ interaction with the polymeric phase of the material. The U-PEO_{1900} calorimetric curves also showed the presence of an endothermic peak at $25\text{ }^\circ\text{C}$ associated to the fusion of the crystalline domains of PEO_{1900} . The second maxima observed in the curves of small angle X-ray scattering (SAXS) confirmed the presence of the crystalline structure of PEO_{1900} in a temperature range of $-100 < T < T_f$. All the samples, undoped and Li^+ or Eu^{3+} doped ones, showed a correlation peak indicating that the OIH nano-structure is not affected by the metallic cations doping. Analysis carried out by Fourier Transform InfraRed (FTIR) and Raman Spectroscopy confirmed the Eu^{3+} cations interaction via the oxygen carbonyl-type present in the urea groups of the hybrid matrix, and that of Li^+ cations with the oxygen ether-type. The accelerate photo-degradation revealed a loss of the photo-luminescence (PL) efficiency due to the changes in the Eu^{3+} cations coordination with the hybrid matrix. The photo-degradation induces the formation of photo-products from the macro-radical β -scission formed in the organic fraction of the hybrid matrix. The β -scission can be responsible for the material PL decrease due to the drop in the antenna effect from organic ligand to luminescent center. The visible emission transition from red \rightarrow blue with the photo-degradation qualify these materials as good candidates to be applied as sensors and optical markers. The ionic conduction of the Li^+ -loaded hybrid matrices was investigated by Impedance Spectroscopy as a function of the temperature. Results showed a correlation between the lamellar superstructure of the PEO_{1900} and the conducting process. The plasticizers addition (PPO_{2000}) alloyed to improve the value of the ionic conductivity in the low temperature range, $-100\text{ }^\circ\text{C} < T < 10\text{ }^\circ\text{C}$ due to the increase of the amorphous fraction used as effective ionic transport pathway in the $\text{U}_x\text{PEO}_{1900}/\text{U}_{1-x}\text{PPO}_{2000}$ polymeric hybrid blend.

Keywords: Organic-inorganic hybrids; Sol-gel process; Photoluminescence, OIH coatings, Solid ionic conductor.

Figures List

#	Description	pg
2.1	Griffon: Hybrid creature from Greek mythology.	12
2.2	Schematic representation of class I (a) and class II (b) OIH materials	13
2.3	Transparent Siloxane-Poly(ether) hybrid materials, based on PEO and PPO polymers. The magnification of the crosslinking nodes exemplifies the Si-O-Si crosslinking structure network of the matrix	14
2.4	Dependency of the Volume with the Temperature for a crystalline (curve 1) and non-crystalline material (curve 2).	16
2.5	Schematic representation of a DSC pattern of a generic semi-crystalline polymer, representing the glass transition (T_g) and the melting point (T_m).	18
2.6	Microlithographic trends in minimum device feature size and imaging technology. The figure illustrates the time evolution of random access memory (RAM) devices. <i>Meaning of acronyms at Glossary</i>	20
2.7	Examples of the future manufacturing of electronic devices utilizing OIH materials.	21
2.8	Chemical formula of monomers constituting PEO and PPO polymers.	21
2.9	(a) Ionic transport interrupted by the active charger transfer saturation and (b) Dependency of the ionic conductivity with the charge transfer (n) concentration.	25
2.10	Schematization of the Li^+ ionic transfer mechanism (a) in the glass state ($T < T_g$) and (b) in the rubbery state ($T > T_g$).	25
2.11	Examples of natural light emitted by glow worms, Aurora Borealis, rotting fish and luminescent wood.	27
2.12	Luminescence spectrum [Eu(tta) ₃ (phen)] at 77 K upon excitation at 396 nm. All of the transitions start from the 5D_0 state	30
2.13	Schematic representation of the Eu^{3+} :OIH complex derived from functionalized dipicolinic acid ligands.	32
2.14	(a) U-PPO ₂₀₀₀ OIH matrix (blue emission) and U-PPO ₂₀₀₀ OIH:Eu ³⁺ complex (red emission) developed at this thesis and (b) CIE chromaticity diagram of a generic support matrix, doped with different Ln^{3+} , showing the photoluminescence dependency of the lanthanide cation.	33
2.15	Schematic diagram of the Antenna Effect by the organic ligand with an efficient energy transfer to the lanthanide center	34
2.16	Acid (a) and Basic (b) catalysis reaction mechanism to the siliceous alkoxide.	39
3.1	Schematic diagram of the different OIH – matrices with their two polar oxygen active sites, I: O_{ether} and II: $O_{carbonyl}$, respectively	42
3.2	Schematic representation of the synthesis of the U-PEO ₁₉₀₀ and U-PPO _n OIH, Metal-unloaded, Li^+ – loaded and Eu^{3+} – loaded OIH materials. An analogous process was adopted in the synthesis of the OIH materials from POs 230, 2000 and 4000 ($n = 2.3$ and 68, respectively)	43
3.3	DSC time and temperature for the control program	44
3.4	(a) Photograph of the SEPAP 12/24 chamber during activity and (b) metallic sample holder with a hollow center	45
3.5	U-PEO ₁₉₀₀ (left) and U-PPO ₂₀₀₀ (right) OIH matrices, non-irradiate, before (black) and after (red) the ammoniac chemical treatment of the hybrid thin film (50 μm). The same results were obtained for the U-PPO ₂₃₀ and U-PPO ₄₀₀₀ OIH matrices – Annex.	46
3.6	(a) SAXS1 beamline at LNLS synchrotron ring – Campinas, Brazil (b) apparatus containing liquid nitrogen for the heating/cooling procedure and (c) a constant flux of air to avoid water crystallization at the sample holder surface	48
3.7	Typical SAXS curve of the U-PEO ₁₉₀₀ OIH matrix (black) and its Porod function (see equation inserted in the figure) fitting (red).	49
3.8	Subtraction of the typical SAXS curve of the U-PEO ₁₉₀₀ OIH matrix by the power law contribution straight line curve. The insert show a schematic representation of the siloxane nodes distance spaced by the polymeric chain.	49

3.9	(Left) Gaussian equation and (Right) Gaussian function.	49
3.10	OIH:Li ⁺ monolith prepared for impedance analyses.	51
4.1	DSC curves of U-PEO ₁₉₀₀ and U-PPO ₂₀₀₀ Eu ³⁺ -unloaded (black) and Eu ³⁺ -loaded (red).	54
4.2	FTIR spectrum of (a) U-PEO ₁₉₀₀ and U-PEO ₁₉₀₀ Eu ³⁺ and (b) U-PPOs with different molecular weight (wt = 230, 2000 and 4000 g.mol ⁻¹) Eu ³⁺ – unloaded OIH materials (solid line) and OIH:Eu ³⁺ complexes (dotted line), films (50 μm) in the ν(C-O-C) backbone (1200 – 950 cm ⁻¹) region	55
4.3	FTIR spectrum of 50 μm films in the amide region of (a) U-PEO ₁₉₀₀ and U-PEO ₁₉₀₀ Eu ³⁺ and (b) U-PPOs with different molecular weight (wt = 230, 2000 and 4000 g.mol ⁻¹) Eu ³⁺ – unloaded OIH materials (solid line) and OIH:Eu ³⁺ complexes (dashed line)	57
4.4	FTIR spectra in the amide region with the 2 nd curve derivate for (a) U-PEO ₁₉₀₀ and (c) U-PEO ₁₉₀₀ :Eu ³⁺ and the Gaussian fitting of the amide region for (b) U-PEO ₁₉₀₀ and (d) U-PEO ₁₉₀₀ :Eu ³⁺ .	59
4.5	Schematization of the Eu ³⁺ coordination with the OIH matrix.	60
4.6	Raman Spectroscopy in situ with the temperature, from -100 °C to 100 °C, in an energy range from 800 to 1300 cm ⁻¹ for a U-PEO ₁₉₀₀ OIH material (a) Eu ³⁺ -unloaded and (b) Eu ³⁺ -loaded.	62
4.7	Raman Spectroscopy in situ with the temperature, from -100 °C to 100 °C, in an energy range from 800 to 1300 cm ⁻¹ for a U-PPO ₂₀₀₀ OIH material (a) Eu ³⁺ -unloaded and (b) Eu ³⁺ -loaded.	63
4.8	Room temperature SAXS curves for the (top) U-PPO ₂₀₀₀ (black) and U-PPO ₂₀₀₀ :Eu ³⁺ (red) and (bottom) U-PEO ₁₉₀₀ (black) and U-PEO ₁₉₀₀ :Eu ³⁺ (red) OIH materials.	64
4.9	Room temperature SAXS curves for the (a) U-PEO ₁₉₀₀ :Eu ³⁺ and (b) U-PPO ₂₀₀₀ :Eu ³⁺ OIH materials exposed to UV-light irradiation at different times.	66
4.10	Effect of UV-light exposure times on the emission spectra of the Eu ³⁺ - OIH complex, (a) U-PEO ₁₉₀₀ and (b) U-PPO ₂₀₀₀ .	68
4.11	Excitation spectra, in the spectral range from 250 to 500 nm, of the OIH:Eu ³⁺ complexes, (a) U-PEO ₁₉₀₀ and (b) U-PPO ₂₀₀₀ , exposed to different UV-irradiation times.	72
5.1	Mechanism of photo-degradation of U-PPO in hydro-peroxide and macro-radical.	76
5.2	Photo-oxidation mechanisms of the PPO macro-radical. Step 1: ketone forming by β-scission from the oxygen ether-type inside in the monomer followed by Norrish I mechanism forming carboxylic acid; Step 2: Cage reaction forming ester (without breaking of the chain) leading a O=C•-CH ₃ radical; and Step 3: A methyl-ester formation by a β'-scission from the oxygen ether-type outside of the monomer	76
5.3	FTIR spectra evolution during accelerated photo-aging assays (a) U-PPO2000 and (b) U-PPO2000:Eu ³⁺ films (50 μm) in different UV-light exposure at λ ≥ 300 nm and 60 °C.	78
5.4	Variation of absorbance at 1720 cm ⁻¹ as a function of UV irradiation time (photooxidation at λ > 300 nm, 60 °C) for the U-PPO films with different molecular weights (230, 2000 and 4000 g.mol ⁻¹), Eu ³⁺ -unloaded (full circles) and Eu ³⁺ -loaded (empty squares).	79
5.5	Variation of absorbance at 1608 cm ⁻¹ as a function of UV irradiation time (photooxidation at λ > 300 nm, 60 °C) for Eu ³⁺ -loaded U-PPO films with different molecular weights (2000 and 4000 g.mol ⁻¹).	79
5.6	Effect of NH ₃ treatment of (a) U-PPO2000 and (b) U-PPO2000:Eu ³⁺ , films photo-degraded by 10 h of UV-light exposure (λ ≥ 300 nm, 60 °C), in IRFT spectra in the carbonyl range.	81
5.7	Schematic diagram of the reactions between ammonia with U-PPO2000 photoproducts.	81
5.8	Schematization of the application of U-PPOn:Eu ³⁺ complexes as optical marker	82

	showing the red → blue transition.	
5.9	Evolution of the U-PPOs:Eu3+ QY-value as a function of the long wavelength ($\lambda > 300$ nm) UV-light irradiation;	83
6.1	DSC curves for U-PEO ₁₉₀₀ ; U-PPO ₂₀₀₀ ; and hybrid blends prepared with PEO ₁₉₀₀ content $x = 0.5$, Li ⁺ -unloaded (dashed curves) and Li ⁺ -loaded (straight curves).	87
6.2	Dependence of the glass transition temperature on the percentage of PPO ₂₀₀₀ at the U _{-x} PPO ₂₀₀₀ :U _{-1-x} PEO ₁₉₀₀ hybrid blend, respectively	88
6.3	Degree of crystallinity, as a function of the percentaging of PPO ₂₀₀₀ at the U _{-x} PPO ₂₀₀₀ :U _{-1-x} PEO ₁₉₀₀ hybrid blend, respectively	89
6.4	Room temperature FTIR pattern, in the spectral range from 1800-1100 cm ⁻¹ , Li ⁺ -unloaded (black) and Li ⁺ -loaded (blue) for thin films (50 μ m) of (a) U-PEO ₁₉₀₀ and (b) U-PPO ₂₀₀₀ .	91
6.5	FTIR spectra in the amide region with the 2 nd curve derivate for (a) U-PEO ₁₉₀₀ and (c) U-PEO ₁₉₀₀ :Li ⁺ and the Gaussian fitting of the amide region for (b) U-PEO ₁₉₀₀ and (d) U-PEO ₁₉₀₀ :Li ⁺ .	92
6.6	Comparison between the relative area of Amide I and of U-PEO ₁₉₀₀ (black) and U-PEO ₁₉₀₀ :Li ⁺ (blue).	94
6.7	Raman spectra of (a) Li ⁺ -unloaded and (b) Li ⁺ -loaded U-PEO ₁₉₀₀ as a function of the temperature from -85 to 100 °C	96
6.8	Raman spectra of (a) Li ⁺ -unloaded and (b) Li ⁺ -loaded U-PPO ₂₀₀₀ as a function of the temperature from -85 to 100 °C.	98
6.9	Room temperature log-log SAXS curves of U _{-x} PPO ₂₀₀₀ :U _{-1-x} PEO ₁₉₀₀ blends prepared with different PPO ₂₀₀₀ content, (a) Li ⁺ - unloaded and (b) Li ⁺ - loaded	102
6.10	Tri-dimensional log-log SAXS curves measured in situ during a temperature range increasing from -100 °C to 100 °C, with the their calorimetric curve of (a) U-PEO ₁₉₀₀ and (b) U-PEO ₁₉₀₀ :Li ⁺ .	104
6.11	Tri-dimensional log-log SAXS curves measured in situ during a temperature range increasing from -100 °C to 100 °C, with the their calorimetric curve of (a) U-PPO ₂₀₀₀ and (b) U-PPO ₂₀₀₀ :Li ⁺ .	105
6.12	Average displacement of the siloxane correlation peak position (ξ) as a function of temperature for (a) U-PEO ₁₉₀₀ , (b) U-PPO ₂₀₀₀ and (c) U _{-0.5} PPO ₂₀₀₀ /U _{-0.5} PEO ₁₉₀₀ OIH blend, unloaded (black) and Li ⁺ -loaded (red).	106
6.13	Straight line equation SAXS curves subtraction at (a) U-PEO ₁₉₀₀ long period semi-crystalline peak and ξ_{SC} peak position as a function of temperature as well and siloxane correlation peak of (b) U-PEO ₁₉₀₀ and (c) U-PEO ₁₉₀₀ :Li ⁺ .	108
6.14	Gaussian fitting of the siloxane correlation peak: (a), (b) and (c) for U-PEO ₁₉₀₀ and (d), (e) and (f) for U-PEO ₁₉₀₀ :Li ⁺ , at -100, +5 and +100 °C. The fitting was made utilizing three components named here as component #1 (red) #2 (black) and #3 (blue).	109
6.15	Sum of the three different components from the Gaussian fitting of the correlation peak of (a) U-PEO ₁₉₀₀ and (b) U-PEO ₁₉₀₀ :Li ⁺ .	109
6.16	Evolution of the average distance (ξ) relative to the three different components from the Gaussian fitting of the correlation peak for (a) U-PEO ₁₉₀₀ and (b) U-PEO ₁₉₀₀ :Li ⁺ .	110
6.17	(a) Evolution of the three different component areas ($\times 10^{-4}$ nm ²) and the middle-q area (nm ²) as a function of the temperature from -100 °C to 100 °C.	112
6.18	Tri-dimensional log-log SAXS curves measured in situ during temperature increase from -100 °C to 100 °C, with their calorimetric curve for U _{-x} PPO ₂₀₀₀ :U _{-1-x} PEO ₁₉₀₀ OIH blends for a x PPO ₂₀₀₀ content equal to (a) 0.8 - unloaded, (b) 0.8 - Li ⁺ -loaded, (c) 0.5 - unloaded, (d) 0.5 - Li ⁺ -loaded, (e) 0.2 - unloaded and (f) 0.2 - Li ⁺ -loaded.	113
6.19	Average displacement of the siloxane correlation peak position (ξ) as a function of temperature for (a) U-PEO ₁₉₀₀ (black), U _{-0.2} PPO ₂₀₀₀ /U _{-0.8} PEO ₁₉₀₀ (green) U _{-0.5} PPO ₂₀₀₀ /U _{-0.5} PEO ₁₉₀₀ (red), U _{-0.8} PPO ₂₀₀₀ /U _{-0.2} PEO ₁₉₀₀ (magenta) and U-PPO ₂₀₀₀ (blue) (a) unloaded and (b) Li ⁺ -loaded.	115

- 6.20 Straight line equation SAXS curves subtraction at siloxane correlation peak (q_{\max}) as a function of the temperature for $U_x\text{PPO}_{2000}:U_{1-x}\text{PEO}_{1900}$ OIH blends for a x PPO_{2000} content equal to (a) 0.8 - unloaded, (b) 0.8 - Li^+ -loaded, (c) 0.5 - unloaded, (d) 0.5 - Li^+ -loaded, (e) 0.2 - unloaded and (f) 0.2 - Li^+ -loaded. 117
- 6.21 (a) Evolution of the three different component areas ($\times 10^{-4} \text{ nm}^2$) and the middle-q area (nm^2) and (b) evolution of the average distance (ξ) relative to the three different components from the Gaussian fitting of the correlation peak for $U_{0.5}\text{PPO}_{2000}/U_{0.5}\text{PEO}_{1900}$ OIH blend. 119
- 6.22 (a) Evolution of the three different component areas ($\times 10^{-4} \text{ nm}^2$) and the middle-q area (nm^2) and (b) evolution of the average distance (ξ) relative to the three different components from the Gaussian fitting of the correlation peak for $U_{0.2}\text{PPO}_{2000}/U_{0.8}\text{PEO}_{1900}$ OIH blend. 121
- 6.23 Nyquist Impedance diagrams of the $U\text{-PEO}_{1900}:\text{Li}^+$ monolith at various temperatures. 123
- 6.24 Nyquist Impedance diagrams of the $U_{0.2}\text{PPO}_{2000}:\text{Li}^+:U_{0.8}\text{PEO}_{1900}:\text{Li}^+$ monolith at various temperatures. 124
- 6.25 Nyquist Impedance diagrams of the $U_{0.5}\text{PPO}_{2000}:\text{Li}^+:U_{0.5}\text{PEO}_{1900}:\text{Li}^+$ monolith at various temperatures. 125
- 6.26 Nyquist Impedance diagrams of the $U_{0.8}\text{PPO}_{2000}:\text{Li}^+:U_{0.2}\text{PEO}_{1900}:\text{Li}^+$ monolith at various temperatures 126
- 6.27 Nyquist Impedance diagrams of the $U\text{-PPO}_{2000}:\text{Li}^+$ monolith at various temperatures 127
- 6.28 (a) $U\text{-PEO}_{1900}:\text{Li}^+$ adjustment of the Nyquist diagram at -10°C using a RQ – RQ – RQ equivalent circuit model, (b) Nyquist diagram at $+80^\circ\text{C}$ and (c) Schematization of the EEC model used for describing the $U\text{-PEO}_{1900}:\text{Li}^+$ electrical response: The blue parallel circuit represents the *bulk* electrical resistance, ascribed to the PEO_{1900} semi-crystalline fraction at the helical conformation. The green parallel connection stands for the influence of PEO_{1900} in the fully amorphous zone. The red parallel circuit represents the anode's charge transfer 132
- 6.29 $U\text{-PPO}_{2000}:\text{Li}^+$ (Left) adjustment of the Nyquist diagram at -10°C using a RQ – RQ model and (Right) Nyquist diagram at $+80^\circ\text{C}$ 133
- 6.30 Temperature-dependent conductivities of (a) $U\text{-PEO}_{1900}:\text{Li}^+$, (b), (c) and (d) for $U_x\text{PPO}_{2000}:\text{Li}^+:U_{1-x}\text{PEO}_{1900}$ blending with χ PEO_{1900} $x = 0.8, 0.5$ and 0.2 , respectively and (e) $U\text{-PPO}_{2000}:\text{Li}^+$. 135
- 6.31 Isothermic evolution of the specific conductivity (σ_s) $U_x\text{PPO}_{2000}:\text{Li}^+:U_{1-x}\text{PEO}_{1900}:\text{Li}^+$ hybrid blend with different PPO_{2000} content (a) -90 to -50°C (b) -0 to 0°C (c) 10 to 50°C and (d) $+60$ to $+100^\circ\text{C}$. 137

Tables List

#		<i>pg</i>
1.1	Different polymers and their respectively value of ionic conductivity at room temperature	5
3.1	Table content the volume of water (μl) and the mass of europium salt (g), to satisfy the relationship $[\text{H}_2\text{O}]/[\text{Si}]=4$ $[\text{O}_{\text{carbonyl}}]/[\text{Li}^+]=15$, and $[\text{O}_{\text{carbonyl}}]/[\text{Eu}^{3+}]=3$, respectively.	42
3.2	Volume of water (μl) and the mass of lithium salt (g) used to satisfy the relationship $[\text{H}_2\text{O}]/[\text{Si}]=4$ and $[\text{O}_{\text{carbonyl}}]/[\text{Li}^+]=15$, and the electrical geometric factor of the $\text{U}_x\text{PPO}_{2000}/\text{U}_{1-x}\text{PEO}_{1900}$ poly-electrolytes.	51
4.1	Table containing the values of the Gaussian fitting parameters for the Amide I and Amide II regions of the U-PEO_{1900} and $\text{U-PEO}_{1900}:\text{Eu}^{3+}$	60
4.2	$I(^5\text{D}_0 \rightarrow ^7\text{F}_2) / I(^5\text{D}_0 \rightarrow ^7\text{F}_1)$ ratio ($\Omega_{1,2}$), of the Eu^{3+} - OIH complex, exposed to different UV-light irradiation times	70
6.1	Attribution of the FTIR spectroscopy bands for the U-PEO_{1900} and U-PPO_{2000} OIH thin film ($50 \mu\text{m}$) matrices, Li^+ -unloaded and Li^+ -loaded	91
6.2	Table containing the mathematical fitting values of the Amide I and Amide II regions of U-PEO_{1900} and $\text{U-PEO}_{1900}:\text{Li}^+$.	93
6.3	Attribution of the Raman bands of Li^+ -unloaded and Li^+ -loaded U-PEO_{1900} and U-PPO_{2000} OIH.	99
6.4	Values of the thermal expansion coefficient represented by the slope of the curve from the average distance of the siloxane correlation peak as a function of the temperature.	116

Glossary

ΔH_f :	PEO melting enthalpy
ΔH_p :	Standard melting enthalpy for 100 % crystalline PEO
CN:	Coordination number
DSC:	Differential Scanning Calorimetry
E_a :	Energy of activation
ED:	Electric dipole
EEC	Electrical Equivalent Circuit
Eu^{3+} :	Europium trivalent ion
FTIR:	Fourier Transformer InfraRed
$I(q)$:	Intensity of the scattered beam as function of the module of the scatter vector
ICR:	Inter-configurational rearrangement
IET:	Internal energy transfer
IsoTREOs:	3-(isocyanate propyl)-triethoxysilane
LIB:	Lithium-ion battery
LIE:	Lanthanide ion emission
Ln^{3+} :	lanthanide trivalent ion
LSI:	large scale integration
K:	Kelvin (temperature)
K :	Geometric factor
RAM:	Random Access Memory
MSI:	medium scale integration
OIH materials:	Organic-Inorganic Hybrid materials
PEO:	Poly(ethylene oxide)
PPO:	Poly(propylene oxide)
PL:	Photoluminescence
SAXS:	Small Angle X-Ray Scattering
SSI:	small scale integration
T_g :	Temperature of glass transition
U:	Ureasiloxane
ULSI:	ultra large scale integration
U-PEO:	Ureasil – Poly(ethylene oxide) OIH material
U-PPO:	Ureasil – Poly(propylene oxide) OIH material
UV:	Ultraviolet
VLSI:	very large scale integration
wt:	molecular weight
3D:	Three-dimensional

Summary

Chapter 1:	1
Introduction and Objectives	1
1.1 Introduction:	2
1.2 General objectives:	8
1.3 Specific objectives:	8
➤ 1.3.1 Europium salt;	9
➤ 1.3.2 Lithium salt;	10
Chapter 2:	11
State of the art	11
2.1 Organic-Inorganic Hybrid Materials:	12
➤ 2.1.1 Origin, properties and synthesis;	12
➤ 2.1.2 Hybrid Siloxane-Poly(ether);	13
2.2 Relationship between Structure/Properties:	15
2.3 Thermal properties:	15
2.4 Ionic Conductivity Properties:	19
➤ 2.4.1 Ionic conductors;	19
➤ 2.4.2 Lithium-ion battery;	23
➤ 2.4.3 Effect of the plasticizers in conductivity;	23
➤ 2.4.4 Others parameters affecting the ionic conductivity;	24
2.5 Optical Properties:	26
➤ 2.5.1 Luminescence;	26
➤ 2.5.2 Europium (III);	28
➤ 2.5.3 Luminescence mechanism of Ln ³⁺ ions and selection rules;	29
➤ 2.5.4 Lanthanide containing OIH materials;	30
➤ 2.5.5 Antenna Effect;	32
➤ 2.5.6 Hypersensitivity;	34
➤ 2.5.7 Lanthanide containing OIH and photo-ageing;	35
2.6 Sol-gel method:	37
Chapter 3:	40
Methodology	40
3.1 Synthesis:	41
3.2 Materials and methods:	43
➤ 3.2.1 U-PPO _n films;	43
➤ 3.2.2 Differential Scanning Calorimetry (DSC);	44
➤ 3.3.3 Raman spectroscopy with temperature-controlled program;	44

➤ 3.3.4 Artificial Accelerated Photo-Oxidation;	45
➤ 3.3.5 Fourier Transform InfraRed (FTIR);.....	46
➤ 3.3.6 Small Angle X-Ray Scattering (SAXS) in situ with the temperature;	47
➤ 3.3.7 Photo-Luminescence;.....	50
➤ 3.3.8 Impedance Spectroscopy;.....	50
Chapter 4:.....	52
OIH:Eu ³⁺ Photo-Luminescence properties.....	52
4.1 Introduction to the Chapter:	53
4.2: Effect of Eu ³⁺ -loading in the thermal/structural properties of the OIH:.....	53
➤ 4.2.1 Thermal behavior;	53
➤ 4.2.2 Room temperature FT-IR analysis of the OIH:Eu ³⁺ complexes;.....	54
➤ 4.2.3 FT-Raman analysis of the OIH:Eu ³⁺ complexes;.....	60
➤ 4.2.4 SAXS analysis of the OIH:Eu ³⁺ complexes;	63
4.3: Effect of the UV-Vis radiation in the Photoluminescence properties of the OIH:Eu ³⁺ complexes:.....	65
4.4: Partial Conclusions:	73
Chapter 5:.....	74
Photo-Stability and Photo-Luminescence Properties	74
5.1 Introduction to the Chapter:	75
5.2 Effect of Eu ³⁺ – loading on photo-degradation:	75
5.3 Effect of PPO molecular weight on photo-degradation kinetics:.....	77
5.4 Identification of the UV-Vis photo-degradation products by ammonia chemical treatment:	80
5.5 Red → Blue photoluminescence transitions and its application:	82
5.6 Partial Conclusions:	84
Chapter 6:.....	85
Thermal, Structural and Electrical Properties hybrid blend	85
6.1 Introduction to the Chapter:	86
6.2 Thermal behavior:	86
6.3 Local structure:.....	89
➤ 6.3.1 FTIR at room temperature;.....	89
➤ 6.3.2 In situ with the temperature FT-Raman Spectroscopy;.....	94
6.4 Nanostructure:	99
➤ 6.4.1 Room Temperature SAXS patterns;.....	99
➤ 6.4.2 Evolution of the SAXS patterns during heating;.....	102
➤ 6.4.3 Quantitative evolution of the nano-structural parameters;	106
➤ 6.4.4 Nano-structure of the U _x PPO ₂₀₀₀ :U _{1-x} PEO ₁₉₀₀ OIH blends;.....	112
➤ 6.4.5 Evolution of nano-structural parameters of blend;.....	118

6.5 Effect of U-xPPO _n :U-1-xPEO ₁₉₀₀ blending and Li ⁺ doping in the electrical properties:	122
6.6: Partial Conclusions:	137
Chapter 7:	139
General Conclusion and Future Perspectives	139
Chapter 8:	142
References	142

Chapter 1:

Introduction and Objectives

1.1 Introduction:

Organic–inorganic hybrid (OIH) materials have tremendous potential as a bridge between the organic, mineral, and biological universes, opening new frontiers for the development of systems and devices for industrial and technological applications. These OIH materials are not simply the sum of two components, but rather, a synergic combination. In fact, the applications of OIH materials penetrate nearly all of the scientific field, for example, environment, human health care, optics, electronics, membranes, protective coatings, catalysts, sensors, barriers, and biology^{1,2,3,4,5,6,7,8,9,10,11}.

The multifunctional OIH materials developed in this thesis are nanocomposites based on an Ureasiloxane (ureasil - U) backbone covalently connected with polyether (PE) chains of either poly(ethylene oxide) (PEO) or polypropylene oxide (PPO). Due to the different polar sites present in the OIH structure, it is possible to have a wide variety of metal cations.

The repeating units grafted onto a siliceous backbone by urea, -NHC(=O)NH-, offers this material a blue emission under ultraviolet (UV) light. Their blue-emission can be tuned by adding cations with luminescent properties. In this way, the new emission color will be characteristic of the cation added into the OIH matrix. The organic templates play a key role, which mainly determines the morphologies, structures and properties of the hybrid materials, allowing them to be modified in different ways. Additionally, organic materials show poor mechanical stability, while inorganic materials show high resistance. In view of that, OIH materials have an enormous potential as protective coatings due the combination of the organic shape modification and the inorganic chemical/thermal/mechanical stability.

Dahmouche, K. et al¹², have studied the dependence of the Eu³⁺ concentration with the oxyethylene repeat units by different spectroscopically techniques and have shown

that in di-ureasils containing long organic segments, and low concentration of Eu^{3+} , the ions interact mainly with the carbonyl-type oxygens of the urea cross-links located at the organic/inorganic interface. In contrast, in the di-ureasils with short organic segments at the same ratio of Eu^{3+} concentration, the ions are unable to disrupt the strong and ordered hydrogen-bonded urea–urea structures and the preferential coordination sites are the ether-type oxygens of the polymer chains. However, for high salt concentration, the coordination of the Eu^{3+} cations with the OIH matrices has a distinct cation local site environment, involving the interaction with the urea carbonyl oxygens atoms.

Ribeiro S. J. L. et al¹³, have studied the photo-luminescence of OIH materials doped with different Eu^{3+} concentrations and have demonstrated that for lower doping concentrations dried gels present statistical distributions of Eu^{3+} , typical of an amorphous environment, while for higher concentrations a crystalline-like environment of Eu^{3+} was observed. This behavior leads to a decreasing radiative decay rates and spectral variations suggest the transformation of Eu^{3+} surroundings from amorphous-like to crystalline-like. The effect of the Eu^{3+} concentration on the photo-luminescence of OIH materials was also studied by Bermudez, V. de Z. et al, and the authors have found similar results¹⁴.

Molina, C. et al¹⁵, have studied the nano-structure of OIH materials with different Eu^{3+} concentrations by EXAFS measurements which indicate a decrease in Eu^{3+} coordination number with the increase in Eu-doping. A higher symmetry around the metal ion was also observed by increasing Eu^{3+} concentration, while a non-radiative decay path from the $^5\text{D}_0$ excited state become more important

Still talking about the reports done by Dahmouche, K. et al¹² the authors have related for OIH materials based on poly(oxyethylene) chains, the possibility to tune the

Eu³⁺ coordination between the carbonyl oxygens of the urea groups and the ether oxygen atoms of the poly(oxyethylene) chains controlling both the salt concentration and the polymer molecular weight. For these reasons, looking for an Eu³⁺ coordination with the urea group from the OIH materials, developed in this PhD thesis, with an amorphous surroundings for the guest cation, was adopted a low concentration of Eu³⁺, and the relationship, $[O_{\text{carbonyl}}] / [Eu^{3+}] = 3$ was kept constant for all materials studied.

Another field of application for OIH materials is in rechargeable lithium-ion batteries (LIBs). The emerging interest in materials with electrical properties comes from the increasing demand for electric vehicles, portable electronics, and implantable medical devices, due to their high energy density, high operating voltage, low self-discharge, long cycle-life and low toxicity. The research and development of new series of polymer electrolytes for LIBs has remained popular for decades because of their better performance in safety and fabrication compared to liquid electrolytes, which could cause safety concerns due to leakage and the explosive nature of volatile organic electrolytes, especially at high temperatures ($T > 60$ °C). Solid OIH electrolytes were considered to be the most promising candidates for high-temperature LIBs by virtue of enhanced safety and dimensional stability.

In the study of Li⁺-loading OIH materials, prepared with different kinds of polyethers macromeres have been investigated, polymeric matrices used for ion-lithium battery application, due to their high values of ionic conductivity^{16,17,18,19}. Some examples of polymers and their respective values of ionic conductivity are found in Table 1.1.

Table 1.1: Different polymers and their respectively value of ionic conductivity at room temperature.

Polymer	Ionic conductivity S/cm ⁻¹	Ref.
AG/CNT-D400 (6%)	3,39x10 ⁻⁴	16
PVDF-HFP/HPMC (4:1)	3,80x10 ⁻⁴	17
P(GMA-PEGMA)-D2000(11)	8,29x10 ⁻⁴	18
P(NA-GMA)-D2000(23)	8,23x10 ⁻⁴	19

However, these polymer still exhibit low value of ionic conductivity for industrial application, which it is necessary the research for new kinds of materials with best electrical properties. Among them the poly(ethylene oxide) (PEO) has tremendous potential to this kind of application due to the ionic transport facilitate by the segmental motion of chain. However, the linearity polyether chain favors the crystallization and the formation of semi-crystalline structure, which makes difficult the ionic motion¹⁸. On the other hand, the development of OIH materials allows the fabrication of materials based on PEO with a lower degree of crystallinity, owing amorphous pathway to the ionic motion.

Dahmouche, K. et al^{20,21}, have evidenced by room temperature AC Impedance Spectroscopy measurements with a maxima in the ionic conductivity for the relationship $[O_{\text{ether}}]/[Li]=15$ in the case of silica-PPG (polypropylene glycol) hybrids. In another paper Dahmouche, K. et al²², have investigated the effect of different Li⁺ concentration in the OIH matrix nano-structure, thermal properties and ionic conductivity. They have shown that for $[O]/[Li] > 20$, the free volume of polymeric framework was filled by Li⁺ ions, and the cation mobility is assisted by segmental motion of the polymer. The increase in the ionic conductivity is due to the increase of the charge transfers.

On the other hand, for $[O_{\text{ether}}]/[Li] < 15$, the contraction of polymer structure is large enough to induce a decrease of the specific volume leading to an increase in the thermal expansion of the material. For higher cation concentrations the decrease in

conductivity is attributed to the formation of cross-linking O-Li⁺-O between ether-type oxygen atoms of different polymer chains, which increases chain rigidity, or to cation-anion interactions. For these materials, increasing the Li⁺ ions concentration or decreasing the polymer chain length increased the glass temperature transition of the organic phase, which hinders the ionic conductivity.

For these reasons, we focused our attention on the well-established [O_{ether}]/[Li]=15 relationship for the U-PEO₁₉₀₀, and the effect caused by the addition of a plasticizer PPO₂₀₀₀, which has an amorphous characteristic, in the OIH blend U-xPEO₁₉₀₀:U-1-xPPO₂₀₀₀

In this point of view, the present thesis intends to discuss the effect of Eu³⁺-loading on OIH materials in order to study the new emission and the local coordination. The first chapter will be devoted to the investigation of the local coordination, carried out by FTIR measurements in transmission mode in the unsupported films (50 μm) of the OIH - Eu³⁺-loaded samples in the (-C-O-C-) backbone and amide region. The luminescence of the unloaded OIH material and Eu³⁺-loaded material was measured using monoliths with a thickness around a few millimeters. The luminescent properties of these OIH matrices were also investigated as a function of the UV-vis irradiation and their nano-structural characterization was obtained by SAXS. Another point of importance for the development of this thesis was to monitor the loss of Eu³⁺ coordination. Therefore, in the second chapter, the study of OIH photo-degradation will be presented to better understand the effect of the loss of Eu³⁺ coordination and of unloaded matrix photoproducts. This study was carried out by FTIR spectral signature and luminescence properties as a function of the artificial accelerated UV-irradiation (λ ≥ 300 nm).

The third chapter will be focused on the study of the LIB, which will be analyzed to find the effect of Li⁺ - loading on thermal, structural and electrical properties of the OIH

matrices based on PEO₁₉₀₀, PPO₂₀₀₀ and U_xPEO₁₉₀₀:U_{-1-x}PPO₂₀₀₀ blends. The thermal features of the OIH matrices were carried out by DSC measurements in a temperature range of -100 °C to 200 °C; these results will be used to examine the structural properties of the OIH matrices. This investigation can be done using FTIR spectroscopy at room temperature and in situ monitoring during programmed temperature variation, which uses time resolved Raman spectroscopy from - 90°C to +100 °C. The nano-structural features of these matrices were carried out by SAXS with in situ monitoring during programmed temperature ranging from - 90°C to +100 °C. Impedance Spectroscopy was used to analyze the thermal/vibrational/structural/nano-structural results to examine their ionic conductivity properties. This kind of study allowed for the proposition of the Electrical Equivalent Circuit and the relationship between the circuit components and the OIH structural building blocks.

The innovative character of this thesis aims to understand the cause of several external influences on the multifunctional OIH materials properties, as Eu³⁺ and/or Li⁺ - loading, temperature, photo-ageing and PEO₁₉₀₀:PPO₂₀₀₀ blending. Photo and thermal stability are important structural features, which need to be explored in depth. Consequently, the objectives of this thesis are given as follows:

1.2 General objectives:

This PhD thesis aims to better understand the optical / electrical properties of the multifunctional OIH materials based on PEO₁₉₀₀ and PPO_n (n = 5, 33 and 68, ascribed to the mw. 230, 2000 and 4000 g.mol⁻¹, respectively) containing Eu³⁺ and Li⁺, synthesized by the sol-gel method.

This general objective is accompanied by the study of the effect of lanthanide and alkaline cation incorporation, photo-oxidation, temperature and the properties of PEO/PPO blending in their structure.

1.3 Specific objectives:

The specific objectives were classified into two sets, based on the functional properties of materials derived from the Eu³⁺ or Li⁺ salts incorporation.

➤ 1.3.1 Europium salt;

The first set of objectives comprises of the expansion of the previous knowledge of lanthanide-containing materials and reports the influence of the polymer conformation from the ligand to metal charge transfer with reference to a detailed investigation of their crystalline-amorphous structures and vibrational properties. This set of objectives was achieved from an in-depth study of the OIH matrix structures, focused on the effect of the Eu^{3+} -loading on the thermal, vibrational, structural and nanostructural properties. Moreover, the optical properties were studied as a function of the artificial polymer photo-oxidation using photoluminescence and FTIR techniques to utilize Eu^{3+} cations to probe its local environment, with special emphases on the loss of the “*antenna effect*” from the organic ligands and the Eu^{3+} *f-f* transition. Thus, the specific objectives are:

- Analysis of the Eu^{3+} -loading effect in the OIH matrix structure by:
 - Differential Scanning Calorimetry (DSC).
 - Room temperature Infrared spectroscopy (FTIR).
 - *In situ* Raman spectroscopy data collection during programmed temperature change.
 - Room temperature Small Angle X-Ray Scattering (SAXS) data collection during programmed temperature change.
- Time effect of the UV-vis light irradiation ($\lambda > 300\text{nm}$), corresponding to mild conditions of accelerated aging, on the structure of the OIH:
 - Room temperature Infrared spectroscopy (FTIR).
- Evaluation of the photo-degradation kinetics and OIH photo-products:
 - Ammoniac chemical treatment.
 - Room temperature Infrared spectroscopy (FTIR).
- Photoluminescence analyses of the OIH: Eu^{3+} complex and its dependence on the UV-vis photo-degradation time:
 - Photoluminescence
- Correlate the evolution of optical and the structural properties during artificial aging.

➤ 1.3.2 Lithium salt;

The second set of objectives aims to assess the effect of $U_x\text{PEO}_{1900}/U_{1-x}\text{PPO}_{2000}$ blending on the relationship of structure vs. ionic conductivity, while focusing on the PPO_{2000} plasticization and the structural conformation of PEO_{1900} in order to better understand the ionic conductivity of OIH polyelectrolytes. This set of objectives was achieved from an in-depth study of the OIH matrix structures, focused on the effect of the Li^+ -loading on the thermal, vibrational, structural and nanostructural properties. This set of objectives consists of the following steps:

- Analysis of the effects on thermal and nanostructural properties in the OIH matrix due to Li^+ -loading and plasticizer (PPO_n) blending by:
 - Differential Scanning Calorimetry (DSC).
 - Room temperature Infrared spectroscopy (FTIR).
 - *In situ* Raman spectroscopy data collection during programmed temperature change.
 - *In situ* Small Angle X-Ray Scattering (SAXS) data collection during programmed temperature change.
- Analysis of the effect of Li^+ -loading on the OIH matrix vibrational properties as well as the active sites in the $-\text{O}-\text{Li}-\text{O}-$ bonding involving a polar oxygen ether type by:
 - Room temperature Infrared spectroscopy (FTIR).
 - *In situ* Raman spectroscopy data collection during programmed temperature change.
- Ionic conductivity analyses of the OIH: Li^+ electrolytes and its dependence on the temperature, PEO_{1900} structural conformation and PPO_{2000} fraction in the $U_x\text{PEO}_{1900}:\text{Li}^+:U_{1-x}\text{PPO}_{2000}:\text{Li}^+$ OIH blend:
 - Impedance Spectroscopy.
- Correlation of Ionic Conductivity/Structural properties.

Chapter 2:

State of the art

2.1 Organic-Inorganic Hybrid Materials:

➤ 2.1.1 Origin, properties and synthesis;

The oldest reference of the existence of hybrids is found in Greek mythology²³, (Υβρίδιο [*hybris*]) where fantastic creatures populate the human imagination. As an example consider the Griffon (Fig. 2.1), a creature that combines the strength of a lion with the shrewdness and flying ability of an eagle, thus resulting in a fearful guardian of the temple of Gods.



Figure 2.1: Griffon: Hybrid creature from Greek mythology²⁴.

Keeping this idea in mind, Organic-Inorganic Hybrid (OIH) materials possess a tremendous interest in commercial applications due to their excellent physical-chemical properties which combine the thermal/chemical stability of ceramics with the workability and flexibility of organic polymers. The ability to conjugate the two (organic and inorganic) worlds into a unique material can lead to the development of a new series of multifunctional materials possessing inherited properties and a wide field of applications, such as: optics²⁵, energy²⁶, engineering²⁷, environmental²⁸, biology²⁹, medicine³⁰, solar cells³¹, catalysis³², sensors³³ and batteries³⁴.

OIH materials are nanocomposites with the phase distribution on a nanometric scale³⁵. The nature of the organic-inorganic interphases is used to categorise the OIH matrix into two classes. In class I, the interphase interaction is defined by weak bonds

(hydrogen bonding, van der Waals, etc), while in class II the interphase interaction is characterized by the covalent bond between the inorganic and organic components³⁶. A schematic diagram of OIH materials in classes I and II are shown in Fig. 2.2.

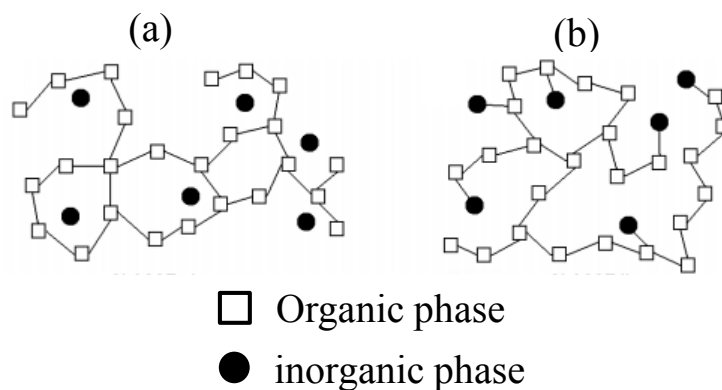


Figure 2.2: Schematic representation of class I (a) and class II (b) OIH materials ^{Adapted from 37}.

➤ 2.1.2 Hybrid Siloxane-Poly(ether);

Poly-siloxanes were synthesized for the first time by Hall, P. G.³⁸ and Fish, D.³⁹, followed by the investigation of similar systems by Spindler, R. and Shriver, D. F. The chemical formula of poly-siloxanes is $(R_2SiO)_n$, where R is typically methylsiloxanes (CH_3), but can also be H, alkyl, or aryl groups. The siloxane-poly(ether) hybrid materials consist of a biphasic system in which the siloxane part acts as crosslinking nodes for the polymeric chain, thus giving rise to a three-dimensional (3D) network. The main features include transparency, thermal/chemical/mechanical stability, flexibility, processability, hydrophilicity/hydrophobicity and good film adhesion to substrate coatings. The Siloxane-Poly(ether) OIH materials developed in this work are nanocomposites based on an Ureasiloxane (U) backbone covalently bonded to polyether – PE, polyethylene oxide (PEO) or polypropylene oxide (PPO) chains (Fig. 2.3).

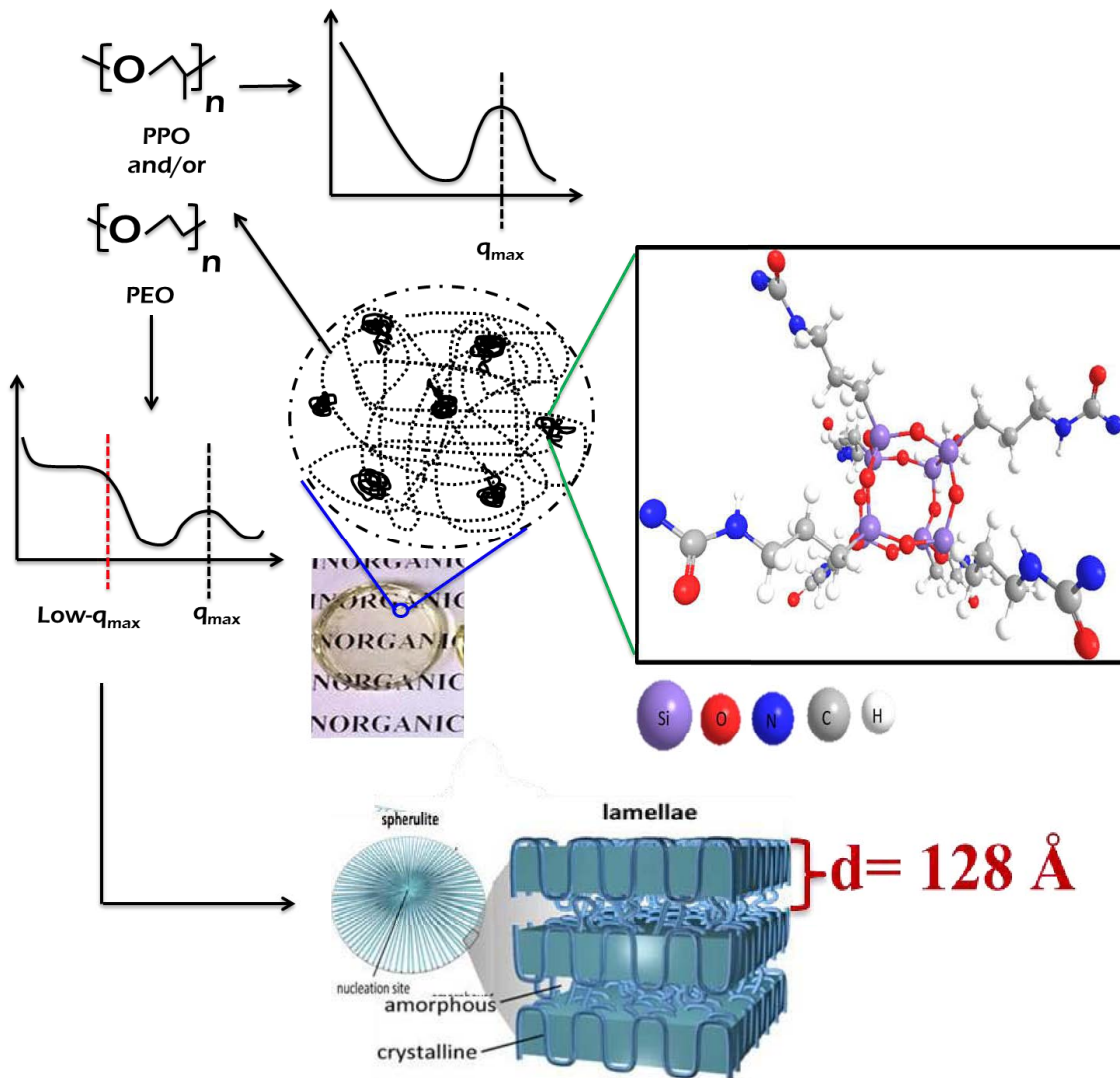


Figure 2.3: Transparent Siloxane-Poly(ether) hybrid materials, based on PEO and PPO polymers. The magnification of the crosslinking nodes exemplifies the Si-O-Si crosslinking structure network of the matrix ^{Adapted from 40}.

The siloxane nodes present in the structure confer to the amorphous OIH materials an electron density contrast easily observed by Small Angle X-Ray Scattering (SAXS). In the case of concentrated system the interference caused by the X-ray scattering from neighboring siloxane nodes led to a maximum at the q_{max} value. However, the intensity can vary with the presence of guest cations, coordinated with the different polar oxygens present in the segment chain⁴¹ and with the polymer backbone conformation, as with the PEO case⁴².

The linearity of PEO segmental chains confers to this polymer a helical conformation forming a semi-crystalline polymer⁴³. The presence of this crystallinity in the OIH matrix affects the correlation peak by the q_{\max} intensity decreases due to a lower electron density contrast between the organic-inorganic phases. Another interesting feature observed in semi-crystalline polymers is the presence of a second maximum located at middle q -range values which can be attributed to the long period peak. As displayed in Figure 2.3, the long period distance L is composed by the sum of the crystalline lamellae thickness LC and of the amorphous layer LA ($L = LC + LA$). This reflection shows a temperature dependency and a persistency above the fusion temperature, which is not well known in literature and will later be discussed in chapter 4.

2.2 Relationship between Structure/Properties:

The multifunctional OIH matrices developed in this thesis have an intrinsic relationship between their different properties and their structure. The properties associated with ionic conductivity are intimately connected with their thermal behavior⁴⁴. In the same way, the presence of the urea group in the OIH structure demonstrates an interesting photo-luminescent property, which shows a dependence on the polymeric nature⁴⁵. The understanding of these properties will be explained in more detail below, which will be helpful for a better comprehension of the interpretation of the results discussed in Chapter 6.

2.3 Thermal properties:

The structure of polymers has an interesting dependence on the temperature. To gain a better understanding of this kind of material, knowledge about the concept of glass transition temperature, T_g , is important. One first definition concerning T_g values

is the division of materials into two main families: Elastomers, when materials have a $T_g < 0\text{ }^\circ\text{C}$, and rigid structures, when polymers have a $T_g > 25\text{ }^\circ\text{C}$.

Additionally, in terms of structure, these non-crystalline materials have different states: *i*) glass state, when $T < T_g$, *ii*) rubber-like state, when $T > T_g$. The representation of the volume variation of a non-crystalline material with the temperature is seen in Fig. 2.4 (curve 2). From this Figure, it is observed that in a temperature range below T_c that approaches the rubber-like state, the specific volume of the non-crystalline material decreases at almost the same rate that is found in the liquid-like state. The slope of the curves is drastically affected when the temperature reaches the T_g of the non-crystalline material, where the volume variation becomes close to 0.

On the other hand, for a crystalline material Fig. 2.4 (curve 1), the cooling of the material in the liquid state shows a large change in of volume, characterizing the crystallization process, in a constant temperature. After that, in a semi-crystalline polymer will be found the mixture of these two effects in the same material⁴⁶. The glass transition temperature dependence for non-crystalline materials, for which the cooling rate is influenced by the relaxation time, is characterized by the time during which the structure adapts itself to a variation in temperature⁴⁷.

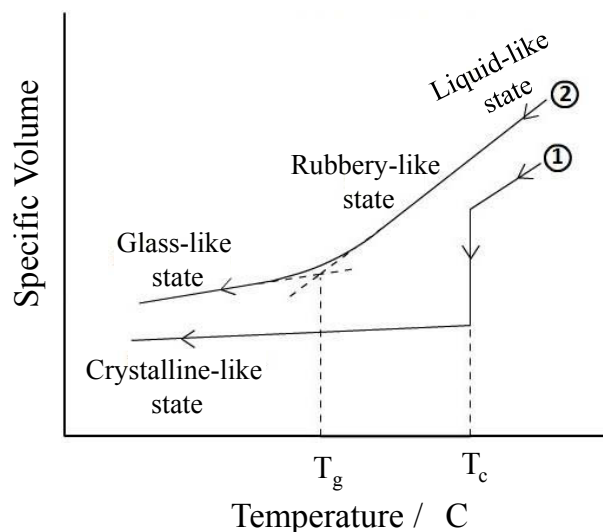


Figure 2.4: Dependency of the Volume with the Temperature for a crystalline (curve 1) and non-crystalline material (curve 2) ^{Adapted from 48}.

At $T > T_g$, polymer chains are capable of achieving equilibrium configurations, consequently, extra hole of “*free volume*” (v_f), is created, thus giving rise to the non-crystalline, rubbery state. The presumption that molecular transport is regulated by free volume was first introduced by Cohen and Turnbull (1959). However, their conceptualization was initially believed to be suitable only for liquids. The “*free volume*” theory for ion diffusion through a polymeric system can be applied on several levels, and can also provide a basis for a qualitative understanding of the influence on diffusional behavior by variables such as temperature, concentration, and solvent molecular size. Elastomers, or non-crystalline rubber-like materials, in conditions far above their respective T_g , possess a large fractional hole of “*free volume*”. In this sense, the ionic motion through the segmental chains is not only large in magnitude, but also dependent on the temperature⁴⁹. The dependence of v_f with T_g is expressed as follows⁵⁰:

$$v_f = v_g[k + \alpha(T - T_g)] \quad (1)$$

As non-crystalline, amorphous materials are cooled, the motion of individual polymer chains becomes so constrained that the cooling rate becomes faster than the rate at which the polymer sample can volumetrically relax. The non-equilibrium condition created is referred to as the glass state. In this way, the glass state is a consequence of the free volume decrease, accompanied by a higher compaction of the organic chain segments⁵¹. This leads to lower organic chain permeability, which results in decreased dissolution properties. Thus, the passage from the rubbery to the glass state is denoted as the glass transition. In this sense, the glass state can be defined as a system possessing solid mechanical properties while also exhibiting the typical structural features of a disordered liquid.

Quantitative information about the temperature at which the T_g occurs in any material can be measured by the change in the ΔC_p slope curves carried out by

Differential Scanning Calorimetry (DSC) measurements (Fig. 2.5). This measurement is based on the classical thermodynamics shown by the Ehrenfest second-order transition, expressed as follows⁵²:

$$\Pi = \frac{1}{VT} \frac{\Delta C_p \Delta k}{(\Delta\alpha)^2} \quad (2)$$

One of the basic characteristics of the glass transition is the Prigogine-Defay ratio Π , which is known to give a general correlation between the compressibility Δk , the thermal expansion coefficient $\Delta\alpha$, and the isobaric heat capacity C_p , while occurring in a temperature range near of the glass transition temperature $T=T_g$ ⁵³.

DSC measurements also provide other important information concerning semi-crystalline polymers. At a temperature range above T_g these materials are not completely amorphous, having a crystalline-amorphous phase equilibrium. The completely amorphous (liquid-like) phase is reached at the melting point (T_m), characterized as an endothermic peak. The peak area can be used to calculate the crystalline mass fraction.

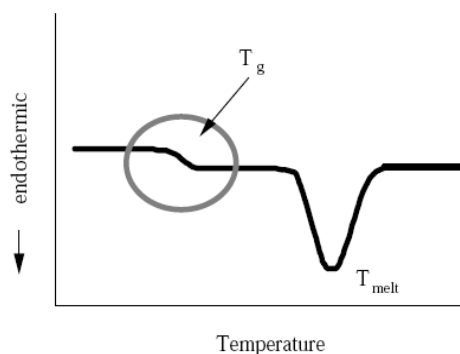


Figure 2.5: Schematic representation of a DSC pattern of a generic semi-crystalline polymer, representing the glass transition (T_g) and the melting point (T_m)⁵⁴.

Miscible blends constituted by two or more non-crystalline polymers interact with each other, thus giving rise to a unique phenomenon of T_g ⁴¹. On the other hand, in the case of blended systems constituted by immiscible non-crystalline polymers, DSC patterns are identified by the presence of more than one glass transition temperature having a clearly defined separation between the two phenomena⁵⁵. The immiscible

blend properties are controlled by their morphology, which is dependent on the thermodynamic properties, rheological properties and thermal history properties⁵⁶.

2.4 Ionic Conductivity Properties:

As a consequence of the thermal properties, polymers show another important feature intimately correlated with the in temperature, ionic conductivity. The ionic conductivity is dependent on the polymer chain motion, which becomes more rigid and less conductive as the value of T_g increases. The dependency of the ionic conductivity with T_g is correlated using the Vogel-Tamman-Fulcher – VTF equation, derived from the Arrhenius-law, as follows^{57,58}.

$$\sigma = \sigma_0 \exp\left(\frac{-Ea}{T - T_0}\right) \quad (3)$$

where σ_0 , T_0 and Ea are fitting parameters. σ_0 is the well-known Arrhenius pre-exponential factor, which represents the frequency of collisions. For polymers, σ_0 can be associated with the organic chain mobility as well as the state density. T_0 is supposed to have a close relationship with the glass transition temperature, and Ea is the activation energy⁵⁹.

➤ 2.4.1 Ionic conductors;

The term “*molecular electronics*” had a strong impact on the scientific community in the 1990s because the idea that a single molecule might function as a self-contained electronic device gave rise to the possibility of developing a computer based on molecular-sized electronic elements⁶⁰. After the first studies conducted by Wright P. V.⁶¹ in 1973 in the field of ionic conductivity of a material based on Poly(ethylene oxide) (PEO), the evolution of electrolytic, solid polymers have shown a wide expansion⁶², reflecting the progress of the understanding of the ionic motion process

and the correlation between the molecular architecture, supramolecular and conductivity.

The possibility of utilizing “*molecular electronics*” was first discussed by Carter, F. L. in 1981⁶³ and 1983⁶⁴, which led to a progression in the semiconductor industry, with the size reduction of electronic devices on the order of micrometers (μm). Extrapolation of information from a timeline composed of research from this time (Fig 2.6) show that within about 30 years, electronic components will reach a size on the order of nanometers.

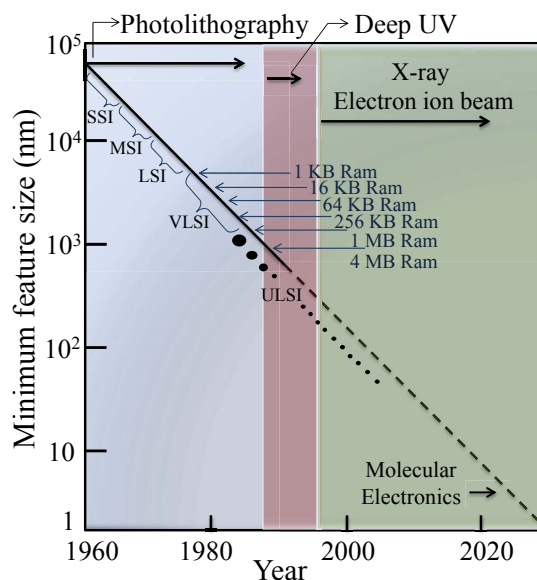


Figure 2.6: Microlithographic trends in minimum device feature size and imaging technology. The figure illustrates the time evolution of random access memory (RAM) devices⁶⁰. *Meaning of acronyms at Glossary.*

Nowadays, 29 years after this publication, OIH materials are in the forefront for this kind of application, and shows several advantages compared to polymeric devices due to the possibility of a fine control of the final material properties, because having the chemical nature of the organic and/or inorganic phases allows for the size and the morphology of the hybrid network to reach a nanometric scale. Beyond the OIH materials characteristics mentioned above, such as their transparency, flexibility, and mechanical stability, the nature of the interface interactions, found in some modified

poly-siloxanes solid polymeric electrolytes, can reach a value of conductivity on the order of 10^{-4} S.cm⁻¹ at room temperature. This new generation of materials will improve the manufacturing of electronic devices, with the human mind being the only limiting factor (Fig. 2.7).

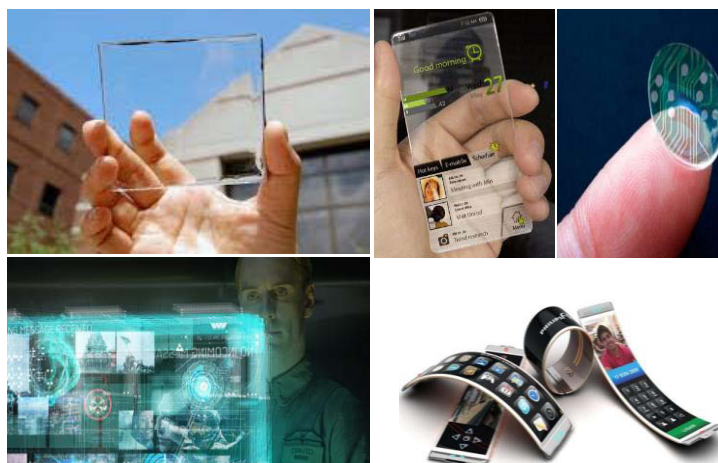


Figure 2.7: Examples of the future manufacturing of electronic devices utilizing OIH materials Compilation from 65,66,67,68

The most known solid polymeric electrolyte is the poly(ethylene oxide)/LiClO₄ system⁵¹, with a lithium salt defined by the ratio [O]/[Li] = 8, where “O” is the polar ether-type present in the polymeric chain. Poly(ethylene oxide) (PEO) and poly(propylene oxide) (PPO), Fig. 2.8, have been the most popular polymers used in the development of new ionic conductors since the ‘70s.

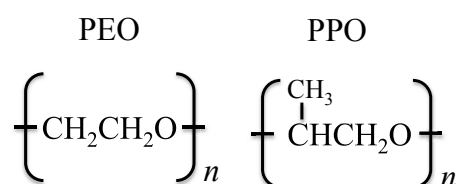


Figure 2.8: Chemical formula of monomers constituting PEO and PPO polymers [elaborated by the author].

A set of polymeric materials shows an ionic conductivity value around 10^{-7} and 10^{-6} S.cm⁻¹ at room temperature, even after lithium salt dissociates into the matrix. However, this range of conductivity is far below those considered attractive for Lithium-ion

battery (LIB) applications ($10^{-3} - 10^{-2} \text{ S.cm}^{-1}$), which have motivated the research of other materials with molecular structures that allow for higher values of ionic conductivity. Wu H-Y and co-authors⁶⁹ studied organic-inorganic hybrid electrolytic membranes based on triblock co-polymers, poly(propylene glycol)-block-poly(ethylene glycol)-block-poly(propylene glycol) bis(2-aminopropyl ether) (ED2003), poly(ethylene glycol) diglycidyl ether (PEGDGE), poly(vinylidene fluoride-co-hexafluoropropylene) (PVdF-HFP), 2,4,6-trichloro-1,3,5-triazine (cyanuric chloride, CC) and 3-(glycidyloxypropyl) trimethoxysilane (GLYMO), synthesized by the sol-gel process. They have found that the plasticized hybrid electrolytic membrane exhibits a high ionic conductivity, with a value of $6.9 \times 10^{-3} \text{ S.cm}^{-1}$ at 30°C .

Poly(ethylene oxide) – PEO₁₉₀₀, i.e.: wt = 1900 g.mol⁻¹, is a semi-crystalline polymer, possessing both amorphous and crystalline phases at room temperature, thus being an excellent candidate to apply as LIBs due to its capability of ionic transport that is facilitated through the polar – oxygens present in the segment of the organic chain, which allows for the dissolution of a wide variety of inorganic cations. Li⁺ ions dissolved in poly-ether-based OIH, have several advantages, such as good compatibility, ease of shaping into thin films of large surface area, leak-proof nature, and manufacturability^{70,71,72,73}. On the other hand, the multiphase nature of semi-crystalline PEO is most often regarded as a major problem in this kind of material due to the transport of Li⁺ ions in these electrolytes, which is associated with the local relaxation and segmental motion of the amorphous regions in the PEO chains⁷⁴. The suppression of crystallinity of polymer chains improves the polymer chain mobility, which in turn, leads to better ionic transfer through the organic chain segments⁷⁵.

➤ **2.4.2 Lithium-ion battery;**

Rechargeable lithium-ion batteries (LIBs) are emerging power sources that are currently used in many portable electronic devices and electric vehicles due to their high energy density, high operating voltage, low self-discharge, long cycle-life and low toxicity⁷⁶.

However, new battery components must be developed for some applications in order to obtain high performance LIBs with better safety and low cost. The electrolyte, an important component of LIBs, plays a critical role in terms of electrochemical performance and safety; however, traditional liquid electrolytes for commercial LIBs could cause safety concerns due to leakage and the explosive nature of volatile, organic electrolytes, especially at high temperatures ($T > 60\text{ }^{\circ}\text{C}$). Solid polymer electrolytes were considered the most promising candidates for high-temperature LIBs by virtue of enhanced safety and dimensional stability. Polymer gel electrolytes have high electrical conductivity values at ambient temperature, but are not mechanically stable and are incompatible with the high temperature range due to the volatility and flammability of the added plasticizer⁷⁷. Because of this, the Siloxane-Poly(ether) OIH Li^+ -containing materials developed in this thesis deserve special attention for this kind of application, which combines their excellent mechanical / thermal properties with the possibility of allowing the organic portion to behave independent of the inorganic one⁷⁸.

➤ **2.4.3 Effect of the plasticizers in conductivity;**

Polymeric blends often exhibit properties that are superior to the single- component polymers. A similar observation was made with enhanced ionic conductivity of PEO: Li^+ -loaded electrolytes with the addition of pyrrolidinium (RTIL), which was reported by Shin J. H. in 2005⁷⁹; the effect was attributed to the formation of a salt-containing amorphous phase of PEO at low temperatures with RTIL leading to an

overall reduction of crystallinity of the system. Plasticizers are often utilized to improve material flexibility by lowering the glass transition temperature⁸⁰. The Li⁺ ions that are bonded with the “O” atoms of PEO segments could be partially or fully freed from that trap by bonding with the anion of RTIL, hence leading to a larger number of charge carriers with improved charge migration. Thus, incorporation of RTIL is an effective way of enhancing the ionic conductivity of PEO-based PEs to an appreciable level⁸¹.

As a result, several approaches have been developed in order to improve the ionic conductivity by increasing the OIH:Li⁺ monoliths amorphous content, such as addition of nanosized particles, copolymerization, dispersion of different fillers, synthesis of block copolymers or blends and use of different plasticizers^{82,83,84}. The high value of conductivity could also be attributed to the presence of plasticizers, which reduces the viscosity of the poly-electrolyte and assists in the metal salt dissociation, thus contributing to the increase in the number of charge carriers in the films⁸⁵. The reduced viscosity improves the segmental motion of the host polymer, therefore increasing its backbone segmental flexibility⁸⁶.

➤ **2.4.4 Others parameters affecting the ionic conductivity;**

Alternatively, the ionic conductivity is not only sensitive to the degree of crystallinity of the polymer matrix, but also to two other important factors:

i) The salt concentration – *i.e.*: the conductivity of an electrolyte is highly dependent on the charge carrier concentration, n , the nominal charge of the carriers, q , and the mobility of the charge carrier, μ , through the relation of $\sigma = nq\mu$ ⁸⁷. Therefore, as the salt concentration increases, the number of the charge carriers will also increase, which then leads to the enhancement of the conductivity. However, a high value for the charge carrier concentration can saturate the polymeric active sites, thus decreasing the ionic motion⁸⁸. Considering this for our work, we have decided to utilize a ratio well-known

by the literature, $[O_{\text{ether}}]/[Li^+] = 15$ ⁸⁹. Fig. 2.9 shows the effect of a high charge carrier concentration on the ionic conductivity.

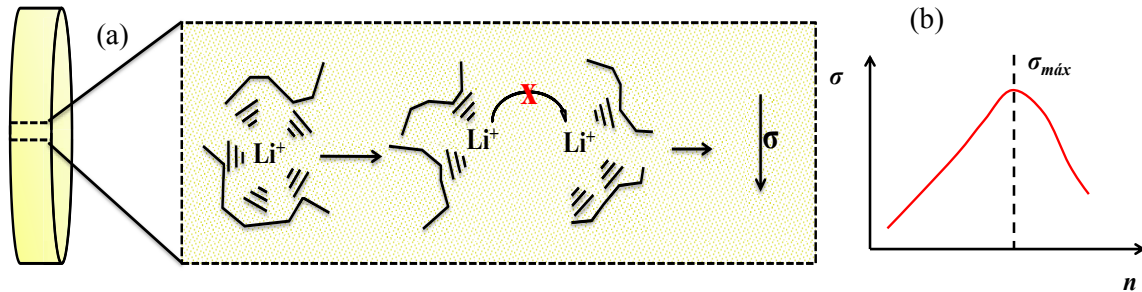


Figure 2.9: (a) Ionic transport interrupted by the active charge transfer saturation and (b) Dependency of the ionic conductivity with the charge transfer (n) concentration [^{elaborated by the author}].

ii) The temperature: the polymer segmental chain motion is highly dependent on the T_g value of the polymer backbone. In a temperature range below T_g , the rigidity is enough to block the ionic motion through the polymeric active sites, preventing ionic conductivity (Fig. 2.10 (a)). The rise in temperature promotes the glass \rightarrow rubbery \rightarrow liquid-like transition, accompanied by the increase of the polymeric free volume, which facilitates the Li^+ migration through the ether-type oxygens from organic chains. This behavior is induced by an increase in solid state diffusion in the poly-electrolyte as well as a decrease in charge transfer resistance between electrode and electrolyte (Fig. 2.10 (b)).

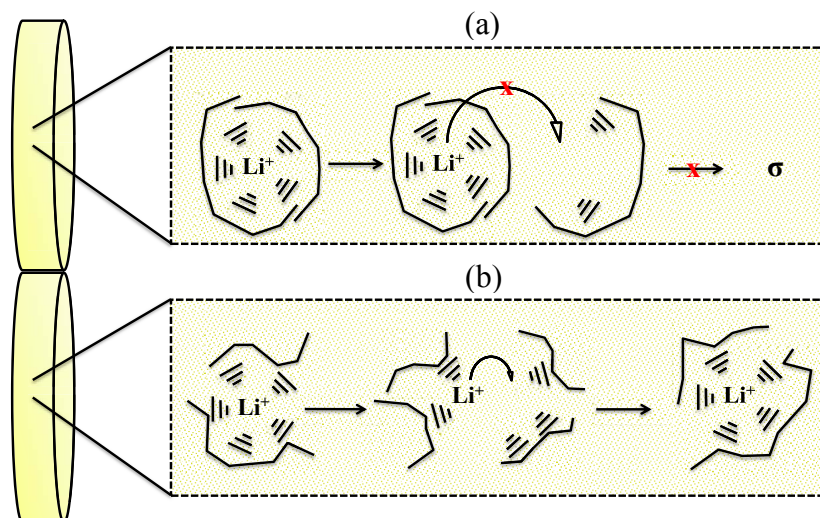


Figure 2.10: Schematization of the Li^+ ionic transfer mechanism (a) in the glass state ($T < T_g$) and (b) in the rubbery state ($T > T_g$) [^{elaborated by the author}].

2.5 Optical Properties:

Siloxane-polyether OIH materials have another interesting property, which is their photoluminescent capacity, emitting a blue light when exposed to UV-radiation. The characteristic blue color of these matrices comes from NH groups from urea bridges and the electron-hole recombination in the siliceous domains in the inorganic backbone, which leads to a broad emission. The photo-luminescent properties offer a new range of possible applications to Siloxane-polyether OIH materials developed in the thesis. This is true once their luminescent features can be tuned, adding most, or all, luminescent cations in the form of trivalent lanthanide ion (Ln^{3+}). For this kind of application, it is important to know that the luminescent properties of the OIH: Ln^{3+} complex can happen independent of the ionic conductivity. This knowledge is important to open new fields of application for this material; as an example, it can be used as the OIH bio-marker material, which was developed by Powell J. A. and co-authors⁹⁰, which is vital to the understanding of metal coordination/ discoordination, life time, bio-compatibility, among others.

➤ **2.5.1 Luminescence;**

Luminescence is a spontaneous radiative recombination process which involves the participation of electrons and holes. According to IUPAC, luminescence is defined as follows: “*Spontaneous emission of radiation, from an electronically or vibrationally excited species not in thermal equilibrium with its environment*”⁹¹. The excitation of carriers prior to recombination requires a potential driving energy, which can be electrical, optical, mechanical or thermal. Although several publications report its radiative emission as phosphorescence or fluorescence, it is recommended to nowadays use the term “*Luminescence*” for all these phenomena. There have been related studies of luminescent materials since the seventeenth century, which was the origin of the

phosphor (*phosphori*) denomination on the study of BaS, believed to be the first-ever synthesized sulfide phosphor, realized by Vincenzo Casciarolo in 1602⁹² i.e.: The word phosphorus derives from the Greek φωσφορος [*fosforos*], combining φωσ (light) and φερω (to carry), therefore meaning light carrying or luminous⁹³; in 1888, Eilhard Wiedemann introduced the terms luminescence, photoluminescence (PL), electroluminescence (EL), thermoluminescence (TL), chemiluminescence, triboluminescence, and crystalloluminescence by creating the first classification of different phosphors based on their type of excitation⁹⁴.

This phenomenon has captivated mankind for a long time, whether it was through natural light emitted by glow worms, Aurora Borealis, rotting fish, or luminescent wood (Fig. 2.11). The utilization of the luminescence properties was documented by the Chinese people as early as 2000 years ago. It was used for paintings which glowed in the dark; the source of this effect belongs to the lanthanides family, more specifically, the trivalent lanthanides ions, Ln^{3+} , whose luminescence occurs naturally⁹⁵.



Figure 2.11: Examples of natural light emitted by glow worms, Aurora Borealis, rotting fish and luminescent wood [Compilation from 96,97,98,99].

➤ 2.5.2 Europium (III);

It is already known that organic ligands and ion concentrations have great influence on the luminescent properties of Eu^{3+} due to the variation of the microenvironments around the cations¹⁰⁰. On the other hand, there are several reasons why the Eu^{3+} ion is so often used as a spectroscopic probe for the symmetry of the first coordination sphere of a trivalent lanthanide ion. First of all, Eu^{3+} ions are excellent activators with strong red-emission and high luminescence quantum efficiencies, good color purity and great radiation stability¹⁰¹. The ground state (${}^7\text{F}_0$) and the most important emitting excited state (${}^5\text{D}_0$) are non-degenerated and thus, are not split by the crystal-field effect. The most important transitions in the luminescence spectra are from the ${}^5\text{D}_0$ excited state to ${}^7\text{F}_J$ levels with a low J value ($J = 0, 1, 2$). This also facilitates the interpretation of the experimental absorption and luminescence spectra. Furthermore, the trivalent europium ion (Eu^{3+}), comparable to Ln^{3+} ${}^5\text{D}_0 \rightarrow {}^7\text{F}_J$ transition intensities, provides an asymmetrical ligand field that drastically facilitates the ${}^5\text{D}_0 \rightarrow {}^7\text{F}_2$ transition to yield an essentially monochromic single-band red photoluminescence emission¹⁰². This characteristic allows for the use of Ln^{3+} to probe its local environment¹⁰³, which shows that the different ${}^5\text{D}_0 \rightarrow {}^7\text{F}_J$ lines are well separated, meaning that there is virtually no overlap between the crystal-field levels belonging to different ${}^7\text{F}_J$ levels. Another interesting characteristic is that the wave functions of the ${}^7\text{F}_J$ levels and of the ${}^5\text{D}_0$, ${}^5\text{D}_1$ and ${}^5\text{D}_2$ excited states are well described within the intermediate coupling scheme and J is a good quantum number. J-mixing is limited so that there is very little flexibility with the selection rules and it is possible to obtain an accurate theoretical description of the energy level structure of the $4f^6$ configuration of Eu^{3+} ¹⁰⁴.

➤ 2.5.3 Luminescence mechanism of Ln^{3+} ions and selection rules;

Ln^{3+} ions have attracted considerable research interest due to their excellent luminescent properties, especially because they have intra 4f-4f luminescence spectra characterized by narrow lines with high color purity. This feature is observed due to the shielding of 4f electrons by outer $5s^2$ and $5p^6$ electrons¹⁰⁵.

A luminescence spectrum (or emission spectrum) is recorded by fixing the excitation wavelength while the detection wavelength of the spectrofluorimeter is scanned. The luminescence spectra of Eu^{3+} compounds are more informative than the corresponding absorption spectra. Many Eu^{3+} compounds show an intense photoluminescence, due to the $^5\text{D}_0 \rightarrow ^7\text{F}_J$ transitions ($J = 0-6$) from the $^5\text{D}_0$ excited state to the J levels of the ground term ^7F . However, $^7\text{F}_5$ and $^7\text{F}_6$ transitions levels are not often observed because they are outside of the wavelength range of the detectors, as represented at Fig. 2.12, which shows the luminescence spectrum of the europium β -diketonate complex $[\text{Eu}(\text{tta})_3(\text{phen})]$ / (tta = 2-thenoyltrifluoroacetylacetonate, phen = 1.10-phenanthroline). The Eu^{3+} emission spectra, in the spectral range from 575 to 725 nm, reveals that the positions of the different $^5\text{D}_0 \rightarrow ^7\text{F}_J$ transitions between the J and the J + 1 line increases with an increasing J value, i.e.: the $^5\text{D}_0 \rightarrow ^7\text{F}_1$ transition is very close to the $^5\text{D}_0 \rightarrow ^7\text{F}_0$ transition, but the $^5\text{D}_0 \rightarrow ^7\text{F}_4$ transition lies more than 50 nm further from the infrared than the $^5\text{D}_0 \rightarrow ^7\text{F}_3$ transition¹⁰⁶. Most transitions observed in the luminescence spectrum for Ln^{3+} compounds are induced by electric dipole transitions (ED transitions), which are a consequence of lanthanide ion and electric field vector interactions through an electric dipole.

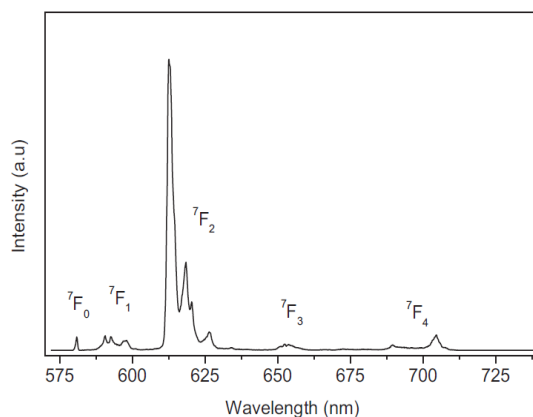


Figure 2.12: Luminescence spectrum [Eu(tta)3(phen)] at 77 K upon excitation at 396 nm. All of the transitions start from the 5D_0 state¹⁰⁴.

Laporte's parity selection rule states that levels with same parity cannot be connected by electric dipole transitions; as a consequence, f–f transitions are forbidden by the ED mechanism. However, under the influence of a ligand-field, non-centrosymmetric interactions result in the mixing of electronic states of opposite parity, which somewhat relaxes the selection rules and the transitions become partially allowed; they are called induced (or forced) electric dipole transitions. Some induced ED transitions are highly sensitive to minute changes in the Ln^{3+} environment and are called hypersensitive. Selection rules are derived under several hypotheses which are not always completely fulfilled in real compounds, so in reality, the terms “forbidden” and “allowed” transitions should be understood as “low probability” and “high probability” transitions¹⁰⁷.

➤ 2.5.4 Lanthanide containing OIH materials;

A search for lanthanide luminescence and related terms in any bibliographic database or web search engine will typically return tens of thousands of articles; even just within the last year, there were more than a thousand publications pointing to its popularity in several fields, such as in catalysis¹⁰⁸, photovoltaics¹⁰⁹, sensors for ethanol¹¹⁰, temperature¹¹¹ and pH¹¹², solar cells¹¹³, bio-imaging¹¹⁴, markers¹¹⁵, etc. Their popularity came from an attractive feature of luminescent lanthanide compounds, their

line-like emission, which results in a high color purity of the emitted light. The emission color depends on the lanthanide ion, but is mainly independent of the environment¹¹⁶.

Due to the shielding by the $5s^2$ and $5p^6$ electrons, the $4f$ electrons weakly interacts with the ligands with an electrostatic nature and the complex geometry is conditioned to steric factors. This phenomenon is accompanied by the high values of ionic radius, which favors the formation of Ln^{3+} compounds with a high coordination number (CN), varying from 6 to 12, with CN numbers 7, 8 and 9 being the most common. This feature motivates the conjugation of Ln^{3+} complex luminescence with nanoparticles^{117,118}, polymer matrices^{119,120,121}, glass-ceramics^{122,123}, mesoporous/microporous materials¹²⁴, ionogels^{125,126}, inorganic hosts such as zeolites/silica^{127,128,129} and metal–organic frameworks (MOFs)^{130,131,132}.

Among the different variety of conjugations, the incorporation of Ln^{3+} on organic-inorganic hybrid (OIH) matrices^{133,134,135,136,137} is the most interesting in terms of processing due to their possibility of tailoring not only the optical response, but also, controlled for specific applications, other properties such as mechanical and chemical resistance, thermal stability, hydrophobicity, and optical quality or refractive index, which must be controlled for specific applications¹³⁸. In general, OIH materials have superior mechanical properties and have a better workability than lanthanide complexes incorporated into ceramic and glass materials.

Franville and coworkers, prepared Eu^{3+} -containing OIH materials based on derivatives of pyridine-2,6-dicarboxylic acid (dipicolinic acid). The Eu^{3+} ions were introduced in the sol as $\text{Eu}(\text{NO}_3)_3 \cdot 6\text{H}_2\text{O}$, and the Eu^{3+} /ligand ratio was $1/3$ ^{139,140}. A schematic representation of the OIH: Eu^{3+} matrix complex is shown in [Fig. 2.13](#).

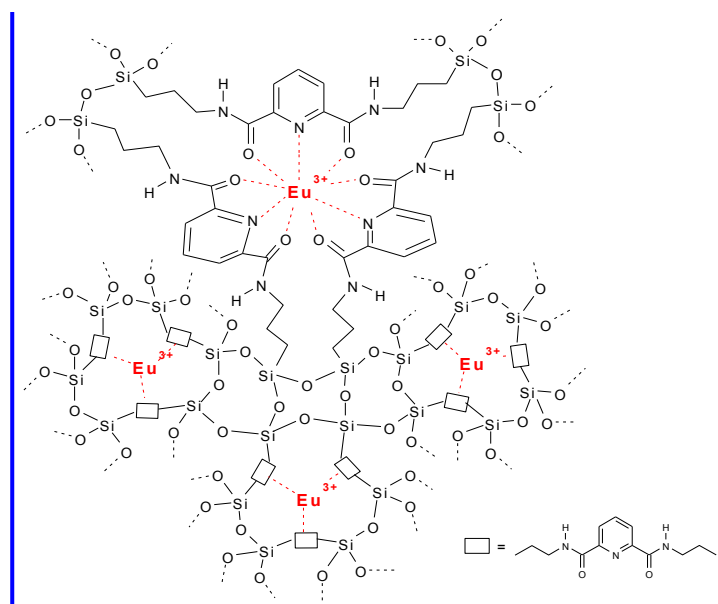


Figure 2.13: Schematic representation of the Eu^{3+} :OIH complex derived from functionalized dipicolinic acid ligands¹⁴¹.

Moreover, the incorporation of lanthanide complex in hybrid matrix is also beneficial for its luminescent characteristics¹³³. The most pronounced effect caused by Ln^{3+} incorporation in silica matrices is the broadening of Ln^{3+} emission peaks, while the relative intensities of the emission bands and the luminescence decay times were relatively unaffected¹³⁶. The luminescence decay times were slightly lower in the hybrid materials than in the Ln^{3+} organic complexes; this was attributed to the residual silanol groups in the OIH. The silanol groups do not directly interact with the Eu^{3+} ion, but their presence in the second coordination sphere influences the luminescence properties, for instance, via hydrogen bonding with the chelating groups of the ligands¹⁰⁴.

➤ 2.5.5 Antenna Effect;

The OIH materials developed in this thesis are composed of macromer grafted onto a siliceous backbone by urea, $-\text{NHC}(=\text{O})\text{NH}-$, which offers a blue emission under ultraviolet (UV) light (Fig. 2.14 (a) - left). Their photoluminescence (PL) can be tuned by adding trivalent lanthanide (Ln^{3+}) cations. In this way, the new emission color is characteristic of the Ln^{3+} added into the hybrid matrix, (Fig. 2.14 (a) – right), showing

that the OIH:Eu³⁺ has a blue → red emission transition. A representation of the incorporation of different Ln³⁺ in a generic OIH matrix is shown in Fig. 2.14 (b), where a to h indicates the luminescent properties resulting from the inclusion of different Ln³⁺ guests into the matrix.

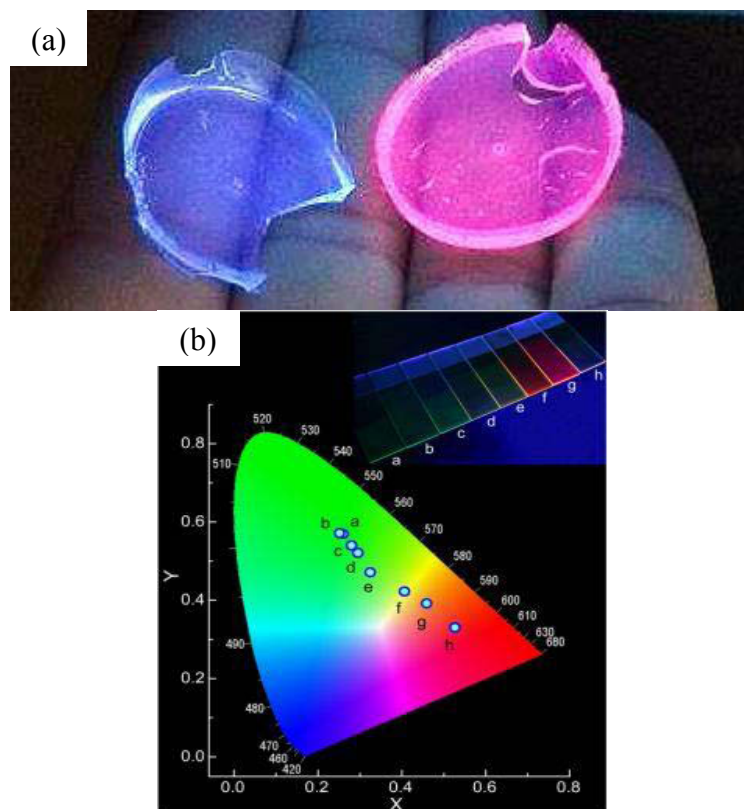


Figure 2.14: (a) U-PPO₂₀₀₀ OIH matrix (blue emission) and U-PPO₂₀₀₀ OIH:Eu³⁺ complex developed at this thesis and (b) CIE chromaticity diagram of a generic support matrix, doped with different Ln³⁺, showing the photoluminescence dependency of the lanthanide cation [elaborated by the author].

It is well known that the PL of Ln³⁺ shows a limited intensity due to the poor UV-absorption from the forbidden Laporte transition and from the intra-configurational nature of the 4*f* transitions¹¹⁶. The trivalent europium ion (Eu³⁺) exhibits an intense red photoluminescence upon irradiation with UV light¹⁰⁰. This PL is observed not only for Eu³⁺ ions doped into crystalline host matrices or glasses, but also for Eu³⁺ complexes with organic ligands¹⁰⁴. Consequently, organic ligands with a high absorbing coefficient are usually utilized in Ln³⁺ coordination, where the characteristic emission observed is the result of the organic ligand energy transfer to the Ln³⁺ center¹⁰³. This phenomenon,

called the “*antenna effect*”^{142,143}, represented in Fig. 2.15, was first reported by Weissman¹⁴⁴. The mechanism consists of UV-light absorption by the organic ligand coupled with an “*Inter-configurational rearrangement*” (ICR) from a singlet state to a triplet state, for example, followed by an “*Internal Energy Transfer*” (IET) of the light to the luminescent center, and a subsequent highly efficient “*Lanthanide Ion Emission*” (LIE)⁴⁵.

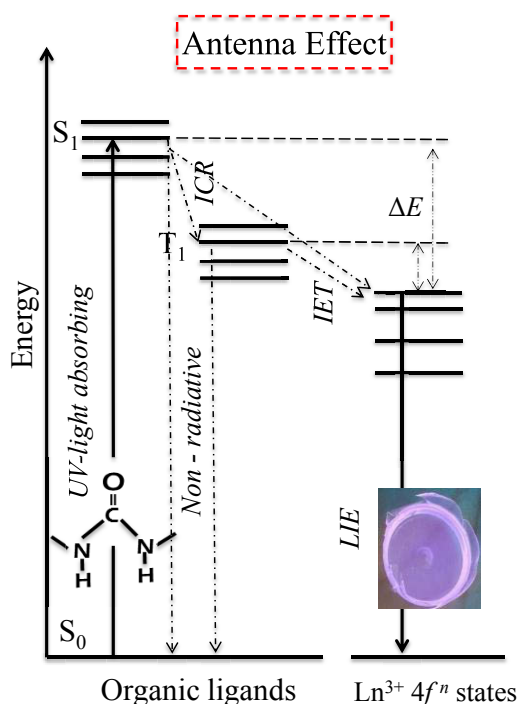


Figure 2.15: Schematic diagram of the Antenna Effect by the organic ligand with an efficient energy transfer to the lanthanide center [elaborated by the author].

➤ 2.5.6 Hypersensitivity;

One of the most interesting phenomena found in the Eu^{3+} emission diagram is the “hypersensitive” ${}^5\text{D}_0 \rightarrow {}^7\text{F}_2$ transition^{145,146}. The intensities of most induced ED transitions of lanthanide ions are not significantly affected by the local environment of the lanthanide ion, and the intensities vary by a factor of no more than two or three. However, the $\text{Eu}^{3+} {}^5\text{D}_0 \rightarrow {}^7\text{F}_2$ transition is very sensitive to the environment, showing to be more intense for a complex ion than for a fully hydrated ion in water; the intensity can be enhanced in some cases by a factor of 100 or even more¹⁰⁴. Sinha, S. P.

described that the $^5D_0 \rightarrow ^7F_2$ transition intensity of Eu^{3+} complexes is about 100 times more intense compared to a water solution in contact with the rare earth ions¹⁴⁷. The observed hypersensitive intensity electric dipole $^5D_0 \rightarrow ^7F_2$ transition enhancement is due to the low local symmetry of the Eu^{3+} , relaxing the forbidden Laporte rules, which is well accepted by literature^{148,149,150}.

➤ **2.5.7 Lanthanide containing OIH and photo-ageing;**

While there are hundreds of publications about polymer photo-ageing, this kind of study for OIH materials does not yet have the same attention. Scopus data base has shown a total of four publications^{151,152,153,154} for the keywords “hybrid materials” and “photoageing”, revealing the real importance of focusing scientific attention on this investigation. However, there are not any photo-ageing studies concerning Siloxane-Poly(ether) OIH matrices.

OIH materials demonstrate a great potential in engineering applications including coatings and films^{155,156,157} based on polyesters, polyurethanes, epoxies, acrylic-melamine composites, among others. Depending on the application, these materials are subjected to several environmental ageing factors, including UV light, temperature and atmospheric oxygen. One of the most important properties that organic coatings must fulfill is weathering resistance. The property changes due to the ageing and external conditions and have to be monitored and quantified to determine the weatherability of materials and the PL stability when exposed to sun radiation. On the other hand, all polymers, without exception, are eventually degraded within the environment to which they are exposed during their life cycle. Degradation and oxidation of the polymers have several serious effects on its physical, chemical and mechanical properties, like mass transport, tensile strength, impact strength, creep, etc¹⁵⁸. The most common processes leading to degradation are photo-initiated oxidation and hydrolysis, resulting from

unavoidable exposure to light, air, temperature and/or water. The rate at which these processes occur varies widely, depending on the exposure site, time of year, coating composition and substrate. However, it is difficult to know the polymer's incident solar energy when exposed to natural weathering conditions due to the variability of the season, time and geography¹⁵⁹. The most common procedure consists of using UV-light irradiation ($\lambda > 300$ nm), which is appropriate to simulate the solar UV-range due to the ability of these materials to absorb light within this wavelength range¹⁶⁰.

Early detection methods are based on highly sensitive techniques for detecting the onset of degradation, which are ideally carried out on samples subjected to ambient weathering in the field. Some works have focused on investigations of the chemical mechanisms based on infrared (IR) spectroscopy data^{161,162,163,164}, which is a useful tool for characterizing the degradation of the chemical structure and the understanding of the pathways of degradation.

The reactivity and the mechanism of degradation for OIH materials are directly related to their chemical structure. Polymeric materials photo-ageing at $\lambda > 300$ nm have been widely studied¹⁶⁵ and involve a mechanism of oxidation via radical, leaving hydroperoxides to form as primary products. The hydroperoxides formed decompose photochemically, thus giving formates, ketones, esters and hemiacetals, (which are thermally unstable and give rise to alcohols and carboxylic acids, given that the degree of reaction propagation depends on the polymeric chain mobility^{166,167}).

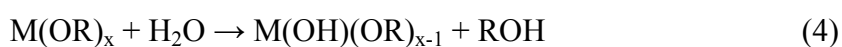
Garlette, J-L. et al. studied amorphous polypropylene (PP) films after UV-irradiation, combining IR analysis with chemical derivatization reactions and physical treatments, which allowed the authors to observe ketone and acids formation as the main photo-products after UV-light irradiation¹⁶⁸. However, several basic aspects of the mechanism of oxidation remain unclear. We intend to combine PL and FTIR

measurements to better understand this phenomenon by observing the emission of light by lanthanide dis-coordinated OIH materials with a special emphasis on the loss of the “*antenna effect*” from the organic ligands and the Eu^{3+} $f-f$ transition.

2.6 Sol-gel method:

OIH materials based on PEO and PPO polymers can be synthesized by the sol-gel process. This procedure allows for effective control of size and homogeneity in the matrix, enabling the covalent bonding between the inorganic-organic phases¹⁶⁹. The sol-gel process has another advantage compared with other synthetic routes since it involves the use of mild conditions of temperature and pressure¹⁷⁰. The sol-gel transition is a phenomenon in which a colloidal suspension becomes a gel by the bonding of nanoparticles, or oligomeric species, leading to the formation of 3D networks¹⁷¹. The chemistry of the sol-gel process is based on an inorganic polymerization reaction^{170,172} and their chemical precursors are often salts or metal alkoxides. The sol-gel procedure can be divided into the following steps: *i*) Precursor hydrolysis *ii*) hydrolyzed precursor poly-condensation – sol formation and gelation, *iii*) aging and *iv*) drying¹⁷³.

The hydrolysis and condensation reactions usually occur together in the initial synthesis steps, the reaction kinetics depend on the kind of precursors, temperature, reaction conditions, pH and ionic strength¹⁷³. For alkoxide precursors, the reaction between the alkoxide M-OR and water can produce aquo or hydroxo (M-OH) complexes (Equation 4). The M-OH species are essential for the condensation reactions leading to the formation of M-O-M poly-condensates¹⁷⁴. The global sol-gel reactions involving alkoxides of transition metals M(OR)_x are expressed as follow¹⁷⁵:

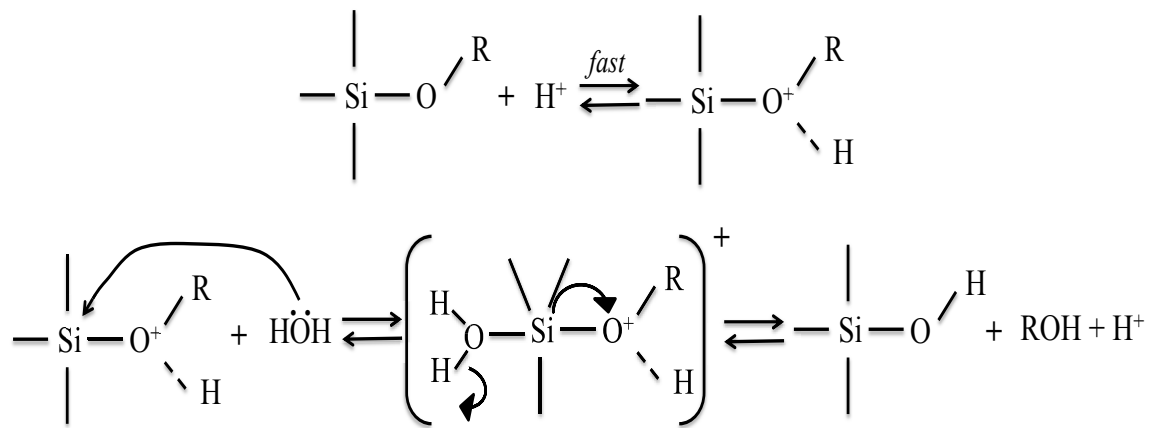


The hydrolysis procedure is strongly dependent on the pH solution, which determines the type of catalysis mechanism. The silicon alkoxide acid hydrolysis involves the protonation of an alkoxide group, followed by the nucleophilic attack of water to form a transition state (Fig. 2.16 (a)). The elevated hydrolysis rate promotes the growth of siliceous networks, thus leading to a polymeric solution. The ramified structure gel that is obtained is called “polymeric gel”.

On the other hand, under basic catalysis conditions, the anion coming from the water dissociation reacts with the siliceous atoms by a nucleophilic attack, thus forming a penta-coordinate intermediate. In this case, the gel formed is called “colloidal gel” having a structure formed by agglomerates leading it to a ramified network (Fig. 2.16 (b))¹⁷¹. At pH neutral conditions, it is expected that the hydrolysis and condensation occur by a nucleophilic addition followed by proton transfer and water and alcohol elimination

The kinetics for the hydrolysis and condensation of siliceous alkoxide is slow, allowing for the control of these reactions during the synthesis procedure from acid/basic catalysis. Due to this fact, both sol and gel can be used in the conformation of objects with different shapes, like thin films, monoliths, and others¹⁸². The step-by-step procedure of the sol-gel process for OIH materials (even the Li⁺/Eu³⁺-loaded) are explained in detail in Chapter 3

(a) Acid catalysis



(b) Basic catalysis

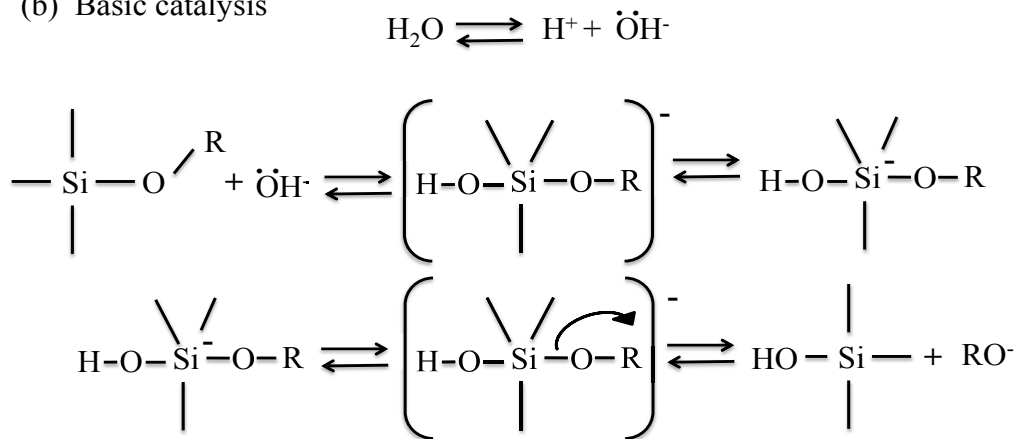


Figure 2.16: Acid (a) and Basic (b) catalysis reaction mechanism to the siliceous alkoxide¹⁷¹.

Chapter 3:

Methodology

3.1 Synthesis:

The OIH precursor was synthesized according to the procedure already well-known by GFQM – UNESP¹⁷⁶. In brief, the ureasil (U) cross-linking agent (3-(isocyanatopropyl) - triethoxysilane – IsoTrEOS) was covalently bonded to both ends of the functionalized PPO (O.O'-bis(2-aminopropyl)poly(propylene oxide)) by reacting their terminal aminopropyl groups in a molar ratio of 1:2. These commercially available reagents (Fluka, Aldrich) were stirred together in ethanolic solution under reflux for 6 h at 78 °C, leading to the formation of the OIH precursor, $(\text{EtO})_3\text{Si}-(\text{CH}_2)_3\text{NHC}(=\text{O})\text{NHCH}_2\text{CH}_2-(\text{polyether})-\text{CH}_2\text{CH}_2\text{CHNH}(=\text{O})\text{NHC}(\text{CH}_2)_3-\text{Si}(\text{OEt})_3$. This procedure has shown to be an efficient method for the preparation of OIH matrices¹⁷⁷ in comparison to the oldest method that uses tetrahydrofuran (THF) as the solvent and 15 h of reflux. This procedure, proved to be a more green route, has shown to be adopted for U-PEO₁₉₀₀ and U-PPO_n with average molecular weight (mw) of 230, 2000 and 4000 g.mol⁻¹ (labelled as U-PPO₂₃₀, U-PPO₂₀₀₀ and U-PPO₄₀₀₀).

The second step involves the sol-gel reactions comprised in the hydrolysis of $\text{Si}(\text{OEt})_3$, generating silanol moieties ensued by the condensation reaction to form ureasil cross-linking nodes. Hydrolysis starts by adding a specific volume of water to satisfy the relationship: $[\text{H}_2\text{O}] / [\text{Si}] = 4$, (Table 3.1), and 12 μl of HCl (10^{-2} mol.l⁻¹) employed as a catalyst in 1.6 mL of the ethanoic precursor solution (this volume is equivalent to 0.5 g of dry precursor). This procedure leads to the formation of a rubbery material with two different polar oxygen active sites, named as I and II (Fig 3.1), ascribed to oxygen ether-type and carbonyl-type, respectively, which allow for a wide variety of guest cations for complexation.

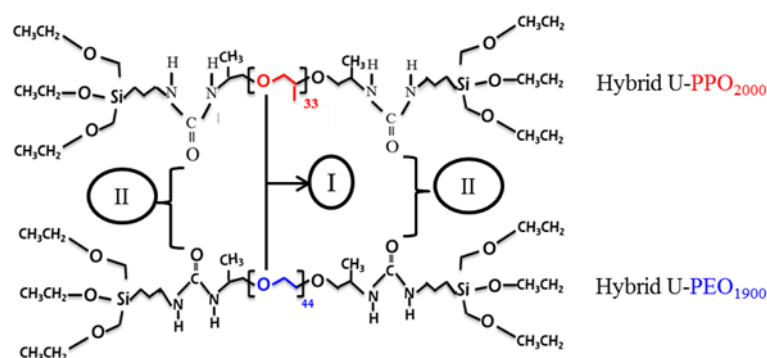


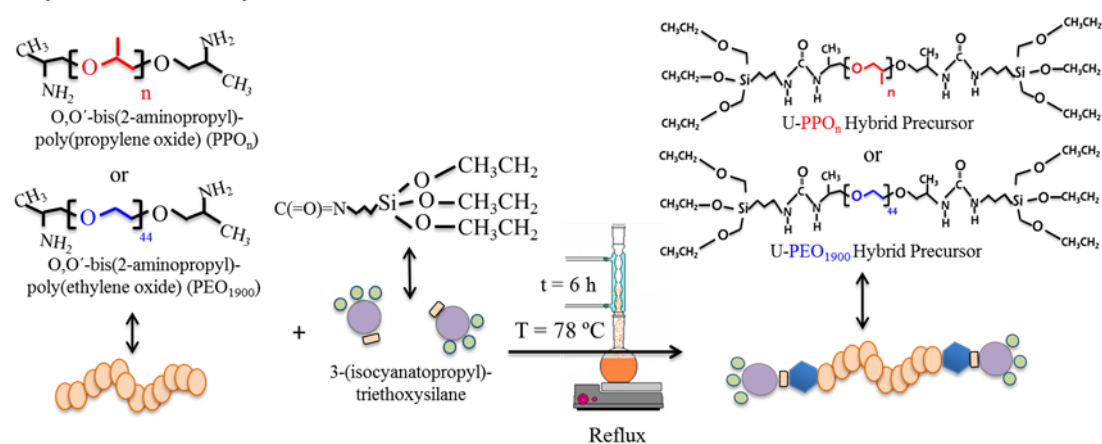
Figure 3.1: Schematic diagram of the different OIH – matrices with their two polar oxygen active sites, I: O_{ether} and II: O_{carbonyl} , respectively ^{adapted from 35}.

$\text{Li}^+ / \text{Eu}^{3+}$ – OIH complex formation was carried out by the solubilisation of a desired proportion of bis(trifluoromethane) sulfonimide lithium salt (Fluka, Aldrich, 99,95 % purity, CAS # 90076-65-6) / europium (III) chloride hexahydrate (Fluka, Aldrich, 99,9 % purity, CAS # 13759-92-7), followed by the relationship $[\text{O}_{\text{ether}}] / [\text{Li}^+] = 15$ / $[\text{O}_{\text{carbonyl}}] / [\text{Eu}^{3+}] = 3$. The different inorganic salt additions were realized at the sol-gel hydrolyses procedure for each OIH containing $\text{Li}^+ / \text{Eu}^{3+}$. The masses (g) of $\text{C}_2\text{F}_5\text{LiNO}_4\text{S}_2$ / $\text{EuCl}_3 \cdot 6 \text{H}_2\text{O}$ utilized for each OIH matrix is found in Table 3.1. Finally, transparent, cylindrical OIH monolithic xerogels were obtained after drying at room temperature for 48 h. The cylindrical OIH monolithic has an average diameter of 2 cm and an average thickness of 0.1 cm. The main steps of the sol-gel procedure are shown in Fig. 3.2.

Table 3.1: Table content the volume of water (μl) and the mass of europium salt (g), to satisfy the relationship $[\text{H}_2\text{O}]/[\text{Si}]=4$ $[\text{O}_{\text{carbonyl}}]/[\text{Li}^+]=15$, and $[\text{O}_{\text{carbonyl}}]/[\text{Eu}^{3+}]=3$, respectively, for a mass of 0.5 g of the precursor.

PEO mw. ($\text{g}\cdot\text{mol}^{-1}$)	H_2O volume (μl)	$\text{C}_2\text{F}_5\text{LiNO}_4\text{S}_2$ mass (g)	$\text{EuCl}_3 \cdot 6$ H_2O mass (g)
1900	30	0.176	0.052
POs mw. ($\text{g}\cdot\text{mol}^{-1}$)			
230	99	0.033	0.230
2000	29	0.127	0.049
4000	16	0.145	0.027

Hybrid Precursor synthesis



Sol-gel reaction

✓ Precursor hydrolyses

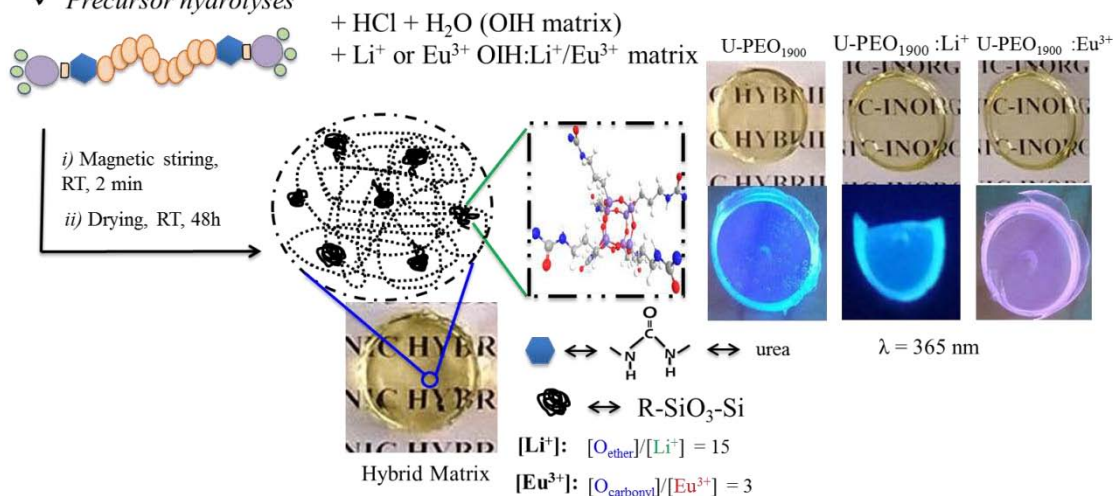


Figure 3.2: Schematic representation of the synthesis of the U-PEO₁₉₀₀ and U-PPO_n OIH, Metal-unloaded, Li⁺ – loaded and Eu³⁺ – loaded OIH materials. An analogous process was adopted in the synthesis of the OIH materials from POs 230, 2000 and 4000 ($n = 2.3$ and 68, respectively)^{Adapted from 177}.

3.2 Materials and methods:

➤ 3.2.1 U-PPO_n films;

Different of cylindrical monolithic xerogels, U-PPO_n unsupported films of $\approx 50 \mu\text{m}$ thickness of unloaded and Eu³⁺ – loaded U-PPO_n with different molecular weights (230, 2000 and 4000 $\text{g}\cdot\text{mol}^{-1}$), were prepared by the Kofler bench method. The method begins with the sol-gel reaction and Si(OEt)₃ hydrolysis in a vial, following by the solution dumping in a thermal plank at 60 °C. The next step consists of obtaining a uniform, desired thickness by running a ruler of a specifically chosen height over the hybrid

solution then drying it for 5 hours. The preparation of films is important to quantify the InfraRed Spectroscopy bands measured in transmission mode.

➤ 3.2.2 Differential Scanning Calorimetry (DSC);

Differential scanning calorimetry (DSC) measurements were carried out using a Q100 analyzer (TA Instruments). Small cylindrical pieces with an average diameter of 0.5 cm, weighing approximately 10 mg, were cut from the OIH samples and placed in aluminum pans. The samples were first heated at a rate of 10 °C/min from room temperature to 100 °C and kept at 100 °C for 10 min in order to eliminate the residual water, then cooled at rate of 10 °C/min to -90 °C. A second heating scan from -90 °C to 100 °C, at 10 °C/min, was used to assess the thermal transitions. Nitrogen was used for the gas purge, supplied at a flow rate of 50 mL/min. The temperature program of the DSC measurement is summarized in Figure 3.3.

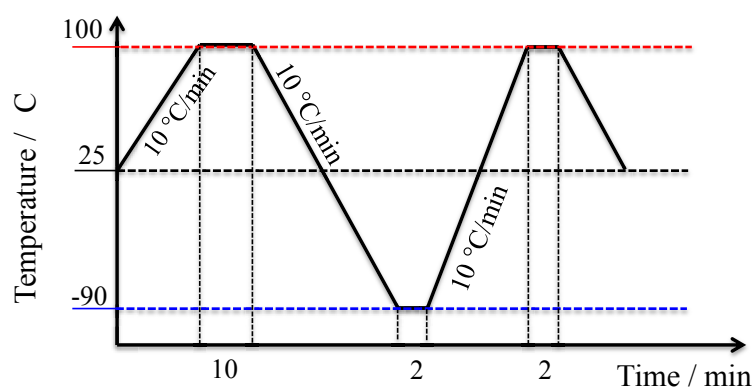


Figure 3.3: DSC time and temperature-control program elaborated by the author.

➤ 3.3.3 Raman spectroscopy with temperature-controlled program;

The Raman spectra were recorded in backscattering geometry using a Raman RXN1 analyzer delivered by Kaiser Optical Systems, Inc (KOSI). It incorporates a near-InfraRed laser diode working at 785 nm, a HoloPlex transmission grating which diffracts the different wavelengths of the polychromatic Raman scattered light into different angular output paths on the Peltier-cooled Charge Coupled Device detector.

The measurements were performed in Soleil, Saint-Aubin – France. Data with a resolution of 2 cm^{-1} was collected, it ranged from 100 to 3100 cm^{-1} . Raman spectra were recorded every 12 seconds during heating from $-85\text{ }^{\circ}\text{C}$ to $+100\text{ }^{\circ}\text{C}$, at $5\text{ }^{\circ}\text{C}/\text{min}$, in order to collect one spectrum of each degree ($^{\circ}\text{C}$).

➤ **3.3.4 Artificial Accelerated Photo-Oxidation;**

UV-light irradiations were carried out in a SEPAP 12/24 unit. This apparatus has been designed for the study of polymer photo-degradation in artificial aging corresponding to medium accelerated conditions¹⁷⁸. The chamber is an elliptical reactor equipped with one medium-pressure mercury lamp (Mazda MA 400) in the vertical position at one axis of the chamber. Wavelengths below 300 nm are filtered by a glass envelope. At the second axis of the chamber, the samples were fixed on a rotating carousel with a 13 cm diameter which can receive 24 samples (Figure 3.4 (a)). The samples (cylindrical OIH monoliths and OIH films) were fixed in the hollow-centered metallic sample holder. A schematization is shown in Figure 3.4 (b). In this series of experiments, the temperature at the surface of the samples was fixed at $60\text{ }^{\circ}\text{C}$

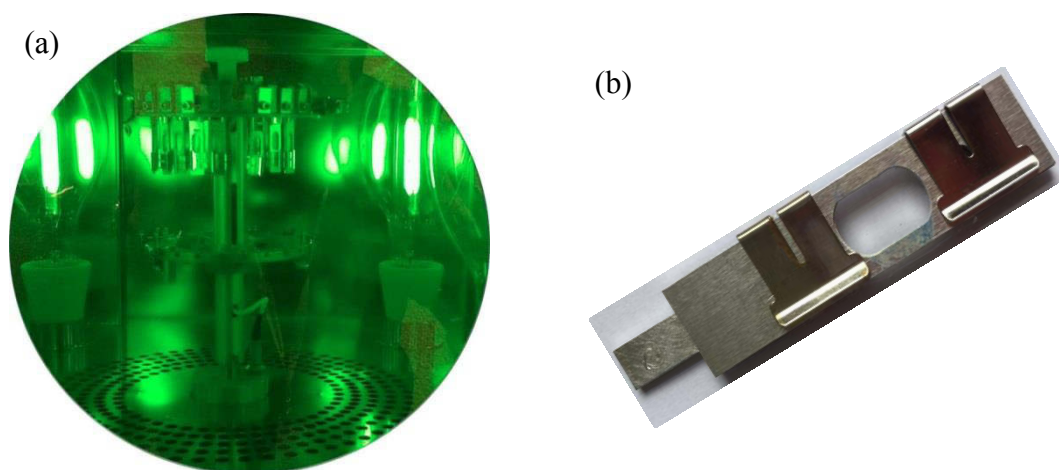


Figure 3.4: (a) Photograph of the SEPAP 12/24 chamber during activity and (b) metallic sample holder with a hollow center elaborated by the author.

➤ 3.3.5 Fourier Transform InfraRed (FTIR);

Infrared spectra were recorded with a Nicolet 760-FTIR spectrometer, working with OMNIC software. Spectra, in transmission mode for the OIH films ($\approx 50 \mu\text{m}$) were obtained using 32 scan summations and a 4 cm^{-1} resolution in a spectral range from 400 to 4000 cm^{-1} .

❖ 3.3.5.1 Qualitative identification of species derived from OIH photo-aging:

The photo-oxidized samples were subjected to a $\text{NH}_3(\text{g})$ chemical treatment in order to identify their photoproducts. The irradiated films were exposed to reactive gas at room temperature in a simple flow system that could be sealed off to permit the reaction to proceed. In parallel to those treatments, ammoniac chemical treatment showed itself to be inert when Eu^{3+} -unloaded because the hybrid matrices were not reacting with the gas (Fig. 3.5). $\text{NH}_3(\text{g})$ treatments were carried out in purely Teflon systems. This procedure was well known in the Laboratoire de Photochimie Moléculaire et Macromoléculaire - Université Clermont Auvergne, AUBIERE, France¹⁷⁹ and was used for photo-oxidation of $\text{U-PPO}_n \text{Eu}^{3+}$ – unloaded and Eu^{3+} – loaded OIH materials by UV-light irradiation ($\lambda > 300 \text{ nm}$).

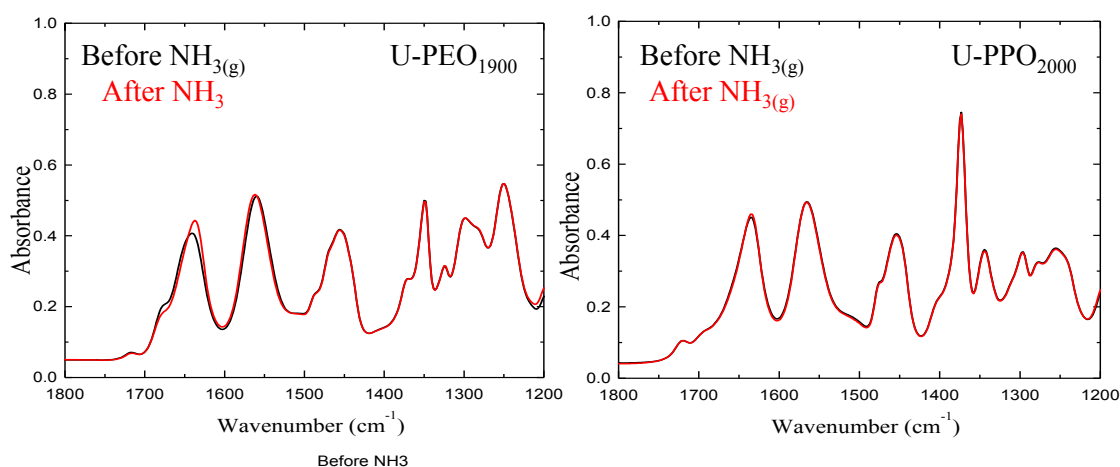


Figure 3.5: U-PEO₁₉₀₀ (left) and U-PPO₂₀₀₀ (right) OIH matrices, non-irradiate, before (black) and after (red) the ammoniac chemical treatment of the hybrid thin film ($50 \mu\text{m}$). The same results were obtained for the U-PPO₂₃₀ and U-PPO₄₀₀₀ OIH matrices – Annex II ^{elaborated by the author}.

➤ **3.3.6 Small Angle X-Ray Scattering (SAXS) *in situ* with the temperature;**

The evolution of the nanostructures of the hybrids was monitored by small angle X-ray scattering (SAXS) recorded in *in situ* during controlled change of temperatures. The measurements were performed at the SAXS1 beamline of the National Synchrotron Light Laboratory (LNLS, Campinas, Brazil). The instrumentation was equipped with a multi-layer monochromator ($\lambda = 1.550 \text{ \AA}$), a 2D Pilatus 300k detector located 910.9 mm from the sample, and a multichannel analyzer to record the scattering intensity, $I(q)$, as a function of the modulus of the scattering vector, $q = 4\pi/\lambda\sin(\varepsilon/2)$, where ε is the X-ray scattering angle. The data was normalized by considering the varying intensity of the direct X-ray beam, detector sensitivity, and sample transmission. The parasitic scattering intensity (due to the cell windows and vacuum) was subtracted from the total scattering intensity. Small pieces of the monolithic hybrids were introduced into thermostated, coupled sample cells and the measurements were performed from $-100 \text{ }^\circ\text{C}$ to $+100 \text{ }^\circ\text{C}$, at $5 \text{ }^\circ\text{C}/\text{min}$. System cooling and heating was carried out by liquid nitrogen using a furnace type Transmission, Capilar and Mica, model DSC6000, allowing for work to be done in a temperature range from $-196 \text{ }^\circ\text{C}$ to $600 \text{ }^\circ\text{C}$ for solid and liquid samples, manufactured by Linkan¹⁸⁰. SAXS patterns were recorded every 12 sec during heating, taking one measurement at each degree ($^\circ\text{C}$). To avoid water crystallization on the glass surface of the sample holder, a constant flux of air was injected in the sample holder surface during the cooling procedure Fig. 3.6 (c).

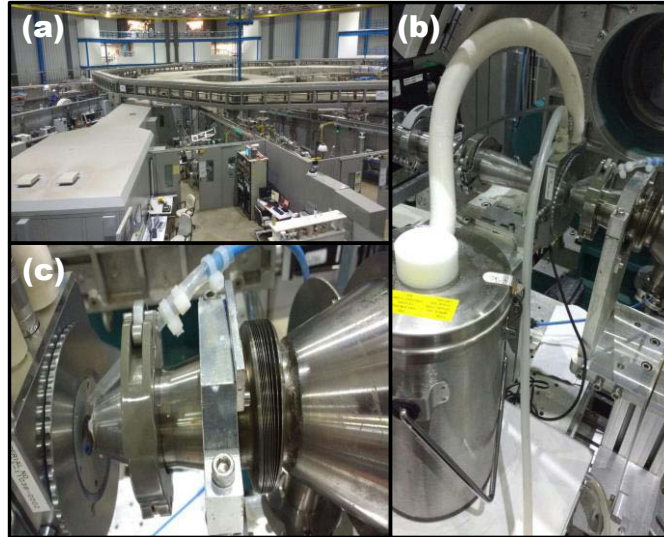


Figure 3.6: (a) SAXS1 beamline at LNLS synchrotron ring – Campinas, Brazil (b) apparatus containing liquid nitrogen for the heating/cooling procedure and (c) a constant flux of air to avoid water crystallization at the sample holder surface elaborated by the author.

❖ 3.3.6.1 Extracting nanostructural information from SAXS patterns.

The U-PEO₁₉₀₀ OIH matrix showed the presence of two maxima in its SAXS patterns (Fig. 3.7). To facilitate the peak analysis, the experimental Porod's function, found from the linear behavior observed at low q (curve in red in Fig 3.7), was subtracted from the whole SAXS curve, leading to a clear visualization of the two maxima contribution (Fig 3.8). Structural information such as *peak area, position, and full width at half maximum (FWHM)* that were calculated by mathematical peak fitting utilizing a Gaussian function (Fig. 3.9), and the effect of temperature, blending and doping of the different OIH matrices will be discussed in Chapter 6.

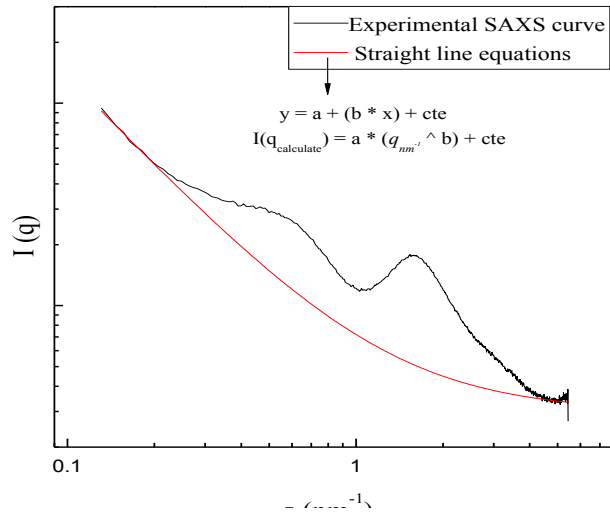


Figure 3.7: Typical SAXS curve of the U-PEO₁₉₀₀ OIH matrix (black) and its Porod function (see equations inserted in the figure) fitting (red) elaborated by the author

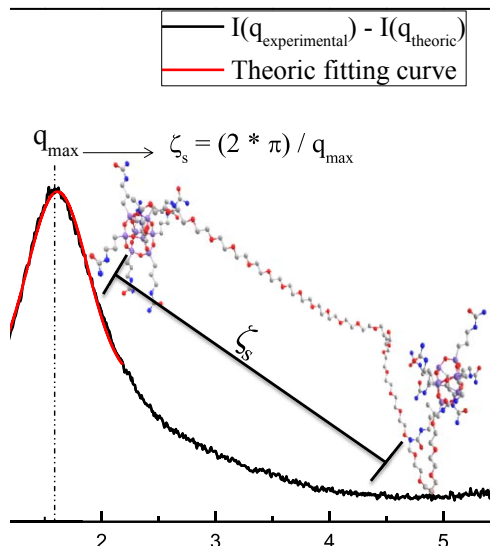


Figure 3.8: Subtraction of power law contribution from the U-PEO₁₉₀₀ SAXS curve. The insert show a schematic representation of the siloxane nodes distance spaced by the polymeric chain elaborated by the author

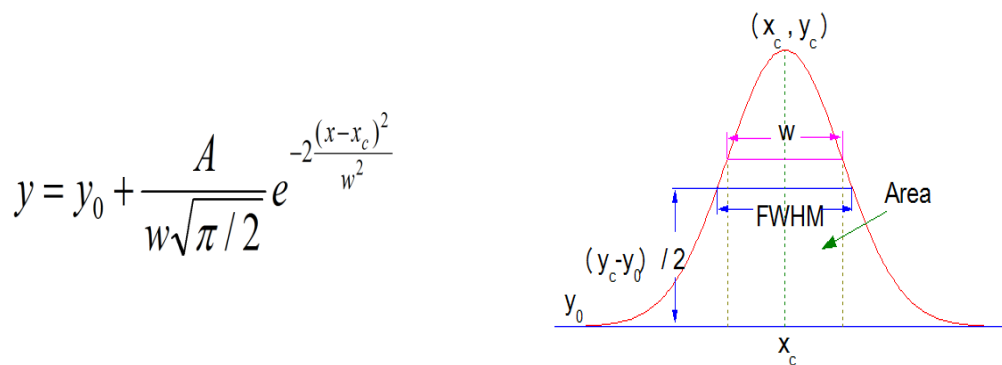


Figure 3.9: (Left) Gaussian equation and (Right) Gaussian function elaborated by the author

➤ 3.3.7 Photo-Luminescence;

The external quantum efficiencies were estimated using the C9920-02G PL-QY measurement system from Hamamatsu. The setup comprised of a 150 W monochromatized Xe lamp, an integrating sphere (Spectralon® Coating, Ø = 3.3 inch) and a high sensitivity CCD camera for detecting the whole spectral luminescence (the emission spectra were integrated from 576 nm to 728 nm for the europium-based compounds). The automatically controlled excitation wavelength range spread from 250 nm to 500 nm with a resolution bandwidth better than 5 nm. Absolute photoluminescence (PL) quantum yield excitation spectra were recorded for PEO₁₉₀₀ and different molecular weight U-PPO_n, Eu³⁺ – loaded OIH materials, in the solid form, and obtained by scanning the excitation and monitoring the overall luminescence of Eu³⁺.

The values reported on the *y* axis correspond to the absolute quantum yield, which is defined as the internal quantum yield ϵ_{in} corrected from the absorption coefficient leading to the ϵ_{ex} ¹⁸¹, as shown below:

$$\epsilon_{in} = \frac{N_{em}}{N_{abs}} \text{ and } \epsilon_{ex} = \frac{N_{em}}{N_{ex}} = \epsilon_{in} \left(\frac{N_{abs}}{N_{ex}} \right) \quad (7)$$

where N_{em} is the number of photons of the emission light of the sample, N_{abs} is the number of photons that are absorbed by the sample, and N_{ex} is the number of photons of the excitation light from a Xe source.

➤ 3.3.8 Impedance Spectroscopy;

Ionic conductivity of OIH:Li⁺ materials were measured as a function of the temperature from -90 °C to + 100 °C, using a SI 1260 Solartron Impedance/Gain Phase Analyser connected to a K-20 programmable temperature controller (MMR Technologies, INC), over the frequency range of 1 MHz to 50 Hz. The hybrid

electrolyte was sandwiched, painting both monolith superficies with a leit-silver ink [®] (sigma-aldrich # 09937). After the evaporation of the solvent, two copper wires were connected at the electrical active area ($l_1 \times l_2$ – Fig. 3.10) by a Leit-C [®] (sigma-aldrich # 09929) and each wire end was glued to the heating source of the sample cells by a silicone heat sink to help the energy transfer. An alternating voltage

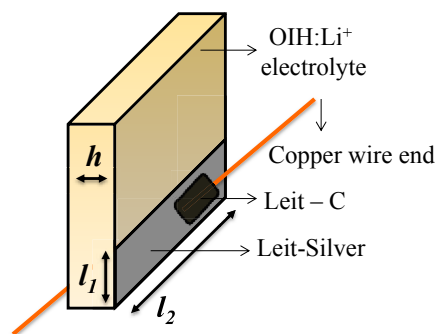


Figure 3.10: OIH:Li⁺ monolith prepared for impedance analyses elaborated by the author

of 0.5 V and a current of 100 mA was applied in the specified frequency range and the impedance patterns were collected as a function of Z' and Z'' by Nyquist diagram. The Nyquist plots were multiplied by the electrolyte geometric factor, $(K) = h / (l_1 \times l_2)$. K values are found in Table 3.2. Z-view analytic software was used to analyze the Nyquist plots obtained from the impedance measurements.

Table 3.2: Volume of water (μl) and the mass of lithium salt (g) used to satisfy the relationship $[\text{H}_2\text{O}]/[\text{Si}]=4$ and $[\text{O}_{\text{carbonyl}}]/[\text{Li}^+]=15$, and the electrical geometric factor of the $\text{U}_x\text{PPO}_{2000}/\text{U}_{1-x}\text{PEO}_{1900}$ poly-electrolytes.

OIH material	H ₂ O volume (μl)	C ₂ F ₅ LiNO ₄ S ₂ mass (g)	K (cm ⁻¹)
U-PPO ₂₀₀₀	28.9	0.127	0.91
U _{-0.8} PPO ₂₀₀₀ /U _{-0.2} PEO ₁₉₀₀	29.0	0.136	0.66
U _{-0.5} PPO ₂₀₀₀ /U _{-0.5} PEO ₁₉₀₀	29.5	0.151	0.66
U _{-0.2} PPO ₂₀₀₀ /U _{-0.8} PEO ₁₉₀₀	29.8	0.160	0.55
U-PEO ₁₉₀₀	30.0	0.176	0.52

Chapter 4:

OIH:Eu³⁺ Photo-Luminescence properties

4.1 Introduction to the Chapter:

The present Chapter will discuss the effects of Eu^{3+} -loading on OIH materials in order to probe local coordination of Eu^{3+} ions and discover its effect on the PL of unloaded ureasil-polyether. In this way, FTIR measurements in transmission mode were carried out in the unsupported films (50 μm) of the OIH: Eu^{3+} samples in both the (C-O-C) backbone and the amide region. The PL was measured using the OIH: Eu^{3+} monoliths with a thickness around a few millimeters. The PL values were confronted with the polymer backbone conformation (*gauche* and/or *trans*) and investigated by FT-Raman. The PL of the OIH: Eu^{3+} complexes were also studied as a function of the UV-vis irradiation varying with the time of exposure. Nano-structural characterization was realized by SAXS in order to help us understand the PL dependence along with the UV-vis irradiation.

4.2: Effect of Eu^{3+} -loading in the thermal/structural properties of the OIH:

➤ 4.2.1 Thermal behavior;

DSC curves (Fig. 4.1), for all OIH materials showed that there was a relatively sharp change of the heat capacity (ΔC_p), characteristic of the glass transition. The T_g event occurred at -58 and -60 C for U-PEO₁₉₀₀ and U-PPO₂₀₀₀, respectively. The Eu^{3+} -loading did not show changes in the T_g value, suggesting that the Eu^{3+} - OIH matrix coordination does not happen in the (-C-O-C-) *backbone*. The DSC curves also revealed an endothermic fusion peak for the U-PEO₁₉₀₀ and U-PEO₁₉₀₀: Eu^{3+} ascribed to the crystalline PEO₁₉₀₀ melting temperature ($T_m \sim 25$ °C) which is absent in the case of the PPO₂₀₀₀ OIH matrix. The presence of the endothermic fusion peak for U-PEO₁₉₀₀: Eu^{3+} is an important indicator that Eu^{3+} cations do not break the helical conformation, typically found in semi-crystalline polymers¹⁸², thus supporting the coordination

between the lanthanide and OIH matrix by another active site. The investigation of Eu^{3+} coordination was carried out by spectroscopy techniques.

Figure 4.1: DSC curves of U-PEO₁₉₀₀ and U-PPO₂₀₀₀ Eu^{3+} -unloaded (**black**) and Eu^{3+} -loaded (**red**).

➤ **4.2.2 Room temperature FT-IR analysis of the OIH:Eu³⁺ complexes;**

One way to study the structural modifications caused by adding an inorganic salt to OIH matrices is by IR spectra analysis on the region of the C-O-C backbone stretching (νCOC) mode, 1200–1000 cm^{-1} (Fig 4.2). The C-O-C backbone region is sensitive to changes occurring in the conformations of the polyether chains as result of the bonding between the guest cation and the polar oxygen ether-type atoms present in the polyether¹⁸³. Figs 4.2 (a) and (b) do not show significant changes in the IR spectra of the OIH materials after Eu^{3+} - loading. In the νCOC region spectra, all studied OIH matrices (unloaded and Eu^{3+} -loaded U-PEO₁₉₀₀ U-PPO₂₀₀₀ and U-PPO₄₀₀₀) show a broad band centered around 1110 cm^{-1} and a shoulder at 1150 cm^{-1} . These events, ascribed to the νCOC vibration mode and to the coupled vibration of the νCOC and rCH_2 modes, respectively, indicate the presence of the C-O-C backbone non-coordinated with the

guest cation¹⁸⁴. From these results we may conclude that the ether linkages are not involved in the Eu^{3+} ion coordination.

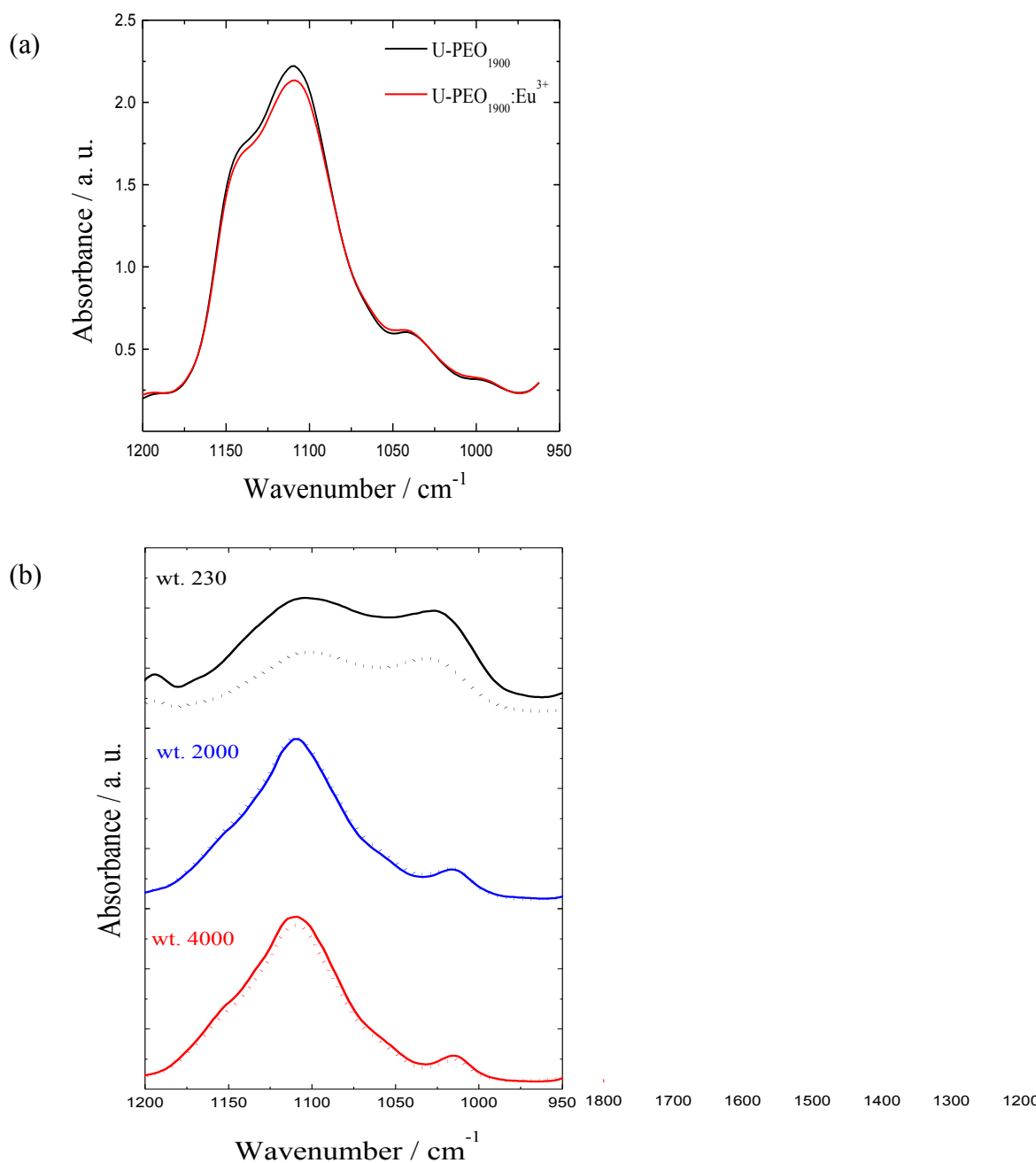


Figure 4.2: FTIR spectrum of (a) U-PEO₁₉₀₀ and U-PEO₁₉₀₀Eu³⁺ and (b) U-PPOs with different molecular weight (wt = 230, 2000 and 4000 $\text{g}\cdot\text{mol}^{-1}$) Eu³⁺ - unloaded OIH materials (solid line) and OIH:Eu³⁺ complexes (dotted line), films (50 μm) in the $\nu(\text{C-O-C})$ backbone (1200 – 950 cm^{-1}) region.

On the other hand, the most significant effect resulting from the Eu^{3+} - loading into OIH matrices is the appearance of a new band in the Amide region (1800 – 1500 cm^{-1})¹⁸⁵, which can be divided into two contributions: Amide I and Amide II. The Amide I

region (around 1640 cm^{-1}) is a highly complex vibration¹⁸⁶ that involves the contribution of C=O stretching, which is sensitive to the specificity and magnitude of hydrogen bonding. Thus, the amide I vibration consists of several components reflecting C=O groups in different environments¹⁸⁷. The Amide II region (around 1545 cm^{-1}) is mainly associated with the N-H in-plane bending vibration¹⁸⁸, which is sensitive to the chain conformation and intermolecular hydrogen bonding²⁰⁵. The coordination between Eu^{3+} ions and carbonyl oxygen atoms from urea linkages have been intensely investigated and so far, well accepted by other researchers¹⁸⁵. Carlos et al have reported modifications in the spectra at the Amide I region due to the presence of a lanthanide salt in ureasil in OIH materials¹⁸⁹. The authors have shown that the polyether chains are not strongly involved in the solvation of the Ln^{3+} cations, and the presence of new components in the urea spectral region suggest that the Eu^{3+} cations are preferentially coordinated by the carbonyl oxygens.

Fig 4.3 presents the spectra for OIH materials (solid line) and OIH: Eu^{3+} complexes (dotted line) at the amide region for the matrices based on PEO_{1900} and PPO_n with different molecular weights. The Amide region in the ureasils (wt. = 1900, 2000 and 4000) is extremely modified by the Eu^{3+} incorporation, evidenced by the new band at 1608cm^{-1} . It is well-known that the Amide I region involves a different C=O environment as follows: “free” C=O groups¹⁹⁰ and/or ordered/disordered hydrogen-bonded aggregates of different strengths, involving the NH from the urea groups with oxygen ether atoms and/or carbonyl type¹⁹¹. Skrovanek et al. have associated the intense band at 1640 cm^{-1} and the shoulder at about 1670 cm^{-1} , observed in IR spectra of amorphous polyamides, with hydrogen-bonded and “free” carbonyl groups, respectively¹⁹².

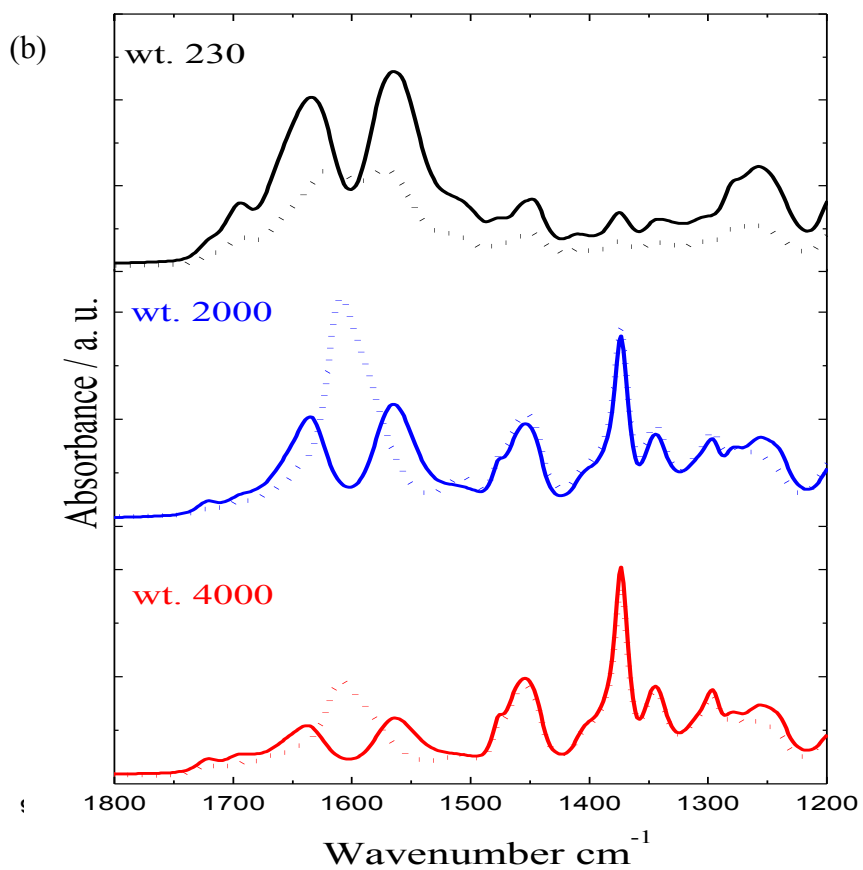
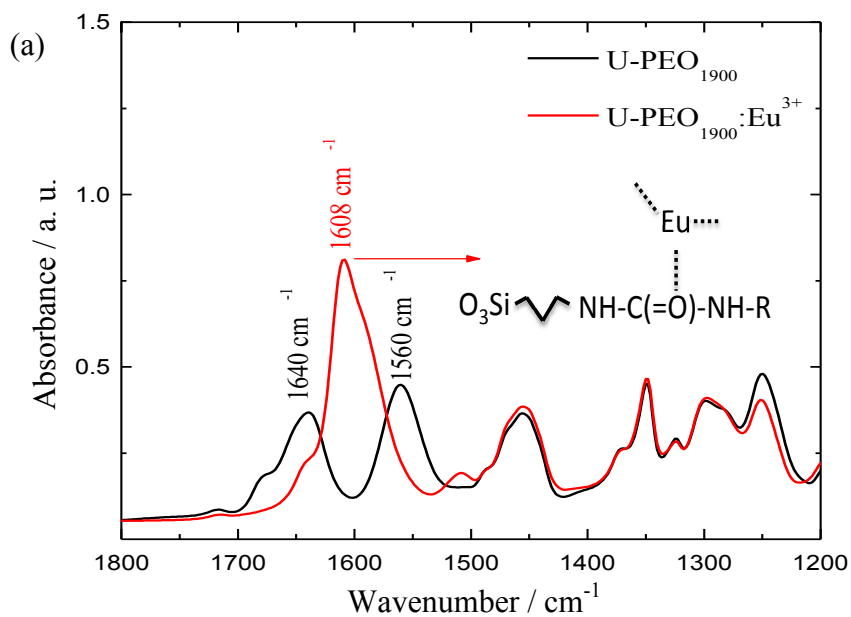


Figure 4.3: FTIR spectrum of 50 μm films in the amide region of (a) U-PEO₁₉₀₀ and U-PEO₁₉₀₀Eu³⁺ and (b) U-PPOs with different molecular weight (wt = 230, 2000 and 4000 $\text{g}\cdot\text{mol}^{-1}$) Eu³⁺ – unloaded OIH materials (solid line) and OIH:Eu³⁺ complexes (dashed line).

In the case of OIH:Eu³⁺ complexes, the free carbonyl oxygen atoms which originate from this process coordinate with the Eu³⁺ cations forming structures of Eu³⁺- - - O = C (urea) probably involving short contact distances. Characteristic spectral changes, manifested as wavenumber shifts or band splitting, are a result of the coordination of polymer chains with guest cations. Analysis of the spectra of different Eu³⁺-loaded OIH di-ureasil matrices leads us to conclude that the complexation by chromophore molecules belonging to the OIH matrix happens by the oxygen carbonyl from the urea groups present in this kind of material. Thus Eu³⁺- (urea) complexes are probably responsible for the downshift of the band from 1641 to 1608 cm⁻¹¹⁹³.

In a different way, U-PPO₂₃₀ does not show a single peak at 1608 cm⁻¹, but rather, a displacement of the Amide I band to lower wavenumber values. The for this is that the U-PPO₂₃₀ OIH matrix has the higher portion of urea groups, showing a band intensity in the Amide I region that is 2 and 8 times higher than the U-PPO₂₀₀₀ and U-PPO₄₀₀₀, respectively. This feature is accompanied by a smaller intensity for the band at 1110 cm⁻¹ by having the smaller number of (-CH(CH₃)-CH₂-O-)_n monomer in the organic chains.

For instance, the Amide I region of U-PEO₁₉₀₀ (Fig 4.4 (a)) displays an intense band around 1640 cm⁻¹ and a shoulder at around 1680 cm⁻¹, attributed to hydrogen bonding and “free” C=O groups, respectively¹⁹⁴. However, the second derivate of the curve reveals that the Amide I region is composed of three components and the Amide II shows a single intense band at 1560 cm⁻¹. In order to quantify these components, Fig 4.4 (b) shows the Gaussian fitting of the amide region spectra, and the best adjustment was obtained by the convolution of three components at 1642, 1660 and 1680 cm⁻¹, for the Amide I region. These distinct components are attributed to ordered hydrogen bonding urea/urea, urea/poly(ether), disordered hydrogen bonding urea/poly(ether), poly(ether)/ poly(ether) and “free” C=O environment, respectively¹⁹².

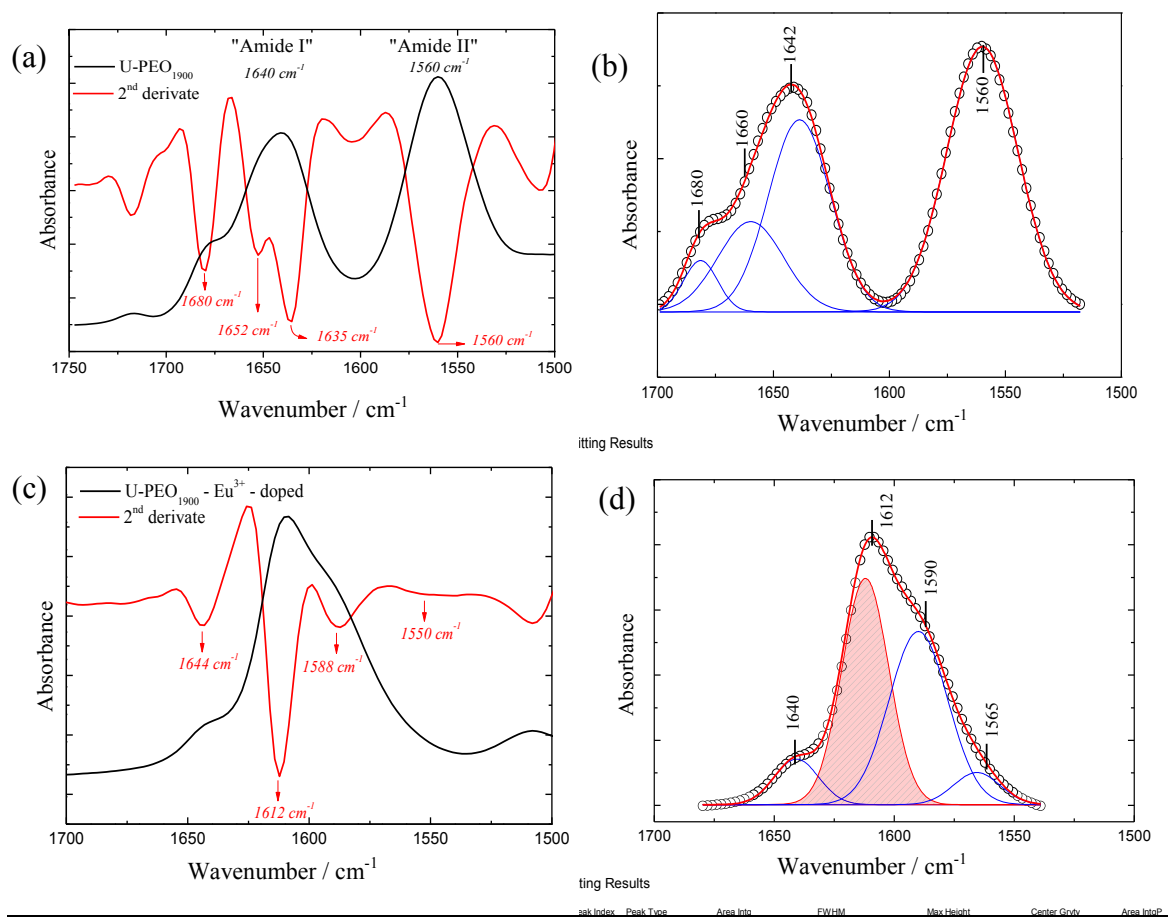


Figure 4.4: FTIR spectra in the amide region with the 2nd curve derivate for (a) U-PEO₁₉₀₀ and (c) U-PEO₁₉₀₀:Eu³⁺ and the Gaussian fitting of the amide region for (b) U-PEO₁₉₀₀ and (d) U-PEO₁₉₀₀:Eu³⁺.

The second derivate of the U-PEO₁₉₀₀:Eu³⁺ curves Fig 4.4 (c) reveals a feature completely different compared to the U-PEO₁₉₀₀. The Gaussian fitting shows a complex deconvolution of bands, possessing two components which differ from the unloaded U-PEO₁₉₀₀. The first one starts with the suppression of the component relative to the “free” C=O, indicating the participation of these oxygen atoms in the Eu³⁺ coordination, giving rise to another C=O environment with a maximum at 1612 cm⁻¹. The second one is the development of a contribution at 1588 cm⁻¹, which may be associated with an interaction of the nitrogen atoms with the anion Cl⁻. In order to complete the coordination number of the metal to a total of 9 (from 3 different organic ligands), it is expected that oxygen ether-type participates of the coordination. A schematic diagram proposed for the Eu³⁺ coordination with OIH is shown in Fig. 4.5. The values of the Gaussian fitting parameters for both U-PEO and U-PEO₁₉₀₀:Eu³⁺ are found in Table 4.1.

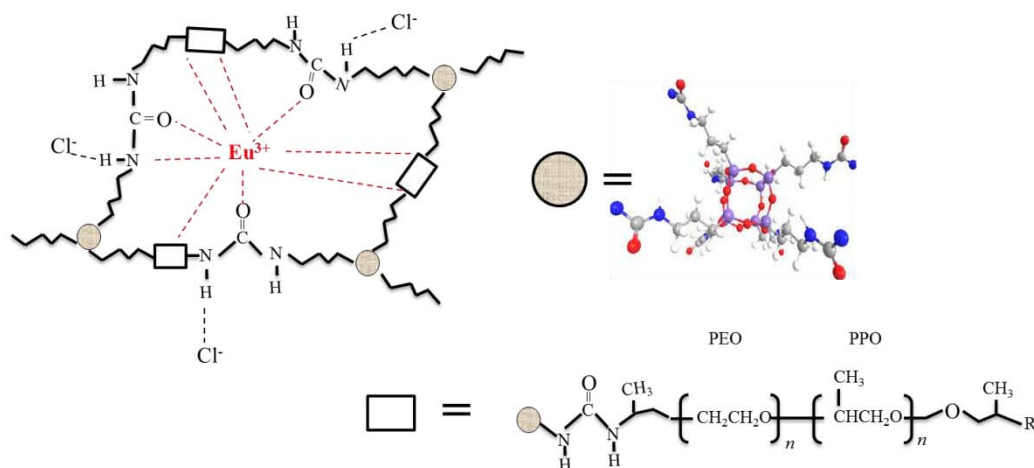


Figure 4.5: Schematization of the Eu^{3+} coordination with the OIH matrix.

Table 4.1: Table containing the values of the Gaussian fitting parameters for the Amide I and Amide II regions of the U-PEO₁₉₀₀ and U-PEO₁₉₀₀:Eu³⁺.

<i>Fitting Parameters</i>	U-PEO ₁₉₀₀	U-PEO ₁₉₀₀ :Eu ³⁺		
Chi ²	9.43E-6	6.97E-5		
Adj. R ²	0.999	0.999		
Frequency (cm ⁻¹)	Area int. (%)		Attribution	Ref
1560				
1564	48.98		N-H <i>in plan</i>	168
1565		6.11		
1590	---	41.93	$\delta(\text{NH}_2)$	172
1612	---	43.65	- -Eu ³⁺ - - -O _{carb.}	
1640		8.3		
1642	31.08		H-O _{carb.} (ordered)	
1656				
1660	15.40	---	H-O _{carb.} (desordered)	187
1674				
1680	4.5	---	C=O _{carb.} <i>free</i>	

➤ 4.2.3 FT-Raman analysis of the OIH:Eu³⁺ complexes;

To get further information about the effect of the OIH matrix - Eu³⁺ coordination and its effect on the conformational state of the poly(ether) chains (PE), FT-Raman was carried out in situ during heating from -85 °C to + 100°C, in the energy range from 700 to 1500 cm⁻¹ corresponding to *rocking*, *wagging* and *twisting* modes of CH₂ ¹⁹⁵. It is well known that this energy range is sensitive to modifications of the PE vs(C-O-C) *backbone* conformations by intermolecular interactions and/or temperature¹⁹⁶. In order

to describe the changes of polymer conformation, it is convenient to use the conformer ratio of *gauche* and *trans* arrangements along the polymer backbone. The *gauche/trans* conformation correlation can be performed by the analyses in FT-Raman as a function of the temperature in the CH₂ *backbone fingerprint* spectral region and the effect of Eu³⁺-loading in the OIH matrix.

Fig 4.6 shows the temperature dependency of the FT-Raman for U-PEO₁₉₀₀ (a) Eu³⁺-unloaded and (b) Eu³⁺-loaded. In regards to the intermolecular interactions of OIH matrix it has been reported^{197,198,199,200,201} that the torsional angle of polymer backbone becomes smaller than the average angle found in net PEO when a 3:1 complex was formed between PEO and a small metal cation, leading to the increase of the *gauche/trans* conformer ratio of the chains. For this reason, the growth of some bands at 809, 890, 1040 and 1140 cm⁻¹ are stronger in the spectra of U-PEO₁₉₀₀:Eu³⁺ complexes (more obvious at low temperature).

In Fig. 4.6 (a), it is observed that when the temperature increases up to the PEO₁₉₀₀ T_m (~ 25 °C), the well-defined bands at 844, 1063, 1144, 1234 and 1278 cm⁻¹ vanish, giving rise to a set of broad bands accompanied by a displacement of the maximum bands to lower values of energy, leading to the increase of the *trans/gauche* conformer ratio of the chains²⁰². The appearance of the broad bands is due to the change of the helical conformation, typical of the crystalline PEO₁₉₀₀, to an amorphous *trans* – like conformation for the PE v_s(C-O-C) *backbone*²⁰³. Thus the local degree of order of the chains increases, meaning that the population of *gauche* conformers increases as well. FT-Raman of U-PPO₂₀₀₀, Fig. 4.7, shows a *trans* v_s(C-O-C) conformational *backbone*, for both Eu³⁺-unloaded and Eu³⁺-loaded, due its amorphous character even below 0 °C.

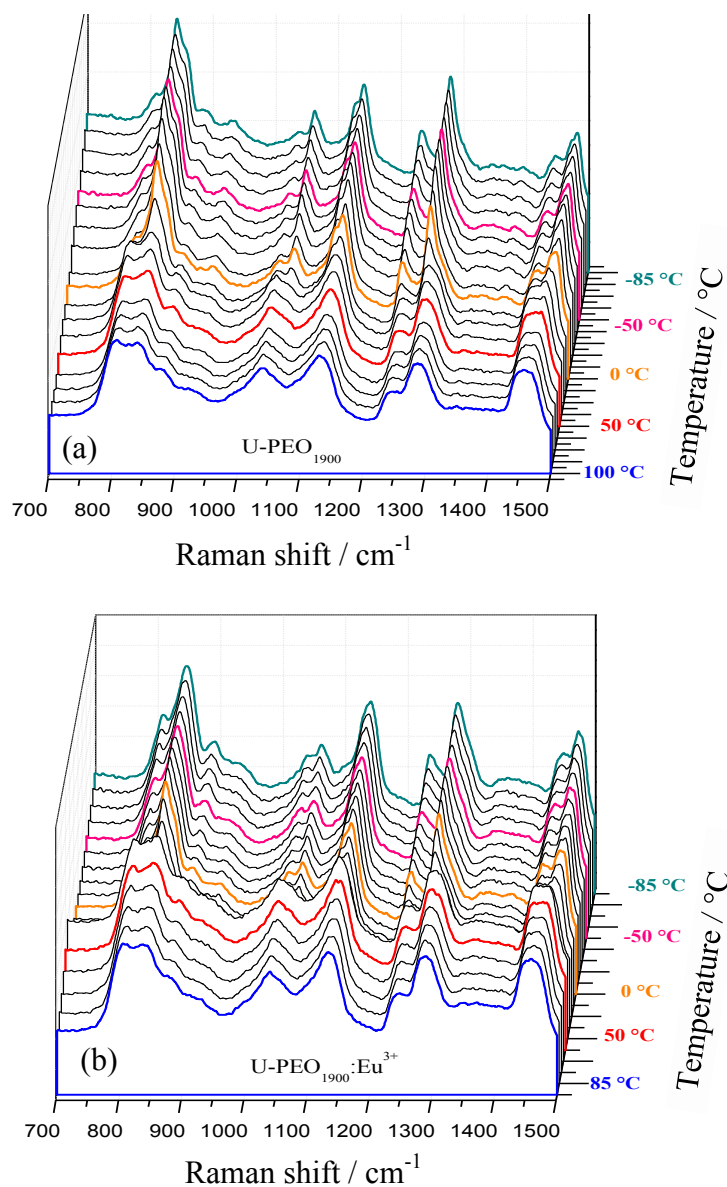


Figure 4.6: Raman Spectroscopy *in situ* with the temperature, from -100 °C to 100 °C, in an energy range from 800 to 1300 cm^{-1} for a U-PEO₁₉₀₀ OIH material (a) Eu³⁺-unloaded and (b) Eu³⁺-loaded.

Fig. 4.7 (a) and (b) shows the Raman spectra measured *in situ* with the heating of U-PPO₂₀₀₀ and U-PPO₂₀₀₀:Eu³⁺, respectively. The Raman spectra for the Eu³⁺-loaded OIH matrix is almost the same as the host U-PPO₂₀₀₀ matrix. Because PPO₂₀₀₀ has an amorphous character, the increase of temperature does not cause appreciable changes in the backbone structure.

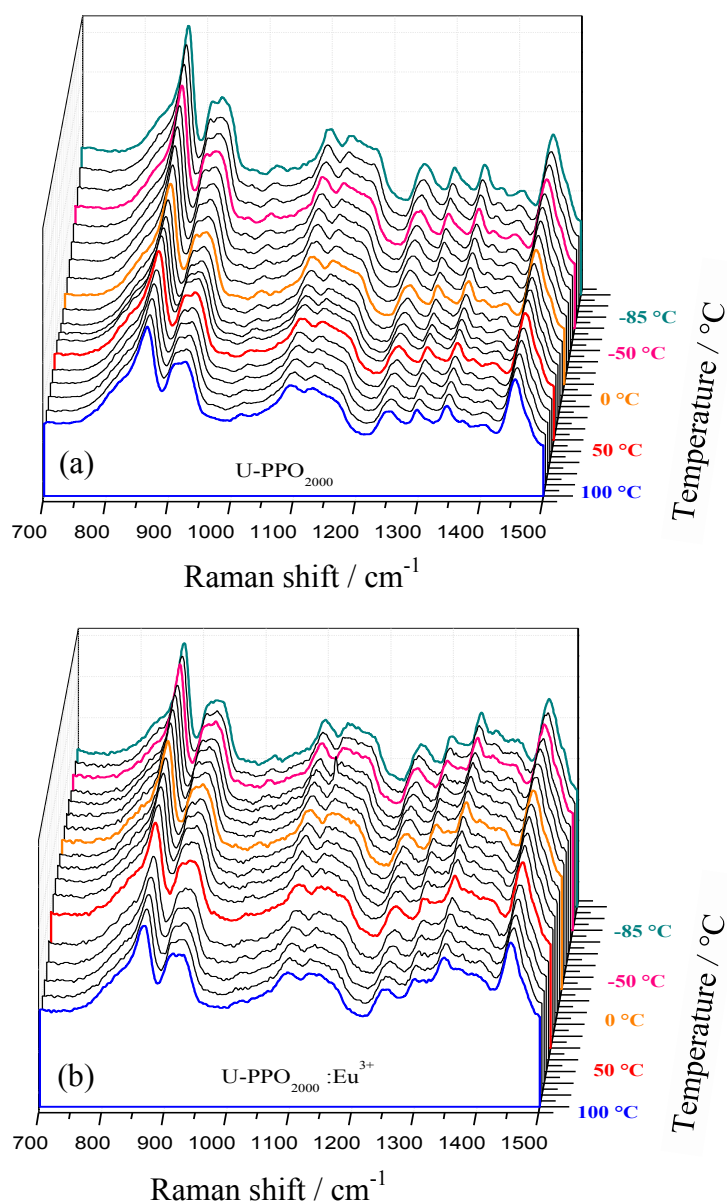


Figure 4.7: Raman Spectroscopy in situ with the temperature, from -100 °C to 100 °C, in an energy range from 800 to 1300 cm^{-1} for a U-PPO_{2000} OIH material (a) Eu^{3+} -unloaded and (b) Eu^{3+} -loaded.

➤ 4.2.4 SAXS analysis of the OIH:Eu^{3+} complexes;

Information concerning the nano-structural features of OIH:Eu^{3+} was obtained by SAXS measurements carried out at room temperature. Black SAXS curves shown in Fig 4.8 and 4.9, ascribed to U-PEO_{1900} and U-PPO_{2000} , respectively, exhibit a single broad peak with a maximum (q_{max}) at 2.13 and 1.49 nm^{-1} . This effect provides evidence for a strong spatial correlation between the regularly spaced siloxane cross-linked nodes²⁰⁴. After Eu^{3+} -loading, red SAXS curves showed a q_{max} displacement of 1.63 and 1.33 nm^{-1}

for U-PEO₁₉₀₀:Eu³⁺ and U-PPO₂₀₀₀:Eu³⁺, respectively. The average correlation distance between two adjacent siloxane nodes (ξ_d) was estimated from the q_{\max} value corresponding to the peak position by the equation $\xi_d = 2\pi/q_{\max}$ ²⁰⁵. The Eu³⁺ incorporation gives rise to a shift of ξ_d from 2.95 to 3.85 nm for U-PEO₁₉₀₀ and from 4.20 to 4.70 nm for U-PPO₂₀₀₀, as well as an increase of the correlation peak intensity. These features prove an increase of the electron density, indicating that the Eu³⁺ are close to the siloxane nodes, which is in agreement with the Eu³⁺ complexation by the oxygen carbonyl of amide group (Fig. 3.1) suggested by FT-IR results.

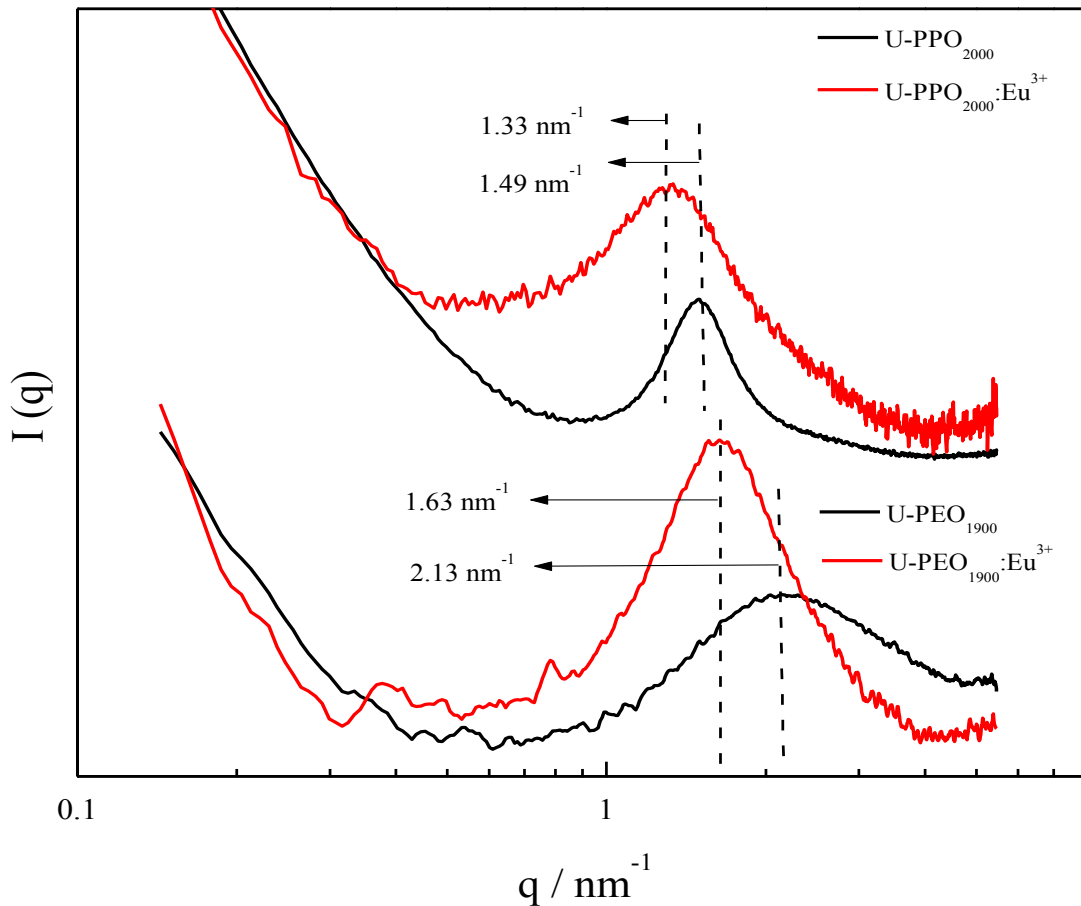


Figure 4.8: Room temperature SAXS curves for the (top) U-PPO₂₀₀₀ (black) and U-PPO₂₀₀₀:Eu³⁺ (red) and (bottom) U-PEO₁₉₀₀ (black) and U-PEO₁₉₀₀:Eu³⁺ (red) OIH materials

4.3: Effect of the UV-Vis radiation in the Photoluminescence properties of the OIH:Eu³⁺ complexes:

When the OIH:Eu³⁺ is exposed to UV-light irradiation at different times (Fig 4.9 (a) and (b)), it is observed that $I(q_{\max})$ decreases which can be ascribed to two effects; *i)* The Eu³⁺ - O_{carbonyl} discoordination, decreasing the O-I electronic contrast difference and *ii)* The poly(ether) - scission chain²⁰⁶, leading to a decrease in the number of spatially correlated siloxane nodes. The comparison of SAXS curves (Fig 4.9 (a) and (b)) reveal that the effect of UV-light irradiation is more pronounced for semi-crystalline U-PEO₁₉₀₀:Eu³⁺ than for non-crystalline U-PPO₂₀₀₀:Eu³⁺.

The PL properties of U-PEO₁₉₀₀ and UPPO₂₀₀₀ OIH:Eu³⁺ complexes and OIH:Eu³⁺ complexes exposed to different UV-light irradiation times were studied by recording their emission spectra (Fig. 4.10) upon excitation at 365 nm at room temperature. Two kinds of emissions were observed: *i)* The PL emission from the organic ligand at 425 nm suggests a weak energy-transfer process from the excited state of the ligand to the Eu³⁺ ion, and *ii)* the narrow lines (at $\lambda_{\text{em.}} > 425$ nm) assigned to transitions connecting the first excited state, ⁵D₀, to the ⁷F₀₋₄ low energy levels of the Eu³⁺ 4f⁶ configuration²⁰⁷.

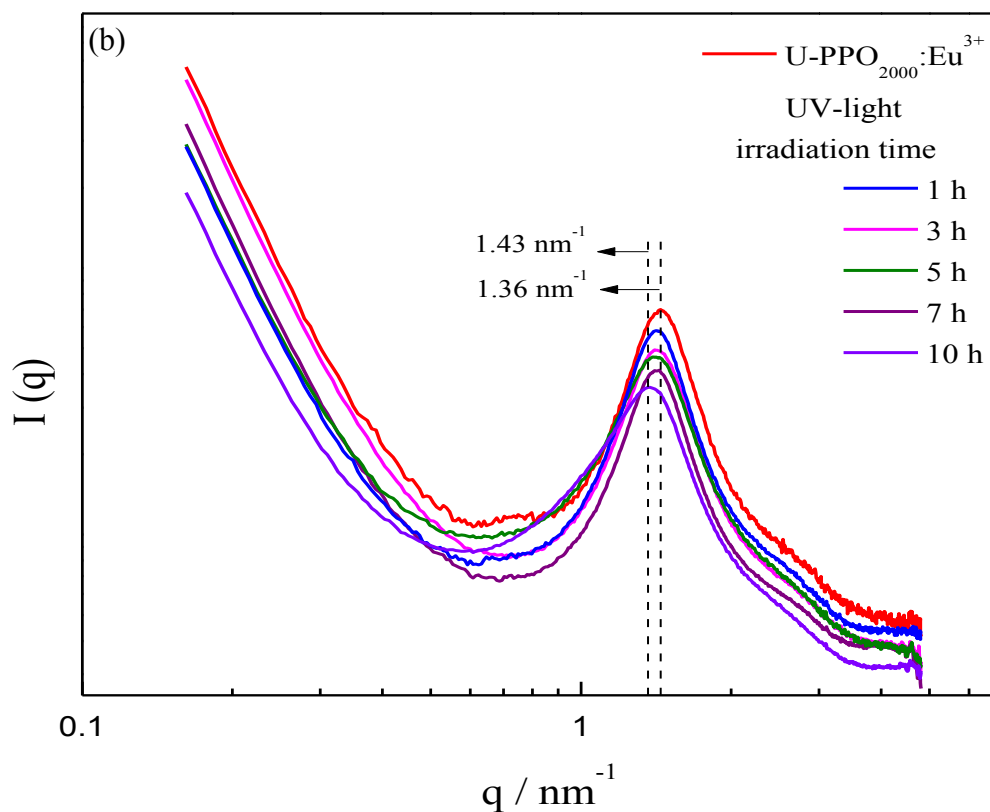
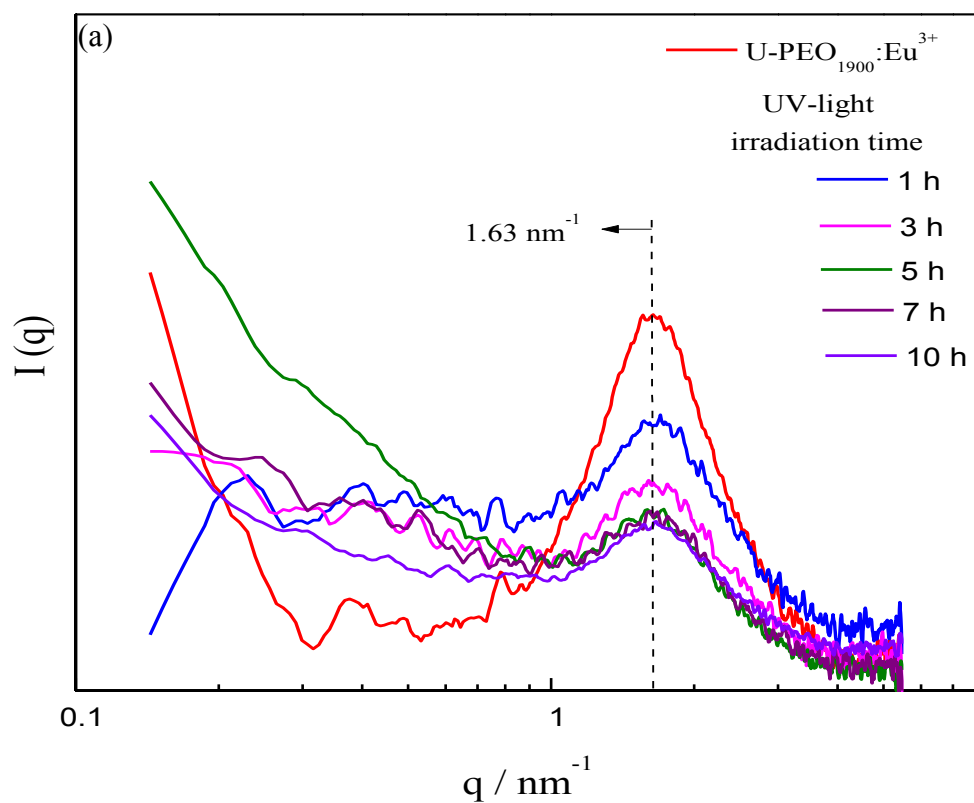


Figure 4.9: Room temperature SAXS curves for the (a) U-PEO₁₉₀₀:Eu³⁺ and (b) U-PPO₂₀₀₀:Eu³⁺ OIH materials exposed to UV-light irradiation at different times.

The broad band in the green-blue spectral range is ascribed to the convolution of the emission from NH groups from urea bridges and the emission originating from electron-hole recombination in the siliceous domains in the inorganic backbone^{208,209,210}, which have already been observed in unloaded matrices²¹¹ of similar hybrids^{212,213}. In the $\lambda_{em.} > 425$ nm region, five emission peaks lying at 578, 590, 615, 652 and 699 nm, belonging to the ${}^5D_0 \rightarrow {}^7F_J$ ($J = 0-4$) Eu^{3+} transitions can be observed⁸⁹.

By increasing the time of UV-light irradiation, a decrease of intensity of all emission bands can be observed. The decrease in the broad band at 425 nm can be associated with polymer β -scission leading to a decrease in the number of spatially correlated siloxane nodes, as shown in Fig. 4.9, while the decrease of the narrow lines is a consequence of the polymer β -scission accompanied by the loss of Eu^{3+} coordination with the carbonyl oxygen. The effect of photo-ageing in the OIH structure will be further discussed in Chapter 5.

The narrow line at 579 nm represents the ${}^5D_0 \rightarrow {}^7F_0$ transition¹¹⁶ – The presence of this electronic transition in both emission spectra of OIH: Eu^{3+} complexes reveal a disordered-like complexation, as observed in oxide glass¹⁰⁸. The ${}^5D_0 \rightarrow {}^7F_1$ transition corresponds to a parity-allowed magnetic dipole transition, which is practically independent of the chemical environment²¹⁴ and therefore, it has been used for normalization. On the other hand, the ${}^5D_0 \rightarrow {}^7F_2$ transition, called “hypersensitive”^{215,216}, is a forced electric dipole (ED) transition, being a forbidden transition by the selection rules. However, the ${}^5D_0 \rightarrow {}^7F_2$ electric dipole transition becomes allowed for molecules without centers of inversion because the Laporte’s rule is relaxed due to odd parity terms in the ligand field Hamiltonian²⁰⁹. The emission strength of this transition is sensitive to the surroundings of Eu^{3+} ²¹⁷, indicating that the Eu^{3+} ions occupy a low symmetry site without an inversion center for both U-PEO₁₉₀₀: Eu^{3+} and U-PPO₂₀₀₀: Eu^{3+} .

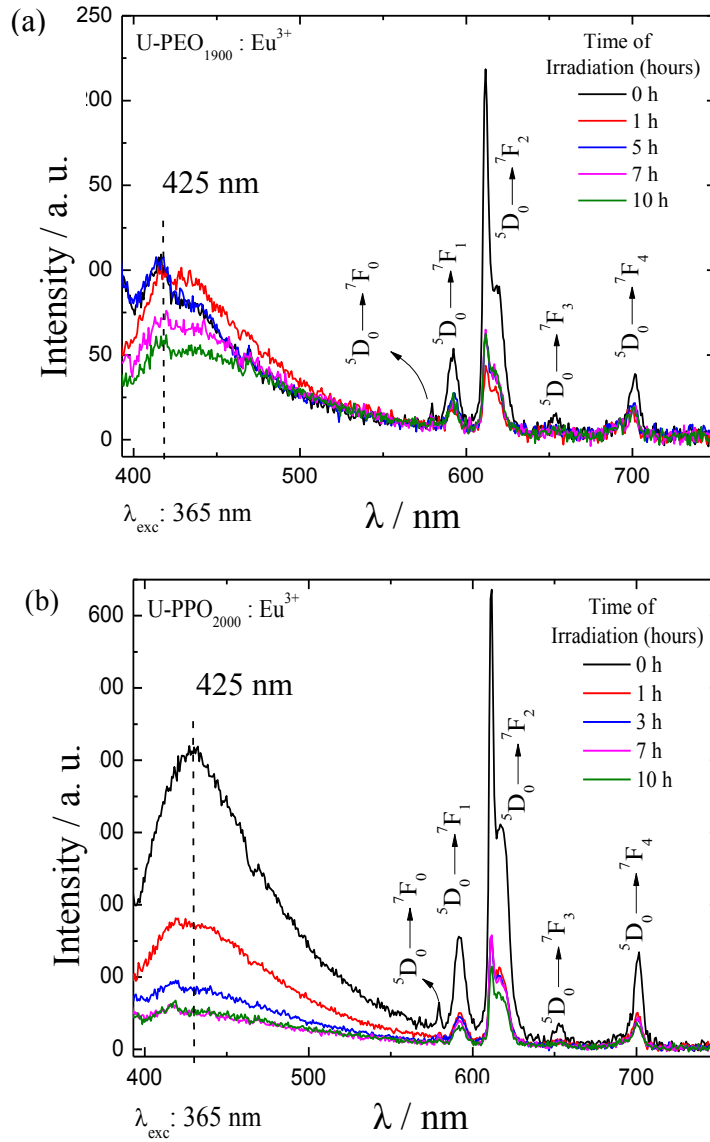


Figure 4.10: Effect of UV-light exposure times on the emission spectra of the Eu³⁺ - OIH complex, (a) U-PEO₁₉₀₀ and (b) U-PPO₂₀₀₀.

For this reason, the ratio between the intensities ($I_{0,j}$) of the ${}^5D_0 \rightarrow {}^7F_2$ and ${}^5D_0 \rightarrow {}^7F_1$ transitions, $I({}^5D_0 \rightarrow {}^7F_2) / I({}^5D_0 \rightarrow {}^7F_1)$, called the Judd-Ofelt parameters ($\Omega_{1,2}$)^{148, 218}, can be considered as a parameter to probe the “asymmetry” of the Eu³⁺ sites^{219,220}. Usually Judd-Ofelt intensity parameters are obtained from absorption data. However, in the case of Eu³⁺, the pure magnetic dipolar character displayed by the ${}^5D_0 \rightarrow {}^7F_1$ transition makes it possible for the determination of the intensity parameters to be obtained from

emission spectra. The dependence of $\Omega_{1,2}$ values as a function of the UV-light irradiation time of the OIH:Eu³⁺ complex is found in (Table 4.2).

Both non-irradiated OIH:Eu³⁺ complexes have been shown to have a high value of Eu³⁺ asymmetry in its local surroundings, which can be seen by their high $\Omega_{1,2}$ parameter value (~ 4.1), which is even higher than several oxide glasses²⁰⁷. This fact is in agreement with the apparition of the forbidden $^5D_0 \rightarrow ^7F_0$ transition. On the other hand, the photo-degradation plays a different role in PEO₁₉₀₀ and PPO₂₀₀₀ materials. It is seen from Table 4.2 that $\Omega_{1,2}$ values decrease in the first stage of exposure, and then increases after 5 and 3 h for U-PEO₁₉₀₀ and U-PPO₂₀₀₀, respectively. It can be explained by an initial formation of chromospheres, which are unstable and undergo photolysis during prolonged irradiation. Kowalonek, J., et al. reported that for PEO + CoCl₂ UV photo-ageing, small crystallites are reordered and replaced by slowly growing of larger crystallites. This means that during the early step of photo ageing of the OIH:Eu³⁺ complex, the formation of chromophores in the hybrid matrix prevails over the photo-products²²¹.

After 3 h of UV irradiation, the $\Omega_{1,2}$ value of U-PPO₂₀₀₀:Eu³⁺ is almost two times higher than U-PEO₁₉₀₀:Eu³⁺. U-PPO₂₀₀₀:Eu³⁺ remains non-crystalline even after the UV-irradiation. On the other hand, there is a slight increase of the symmetry for the U-PEO₁₉₀₀:Eu³⁺, which can be explained in following way: for semi-crystalline polymers, like PEO₁₉₀₀, photo-ageing starts in the amorphous phase due to the easy diffusion of oxygen to the unordered chains. It was already well-known that PEO₁₉₀₀ has an ordered helical (*gauche*) conformation below the fusion temperature²²². This ensures that Eu³⁺ cations are accommodated in a distinctly, more distorted environment in PPO₂₀₀₀ (*trans*) than in PEO₁₉₀₀ (*gauche*)

Table 4.2: $I(^5D_0 \rightarrow ^7F_2) / I(^5D_0 \rightarrow ^7F_1)$ ratio ($\Omega_{1,2}$), of the Eu^{3+} - OIH complex, exposed to different UV-light irradiation times.

Time of Irradiation (hours)	$\Omega_{1,2}$	
	U-PEO ₁₉₀₀ :Eu ³⁺	U-PPO ₂₀₀₀ :Eu ³⁺
0	4.07	4.13
1	2.73	2.95
3	1.70	3.49
5	2.48	4.72
7	2.79	4.11
10	2.25	4.43

The low intensity found for the $^5D_0 \rightarrow ^7F_3$ is due to its forbidden origin by the selection rules, happening in a forced way through the electric dipoles²²³. At the same time, the “hypersensitive” transition, $^5D_0 \rightarrow ^7F_2$, the band observed at 699 nm, ascribed to the $^5D_0 \rightarrow ^7F_4$ transition, is also a forced electric dipole transition, as defined by the selection rules. Therefore, its intensity (I_4) should become lower as its symmetry becomes higher. Fig. 4.10 reveals that (I_4) -U-PPO₂₀₀₀ is almost 3 times higher than (I_4) -U-PEO₁₉₀₀. These results suggest that amorphous polymers have better PL properties than semi-crystalline ones. The relatively high values of PPO₂₀₀₀ intensity parameters, Ω_2 and Ω_4 , compared to PEO₁₉₀₀, indicate highly polarizable Eu^{3+} cations in the local environment of these hybrids²⁰⁹. One way to quantify the transferred energy is from the photoluminescence quantum yield (PL-QY). Absolute QY values in different times of UV-light irradiation are shown in Fig. 4.11. The maximum observed at different wavelengths correspond to the percentage of excitation in different Eu^{3+} environments.

Fig. 4.11 (b) shows a maximum displacement from 340 nm (black) to 368 nm (red) after irradiation of U-PPO₂₀₀₀:Eu³⁺. The band observed at 340 nm comes from the energy absorption of the organic ligands, while the band at 368 nm is due to the Eu^{3+} cation excitation by the *antenna effect*¹⁰³. The PL-QY for this material before the UV-light irradiation was found to be around 9%. On the other hand, the U-PEO₁₉₀₀:Eu³⁺ material before UV-light irradiation showed a poor PL-QY value (QY ~1.5 %). The significant difference between these values points out the crucial role of the ureasil

substituent's nature in the PL-QY features, particularly the hydrophilic/hydrophobic properties, where the water molecules typically found coordinate with the PEO backbone and can quench the Eu^{3+} PL features.

After 1 h of UV-light irradiation, the U-PPO₂₀₀₀: Eu^{3+} PL-QY decreases 45% from its initial value, accompanied by the intensity increase of three bands, located at 380, 395 and 465 nm. These bands are well-known in literature and are attributed to the ${}^7\text{F}_0 \rightarrow {}^5\text{L}_7$, ${}^7\text{F}_0 \rightarrow {}^5\text{L}_6$, and ${}^7\text{F}_0 \rightarrow {}^5\text{D}_2$ Eu^{3+} transitions, respectively. This kind of electronic transition is not characteristic to the Eu^{3+} cation coordinated in a complex system environment without a symmetry center. As the time of the UV-light irradiation increases, the intensity of the bands from the Eu^{3+} non-coordinated environment increases as well, showing a dependence of Eu^{3+} - OIH matrices complexation on UV-light irradiation. This finding allows for the proposal of applying this material in the field of coatings as optical-markers and UV-sensors.

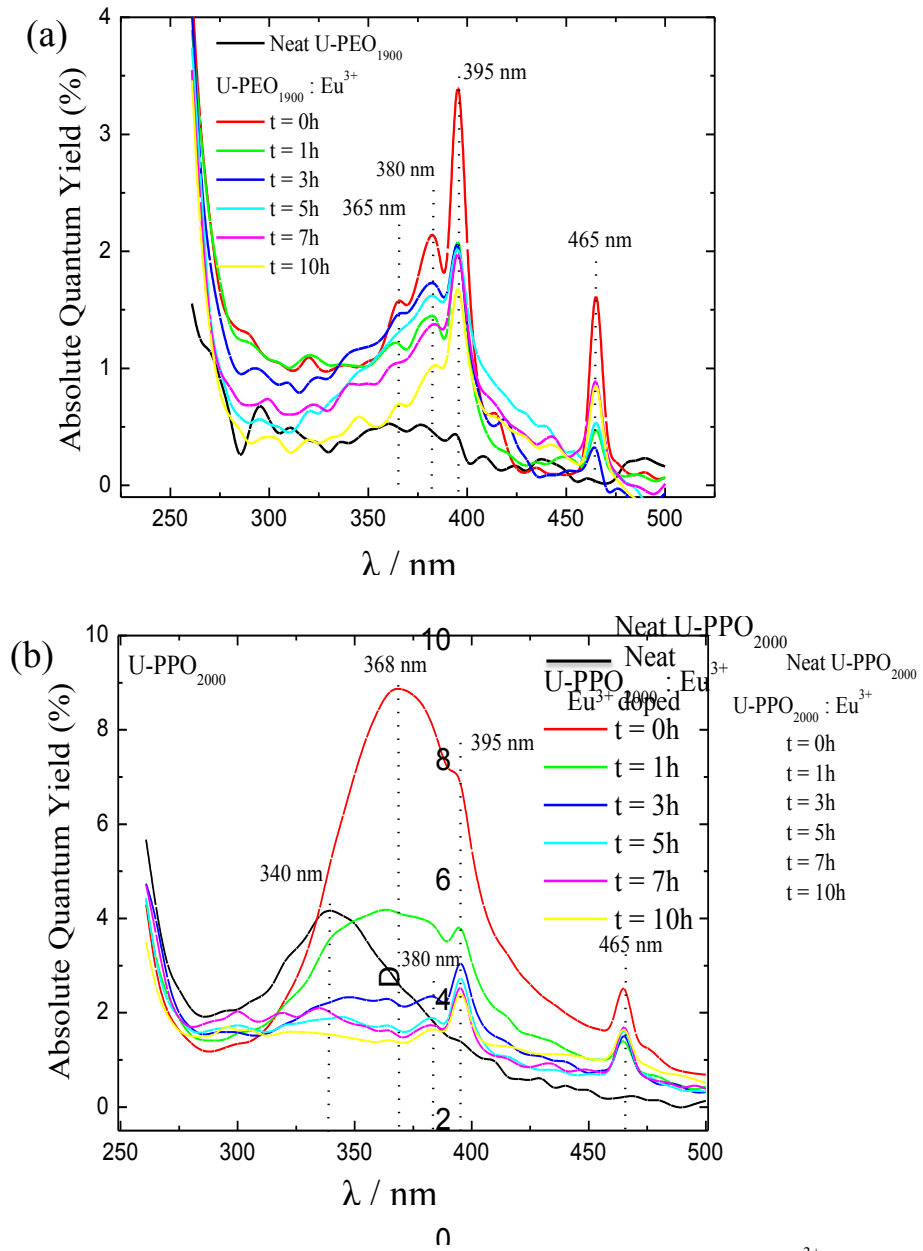


Figure 4.11: Excitation spectra, in the spectral range from 250 to 500 nm, of the OIH:Eu³⁺ complexes, (a) U-PEO₁₉₀₀ and (b) U-PPO₂₀₀₀, exposed to different UV-irradiation times.

4.4: Partial Conclusions:

Eu³⁺ luminescence OIH complexes based on PEO₁₉₀₀/PPO₂₀₀₀ (semi-crystalline / amorphous) polymers were synthesized by the sol-gel method. Through several techniques (DSC, FT-IR, FT-Raman and SAXS) we were able to prove the local Eu³⁺ coordination into OIH matrices. The results led us to conclusion that the complexation happens by the carbonyl polar oxygen present in the amides group, leaving the C-O-C backbone of the poly(ether) untouched, as was found by the presence of the PEO *gauche* state, where Eu³⁺ loading preserved the (νCOC) stretching mode at 1100 cm⁻¹. Both polymer complexes showed narrow emission lines, ascribed to the ⁵D₀ → ⁷F_j europium transitions, confirming Eu³⁺ dissociation into the matrix. The poor PL-QY observed for the U-PEO₁₉₀₀:Eu³⁺ complexes were shown to be ascribed to the PEO₁₉₀₀ *tgt* helical conformation, which coordinates with water molecules, thus preventing an efficient ligand-metal energy transfer. On the other hand, U-PPO₂₀₀₀, with a *trans*-conformation, showed a reasonable PL-QY value and a good dependency on Eu³⁺ - O_{carbonyl} complexation as a function of the UV-irradiation time. The intensity decrease of the broad green-blue band and the narrow lines (ascribed to the ⁵D₀ → ⁷F_j europium transitions) was enlightened. This new knowledge of lanthanide-containing materials combined with the excellent mechanical properties and bio-compatibility of OIH materials allows for their application in different fields such as UV-sensor coatings and biological optical-markers.

Chapter 5:

Photo-Stability and Photo-Luminescence Properties

5.1 Introduction to the Chapter:

In this Chapter, we intend to evaluate the role played by the carbonyl oxygen atoms in the loss of coordination with Eu^{3+} cations suggested by the visible red \rightarrow blue transition in order to gain an in-depth understanding of these luminescent features, which were discussed in Chapter 4. We will analyze the FTIR spectral signature and photoluminescence properties of U-PPO of different molecular weights in the carbonyl range ($1800 - 1500 \text{ cm}^{-1}$) for OIH: Eu^{3+} thin films as a function of the duration of artificially accelerated UV-irradiation ($\lambda \geq 300 \text{ nm}$). Our efforts were focused on OIH: Eu^{3+} complexes based on PPO, aiming to evaluate the effect of the polymers' molecular weight on the photo-aging rate. U-PEO₁₉₀₀: Eu^{3+} was not discussed in detail due to the complexity of the mass transport properties in semi-crystalline polymers. Therefore, the detailed studies that were carried out refer to the set of amorphous polymers that can give us more reliable results.

5.2 Effect of Eu^{3+} – loading on photo-degradation:

The UV-vis irradiation at $\lambda > 300 \text{ nm}$ for the Eu^{3+} – unloaded and Eu^{3+} – loaded OIH material matrices of the U-PPO films (thickness = $50 \mu\text{m}$) (wt. = 230, 200 and 4000 gm^{-1}) caused notable modifications in the IR spectra. However, UV-irradiation had to be limited to moderate extents of oxidation times because the samples completely degrade in a very short amount of time, especially in the case of thin films.

For polymers, as in the case of PEO and PPO, the first step of photo-oxidation, occurring at $\lambda > 300 \text{ nm}$, is the formation of hydroperoxides (Fig. 5.1). This process occurs on a secondary carbon in the β -position from an ether-type²²⁴ oxygen, and was well defined by J-L Gardette and S. Therias²²⁵. The molecular structure of hydroperoxides produced from photo-aging of U-PPO OIH materials can result in three

different photoproducts (Fig. 5.2). The different possibilities of the photo-products for U-PPO hydroperoxide are consequences of ageing, which produces heterogeneous effects mostly caused at a macroscopic level due to the oxygen diffusion-limited effects²²⁶. These heterogeneous effects are dependent on the coupling of chain with the oxygen consumption rate, which depends on the reactivity of the polymer and the oxygen permeability in the material²²⁷.

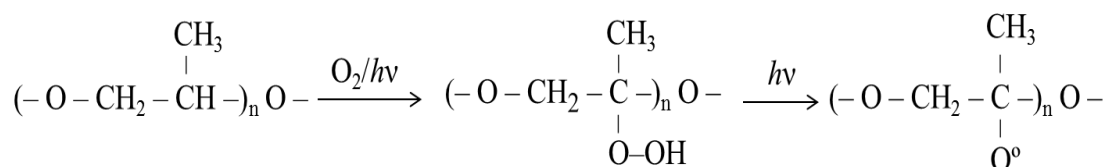
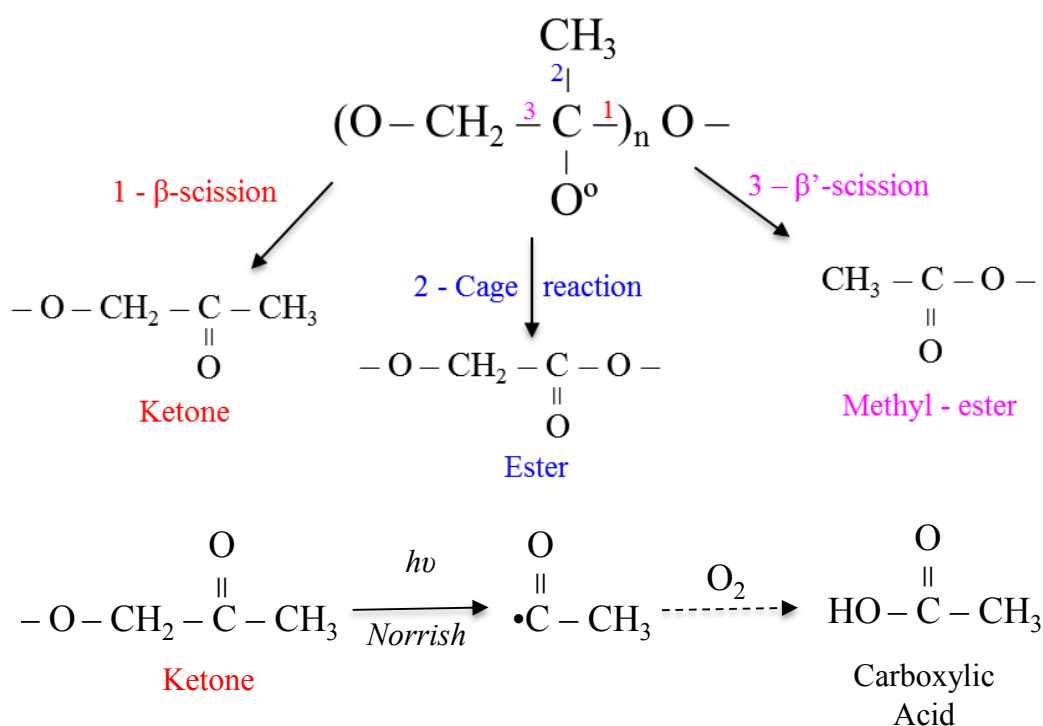


Figure 5.1: Mechanism of photo-degradation of U-PPO in hydro-peroxide and macro-radical.



Scheme 5.2: Photo-oxidation mechanisms of the PPO macro-radical. Step 1: ketone forming by β -scission from the oxygen ether-type *inside* in the monomer followed by Norrish I mechanism forming carboxylic acid; Step 2: Cage reaction forming ester (without breaking of the chain) leading a $\text{O}=\text{C}^\bullet-\text{CH}_3$ radical; and Step 3: A methyl-ester formation by a β' -scission from the oxygen ether-type *outside* of the monomer
 Adapted from 168

5.3 Effect of PPO molecular weight on photo-degradation kinetics:

The effect of photo-oxidation of U-PPO₂₀₀₀ films (50 μm), Eu³⁺ – unloaded and Eu³⁺ – loaded OIH materials, are presented in the FTIR spectra of Fig. 5.3 (a) and (b), respectively. In both cases, for U-PPO and Eu³⁺ U-PPO, it is observed the formation of a new IR band at 1720 cm⁻¹ with a shoulder at 1740 cm⁻¹ with UV-irradiation time.

For U-PPO₂₀₀₀, the IR spectra during 10 hours of UV-irradiation (Fig. 5.3 (a)) shows the formation of a new absorption band in the carbonyl domain, whose intensity increases with the time of the UV-irradiation, with a maximum at 1720 cm⁻¹ and a shoulder at 1740 cm⁻¹, which are the contribution of different carbonylated species, from the OIH material photo-ageing, resulting in the photo-products of the polymer oxidation.

For OIH:Eu³⁺ complex based on PPO, the IR spectra (Fig. 5.3 (b)) shows the formation of the same absorption bands with a maximum at 1720 cm⁻¹ and a shoulder at 1740 cm⁻¹, whose intensity increases with the UV-irradiation duration. This reveals that the same oxidation products are formed in both cases. On the other hand, the IR band at 1608 cm⁻¹ which corresponds to the Eu³⁺ complex and previously characterized as $\nu(\text{C}=\text{O})$ from the Eu³⁺ – O_{carbonyl} complexation, decreases whereas two bands appear at 1620 and 1575 cm⁻¹ with the increase of the UV-irradiation time. This phenomenon suggests a decomplexation of Eu³⁺ cations with the U-PPO ligands upon UV-vis irradiation, once these maximums have already been attributed to the Amide region, originated from the loss of the Eu³⁺ – OIH coordination with the increase of UV irradiation time.

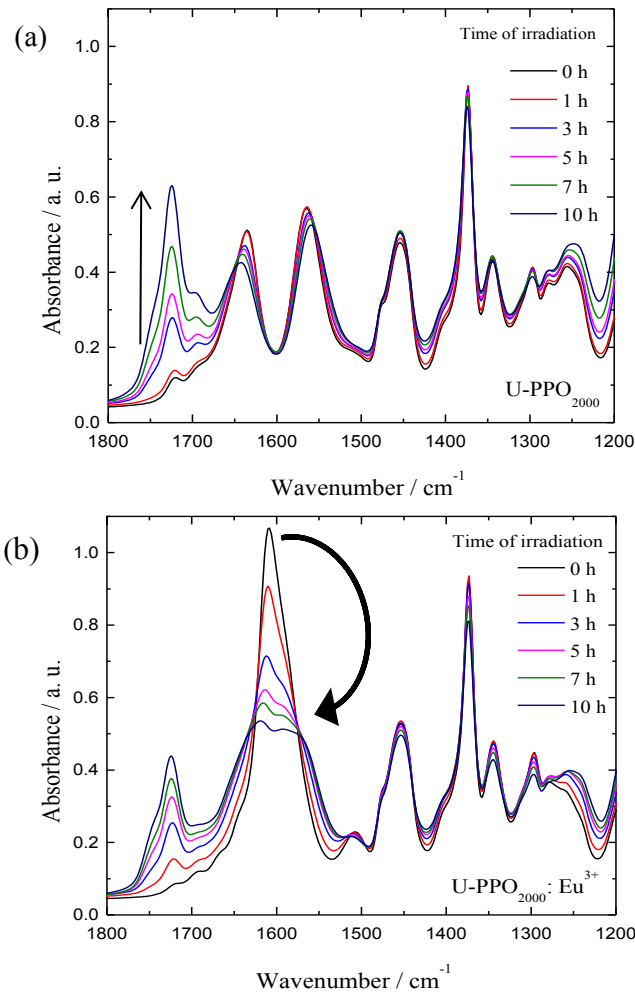


Figure 5.3: FTIR spectra evolution during accelerated photo-aging assays (a) U-PPO₂₀₀₀ and (b) U-PPO₂₀₀₀:Eu³⁺ films (50 μm) in different UV-light exposure at $\lambda \geq 300$ nm and 60 °C.

Other feature found by comparing the FTIR photo-aging results of the U-PPO hybrid prepared with PPO of different molecular weights (wt. 230, 2000 and 4000 g.mol⁻¹), is the effect of the Eu³⁺ loading on rate of photo-oxidation products formation. The rates of photo-oxidation of the unload and Eu³⁺ loaded U-PPO, Fig. 5.4, respectively, can be compared by the subtraction of the band at 1720 cm⁻¹. In case of the thin films, with the same thickness, this rate can be directly compared with each other. Figure 5.4 displays the time evolution of the area of the band at 1720 cm⁻¹ for the U-PPO prepared with PPO of different molecular weights. From Fig. 5.4 (a), at 1720 cm⁻¹, a remarkable variation in curves profiles with the Eu³⁺-loading and with PPO molecular

weight is observed. The curve profiles of carbonylated formation (Fig. 5.4) are sensitive to the PPO molecular weight and the Eu^{3+} -loading as well. U-PPO₂₀₀₀ Eu^{3+} - unloaded was the OIH material with the higher carbonylated products formation, while the U-PPO₂₃₀ Eu^{3+} - unloaded was the lower one²²⁸.

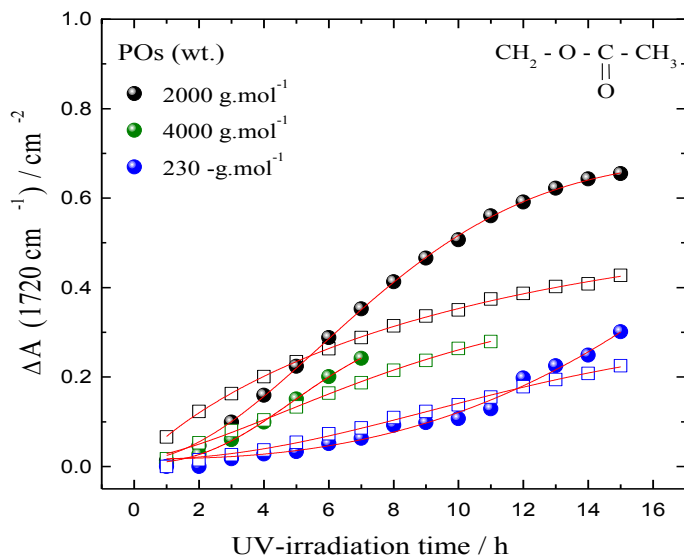


Figure 5.4: Variation of absorbance at 1720 cm^{-1} as a function of UV irradiation time (photooxidation at $\lambda > 300 \text{ nm}$, 60 °C) for the U-PPO films with different molecular weights (230, 2000 and 4000 g.mol^{-1}), Eu^{3+} -unloaded (full circles) and Eu^{3+} -loaded (empty squares).

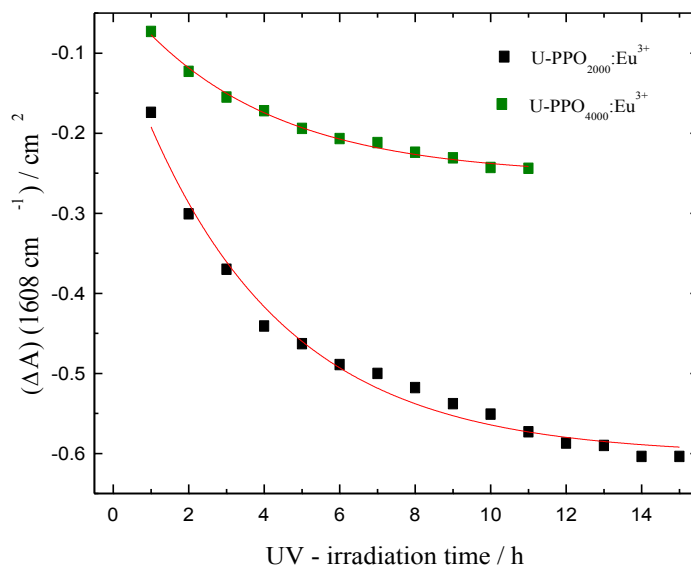


Figure 5.5: Variation of absorbance at 1608 cm^{-1} as a function of UV irradiation time (photooxidation at $\lambda > 300 \text{ nm}$, 60 °C) for Eu^{3+} -loaded U-PPO films with different molecular weights (2000 and 4000 g.mol^{-1}).

On the other hand, Fig. 5.5, which displays the time evolution of the area of the band at 1608 cm^{-1} for the U-PPO₂₀₀₀ and U-PPO₄₀₀₀ – Eu³⁺-loading, shows a decrease in intensity due to the loss of Eu³⁺-O_{carbonyl} coordination. In order to prove both, ketone and ester as photo-products and the loss of Eu³⁺-O_{carbonyl} coordination, chemical treatment with NH_{3(g)} was carried out.

5.4 Identification of the UV-Vis photo-degradation products by ammonia chemical treatment:

Derivatization reactions have been carried out to identify the oxidation photoproducts observed in the carbonyl region of the FTIR spectrum. These reactions occur through treatment of the photo-oxidized samples with gaseous reactants like ammonia. Chemical treatments were performed following the procedure previously described^{165,166}. The results of NH₃ treatments carried out for 10 h photo-oxidized Eu³⁺ – unloaded and Eu³⁺ – loaded OIH material U-PPO₂₀₀₀ films (50 μm), are shown in the carbonyl region of FTIR spectra in Figs. 5.6 (a) and (b), respectively.

From Fig. 5.6 (a) and (b), it is observed that there is an intensity decrease of the main oxidation band at 1720 cm^{-1} correlates with an increase of two bands at 1680 cm^{-1} and 1640 cm^{-1} . These bands originated from the reaction between ammonia with U-PPO₂₀₀₀ photoproducts. The host structure reaction (Fig. 5.6 (a)) leads to an increase of absorbance at 1680 cm^{-1} (peak # 1) attributed to amide groups, which are formed by the reaction between ammonia and ketone (1720 cm^{-1})²²⁴:

On the other hand, unclear in Fig. 5.6 (a), a new band referred to the amides formed from the reaction of NH₃ with ester. In fact this new band is expected to be in the same wavenumber range of the Amide groups that already exist in the OIH material structure^{185,229}, hidden from the observation of the band formed from the ammonia –

photoproducts reaction. However, in Fig. 5.6 (b), it was possible to observe the band at 1640 cm^{-1} due to the presence of the $\text{Eu}^{3+} - \text{O}_{\text{carbonyl}}$ complexation band at 1608 cm^{-1} . This result helps to prove the ester groups to be one of the PPO photoproducts, Fig. 5.7 (b)¹⁶⁸.

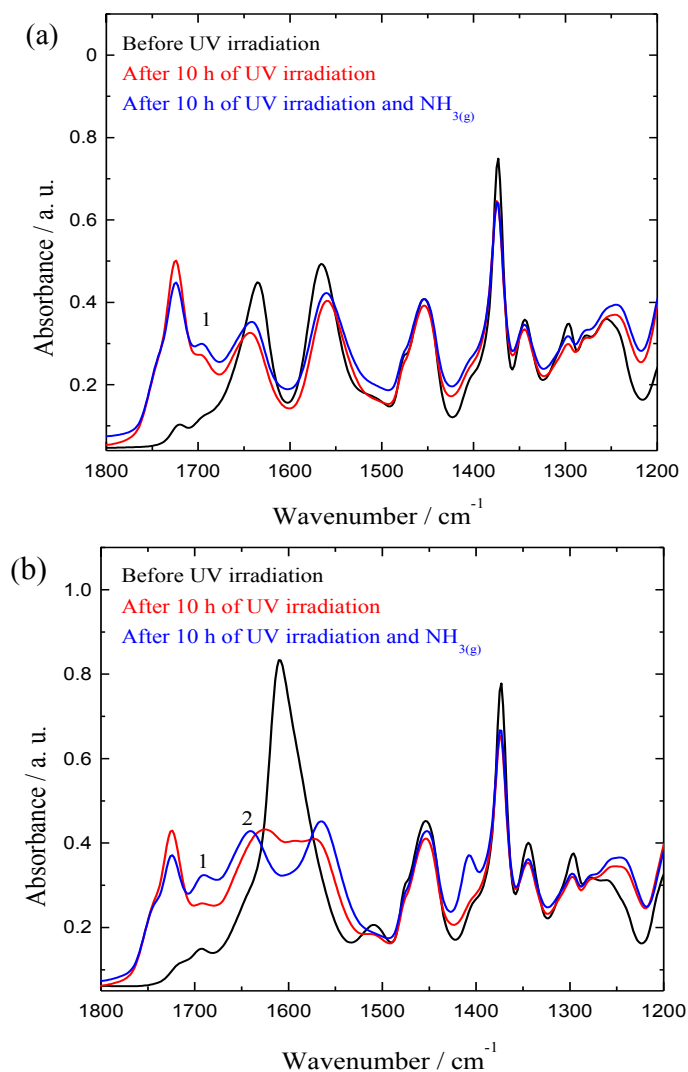


Figure 5.6: Effect of NH_3 treatment of (a) U-PPO_{2000} and (b) $\text{U-PPO}_{2000}:\text{Eu}^{3+}$, films photo-degraded by 10 h of UV-light exposure ($\lambda \geq 300\text{ nm}$, $60\text{ }^\circ\text{C}$), in IRFT spectra in the carbonyl range.

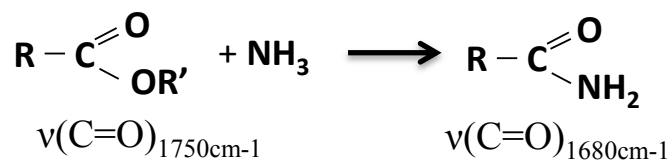


Figure 5.7: Schematic diagram of the reactions between ammonia with U-PPO_{2000} photoproducts.

Unloaded and Eu^{3+} – loaded OIH U-PPO materials showed two different, main photoproducts, confirmed by the NH_3 reaction; one of the photoproducts comes from a hydroperoxide β -scission resulting in ketone groups, and the other one comes from a cage reaction forming ester groups, leaving a $-\text{CH}_2^\circ$ radical (Fig 5.3).

5.5 Red \rightarrow Blue photoluminescence transitions and its application:

The loss of Eu^{3+} coordination with the UV irradiation allow for these complexes to have a transition in the visible range from red to blue. The red \rightarrow blue transition (Fig.5.8) is responsible for the second effect on the polymers photo-oxidative behavior. This effect came from the efficient intermolecular energy transfer of the UV-light absorbed, realized by the urea organic chromophore $-\text{NH}-\text{C}(=\text{O})-\text{NH}-$ to the luminescent center. These results give the material the possibility to be applied as optical marker coatings for monitoring exposure to excessive UV-light for packaging. For that, the photoluminescence of Eu^{3+} – loaded OIH matrices as a function of UV irradiation time was carried out to measure the energy transfer from the organic ligand to the Eu^{3+} luminescent center.

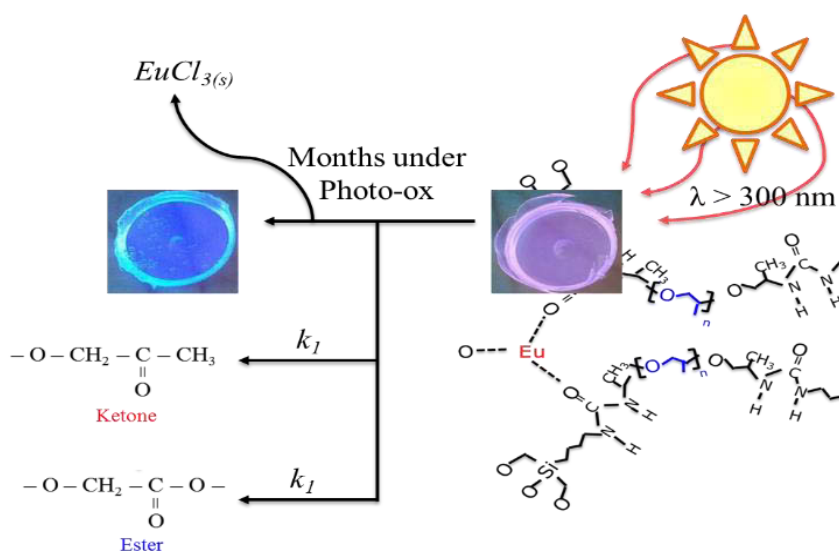


Figure 5.8: Schematization of the application of $\text{U-PPO}_n:\text{Eu}^{3+}$ complexes as optical marker showing the red \rightarrow blue transition.

The quantification of the absolute PL quantum yield values (%) recorded for U-PPO:Eu³⁺ complexes with different molecular weights, considering the overall luminescence of the Eu³⁺ cation, as function of the UV-irradiation time, is reported in Fig. 5.9. U-PPO₂₀₀₀:Eu³⁺ and U-PPO₄₀₀₀:Eu³⁺ showed a PL decreasing from 9% to 4% and 8 % to 3%, respectively, after 1 h of UV-light irradiation. U-PPO₂₃₀:Eu³⁺ does not show a considerable value of PL in the red emission range, which may be explained by the high europium concentration in the matrix, thus causing an inefficient energy transfer. U-PPO₂₀₀₀:Eu³⁺ showed the best performance in the field of Eu³⁺ energy transfer. Following these results, this U-PPO material is the most appropriate for this kind of application, combining its PL properties with the excellent physical-chemical properties and its remarkable capacity to holding its structure during high wavelength irradiation.

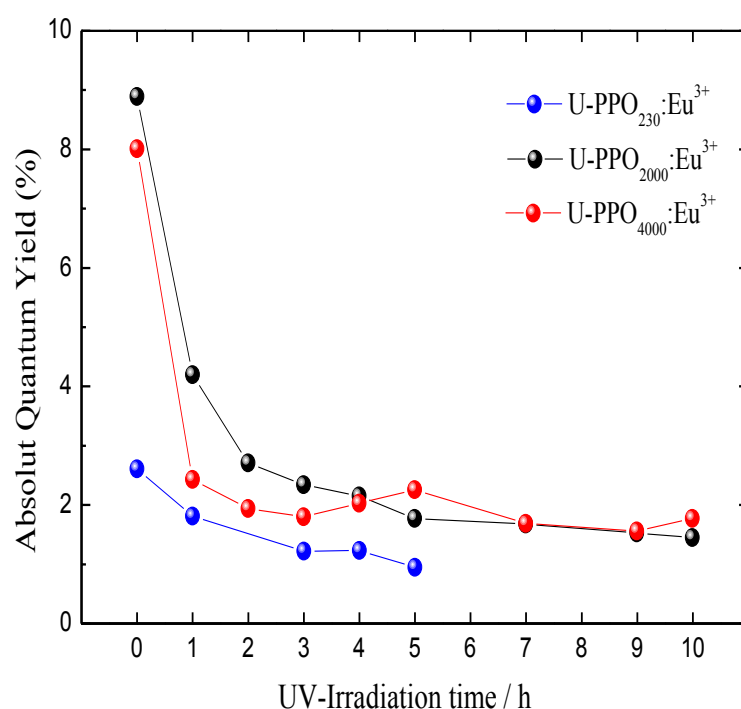


Figure 5.9: Evolution of the U-PPOs:Eu³⁺ QY-value as a function of the long wavelength ($\lambda > 300$ nm) UV-light irradiation.

5.6 Partial Conclusions:

The aim of this Chapter was to utilize of the knowledge of polymer degradation mechanisms to confirm the coordination of Eu^{3+} - $\text{O}_{\text{carbonyl}}$ from urea groups and to complement the results obtained in Chapter 4. Room temperature FTIR of the OIH thin films showed a 1608 cm^{-1} band intensity decrease that depended on the UV-vis irradiation time. These results are coherent with the loss of Eu^{3+} coordination when the materials are exposed to intense UV-light. The loss of Eu^{3+} coordination reveals a dependence of PPO molecular weight present in OIH materials, leading to different photo-degradation kinetics rates.

These set of results enable proposing a mechanism of degradation. Furthermore, the difference in the kinetics parameters after Eu^{3+} -loading shows a slower rate of β -scission reaction compared with the Eu^{3+} -unloaded OIH materials, allowing us to propose that the presence of Eu^{3+} atoms protects the OIH material from β -scission of organic chain.

The formation of new absorption bands at 1720 and 1740 cm^{-1} with the increases of UV-vis exposure allowed the OIH photo-products determination by the ammoniac chemical treatment of the photo-degraded OIH materials. It was observed the formation of formate and ester as the main photo-products, even to the $\text{OIH}:\text{Eu}^{3+}$ complex, from the hydroperoxides organic chain β -scission and cage reaction, respectively. The satisfactory value of PL absolute quantum yield for the $\text{U-PPO}_{2000}:\text{Eu}^{3+}$ and $\text{U-PPO}_{4000}:\text{Eu}^{3+}$ before the UV-vis irradiation accompanied with their quickly loss of Eu^{3+} coordination showing to own a red \rightarrow blue PL transition. The Eu^{3+} β -scission chain protecting make these $\text{OIH}:\text{Eu}^{3+}$ complexes emerging materials for application as optics markers and/or packaging monitoring of intense UV exposure.

Chapter 6:

Thermal, Structural and Electrical Properties hybrid blend

6.1 Introduction to the Chapter:

This Chapter will focus on the effect of Li^+ -loading on the thermal, structural and electrical properties of OIH matrices based on PEO_{1900} , PPO_{2000} and $\text{U}_x\text{PEO}_{1900}:\text{U}_{1-x}\text{PPO}_{2000}$ blends. The thermal properties were analyzed by DSC and the effect of blending in the melting of the semi-crystalline phase and glass transition temperature, T_g , is discussed. The thermal events are compared with their structural features by room temperature FTIR spectroscopy and in situ monitoring during programmed temperature variation using time resolved Raman spectroscopy and SAXS. This set of results allowed for the correlation of nano-structural features and ionic conductivity of OIH with the polyether backbone conformation, the PEO crystallinity, and the amount of PPO in the hybrid blend. The ionic conductivity was carried out by impedance spectroscopy for the OIH: Li^+ electrolytes monoliths. This kind of study allowed for the proposal of the Electrical Equivalent Circuit and the relationship between the circuit components and the OIH structural building blocks.

6.2 Thermal behavior:

Fig. 6.1 (a) shows the DSC trace of PEO_{1900} , PPO_{2000} , $\text{U}_{0.5}\text{PPO}_{2000}:\text{U}_{0.5}\text{PEO}_{1900}$ blend and Li^+ loading samples, measured during heating from $-90\text{ }^\circ\text{C}$ to $+200\text{ }^\circ\text{C}$. Any thermal event associated with the thermal-decomposition was observed in this temperature range, even for the unloaded and Li^+ -loaded samples (OIH: Li^+), thus confirming the good thermal-stability of the OIH materials. The DSC trace of all OIH materials that were analysed displayed a relatively sharp discontinuity, showing evidence of the variation of the heat capacity (ΔC_p), characteristic of the glass transition (T_g). The T_g event occurred at -58 and $-60\text{ }^\circ\text{C}$ for U-PEO_{1900} and U-PPO_{2000} ,

respectively, and shifted to higher temperatures for the U-PEO₁₉₀₀:Li⁺ and U-PPO₂₀₀₀:Li⁺, -40 and -48 °C, respectively. The blending with χ PPO₂₀₀₀ fraction $x = 0.5$ showed only one change in the T_g region, owing its thermal event at -59 and -45 °C, respectively, to the unloaded and Li⁺-loaded. The existence of a single T_g for all blending compositions confirms the miscibility and homogeneity of these OIH blends.

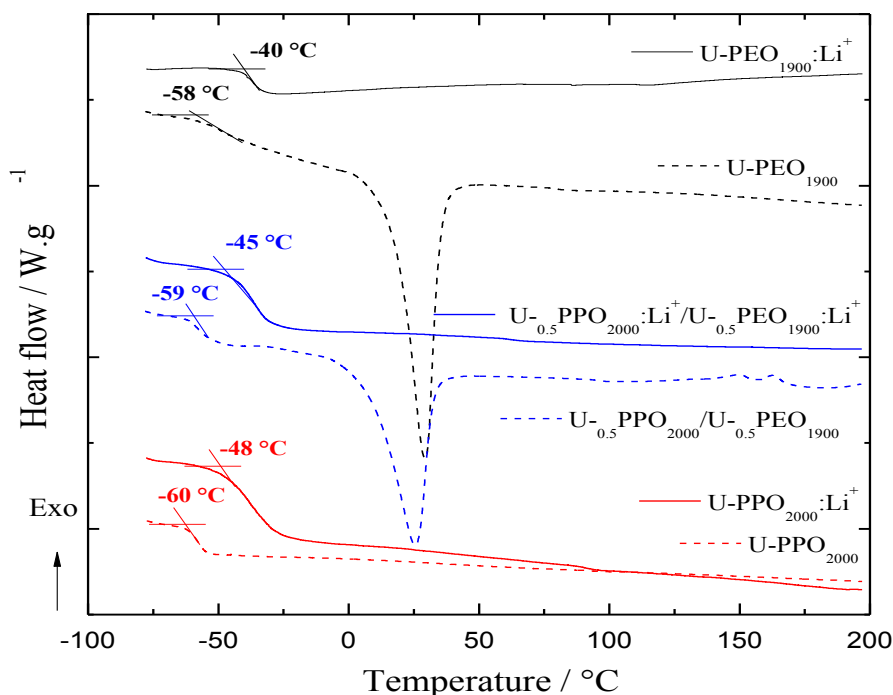


Figure 6.1: DSC curves for U-PEO₁₉₀₀; U-PPO₂₀₀₀; and hybrid blends prepared with PEO₁₉₀₀ fraction $x = 0.5$, Li⁺-unloaded (dashed curves) and Li⁺-loaded (straight curves).

The evolution of T_g with the composition for unloaded and Li⁺-loaded samples is shown in Fig. 6.2. The comparison of unloaded and Li⁺-loaded samples reveals a high value of T_g for the OIH:Li⁺. This feature suggests that the polymeric organic chain is interacting with the guest cation by the ether-type oxygen, thus leading to a more rigid organic chain with lower organic chain motion compared to the unloaded OIH matrices³⁵. On the other hand, as the PPO₂₀₀₀ fraction increases in the blend, the T_g value decreases in a similar way for the unloaded and Li⁺-loaded materials. This finding suggests that partition of the Li⁺ atoms between the two polymers is almost unaffected by the blend composition.

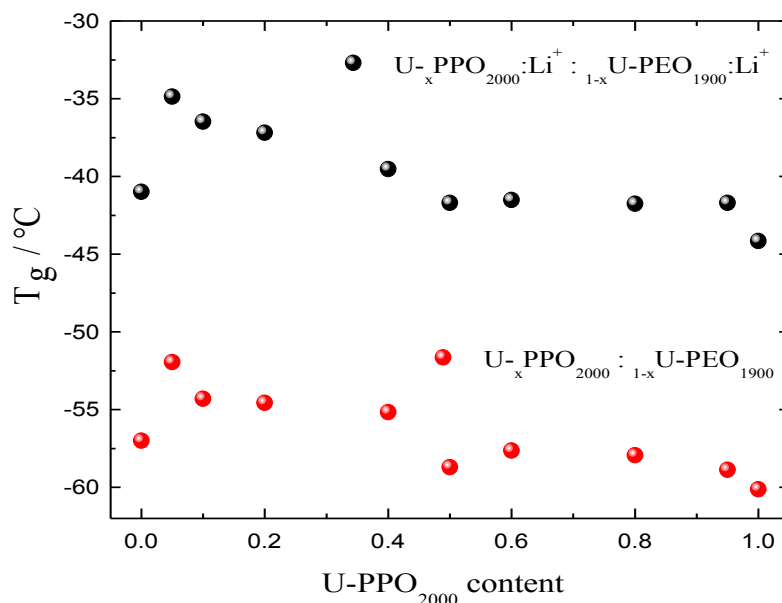


Figure 6.2: Dependence of the glass transition temperature on the percentage of PPO₂₀₀₀ at the U-_xPPO₂₀₀₀:U-_{1-x}PEO₁₉₀₀ hybrid blend, respectively.

The U-PEO₁₉₀₀ DSC curves in Fig. 6.1 reveals an endothermic peak around 25 °C, corresponding to the melting of crystalline PEO domains²³⁰. This event is not observed for U-PEO₁₉₀₀:Li⁺, showing evidence that Li⁺ cations completely restrain the crystalline helical PEO *backbone* conformation²³¹. In fact the strong coordination of small cations by the PEO chains induces the “crown ether” conformations, restraining the helical PEO conformations of crystalline polymers¹⁸². This result is the first indicator of the Li⁺ interaction with the polar ether-type oxygen of PEO.

On the other hand the endothermic fusion peaks of crystalline U-PEO₁₉₀₀ hybrid moieties decreases in area as the U-PPO₂₀₀₀ fraction increases in the blend, which is absent for U-PPO₂₀₀₀ $x \geq 0.8$. This simultaneous decrease of T_m and the degree of crystallinity (D_c) is in accordance with the Flory–Huggins theory, which predicts that the $T_m - D_c$ dependence can only be achieved if the interaction parameter for crystalline polymer-amorphous polymer systems (X_{12}) is negative²³². A negative value of X_{12} implies that the polyether component of the hybrid can form a thermodynamically stable, compatible mixture at temperatures above the melting point, and that the amorphous phase acts as a diluent of the crystalline polymer²³³. In order to confirm this

crystalline polymer/amorphous diluent behaviour, the D_c of the PEO₁₉₀₀ in the hybrid blending was calculated from the relationship between the observed melting enthalpy (ΔH_m) and the standard melting enthalpy for 100 % crystalline PEO (ΔH_p) (188.9 J/g)²⁹.

$$D_c (\%) = \frac{\Delta H_m}{\Delta H_p} \times 100\% \quad (9)$$

Fig. 6.3 reveals that the D_c follows the dashed, straight line corresponding to a crystallization process that was influenced by the number of EO units present in the PEO₁₉₀₀ matrix in the U-_xPPO₂₀₀₀:U-_{1-x}PEO₁₉₀₀ blending. This behavior is in agreement with the expected dilution effect.

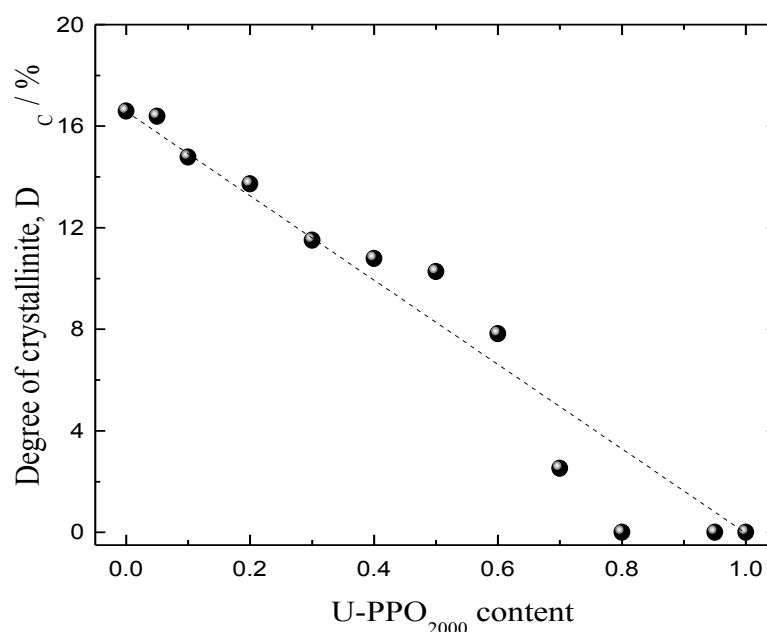


Figure 6.3: Degree of crystallinity, as a function of the percentage of PPO₂₀₀₀ in the U-_xPPO₂₀₀₀:U-_{1-x}PEO₁₉₀₀ hybrid blend, respectively.

6.3 Local structure:

➤ 6.3.1 FTIR at room temperature;

Figs. 6.4 show the room temperature FTIR pattern, in the spectral range from 1800-1100 cm⁻¹, for unloaded (black) and Li⁺-loaded (blue) (a) U-PEO₁₉₀₀ and (b) U-PPO₂₀₀₀ samples shaped as thin films (50 μm). As discussed at Chapter 4, the C-O-C backbone region is sensitive to changes in the conformations of the polyether chains caused by

interactions between the guest cation and the polar oxygen ether-type atoms present in the polymers¹⁴². Different from negligible effects of Eu^{3+} importation observed in Fig 4.2, Fig 6.4 shows significant changes in the spectra of OIH materials after Li^+ - loading. Chemically, the Li^+ and Eu^{3+} ions differ substantially in terms of charge density and coordination number. These different characteristics are the responsible for the distinct spectral behavior.

Both of the Li^+ -unloaded OIH materials (U-PEO₁₉₀₀ and U-PPO₂₀₀₀) show a broad band centered around 1108 cm^{-1} (Fig. 6.4 (a) and (b) – black curves). This feature is ascribed to the COC vibration mode, characteristic of non-coordinated poly-ether chains²²³. After Li^+ -loading, several changes in the spectra can be observed. The new bands at 1060 and 1195 cm^{-1} can be ascribed to the SO_3^- aggregates and CF_3^- anion, indicative of the good inorganic salt dissociation into the OIH matrices. The displacement accompanied by intensity decrease of the band at 1108 to 1105 show evidence of the interaction of O_{ether} with Li^+ cations¹⁸². The spectra also shows a set of bands which increases in intensity at 1135 , 1334 , 1355 and 1457 cm^{-1} , ascribed to the environmental changes of the coupling of CH_2 modes, as *wagging*, *rocking* and *twisting*.

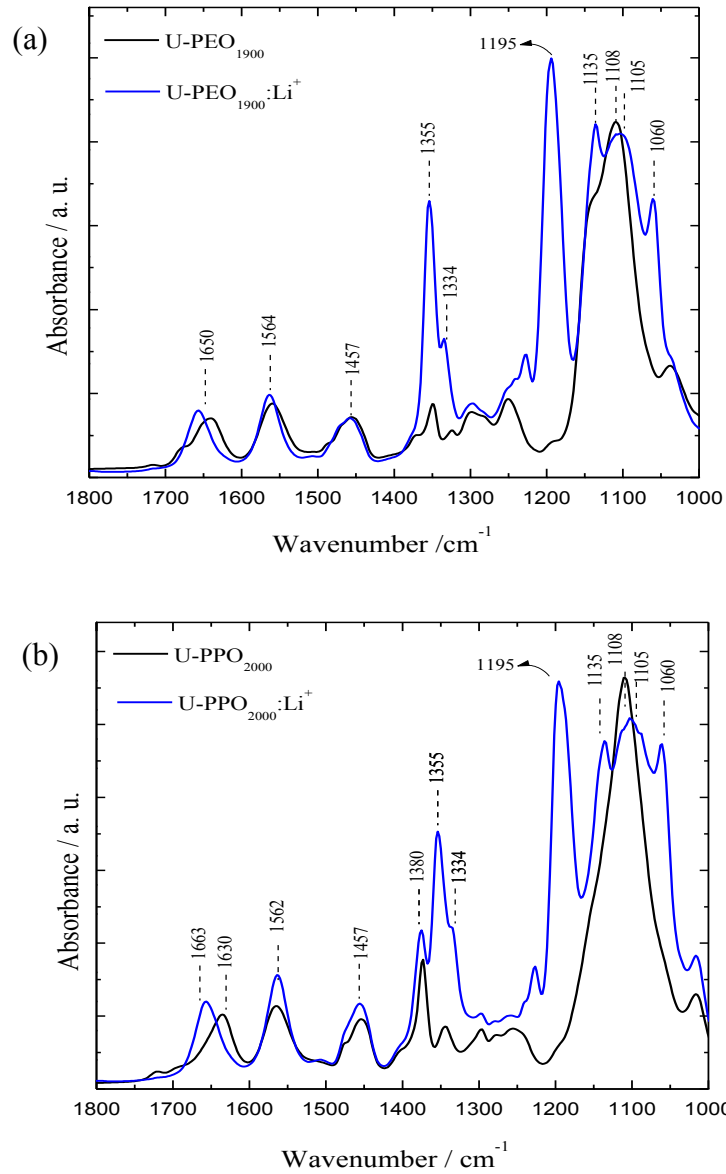


Figure 6.4: Room temperature FTIR pattern, in the spectral range from 1800-1100 cm^{-1} , Li^+ -unloaded (black) and Li^+ -loaded (blue) for thin films (50 μm) of (a) U-PEO₁₉₀₀ and (b) U-PPO₂₀₀₀.

Table 6.1: Attribution of the FTIR spectroscopy bands for the U-PEO₁₉₀₀ and U-PPO₂₀₀₀ OIH thin film (50 μm) matrices, Li^+ -unloaded and Li^+ -loaded.

Frequency (cm^{-1})	Attribution		Refs
	U-PEO ₁₉₀₀	U-PEO ₁₉₀₀ :Li	
1060	---	Anion SO_3	103, 142, 185, 187, 189, 190, 209, 217, 236
1105	---	Li - O_{ether}	
1108	$\nu_{\text{as}}(\text{C-O-C})$	---	
1135	Rock $(\text{CH}_2)_{\text{cryst}}$	Rock $(\text{CH}_2)_{\text{amorph}}$	
1195	Anion CF_3	Anion CF_3	
1334	Bending $(\text{CH}_2)_{\text{cryst}}$	Bending $(\text{CH}_2)_{\text{amorph}}$	
1355	Wagging $(\text{CH}_2)_{\text{cryst}}$	Wagging $(\text{CH}_2)_{\text{amorph}}$	
1457	Bending $(\text{CH}_2)_{\text{cryst}}$	Bending $(\text{CH}_2)_{\text{amorph}}$	
1564	'Amide II'	'Amide II'	
1654	'Amide I'	'Amide I'	

On the other hand, Li^+ -loading in the OIH matrix does not cause an abrupt damage in the Amide region, as was observed in the case of the Eu^{3+} cations (Fig 4.4 (d)). The effect of the hydrogen-bonding in the U-PEO_{1900} Amide region after a Li^+ -addition is shown in Fig 6.5.

Fig 6.5 (c) shows the second derivate of the $\text{U-PEO}_{1900}:\text{Li}^+$ -loading OIH matrix and reveals that the amide I region is composed of three maxima, located at 1642, 1656 and 1674 cm^{-1} , and amide II region composed of a single intense band at 1560 cm^{-1} . The Gaussian fitting, Fig 6.5 (d), reveals a difference in the percentage of the components compared to the unloaded U-PEO_{1900} OIH matrix. The Gaussian fitting results for unloaded PEO_{1900} and Li^+ -loaded are found in Table 6.2.

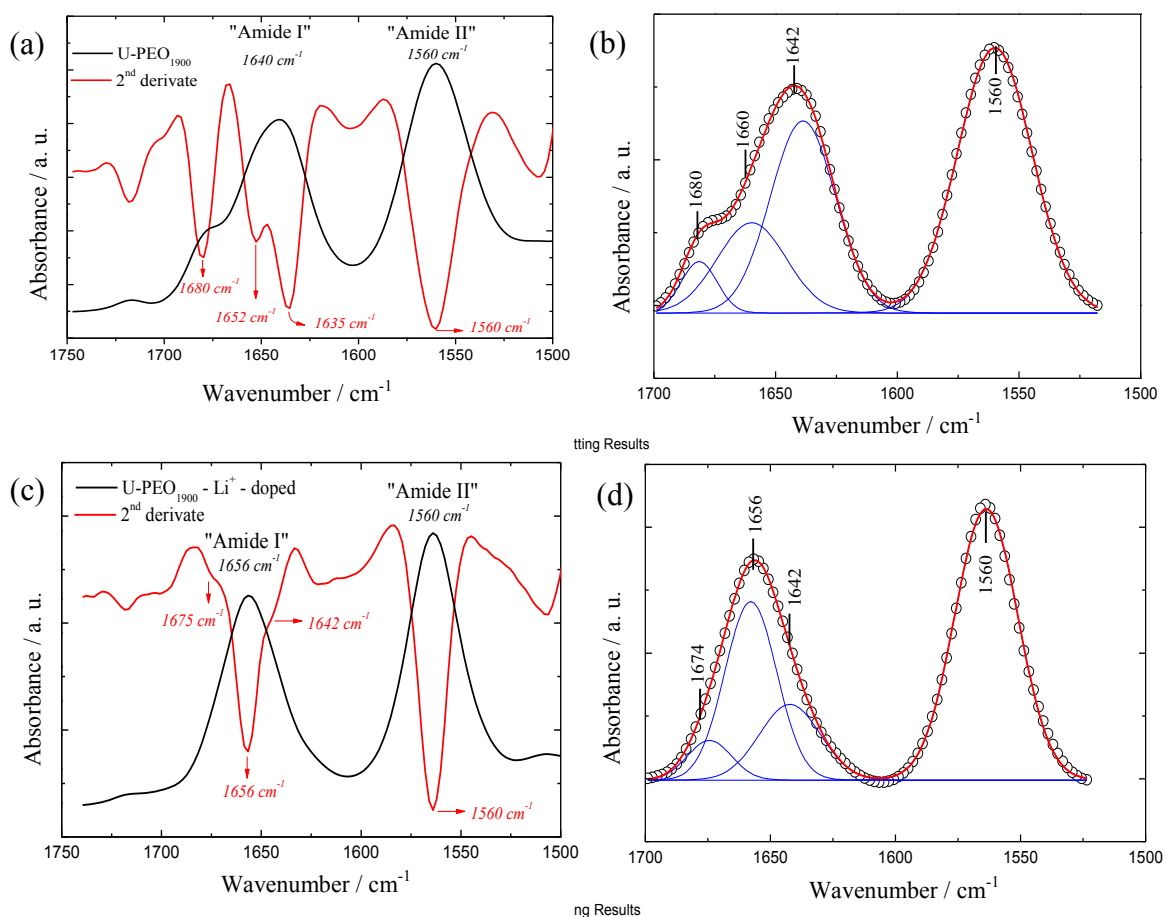


Figure 6.5: FTIR spectra in the amide region with the 2nd curve derivate for (a) U-PEO_{1900} and (c) $\text{U-PEO}_{1900}:\text{Li}^+$ and the Gaussian fitting of the amide region for (b) U-PEO_{1900} and (d) $\text{U-PEO}_{1900}:\text{Li}^+$.

Table 6.2: Table containing the mathematical fitting values of the Amide I and Amide II regions of U-PEO₁₉₀₀ and U-PEO₁₉₀₀:Li⁺.

<i>Fitting Parameters</i>	U-PEO ₁₉₀₀	U-PEO ₁₉₀₀ :Li		
Chi ²	9.43E-6	1.89E-5		
Adj. R ²	0.999	0.999		
Frequency (cm ⁻¹)		Area int. (%)	Attribution	Refs
1560		52.22		
1564	48.98		N-H <i>in plan</i>	185, 187
1565				
1640			H-O _{carb.} (ordered)	
1642	31.08	14		
1656		28.36	H-O _{carb.}	168,236
1660	15.40		(desordered)	
1674		5.3	C=O _{carb.} <i>free</i>	
1680	4.5			

The three components of the Amide I region for U-PEO₁₉₀₀(Fig. 6.6 (black)) are dominated by an intense band centered at 1564 cm⁻¹. As discussed earlier, these components are attributed to the ordered urea/urea, urea/poly(ether) hydrogen bonding. On the other hand, in the case of the same OIH matrix Li⁺-loaded,(Fig. 6.6 (blue)) the area maxima are observed for the band at 1656 cm⁻¹, ascribed to disordered urea/poly(ether), poly(ether)/poly(ether) hydrogen bonding. These results are consistent with the amorphous nature of U-PEO₁₉₀₀ – Li⁺-loaded observed by DSC. However, U-PEO₁₉₀₀ – Li⁺-loaded, showed a small area integral (14 %), ascribed to an ordered hydrogen bond. Considering that the O_{ether} in the (O-C-C-O) structural backbone is interacting with Li⁺ cations which restrain the PEO helical conformation, the presence of this component could come from urea/urea aggregates. This effect will be further discussed below.

In the case of the component at 1674/1680 associated to the “*free*” C=O, it is observed that the area remains invariant with the Li⁺ loading, indicating that Li⁺ cations do not interact with the OIH matrix via the polar oxygen-carbonyl.

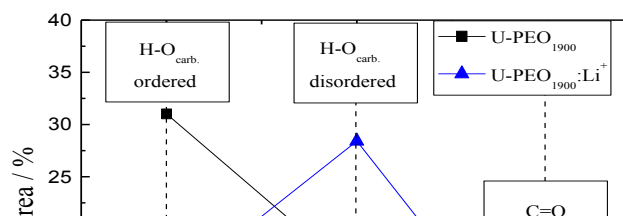


Figure 6.6: Comparison between the relative area of Amide I and of U-PEO₁₉₀₀ (black) and U-PEO₁₉₀₀:Li⁺ (blue).

➤ 6.3.2 *In situ with the temperature FT-Raman Spectroscopy;*

Using in situ Raman spectroscopy with increasing temperature, more information was obtained about Li⁺ interactions with the polar groups of OIH and the effect on the polymeric backbone conformation. The analysis of Li⁺ coordination with polar oxygen ether-types present in the segments of PEO and PPO polymer chains are usually studied in the spectral region of in-plan CH₂ deformations and C-O-C stretches in the polymer backbone. These vibrational modes, observed in the spectral range from 800 to 1300 cm⁻¹ (polymer backbone region), are sensitive to polymeric chain conformation changes due to temperature, i.e.; for semi-crystalline polymers and the presence of guest metallic cations.

Fig. 6.7 (a) shows the evolution of U-PEO₁₉₀₀ Raman spectra in the spectral range from 700 – 1500 cm⁻¹ as a function of the temperature increase from -85 to + 100 °C. This spectral region shows the vibrational modes referring to the ν C-O_{ether}-C stretch, poly-ether backbone (O-C-C-O) conformational deformation and phase vibration of the -(CH₂)_n- like *rocking*, *twisting* and *wagging*²³⁴.

The effect of the melting of semi-crystalline PEO is clearly evidenced (Fig. 6.7(a)) from the loss of definition of the bands associated to the backbone (O-C-C-O)

conformation. At $T < T_f$, two well defined bands were observed at 846 and 861 cm^{-1} that are associated with the helical ordered conformation. In this range of temperatures, the backbone (O-C-C-O) is found in the *gauche* state. The PEO helical conformation *gauche* state is constructed by the following conformations: *trans* (CO-CC), *gauche* (OC-CO), then *e trans* (CC-OC), represented as *tgt*, along the polymeric chain¹⁹⁶. In the *tgt* conformation, the polar oxygens present in the chain segments are turned inwards into the tunnel of the conformation, while the CH_2 groups show up outside of the tunnel. This preferable configuration helps to explain how a wide concentration of guest metallic cations can be complexed by these poly-ethers.

As the temperature increases, the helical PEO backbone is lost (at $T > T_f$) and a new, broad band arises at 810 cm^{-1} due to the *trans* backbone conformation (CCOC or COCC).

In the same way, the bands observed at 1040 and 1242 cm^{-1} in the *gauche* conformation are attributed to $\nu_s(\text{C-O-C})$ and to in-plan C-H deformations. The increments of temperatures above T_f cause the loss of these band definitions and a broad band with a displacement for lower frequency values is observed. These changes can be the result of the breaks in intermolecular hydrogen bonds, found in the ordered helical configuration²³⁵.

The evolution of the U-PEO₁₉₀₀:Li⁺ loaded Raman spectra as a function of the temperature increase from -85 to 100 °C is shown in Fig. 6.7 (b), which reveals an intense band at 740 cm^{-1} associated with the free anions $[\text{C}_2\text{F}_5\text{NO}_4\text{S}_2]^-$ ³⁵, which reveal the inorganic lithium salt dissociating into the OIH matrix. Also, two weak bands are observed at 1040 cm^{-1} , which can be associated with the weak interaction between the triflate ions with the OIH matrices, while the band at 1067 is due to the bi- or tridentate aggregate formation $(\text{Li}_2(\text{CF}_3\text{SO}_3))^+$ or $[\text{Li}_3(\text{CF}_3\text{SO}_3)]^{2+}$ ²³⁶. The absence of the band at

1077 cm^{-1} in the range of all temperatures excludes the presence of crystalline lithium salt.

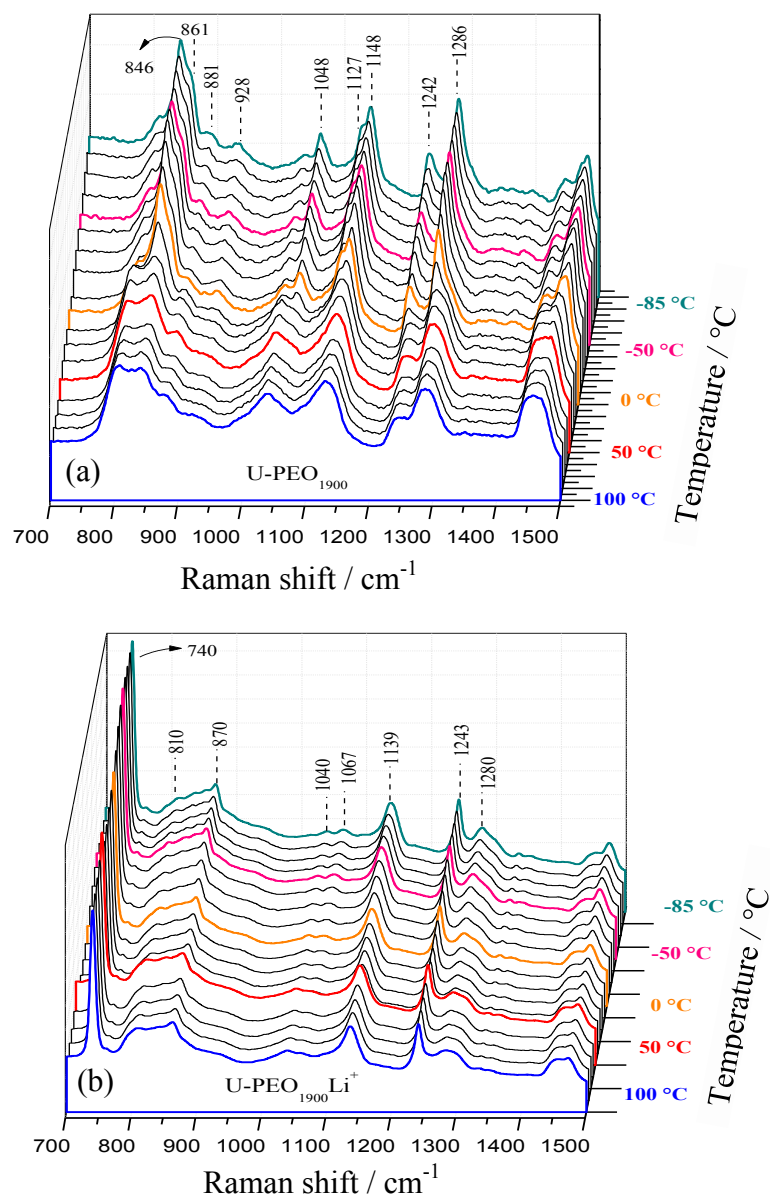


Figure 6.7: Raman spectra of (a) Li^+ -unloaded and (b) Li^+ -loaded U-PEO_{1900} as a function of the temperature from -85 to 100 $^{\circ}\text{C}$.

On the other hand, the structural backbone conformation characterized by the set of bands in the 836 – 869 cm^{-1} region remains almost invariant in the range of all temperatures. These results allowed us to conclude that $\text{U-PEO}_{1900} - \text{Li}^+$ complexing has a *trans* conformation for the (O-C-C-O) backbone, even in low temperature values. In this kind conformation, the metal coordination is similar to the crown-ether, in which the Li^+ cations are typically coordinated by 5 ether-type oxygen atoms. This crown-ether

conformation deviates from PEO helical conformation, usually found in bulk PEO crystalline structures, giving the material an amorphous character. Moreover, the addition of small cations in the form of salts has been shown to hinder PEO crystallinity, which is in agreement with DSC and FTIR results.

Fig. 6.8 shows the Raman spectra of Li^+ -unloaded and Li^+ -loaded U-PPO₂₀₀₀ as a function of the temperature from -85 to 100 °C. Due to the amorphous nature of PPO₂₀₀₀ polymers, any remarkable change in the spectra is observed with temperature. The bands are characteristic of *trans* conformation in a range of all temperatures, even for the Li^+ -unloaded OIH matrix. On the other hand, U-PPO₂₀₀₀ shows the band ascribed to the $[\text{C}_2\text{F}_5\text{NO}_4\text{S}_2]^-$ anions at 740 cm^{-1} , revealing the capability to solubilize the lithium triflate, even having a dielectric constant lower than PEO ($\epsilon_{\text{PPO}} = 1.5$, $\epsilon_{\text{PEO}} = 2.2\text{-}2.5$). The comparison between the spectra displayed in Fig. 6.8 (a) and (b) reveals a new band at 810 cm^{-1} accompanied by a displacement of the band at 870 to 865 cm^{-1} after Li^+ -loading, indicating that the presence of the guest cation disturbs the system even for a *trans* conformational backbone structure

Furthermore, the bands observed at 1048 and 1016 cm^{-1} are attributed to the Si-OCH₃ vibration mode of unloaded U-PEO₁₉₀₀ and U-PPO₂₀₀₀, respectively. These stretches are ascribed to the tri-siloxane (Si-O₃), found around $1010 - 1020\text{ cm}^{-1}$, easily distinguished from the tetra-siloxane (Si-O₄) typically found at 1080 cm^{-1} . The presence of the tri-siloxane bands in both OIH matrices prove the poly-condensation of the alkoxisiloxanes existing at the end of the OIH materials..

The bands at 1450 and 1473 cm^{-1} and 1406 and 1456 cm^{-1} , for the U-PEO₁₉₀₀ and U-PPO₂₀₀₀, respectively, are usually attributed to the CH and CH₂ symmetric deformation and asymmetric CH₃²³⁰. However, the O-CH₂ deformations can also contribute to this absorption²³⁷. U-PPO reveals a band at 1350 cm^{-1} , which is not

observed for U-PEO₁₉₀₀. This band is characteristic of the tertiary carbon CH deformation coupled with the symmetric deformation modes of the two adjacent carbons²³³. Table 6.3 shows the attribution of the main bands observed in Raman spectra of different OIH materials.

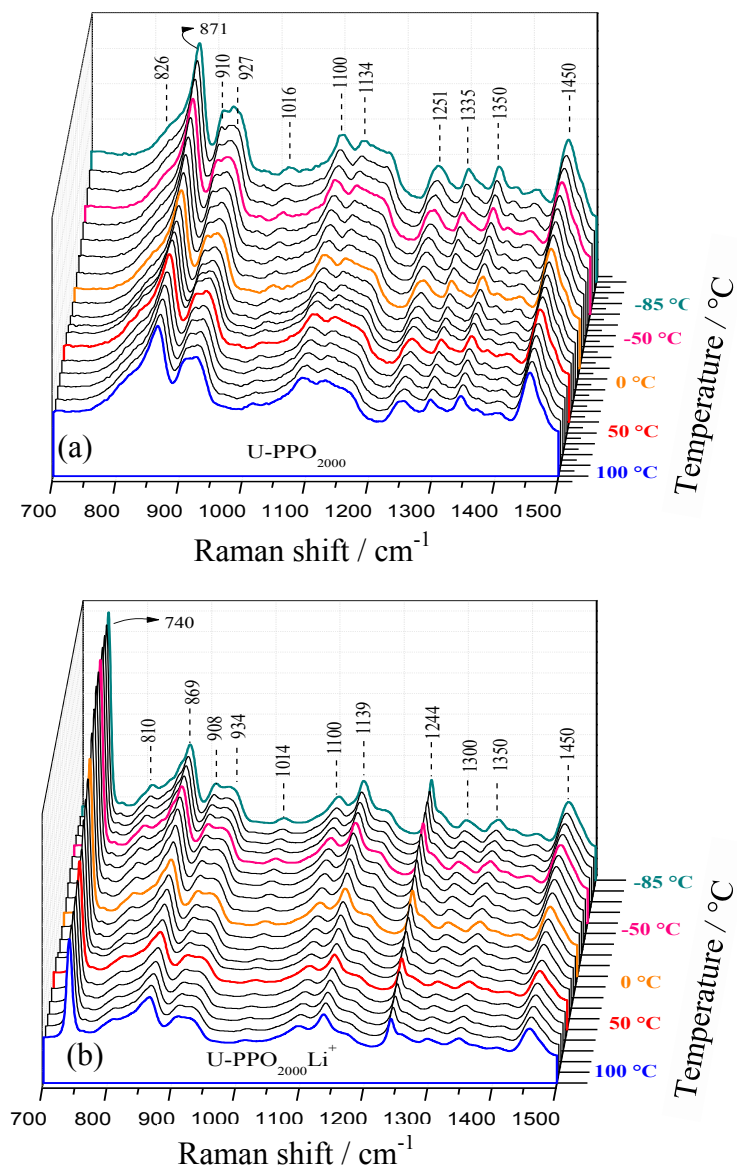


Figure 6.8: Raman spectra of (a) Li⁺-unloaded and (b) Li⁺-loaded U-PPO₂₀₀₀ as a function of the temperature from -85 to 100 °C.

Table 6.3: Attribution of the Raman bands of Li⁺-unloaded and Li⁺-loaded U-PEO₁₉₀₀ and U-PPO₂₀₀₀ OIH.

Band frequency (cm ⁻¹) U-PEO ₁₉₀₀ / U-PPO ₂₀₀₀	Attribution	Reference
740	[C ₂ F ₅ NO ₄ S ₂] ⁻ free anions	35
807 / 810 845 / 866 883 / 933	Poly-ether conformational backbone (O-C-C-O)	231
1048 / 1015	δ _S (Si-O) ₃ deformations	35
1098 / 1095	Si-OCH ₃ groups	
1140 / 1139	Asymmetric stretch of aliphatic ether ν _S (C-O-C)	233
1286 / 1297	phase <i>twisting</i> mode of the -(CH ₂) _n -	196
--- / 1347	δ _S (CH) symmetric deformation from tertiary carbon	229
--- / 1406	δ _S (CH ₃) symmetric deformation	
1450 / 1456 1473 / ---	δ _S (CH), δ _S (CH ₂) and δ _A (CH ₃) deformations	202

6.4 Nanostructure:

➤ 6.4.1 Room Temperature SAXS patterns;

The modifications of the nano-structural features of OIH materials caused by the addition of Li salts and the composition of U-_xPPO₂₀₀₀:U-_{1-x}PEO₁₉₀₀ blends were studied by SAXS measurements carried out both at room temperature and during heating.

The effect of the U-_xPPO₂₀₀₀:U-_{1-x}PEO₁₉₀₀ blend composition on the nano-structural features of hybrids is evidenced from the comparison of the room temperature SAXS pattern displayed in Fig. 6.9 (a). All SAXS curves exhibit a broad peak with a maximum (q_{max}) centered at 1.75 and 1.64 nm⁻¹ for the unblended U-PEO₁₉₀₀ and U-PPO₂₀₀₀ samples, respectively. This maximum is due to effect of scattered interference resulting from spatial correlation of regularly spaced siloxane cross-link nodes²⁰⁴. The average correlation distance between two adjacent siloxane nodes (ξ) is estimated from the peak position, q_{max} (ξ = 2π/q_{max})²⁰⁵, 3.60 and 3.83 nm for U-PEO₁₉₀₀ and U-PPO₂₀₀₀, respectively. OIH blends showed intermediate ξ values. The increase of both ξ and peak intensity as the amount PPO₂₀₀₀ increases reflects the differences in the polymeric chain length and the electron density between the siloxane nodes due to the formation of less

compact structures. In addition, some SAXS patterns exhibit an ill-defined second peak maximum located at a middle q -range, ($q_{\max} \sim 0.58 \text{ nm}^{-1}$). This maximum, corresponding to a Bragg distance of $\xi_{\text{sc}} - \text{spacing} = 10.8 \text{ nm}$, has been well associated with the long period distance of superstructures formed by lamellar arrangements and amorphous parts of semi-crystalline (SC) PEO homo-polymers²³⁸.

In the case of OIH:Li⁺ materials, Fig. 6.9 (b), similar SAXS patterns are observed, indicating that Li⁺ - loading does not lead to considerable modifications on the general nano-structural features of OIH materials. However, it is evident that the displacement of the siloxane correlation peak to higher q values after Li⁺ - loading, leads to an increase of ξ from 3.20 to 3.59 and from 3.25 to 3.83 nm for U-PEO₁₉₀₀ and U-PPO₂₀₀₀, respectively, accompanied by a decrease in $I(q_{\max})$. This behavior is accompanied by decreases of the peak intensity, showing evidence that Li⁺ additions lead to the decrease of the electron density contrast between the siloxanes nodes and the polyether matrix. This finding allowed us to conclude that the interaction between the OIH matrix and the guest cation occurs by the polar ether oxygen-type present in the segments of the PEO or PPO chains.

The second maximum at the middle q -range is ascribed to the long period distance of superstructures²³⁴, which was also observed for some blend compositions of the OIH:Li⁺ materials. The presence of this maximum was found for blends with PPO₂₀₀₀ fraction $x = 0.5$ and 0.8 . A possible explanation for this phenomenon is the presence of the amorphous PPO₂₀₀₀ content in the homogenous OIH mixture, which contains a crystalline fraction of PEO₁₉₀₀. The presence of semi-crystalline PEO₁₉₀₀ in Li⁺ loaded blends can be explained by the preferential dissolution of Li - salts by the U-PPO₂₀₀₀ chain matrix, thus leading to the depletion of Li⁺ cations in PEO₁₉₀₀ chains with helical conformations. The characteristic melting event in the presence of semi-

crystalline PEO₁₉₀₀ was inexplicably masked in the DSC trace of Li⁺ loaded blends (Fig. 6.1).

The above results are in reasonable agreement with the DSC and also indicate that the nanostructure of the hybrid blends could be described by the existence of an extensive mixture between the amorphous fraction of PEO₁₉₀₀ and PPO₂₀₀₀ chains and a small fraction consisting of lamellar domains associated with the PEO₁₉₀₀ crystallinity even for OIH:Li⁺ blends. In fact, all U_{-x}PPO₂₀₀₀:U_{-1-x}PEO₁₉₀₀ hybrid blends are transparent, indicating the absence of macroscopic phase separation.

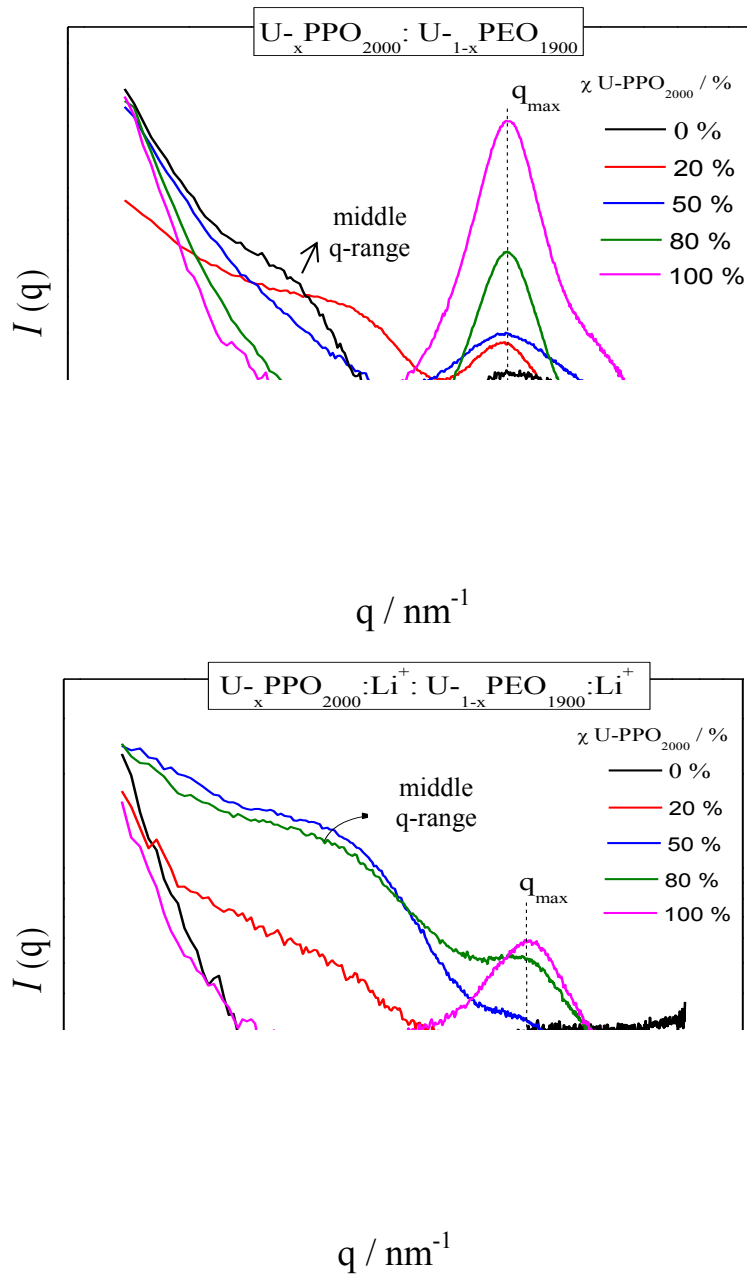


Figure 6.9: Room temperature log-log SAXS curves of $U-x-PPO_{2000}:U-_{1-x}-PEO_{1900}$ blends prepared with different PPO₂₀₀₀ fraction, (a) Li^+ - unloaded and (b) Li^+ - loaded.

➤ 6.4.2 Evolution of the SAXS patterns during heating;

In order to better understand the effect of the presence of crystalline PEO₁₉₀₀ in the nano-structural features of OIH matrices, *in situ* SAXS measurements were carried out during heating with a range from -100 to +100 °C. Fig.6.10 presents the three-dimensional log-log SAXS curves stacked with a temperature interval of 5 °C for the U-

PEO₁₉₀₀ hybrid indexed with the DSC calorimetry trace. At low temperatures, $-100 < T < \sim 25$ °C, the SAXS curves display two maxima, attributed to the long distance period of semi-crystalline PEO ($q < 1 \text{ nm}^{-1}$), and to spatially correlated siloxane ($q > 1 \text{ nm}^{-1}$). The vanishing of maxima at the middle q -range for temperatures above the melting point of PEO₁₉₀₀ ($T_m = 25$ °C) confirm the attribution of this peak to the periodicity of the superstructure formed by the semi-crystalline PEO₁₉₀₀ phase. Moreover, this feature is in full agreement with the temperature dependence of PEO₁₉₀₀ organic chain conformation revealed from Raman spectra (Fig. 6.7 (a)), in which a transition from a *gauche* state to *trans* state is found at the same temperature range where the disappearance of the middle q -range maximum was observed. This phenomenon leads us to conclude that the long-distance period peak found for U-PEO₁₉₀₀ above T_m also has a backbone conformation dependence²³⁹. On the other hand, all OIH materials have shown increases of the correlation peak intensity during heating. This feature is due to the increase of the electron density contrast difference associated with the thermal expansion of the polymeric framework as shown by the displacement of the siloxane correlation peak position during heating (Fig 6.12 (a) and (b)).

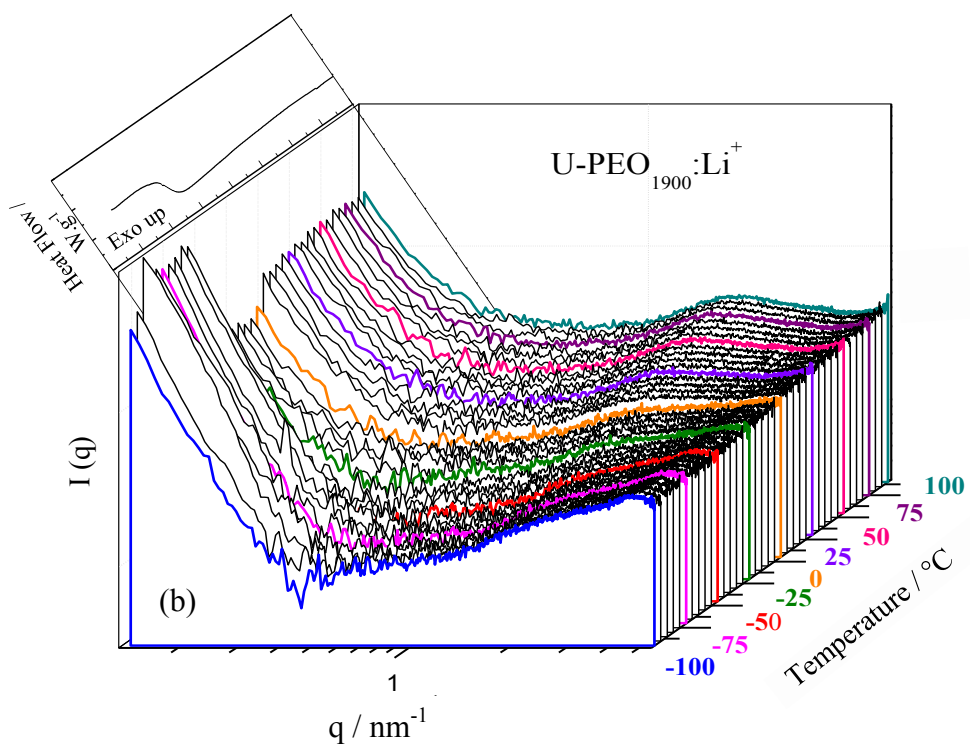
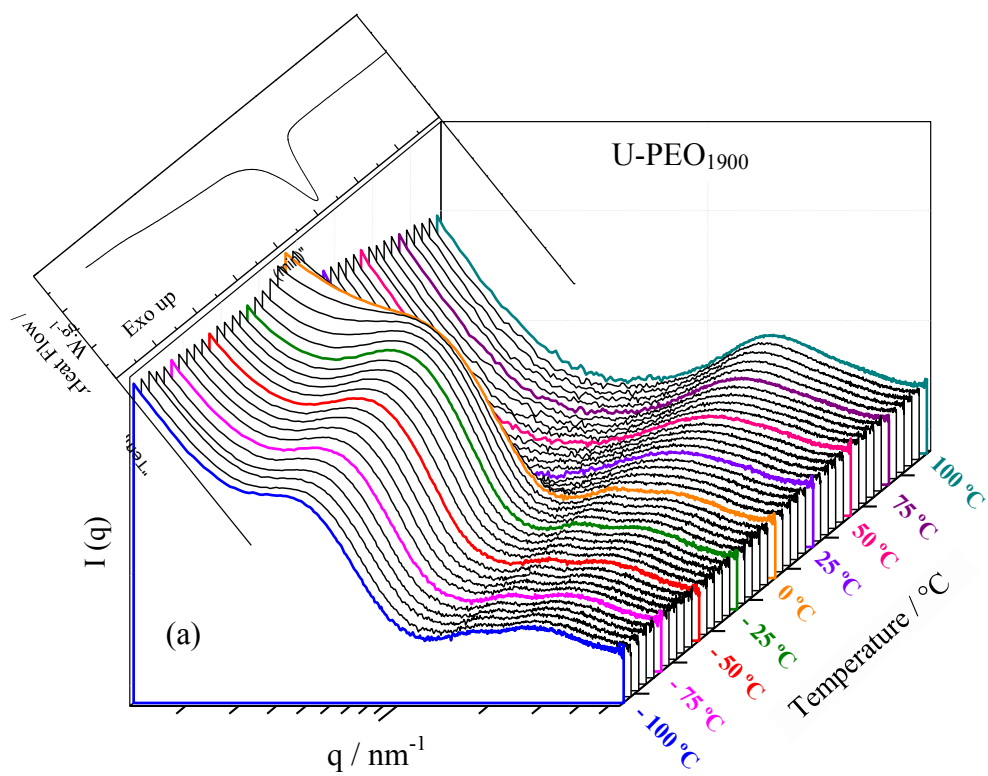


Figure 6.10: Tri-dimensional log-log SAXS curves measured in situ during a temperature range increasing from -100°C to 100°C , and their calorimetric curve (a) U-PEO₁₉₀₀ and (b) U-PEO₁₉₀₀:Li⁺.

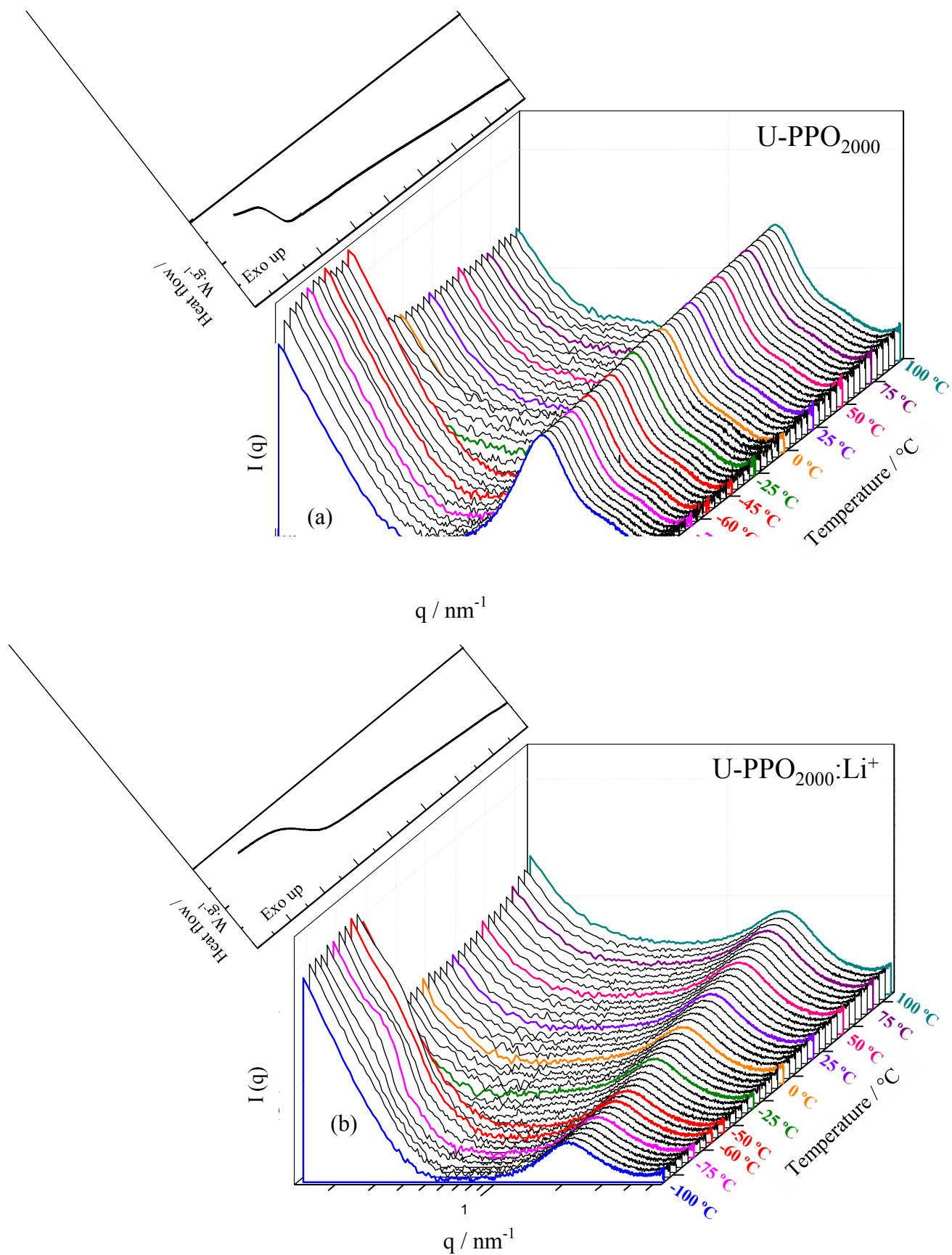


Figure 6.11: Tri-dimensional log-log SAXS curves measured in situ during a temperature range increasing from -100°C to 100°C , and the their calorimetric curve (a) U-PPO_{2000} and (b) $\text{U-PPO}_{2000}:\text{Li}^+$.

Fig 6.12 displays the temperature dependency of the average correlation distance calculated from the maximum of the peak position for U-PEO₁₉₀₀ and U-PPO₂₀₀₀ unloaded and Li⁺-loaded materials. For all samples the threshold of the thermal expansion are in agreement with the T_g value found from DSC. The invariance of the average correlation distance below T_g is consistent with the rigidity of the polymeric framework in the glass state, which relaxes and expands for T > T_g. After T_g, the slope of the thermal expansion curves (θ), distinctly increases for U-PEO₁₉₀₀, unloaded and Li⁺-loaded. Moreover, an abrupt increase of ξ is observed between 0 and 10°C for unloaded U-PEO₁₉₀₀, evidencing a strong contribution of Li⁺-H₂O interactions on the relaxation of the polymer chain. The slope of the thermal expansion curves for the unloaded U-PEO₁₉₀₀ and U-PPO₂₀₀₀ tend to approach the same final values (T > 50°C). The same behavior is observed for Li⁺-loaded samples.

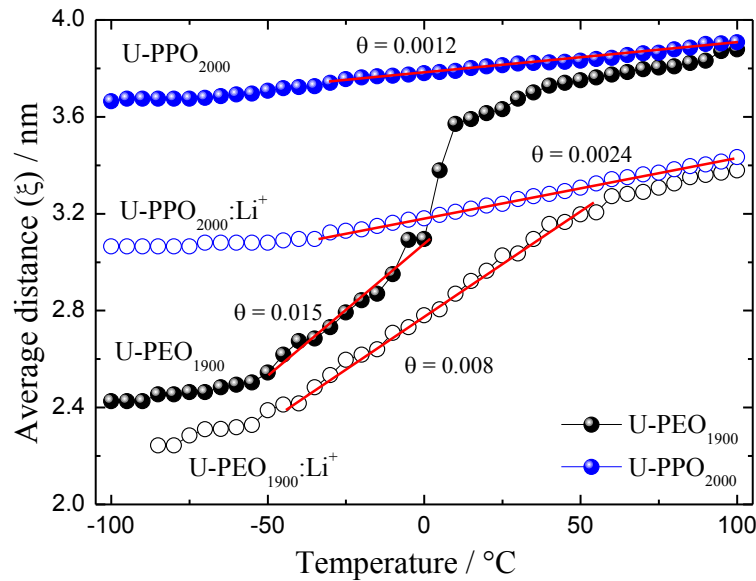


Figure 6.12: Average displacement of the siloxane correlation peak position (ξ) as a function of temperature for (a) U-PEO₁₉₀₀ (black) and U-PPO₂₀₀₀ (blue), unloaded (full circles) and Li⁺-loaded (empty circles).

➤ 6.4.3 Quantitative evolution of the nano-structural parameters;

A common feature observed in log-log SAXS patterns of all OIH materials is the linear decay of intensity found at the low-*q* range. In this case, the scattered intensity

follows a power law, $I(q) = q^{-\alpha}$, characteristic of Porod's law, which gives information concerning the interface structure²⁴⁰. It is expected that this power law contributes in a constructive way to the intensity of the entire SAXS curve. According to obtained quantitative information about the evolution of the structure of long period semi-crystalline materials and the spatially correlated siloxane domains, the experimental SAXS curve was subtracted from the power law decay (Porod law: $I = K q^\alpha$) observed at the low q -range. The linear Porod subtraction was carried out according to the following equation (10), and the results were plotted in Fig. 6.13:

$$I(q_{theoric}) = K \cdot q^\alpha + B \quad (10)$$

Where K and α represent the linear and angular coefficient obtained from Porod's region and B is a high q -range constant due to the diffuse scattered intensity.

The corrected U-PEO₁₉₀₀ SAXS curves using equation 9 are displayed in Fig. 6.13(a) and (b), which reveal two well defined maxima associated with the semi-crystalline domains of PEO₁₉₀₀ (middle q -range, Fig. 6.13(a)) and with the correlation peak of the siloxane nodes (high q -range, Fig. 6.13(b)). The first one, Fig. 6.13(a) shows a continuous increase of intensity until the H₂O fusion temperature, followed by a pronounced decrease until a complete disappearance at the PEO₁₉₀₀ melting point. Moreover, the average long period distance ξ_{sc} is invariant below T_g and shows a linear expansion between T_g and $\sim 10^\circ\text{C}$. This finding suggests that the water molecule participates of the PEO₁₉₀₀ lamellae crystallite organization by hydrogen bonding with the polar oxygens present in the amorphous polymer chain segments, leading to an increase in the electron density contrast between the crystalline lamellae and the amorphous phase as the temperature increases from T_g to 0°C . On the other hand, the siloxane correlation peak measured at the lowest temperature (curve blue in Fig. 6.13 (b)) can be separated by the naked eye in at least two maxima. As temperature rises, the

intensity of the component at the low q - side becomes higher, and we are no longer able to separate it in two maxima. In the case of U-PEO₁₉₀₀:Li⁺, the corrected SAXS curves in the region of the correlation peak of siloxane nodes (high q -range), Fig. 6.13 (c) displays low intensity, hampering the deconvolution component through the multiple peak fitting procedure.

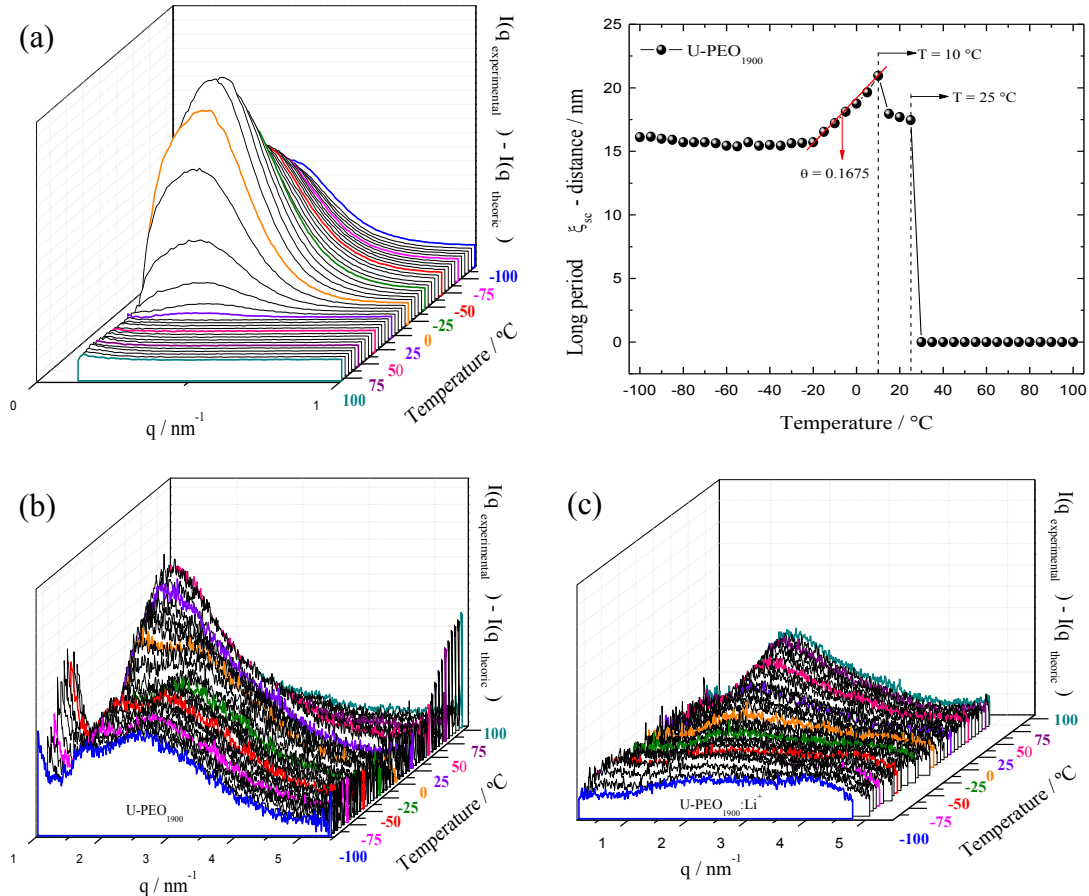


Figure 6.13 Corrected SAXS curves of (a) U-PEO₁₉₀₀ long period semi-crystalline peak and ξ_{SC} peak position as a function of temperature and siloxane correlation peak of (b) U-PEO₁₉₀₀ and (c) U-PEO₁₉₀₀:Li⁺.

The Gaussian fitting for U-PEO₁₉₀₀, Fig. 6.14, reveals a peak profile composed of three different components in the entire studied temperature range, named here as component #1 (red), #2 (black) and #3 (blue). The components of unloaded and Li⁺-loaded U-PEO₁₉₀₀ show a strong dependence on temperature. Example Fig. 6.15 (a) and (b) shows the sum of the area of the three different components as a function of temperature. The unloaded U-PEO₁₉₀₀ displays (Fig. 6.15 (a)) a maximum near the

melting point of semi crystalline PEO, while a continuous increase of area is verified for

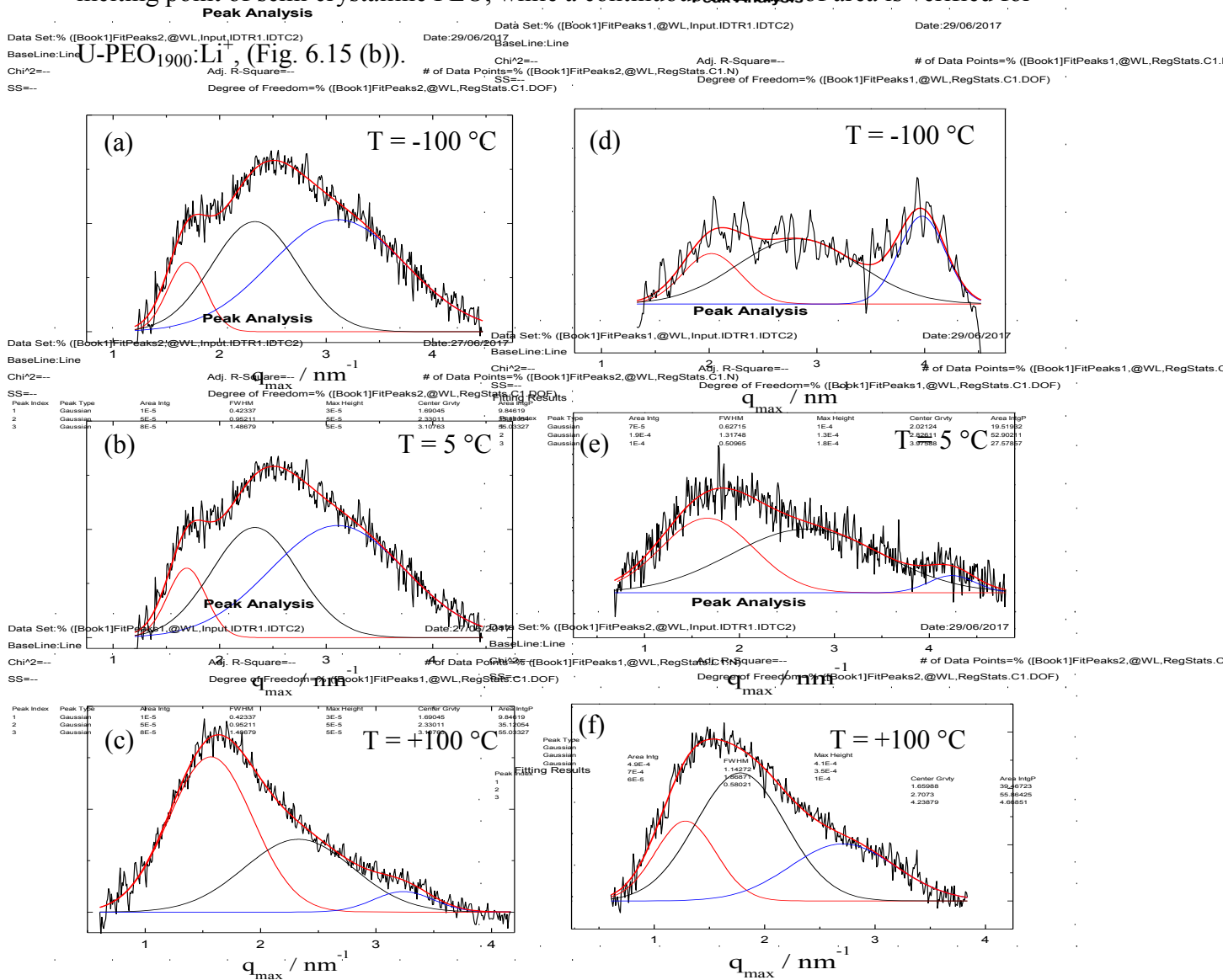


Figure 6.14: Gaussian fitting of the stoxane correlation peak: (a), (b) and (c) for U-PEO₁₉₀₀ and (d), (e) and (f) for U-PEO₁₉₀₀:Li⁺, at -100, +5 and +100 °C. The fitting was made utilizing three component named here as components #1 (red) #2 (black) and #3 (blue).

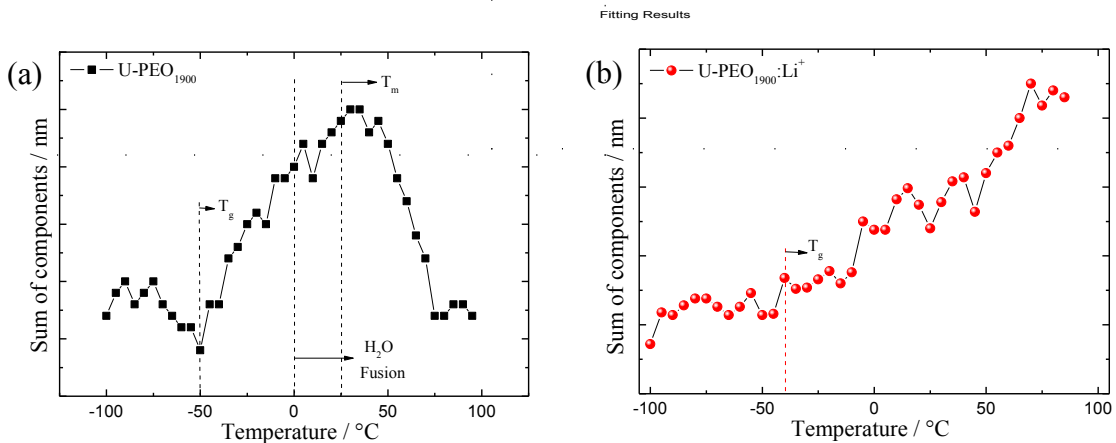


Figure 6.15: Sum of the three different components from the Gaussian fitting of the correlation peak of (a) U-PEO₁₉₀₀ and (b) U-PEO₁₉₀₀:Li⁺.

Fig 6.16 (a) and (b) show the temperature evolution of the correlation distances of different Gaussian components of siloxane correlation peak of U-PEO₁₉₀₀ and U-PEO₁₉₀₀:Li⁺, allowing a fine analyses of the global displacement displayed in Fig 6.12

(a).

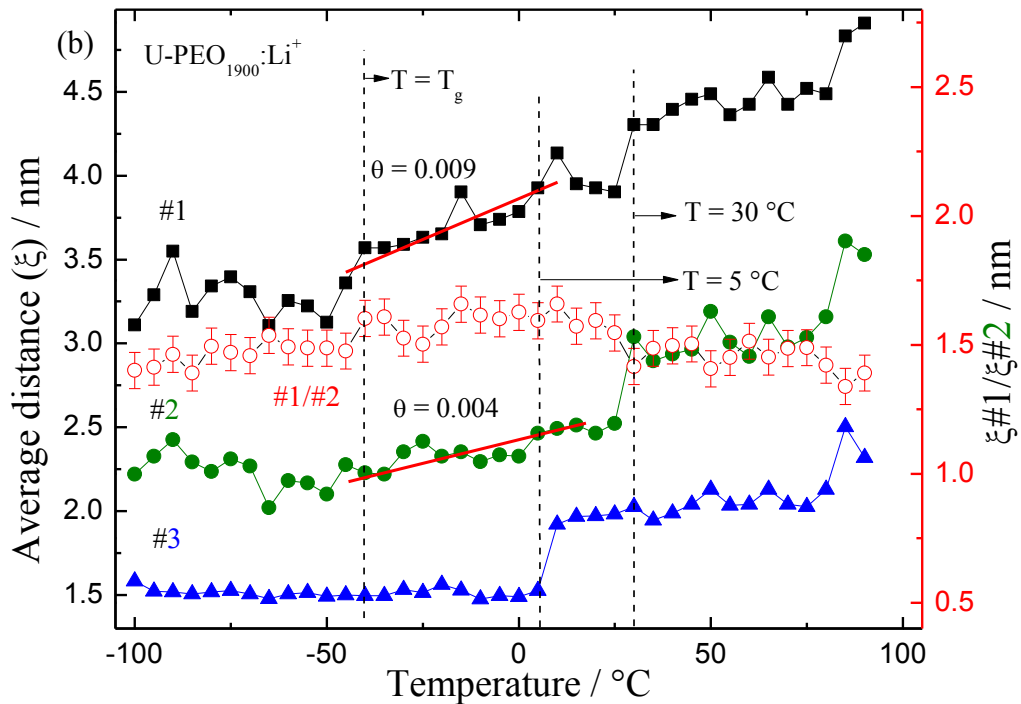
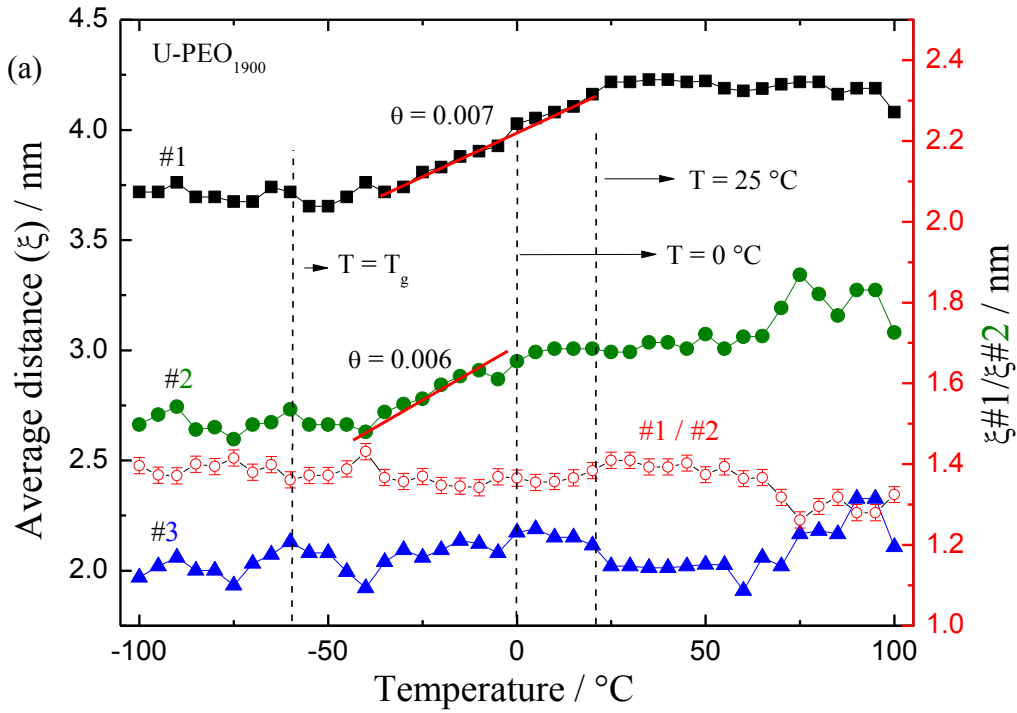
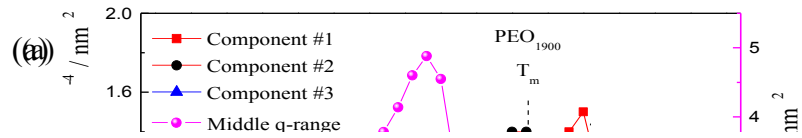


Figure 6.16: Evolution of the average distance (ξ) of three Gaussian components of the correlation peak of (a) U-PEO₁₉₀₀ and (b) U-PEO₁₉₀₀:Li⁺.

In the case of U-PEO₁₉₀₀ (Fig 6.16 (a)), there is an increase of the average distance for components # 1 and 2 in the temperature range between T_g and 25°C (beginning of melting event, Fig 6.1), revealing their dependence on the glass → rubber transition. Moreover, curves #1 and #2 are almost parallel and a ratio of $\xi_{\#1}/\xi_{\#2} = 1.42 \pm 0.02$ is verified for all temperatures. This ratio value corresponds to the expectation for a short-range order arrangement of particles with cubic symmetry. On the other hand, component # 3 is essentially temperature invariant. A similar behavior of components #1 and 2 is verified for PEO₁₉₀₀:Li⁺ (Fig 6.16 (b)), indicating that the short-range order of the siloxane arrangement is unaffected by the incorporation of Li⁺. It is important to note that component #3 shows a sharp increase at 0 °C, suggesting that the Li⁺ cation interaction with polar ether-type oxygen is mediated by a water molecule (Li⁺ - - - H₂O - - - O_{ether}).

Fig. 6.17(a) shows the evolution of area with temperature for each component of the U-PEO₁₉₀₀ correlation peak for siloxane nodes as well as the area of the long-distance peak of the semi-crystalline PEO₁₉₀₀. Focusing the attention on the long-distance peak of low-q (magenta) and component #3 of the siloxane correlation (blue), it is evident that both of them display an area decrease in the same temperature range between 0°C and T_m . These results again suggest the participation of water molecules in hydrogen bonding in U-PEO₁₉₀₀ OIH matrices. Moreover, it is observed that the area of component #3 as a function of the electronic density difference between the inorganic – organic phases decreases above 0°C, suggesting a key contribution of the amorphous polymer chain segments on the definition of the siloxane correlation distance.



(b)

Figure 6.17: (a) Evolution of the three different component areas ($\times 10^{-4} \text{ nm}^2$) and the middle-q area (nm^2) as a function of the temperature from $-100 \text{ }^\circ\text{C}$ to $100 \text{ }^\circ\text{C}$.

➤ **6.4.4 Nano-structure of the $U_x\text{PPO}_{2000}:U_{1-x}\text{PEO}_{1900}$ OIH blends;**

The effect of PPO_{200} polymer content and of Li^+ -loading in the nano-structure of OIH blends can be evaluated from the three-dimensional log-log SAXS curves stacked with a temperature interval of $5 \text{ }^\circ\text{C}$, coupled with the DSC trace displayed in Fig. 6.18.

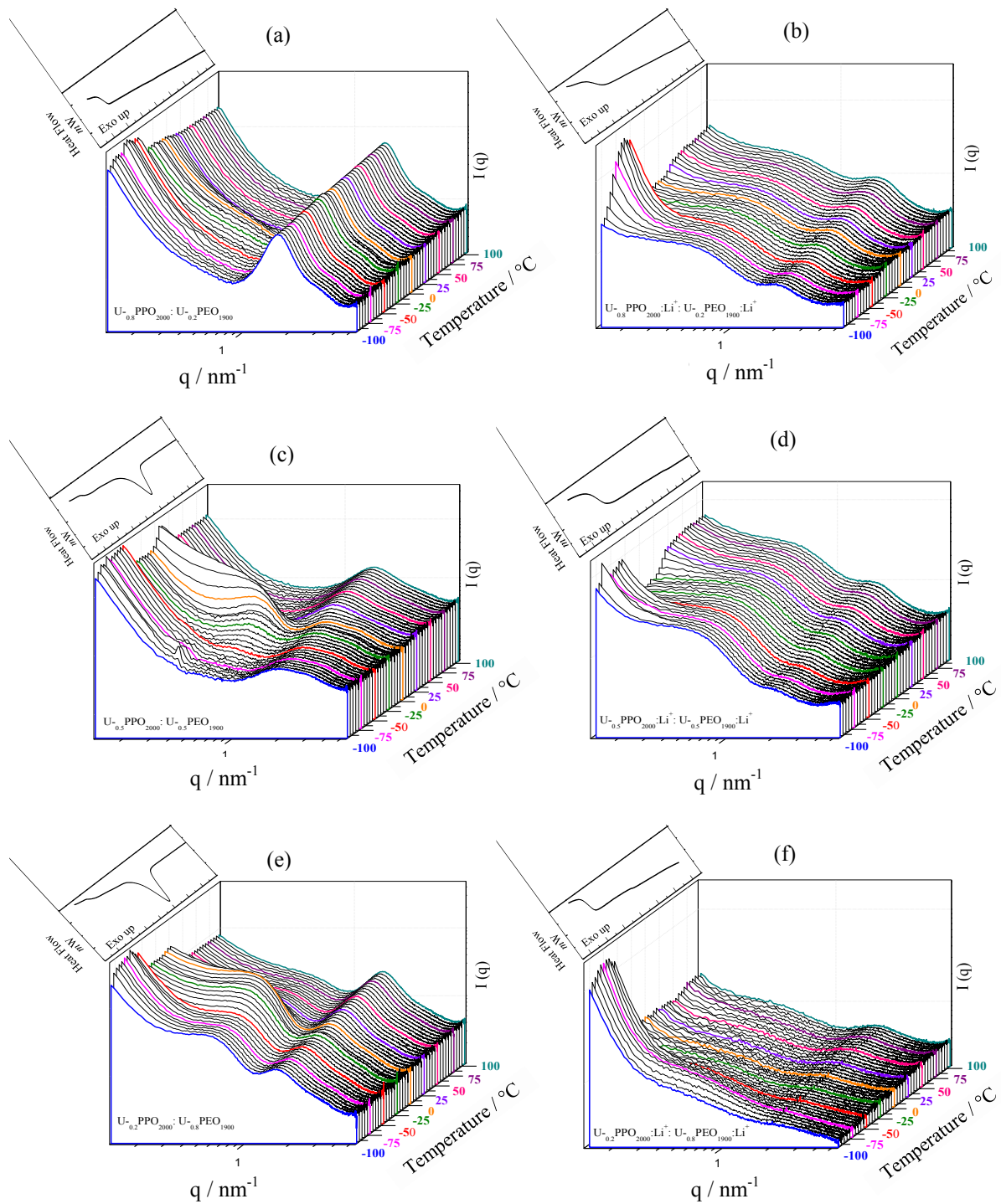


Figure 6.18: Tri-dimensional log-log SAXS curves measured in situ during temperature increase from -100 °C to 100 °C, with their calorimetric curve for U_x PPO₂₀₀₀:U_{1-x}PEO₁₉₀₀ OIH blends for a x PPO₂₀₀₀ fraction equal to (a) 0.8 - unloaded, (b) 0.8- Li⁺-loaded, (c) 0.5 - unloaded, (d) 0.5 - Li⁺-loaded, (e) 0.2 - unloaded and (f) 0.2 - Li⁺-loaded.

Any maximum found in the middle- q range (Fig. 6.18 (a)) for the blend with 0.8 U-PPO₂₀₀₀ confirms the complete solubilization of semi-crystalline PEO₁₉₀₀ in amorphous U-PPO₂₀₀₀ matrices, as suggested by the DSC results. After the Li⁺ incorporation in the

blend with 0.8 PPO₂₀₀₀ (Fig. 6.18(b)), a very broad band with low intensity is found at the middle q-range for all temperatures. The origin of this phenomenon is unclear and a speculative explanation is the non-homogeneous partition of Li⁺ in the OIH blend. However, Fig. 6.18 (c) and (d) shows a dissimilar behavior for the blend with 0.5 PPO₂₀₀₀. In the case of the Li⁺ unloaded blend (Fig. 6.18 (c)), the emergence of the maximum at the middle q-range is found in the temperature range between 0 and 25°C. For the unloaded Li⁺ blend, this maximum at the middle q-range is found at all temperatures. In a different way, for the blend with 0.2 PPO₂₀₀₀, the middle q-range maxima is present for the entire low temperature range (T < 25°C) of the unloaded sample (Fig. 6.18 (e)) and is absent for the Li⁺-loaded one (Fig. 6.18 (f)).

Fig 6.19(a) and (b) displays the temperature dependency of the average correlation distance, calculated from the maximum of the peak position for U-PEO₁₉₀₀, U-PPO₂₀₀₀, and unloaded and Li⁺-loaded U-xPPO₂₀₀₀:U_{1-x}PEO₁₉₀₀ OIH blend, respectively. U-PEO₁₉₀₀ proved to be more sensitive to temperature and all blends have their threshold of thermal expansion in agreement with the T_g value found from DSC. The invariance of the peak position below T_g is consistent with the rigidity of the polymeric framework in the glass state, which relaxes and expands for T > T_g. U-PPO₂₀₀₀ and the blends with 0.2 and 0.8 of PPO₂₀₀₀ show similar thermal expansion curves. On the other hand, the U-0.5PPO₂₀₀₀:U-0.5PEO₁₉₀₀ OIH blend, similar to U-PEO₁₉₀₀, shows a pronounced break of linearity of the thermal expansion at T = 0 °C, again indicating that the water molecule interacts with hydrophilic PEO₁₉₀₀ chains, thus affecting the thermal transformation of these hybrid materials. This event disappears after Li⁺-loading, suggesting that H₂O and Li⁺ concur with the interaction of PEO₁₉₀₀ chains. The values of the slopes of the observed linear thermal expansion after T_g are shown in Table 6.4. As expected, the slope of the sample with U-PEO₁₉₀₀ is almost 10 times higher than the

other OIH samples. A classical mixture law involving intensive properties, like the linear expansion coefficient, is not followed for the hybrid blends. The experimental values are lower than the calculated values from the mixture law, indicating that the slope of PEO₁₉₀₀ for both unloaded and Li⁺-loaded have a lower contribution in the thermal expansion of OIH blend materials.

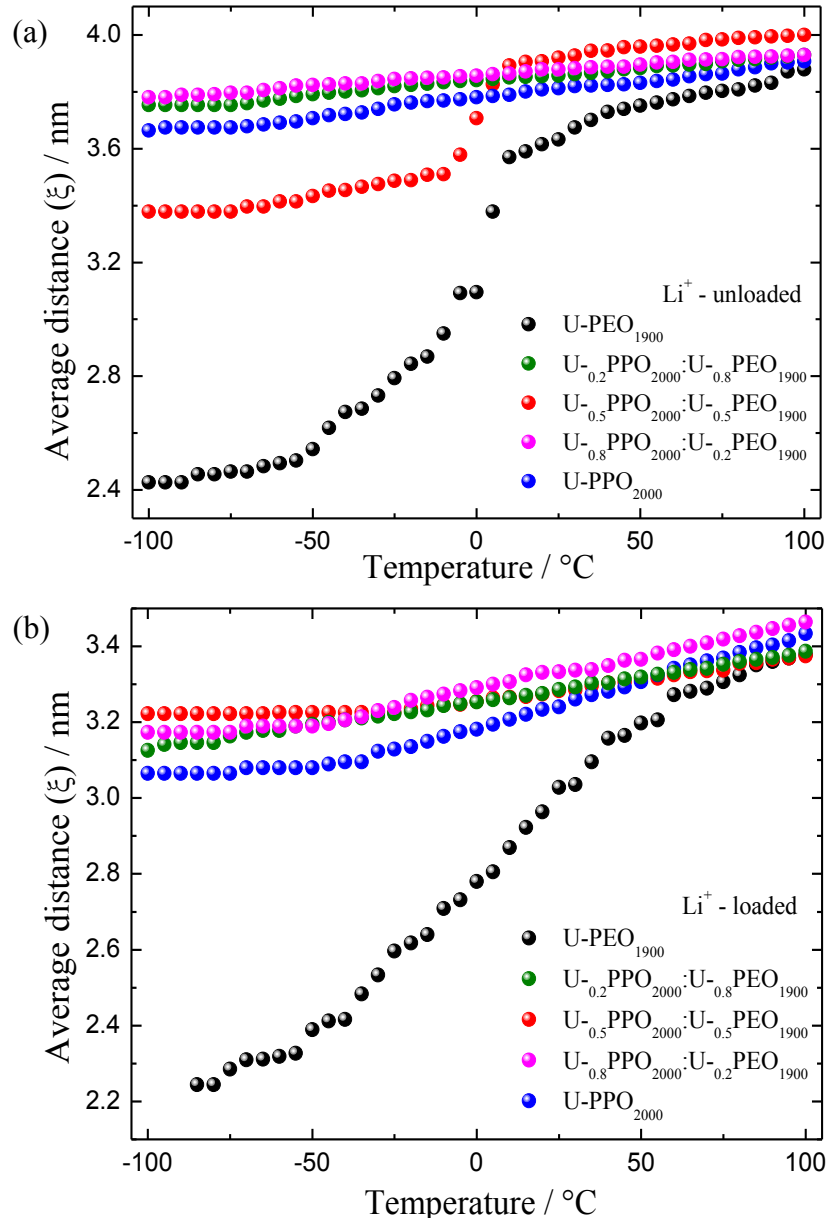


Figure 6.19: Average displacement of the siloxane correlation peak position (ξ) as a function of temperature for (a) U-PEO₁₉₀₀ (black), U-_{0.2}PPO₂₀₀₀/U-_{0.8}PEO₁₉₀₀ (green), U-_{0.5}PPO₂₀₀₀/U-_{0.5}PEO₁₉₀₀ (red), U-_{0.8}PPO₂₀₀₀/U-_{0.2}PEO₁₉₀₀ (magenta) and U-PPO₂₀₀₀ (blue) (a) unloaded and (b) Li⁺-loaded.

Table 6.4: Values of the thermal expansion coefficient represented by the slope of the curve from the average distance of the siloxane correlation peak as a function of the temperature.

PPO ₂₀₀₀ fraction		θ at a middle range of temperature	Mixture Law
0	Puro	0.0091	---
	Li ⁺	0.0087	---
0.2	Puro	0.0009	0.0075
	Li ⁺	0.0013	0.0022
0.5	Puro	0.00200	0.0051
	Li ⁺	0.00110	0.0056
0.8	Puro	0.0007	0.0028
	Li ⁺	0.0017	0.0037
1	Puro	0.00120	---
	Li ⁺	0.00250	---

The SAXS curves of U-_xPPO₂₀₀₀:U-_{1-x}PEO₁₉₀₀ corrected using equation 10 are displayed in Fig. 6.20. This correction makes the absence of maxima associated with semi-crystalline domains of PEO₁₉₀₀ in the unloaded (Fig 6.20(a)) and Li⁺-loaded (Fig 6.20 (b)) blend prepared with the higher amount of PPO₂₀₀₀ (0.8) evident. The two well defined maxima associated with semi-crystalline domains of PEO₁₉₀₀ and with the correlation peak of siloxane nodes are evident in the Li⁺-unloaded blend with $x = 0.5$ and 0.2 of U-PPO₂₀₀₀ (Fig. 6.20(c) and (e)). In fact, we can observe the emerging intensity of the middle q-range peak after the H₂O fusion temperature followed by a pronounced decrease near the PEO₁₉₀₀ melting point, again revealing the participation of hydrogen bonding from the H₂O in the OIH blend.

On the other hand, the SAXS curves of Li⁺-loaded OIH blends (Fig. 6.20(b), (d) and (f)) show the intriguing presence of the middle q-range maxima in all studied temperatures, despite the amorphous character of these samples revealed from DSC (Fig 6.1). This feature coexists with the broad siloxane correlation peak of very weak intensity, which prevents the deconvolution of the band by a Gaussian function. These findings reveal that Li⁺ cation incorporation causes drastic changes in the nano-structure of OIH materials. Afterwards, the comparison between the unloaded matrix with their respective Li⁺-loaded OIH matrix will be qualitative.

Thus, the quantitative nano-structural parameters of $U_xPPO_{2000}:U_{1-x}PEO_{1900}$ was determined only for Li^+ unloaded $U_xPPO_{2000}:U_{1-x}PEO_{1900}$ OIH blends and the results are discussed in the next section.

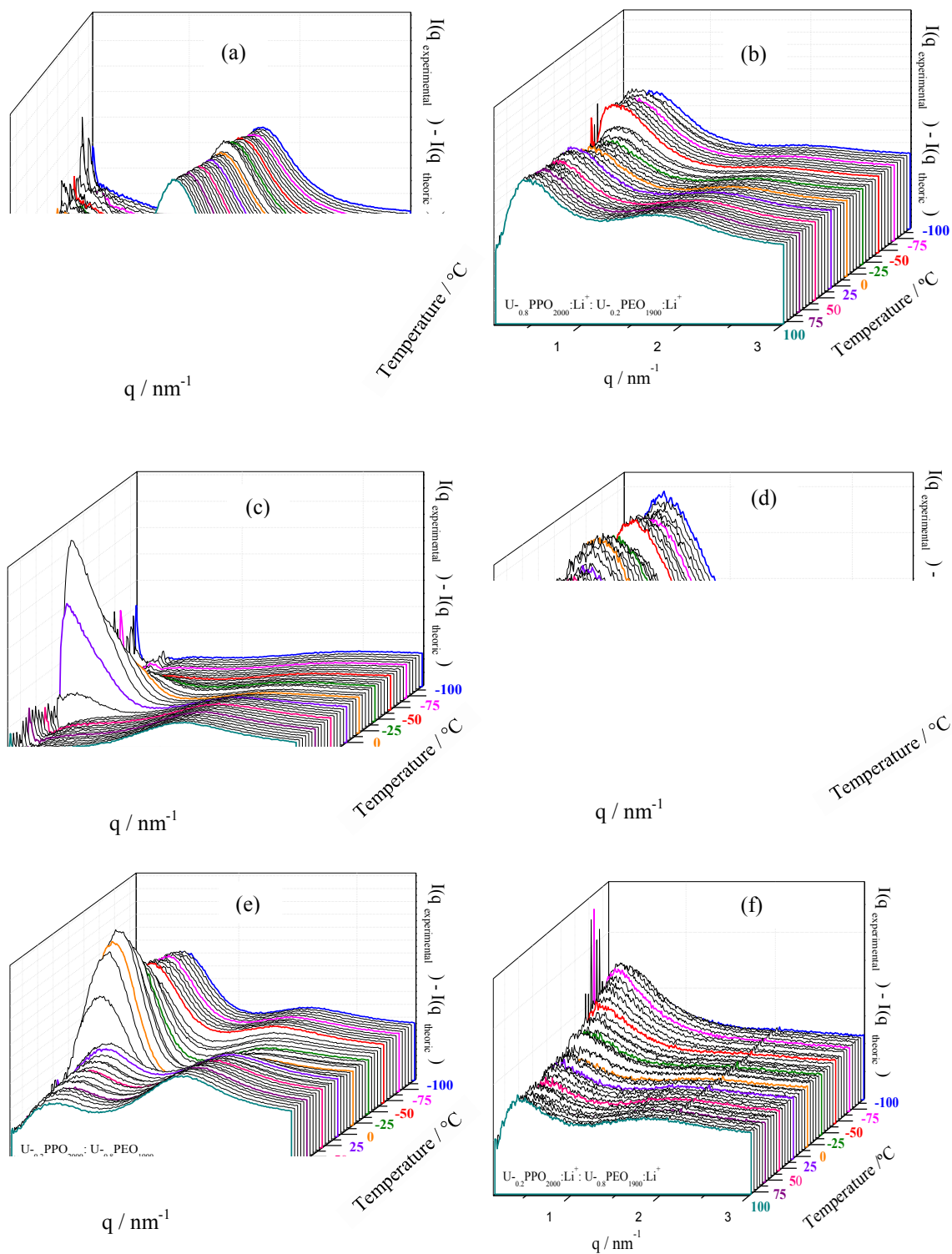


Figure 6.20: Straight line equation SAXS curves subtraction at siloxane correlation peak as a function of the temperature for $U_xPPO_{2000}:U_{1-x}PEO_{1900}$ OIH blends for a x PPO₂₀₀₀ fraction equal to (a) 0.8 - unloaded, (b) 0.8 - Li^+ -loaded, (c) 0.5 - unloaded, (d) 0.5 - Li^+ -loaded, (e) 0.2 - unloaded and (f) 0.2 - Li^+ -loaded.

➤ **6.4.5 Evolution of nano-structural parameters of blend;**

The Gaussian components from the siloxane correlation peak of U- x PPO₂₀₀₀:U- $1-x$ PEO₁₉₀₀ prepared with 0.8 U-PPO (Fig. 6.20 (a)) was not calculated because the SAXS patterns are essentially temperature invariant. Furthermore, there is no evidence of the maxima associated with the average long period distance (ξ_{SC}). Therefore, our attention was focused on the Gaussian fitting for OIH blends with $x = 0.5$ and 0. PPO₂₀₀₀ and the results are shown in Fig. 6.21 and 6.22.

Fig. 6.21(a) shows the evolution of the area of each Gaussian component of the siloxane correlation peak of U- 0.5 PPO₂₀₀₀:U- 0.5 PEO₁₉₀₀OIH blend as well as the area of the middle q -range peak associated with the semi-crystalline super-structure of PEO₁₉₀₀ as a function of the temperature. Another observation can be made in U-PEO₁₉₀₀ homo-hybrids (Fig. 6.17 (a)), where component # 3 remains almost constant in the entire range of temperatures. This behavior can be due to the hydrophobic contribution from PPO₂₀₀₀ present in the blend. On the other hand, the maxima ascribed to the long period distance (middle q -range – magenta) display transient contribution between 0 and 15°C, which can result from PEO₁₉₀₀ cold crystallization. The vanishing of this peak occurs at the same temperature which the area of components # 2 and 3 start to increase. We also observe in this temperature range an acceleration of the siloxane correlation distance increasing for components #1 and # 2 (Fig. 6.21 (b)). These findings indicate the presence of water in the PEO₁₉₀₀ lamellae crystallite organization, hydrogen bonded with polar ether-type oxygens present in the polymer chains. Moreover, we again observe that the ratio between the correlation distance $\xi_{\#1}/\xi_{\#2}$ stays almost temperature invariant and the average value ($\xi_{\#1}/\xi_{\#2} = 1.3 \pm 0.05$) became lower than the expected for the cubic packing of the siloxane node Figs. 6.21(a).

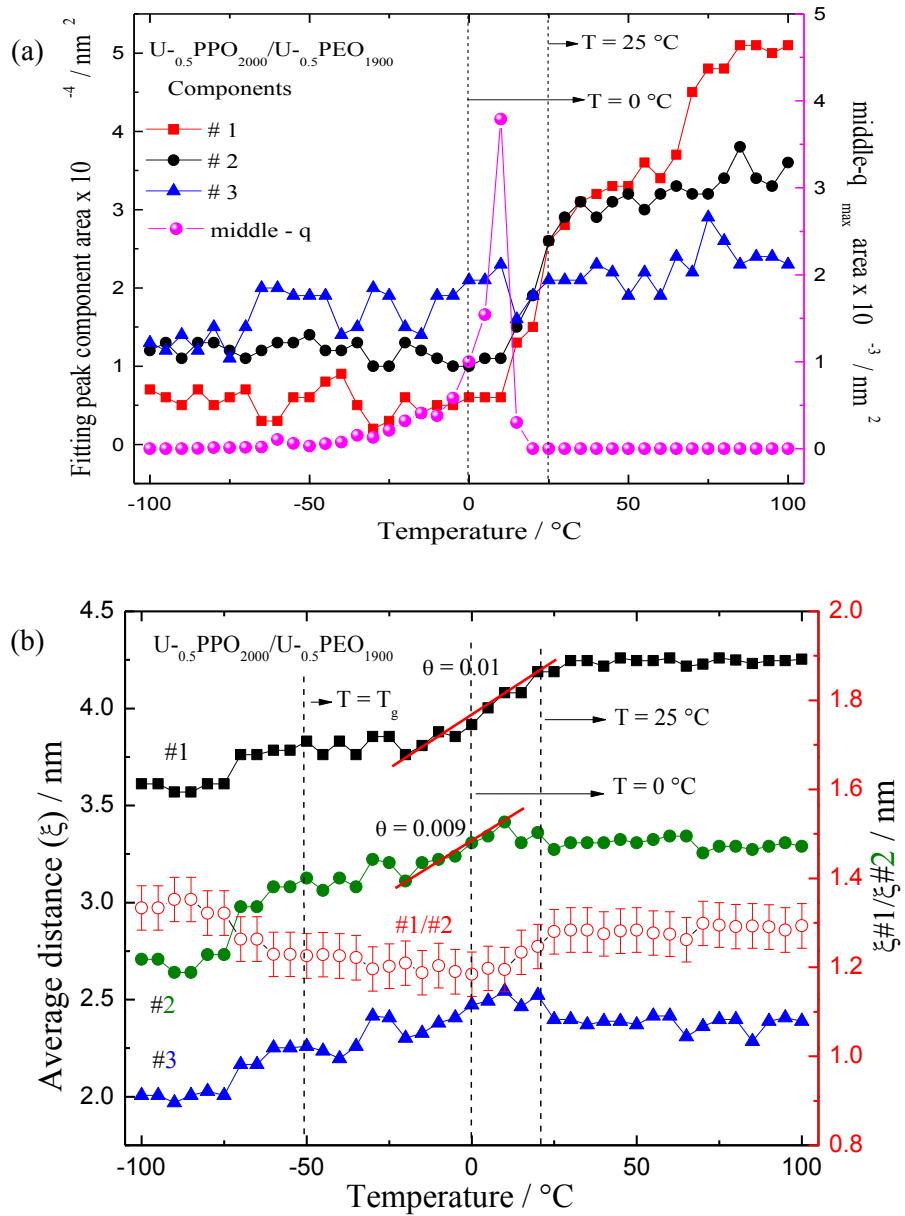


Figure 6.21: (a) Evolution of the three different component areas ($\times 10^{-4} \text{ nm}^2$) and the middle-q area (nm^2) and (b) evolution of the average distance (ξ) relative to the three different components from the Gaussian fitting of the correlation peak for $U_{-0.5}PPO_{2000}/U_{-0.5}PEO_{1900}$ OIH blend.

Fig. 6.22 (a) shows the evolution of the area of each Gaussian component of the siloxane correlation peak of U_{-0.2}PPO₂₀₀₀:U_{-0.8}PEO₁₉₀₀OIH blend as well as the area of the middle q-range peak associated with the semi-crystalline super-structure of PEO₁₉₀₀ as a function of the temperature. Different from the observation in Fig. 6.21 (a), the maxima ascribed to the long period distance (middle q-range – magenta) is present in the OIH blend structure in the entire range of temperatures, even for $T > 25^{\circ}\text{C}$ (PEO₁₉₀₀ T_m). These findings show evidence of a memory effect of the long period distance (middle q-range) observed in Fig 6.20 (e), even after the melting of semi-crystalline U-PEO₁₉₀₀ present in the OIH blend structure. Fig. 6.22 (a) also reveals that the maximum area for the middle q-range peak and of component # 3 occurs in the same temperature range. After this event the area of components # 1 and 2 starts to increase with the temperature, again indicating that the water molecules participate in the PEO₁₉₀₀ lamellae crystallite organization. On the other hand, the average correlation distance of components # 1 and 2 is almost invariant with the temperature, different from the accentuated discontinuity verified between T_g and T_m , for U-PEO₁₉₀₀ (Fig 6.16 (a)) and U_{-0.5}PPO₂₀₀₀:U_{-0.5}PEO₁₉₀₀ (Fig 6.20 (b)). Moreover, the average value $\xi_{\#1}/\xi_{\#2} = 1.2 \pm 0.02$ is also invariant with the temperature and is lower than expected for cubic packing of the siloxane node Figs. 6.22 (b). These results show that adding PPO in the OIH blend disturbs the cubic arrangement of the siloxane nodes.

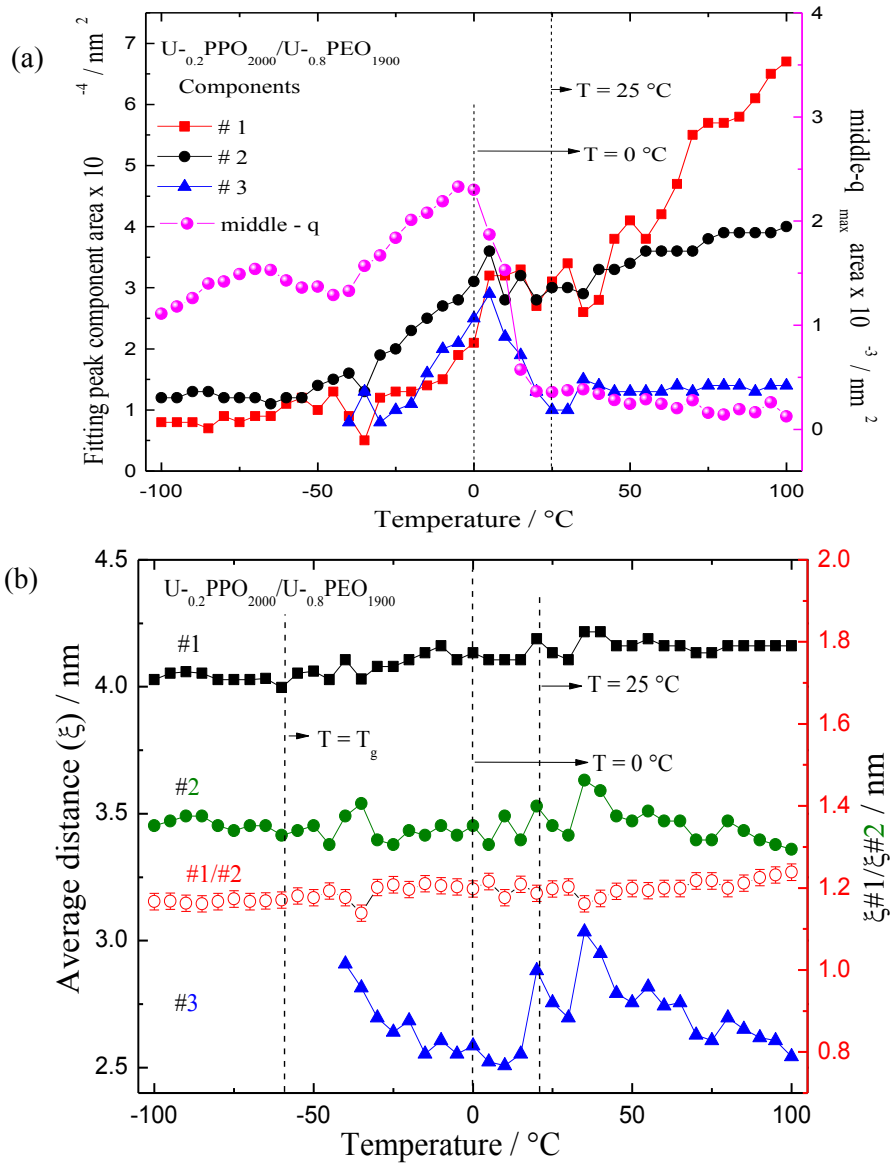


Figure 6.22: (a) Evolution of the three different component areas ($\times 10^{-4} \text{ nm}^2$) and the middle-q area (nm^2) and (b) evolution of the average distance (ξ) relative to the three different components from the Gaussian fitting of the correlation peak for $U_{0.2}PPO_{2000}/U_{0.8}PEO_{1900}$ OIH blend.

6.5 Effect of $U_xPPO_n:U_{1-x}PEO_{1900}$ blending and Li^+ doping in the electrical properties:

In view of the water dependence in the OIH materials organization, the temperature dependence of ionic conductivity of OIH: Li^+ monoliths have been studied by AC impedance spectroscopy +100 °C to – 100 °C to water elimination. Figures 6.23 – 6.27 show the Nyquist impedance diagrams of $U-PEO_{1900}:Li^+$, $U-PPO_{2000}:Li^+$ and $U_xPPO_{2000}:Li^+:U_{1-x}PEO_{1900}:Li^+$ OIH blends for $x = 0.2, 0.5,$ and 0.8 in a temperature range from 183 K to 370 K (-90 C to 100°C) multiplied by their respective geometric factor (K) (Table 3.2). The numbers (between 6 and 1) shown inside the figures give the \log_{10} (signal frequency) for the corresponding point. In a temperature range below the material's T_g , the impedance curves show an incomplete semicircle due to the high resistivity of OIH: Li^+ . As expected, these results demonstrate that the cation mobility assisted by the segmental motion of chains is negligible for polymers in the glass state. The polymer chain rigidity in this range of temperatures blocks the ionic transfer through the polar ether-type oxygens hampering the macroscopic ionic conductivity. However, in the same range of temperatures, a complete semi-circle for the $U-PPO_{2000}:Li^+$ can be clearly observed. On the other hand, as the temperature rises above the glass transition, the semicircle for OIH: Li^+ with low PEO_{1900} fraction becomes complete. The point in the real axis touched by the arc ends is associated with the OIH: Li^+ polymer electrode specific electrical resistivity (ρ). As expected, above T_g , the overall resistance decreases with increasing temperature investigated for all OIH: Li^+ monoliths. This behavior is induced by an increased solid state diffusion in the electrode due the increase of the polymer free volume (Fig 2.10).

U-PEO₁₉₀₀:Li⁺

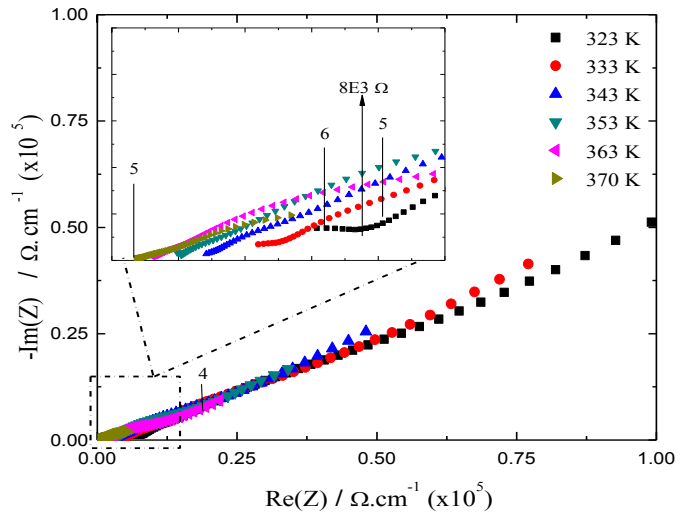
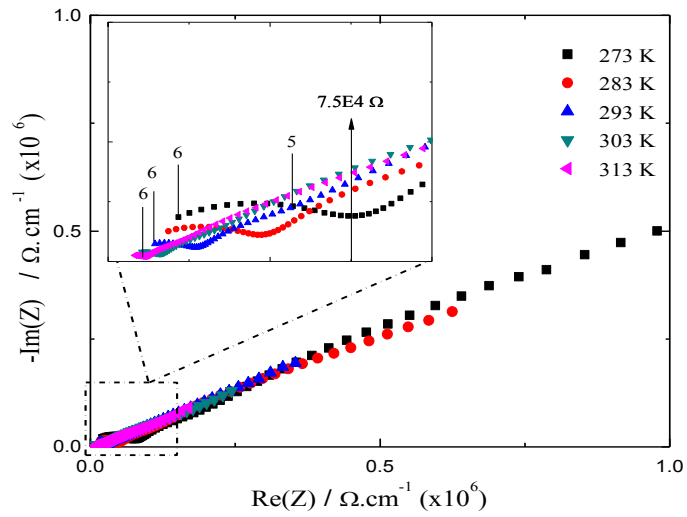
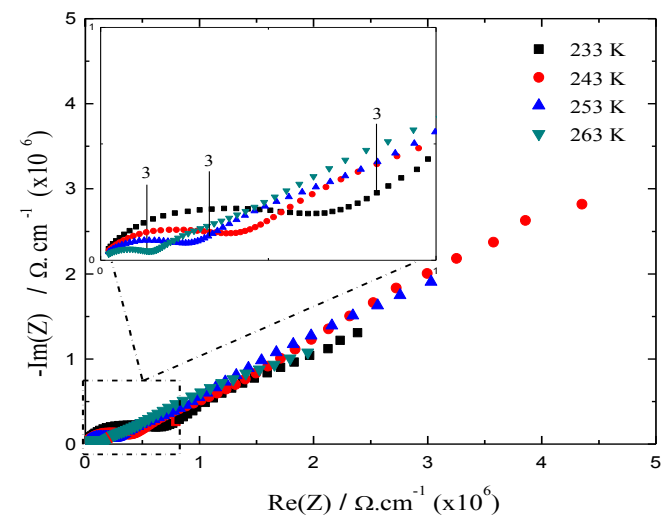
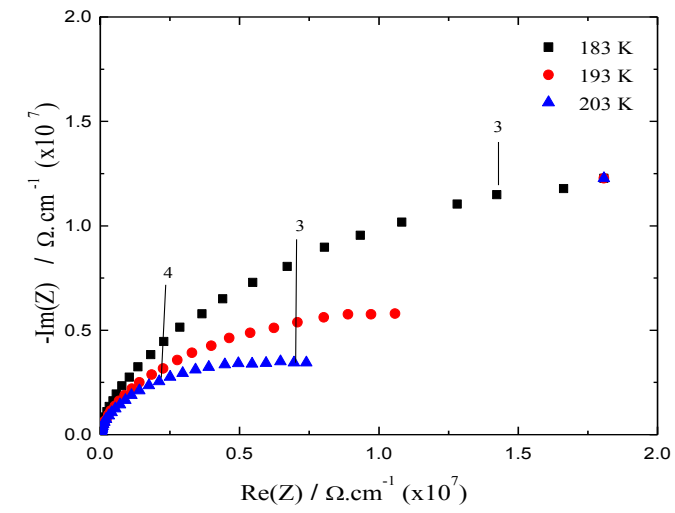


Figure 6.23: Nyquist Impedance diagrams of the U-PEO₁₉₀₀:Li⁺ monolith at various temperatures.

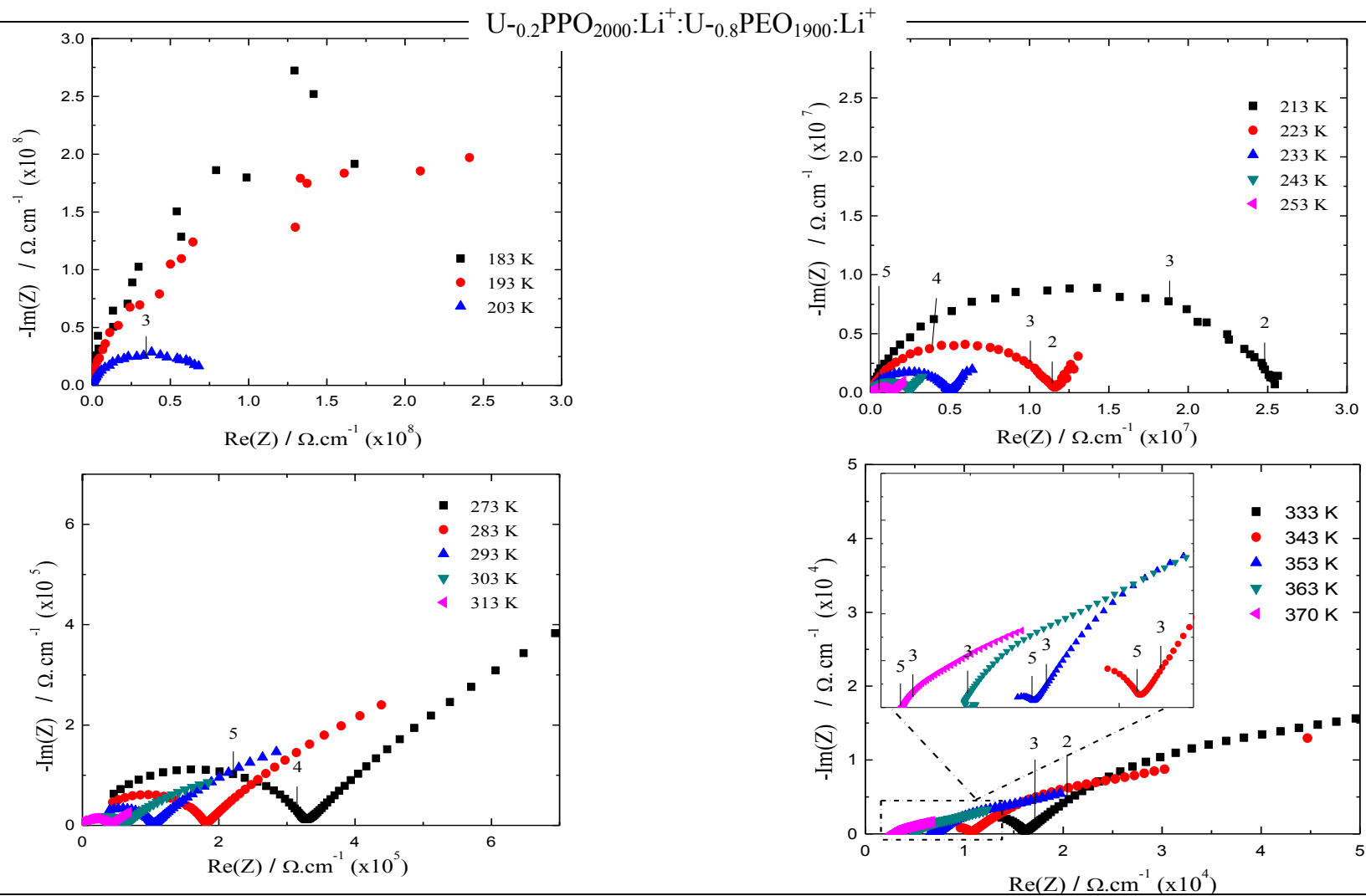


Figure 6.24: Nyquist Impedance diagrams of the $U_{-0.2}PPO_{2000}:Li^+:U_{-0.8}PEO_{1900}:Li^+$ monolith at various temperatures.

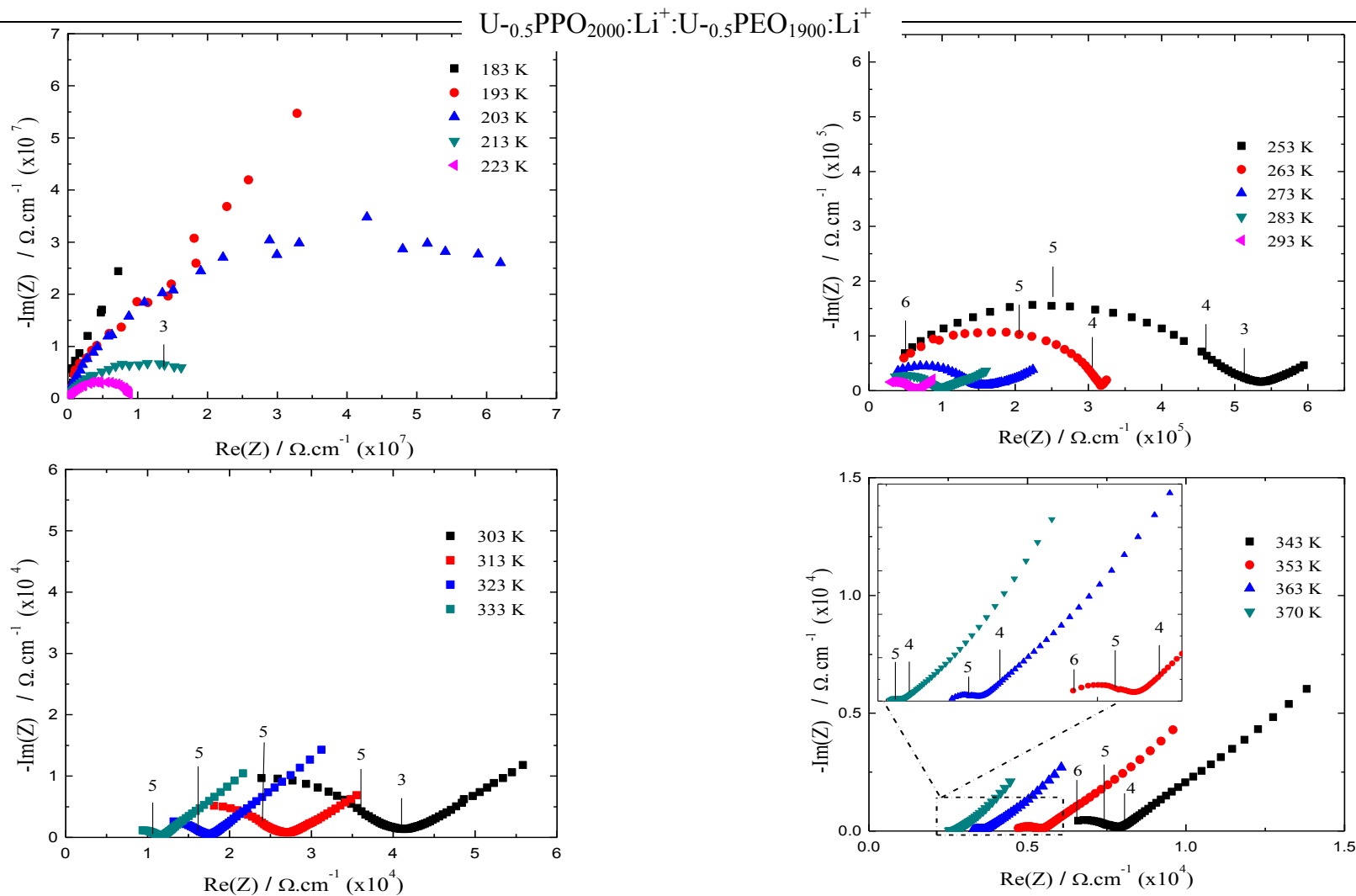


Figure 6.25: Nyquist Impedance diagrams of the $U_{-0.5}PPO_{2000}:Li^+:U_{-0.5}PEO_{1900}:Li^+$ monolith at various temperatures.

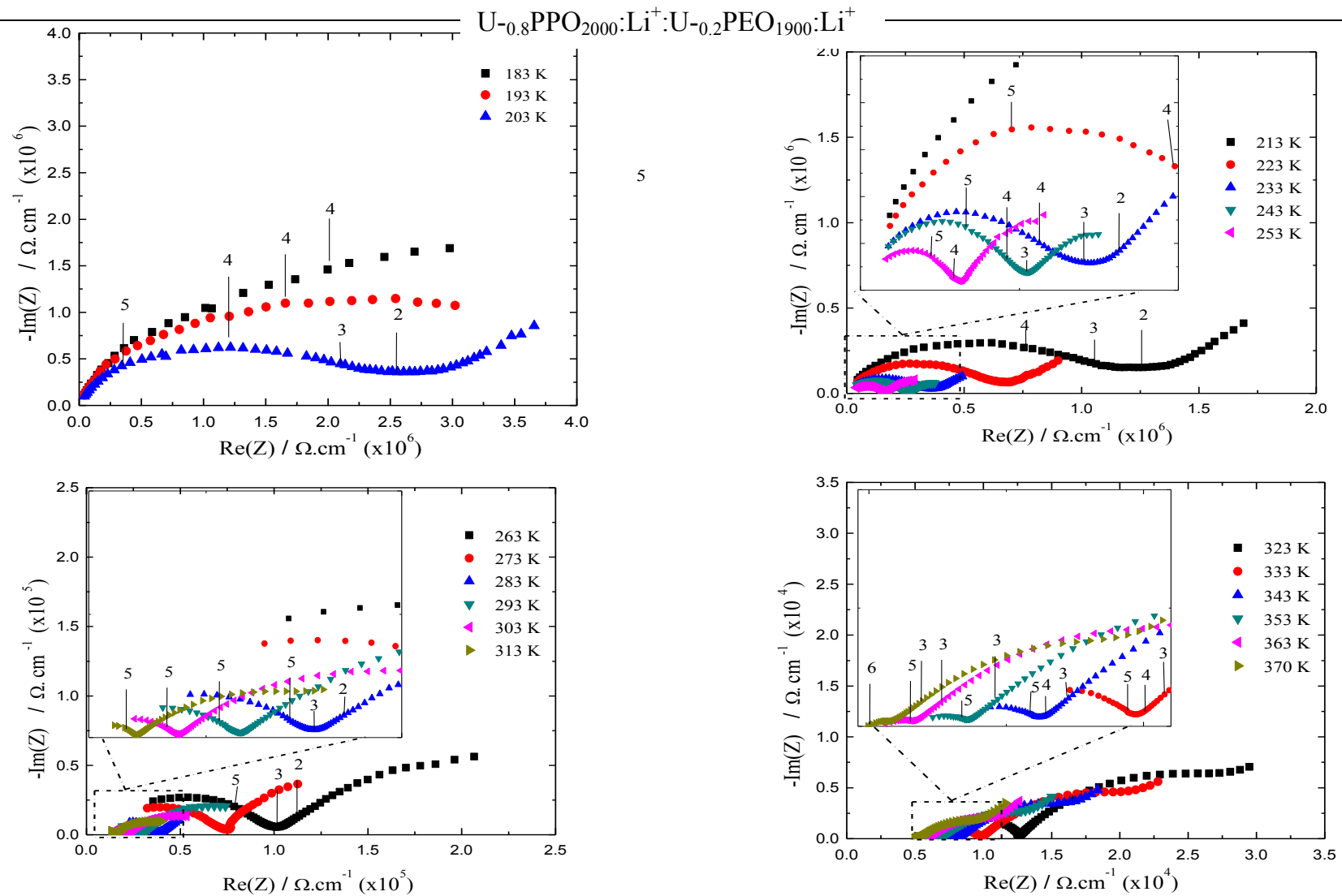


Figure 6.26: Nyquist Impedance diagrams of the $U_{-0.8}PPO_{2000}:Li^+:U_{-0.2}PEO_{1900}:Li^+$ monolith at various temperatures.

U-PPO₂₀₀₀:Li⁺

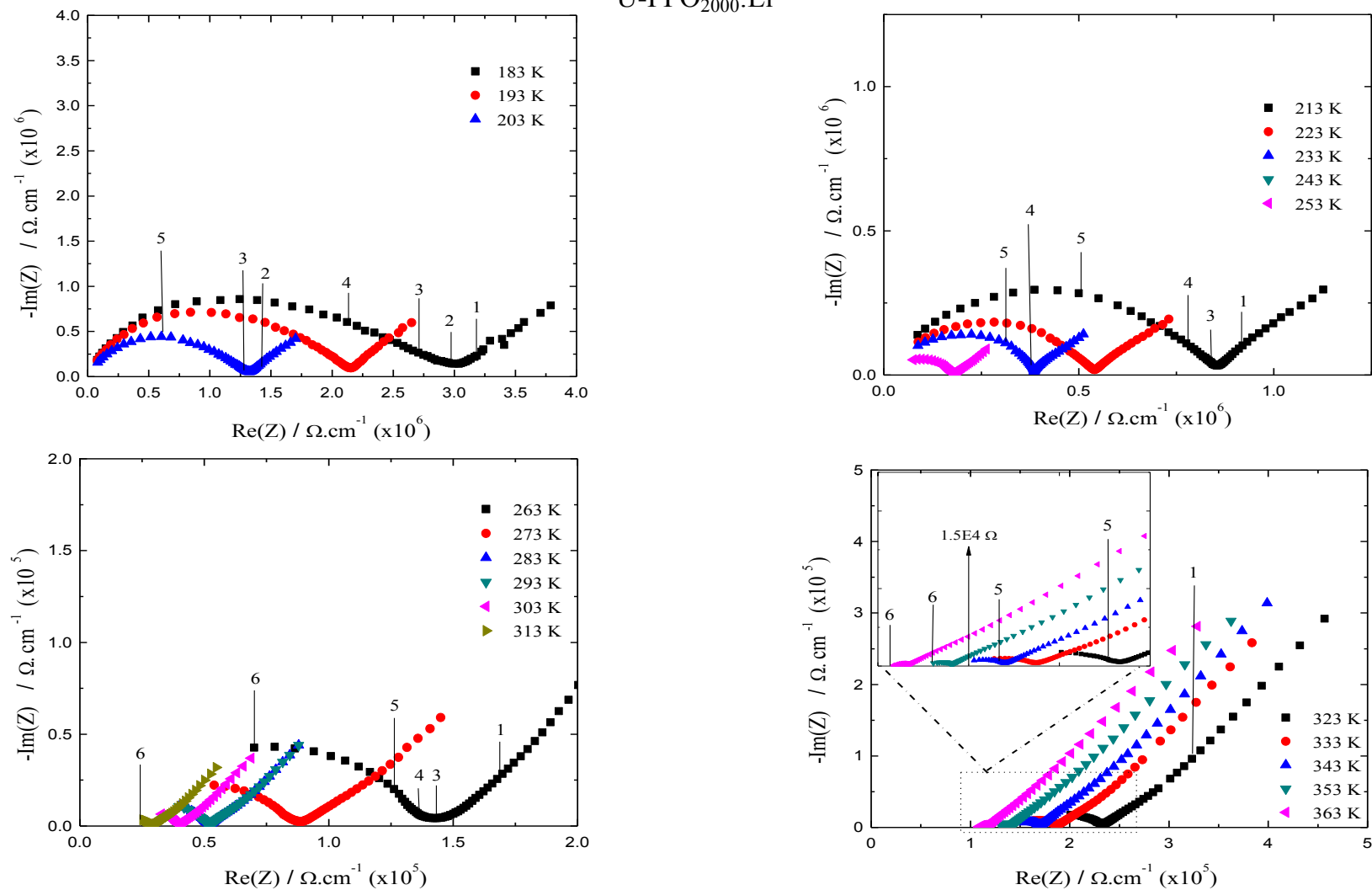


Figure 6.27: Nyquist Impedance diagrams of the U-PPO₂₀₀₀:Li⁺ monolith at various temperatures.

For a temperature range above the melting point of semi-crystalline Li^+ unloaded PEO_{1900} ($T > \sim 30$ °C), the $\text{OIH}:\text{Li}^+$ matrices have impedance spectra characteristic of *sandwich*-like, polymeric electrolytes, where the OIH material is placed between two metallic electrodes²⁴¹. The semicircles are incomplete on their high frequency side (6 ~ 5), indicating that the spectral frequency utilized is not high enough to follow the cation jump frequency. This high frequency semicircle corresponds to the specific ionic transfer property of the OIH *bulk* electrolyte. At the low frequency region (3 ~ 1), a tail arises, attributed to electrode polarization due to the electric double layer capacitance coming from the contact between the electrolyte ($\text{OIH}:\text{Li}^+$ material) / electrode²⁴².

For $\text{U-PEO}_{1900}:\text{Li}^+$ blends with a low PPO_{2000} fraction $x = 0.2$ and 0.5 , the semicircle at the high-frequency domain vanishes with the increase of temperature ($T > 60$ °C) and the impedance diagram is dominated by a tail in the entire frequency range. It has been reported that the high frequency semi-circle does not appear in impedance plots for ion-facilitated plasticized polymer electrolytes²⁴³. The range of temperatures which the semi-circle disappears coincides with PEO_{1900} semi-crystalline melting, observed by DSC and SAXS (as a function of the temperature). This phenomenon confirms that the fully rubber structure of $\text{OIH}:\text{Li}^+$ monoliths behave similar to a liquid electrolyte^{244,245}. Comparing the set of Nyquist diagrams and the thermo-event revealed for DSC, it is inferred that ionic conductivity values depend on two factors: *i*) The temperature, due to the increase of free volume with the temperature. In this process, the segmental motion of the chain helps the cation hopping between the ether-type oxygen, thus increasing the Li^+ diffused through the OIH material²⁴⁶ and *ii*) the dependency of T_g electrolytes, since it is well known that the lower the T_g value is, the higher the free volume, v_f , will be.

In order to correlate the thermal and the nano-structural features with the ionic transfer properties of OIH:Li⁺, an in depth analysis by Electrical Equivalent Circuit (EEC) was employed and the main results are shown in Figs. 6.28 and 6.29. Different EEC were considered depending on the OIH blend composition and temperature.

As discussed above, PEO₁₉₀₀ is a semi-crystalline polymer, having helical and ether crown conformation in equilibrium at room temperature ($T < T_m$). From the nano-structure point of view, the SAXS results indicate the coexistence of full amorphous and periodic semi-crystalline superstructures on the blend rich in PEO₁₉₀₀. Based on these findings, in a temperature range between T_g and T_m of Li⁺-unloaded PEO₁₉₀₀, there was a consideration of an EEC formed from the connection in series with three parallel elements related to resistance and constant phase elements – CPE (denominated as -RQ-). In this case R represents the specific electric resistivity of the material and Q is a charge accumulation when a voltage (V) is applied through a sandwich capacitor (C) constituted of two parallel electrodes with an area (A) defined separated by a distance (l) in the vacuum. The relationship is defined as:

$$Q = \epsilon_0 \frac{A}{l} V = CV \quad (11)$$

where ϵ_0 is the vacuum dielectric constant (8.885×10^{-12} F.m⁻¹) and C the system capacitance (Farads – F).

The impedance data and ECC fitting attained at -10 °C for U-PEO₁₉₀₀:Li⁺ is shown in Fig 6.27 (a). According to previous results, we strongly believe that the first parallel circuit represents *bulk* electrical resistance, ascribed to the relaxation time of PEO₁₉₀₀ at the helical (*gauche*) conformation associated with the memory of the semi-crystalline state. The segmental relaxation process has an important role in controlling ion transport in these solid polymer electrolytes²⁴⁷. The completely glass structure is found in this

range of temperatures, which could have a relaxation time near the PEO₁₉₀₀ crystal. With the increase in temperature, the relaxation time at the high frequency arises from the motion of the polymer chains due to the glass → rubber transition. Temperature has the effect of decreasing relaxation times²⁴⁸, consistent with the increase of ionic conductivity. On the other hand, the amorphous layer fraction present between the crystalline lamellae of the long period PEO₁₉₀₀ superstructure must have a different relaxation time, ascribed to the second parallel circuit in the middle frequency region from 5 kHz to 50 Hz.

The third parallel circuit in lower-frequency ranges represents the charge transfer at the anode interface²⁴⁹. The relaxation in the low frequency region is the electrode polarization phenomenon occurring as a result of an accumulation of ions near the electrodes²⁴⁷. Fig. 6.28 (c) shows a schematic diagram of the (– RQ – RQ – RQ –) model used, indicating where the different processes take place.

U-PPO₂₀₀₀:Li⁺ (Figs 6.29) and U-xPEO₁₉₀₀:Li⁺/_{1-x}PPO₂₀₀₀:Li⁺ OIH blends (Annex) show the Nyquist impedance diagrams that are in agreement with the well-known RQ – RQ model (inserted in Figs 6.28 and 6.29). In this kind of model, the first parallel circuit represents *bulk* electrical contribution of the hybrid electrolyte and the second parallel circuit represents the low-frequency charge transfer at the anode interface. It is well accepted that PPO₂₀₀₀ is an amorphous polymer, making the ECC composed of two parallel associations – RQ – RQ – physically consistent with the experimental results and with the nano-structural feature of OIH:Li⁺. This ECC is physically consistent with the mechanism of ionic transfer, in which the ions hoop through the amorphous fraction of PEO₁₉₀₀ and PPO₂₀₀₀ polymers and not by the PEO₁₉₀₀ semi-crystalline region.

According to the – RQ – RQ – equivalent circuit, the impedance spectra of all xPPO₂₀₀₀:1-xPEO₁₉₀₀ blend compositions can be explained by two different hypotheses

obtained from previous DSC previous results: *i)* The DSC results for blending with high PPO₂₀₀₀ fraction ($x = 0.5$ and 0.8) have shown that PPO₂₀₀₀ acts as an amorphous diluent, embedded with PEO₁₉₀₀ crystalline fraction. *ii)* As discussed above, the blending with low PPO₂₀₀₀ fraction ($x = 0.2$) does not show enough of a PPO₂₀₀₀ fraction to be capable of solubilizing all of the crystalline PEO₁₉₀₀ present in the blend. On the other hand, PEO₁₉₀₀ solubilizes metallic cations easier than PPO₂₀₀₀ due to its higher dielectric constant ϵ , compared with PPO₂₀₀₀ ($\epsilon_{\text{PEO}} = 2.2 \sim 2.5$ and $\epsilon_{\text{PPO}} = 1.5$). Therefore, the Li⁺ content (%) present in the PEO₁₉₀₀ fraction of U_{-0.2}PPO₂₀₀₀Li⁺:U_{-0.8}PEO₁₉₀₀:Li⁺ is higher compared to the U-PEO₁₉₀₀:Li⁺ homo-polymer. The increase of the PEO₁₉₀₀ $[\text{O}_{\text{ether}}] / [\text{Li}^+]$ relationship hinders the PEO₁₉₀₀ helical conformation, which is in agreement with the proposed RQ – RQ model. Ions, solvated molecules, or polymer segments can move now into the free volume with an increase in temperature. This leads to an increase in ion mobility and segmental mobility, which will assist ionic transport and virtually compensate for the hindering effect of ion clouds.

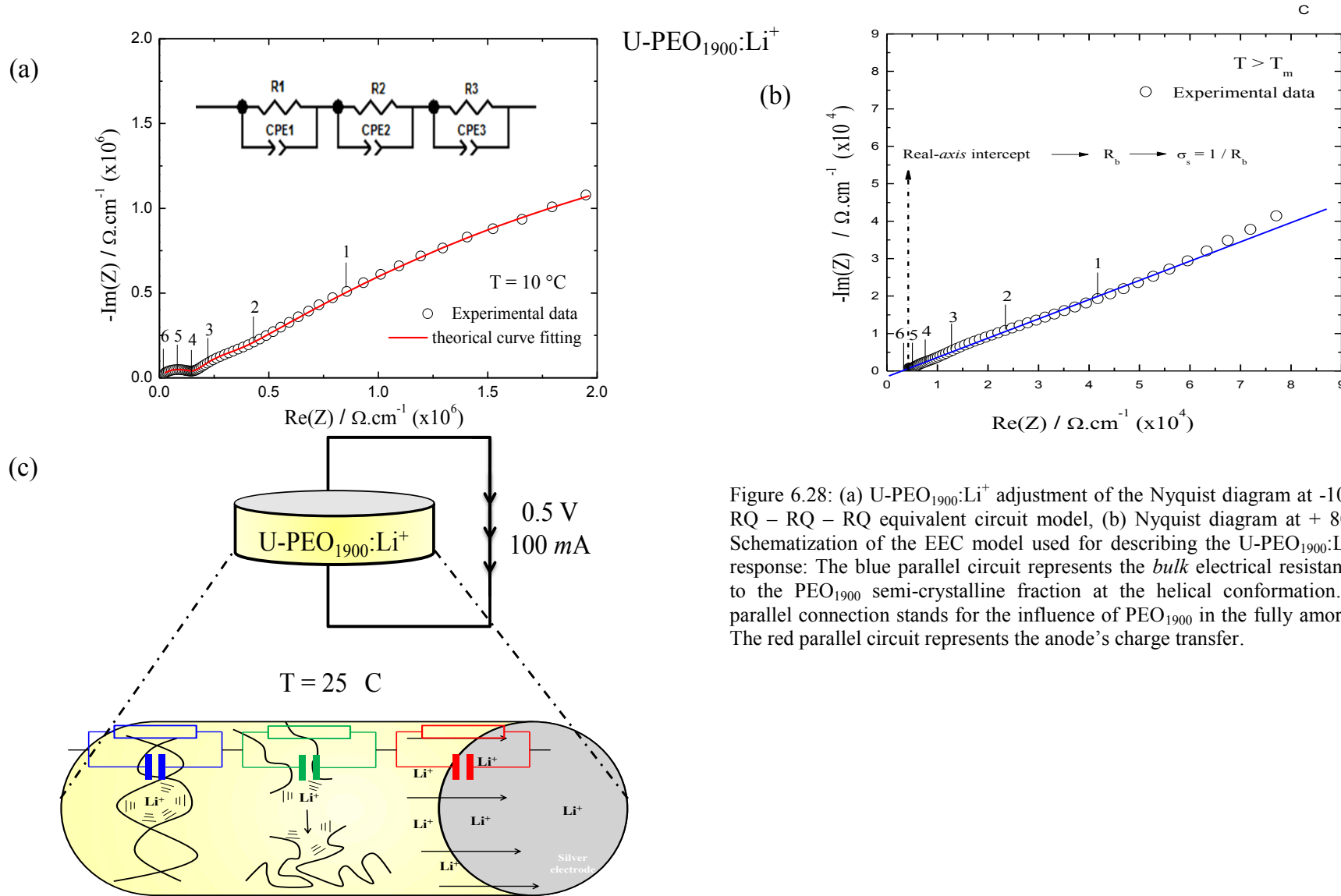
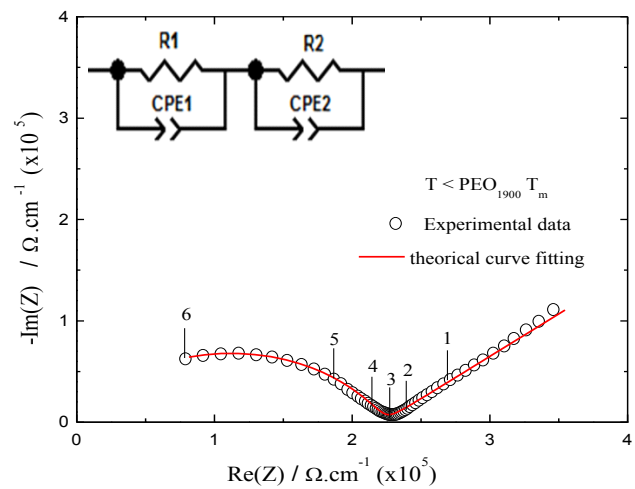


Figure 6.28: (a) U-PEO₁₉₀₀:Li⁺ adjustment of the Nyquist diagram at -10 °C using a RQ – RQ – RQ equivalent circuit model, (b) Nyquist diagram at + 80°C and (c) Schematization of the EEC model used for describing the U-PEO₁₉₀₀:Li⁺ electrical response: The blue parallel circuit represents the *bulk* electrical resistance, ascribed to the PEO₁₉₀₀ semi-crystalline fraction at the helical conformation. The green parallel connection stands for the influence of PEO₁₉₀₀ in the fully amorphous zone. The red parallel circuit represents the anode's charge transfer.



$\text{U-PPO}_{2000}:\text{Li}^+$

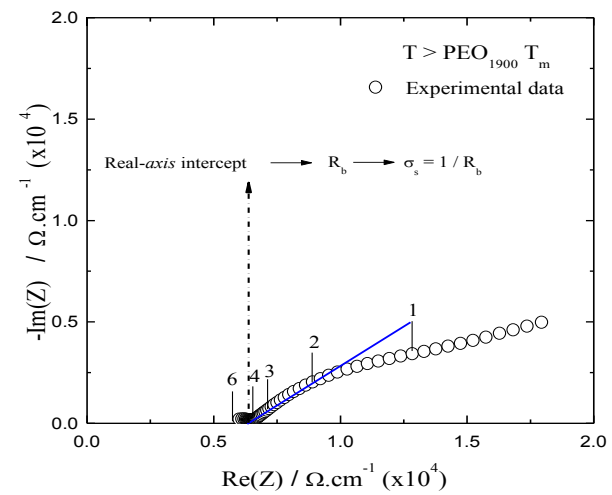


Figure 6.29: $\text{U-PPO}_{2000}:\text{Li}^+$ (Left) adjustment of the Nyquist diagram at $-10\text{ }^\circ\text{C}$ using a RQ – RQ model and (Right) Nyquist diagram at $+80\text{ }^\circ\text{C}$.

These equivalent circuit models were applied to determine the specific *bulk* conductivity (σ_s) of U-PEO₁₉₀₀:Li⁺, U-PPO₂₀₀₀:Li⁺ and _xPPO₂₀₀₀:_{1-x}PEO₁₉₀₀ blends in the entire range of temperatures. The σ_s is inversely proportional to the specific *bulk* electrical resistivity (ρ) since it is also dependent of the geometry of the sample.

Fig. 6.30 analyzes the dependence of the specific ionic conductivity of OIH:Li⁺ electrolytes with the temperature is in terms of the Arrhenius ($\ln(\sigma_s)$ vs. $1000/T$ (K)) plots. The observed linear behavior suggests that the thermally activated process follows an Arrhenius-type expression²⁵⁰:

$$\sigma_s = \sigma_0 \exp^{-E_a/kT} \quad (12)$$

where σ_0 is a pre-exponential factor, T is the temperature in Kelvin, E_a is the activation energy of the conduction process and k is the Boltzman constant (8.614×10^{-5} eV.K⁻¹).

The Arrhenius plot of the U-PEO₁₉₀₀:Li⁺ material displays three different linear regimes; *i*) from -90 °C to -55 °C, where the conductivity is almost independent of the temperature and the activation energy is close to zero ($E_a = 0.04$ eV), which is consistent with the rigidity of PEO₁₉₀₀ in the glass state ($T < T_g$); *ii*) between T_g and 15 °C, a linear step is observed with $E_a = 0.3$ eV); and *iii*) the third linear step is observed above 20 °C, which has the highest slope ($E_a = 0.4$ eV). These steps are in agreement with the RC component of the proposed EEC above. These two steps with nearly the same slope values are observed for _xPPO₂₀₀₀:Li⁺:U-_{1-x}PEO₁₉₀₀ blend with $x = 0.2$ and 0.5 U-PPO₂₀₀₀. A single linear behavior with a lower activation energy ($E_a = 0.19 - 0.22$ eV) is found for OIH:Li⁺ blend samples with a high amount of PPO₂₀₀₀ ($x = 0.8$ and 1), suggesting a single transport mechanism in the entire temperature range. This different behavior of thermo-activation of ionic conductivity suggests that the presence of poly(propylene oxide) chains play an important role in the conduction mechanism.

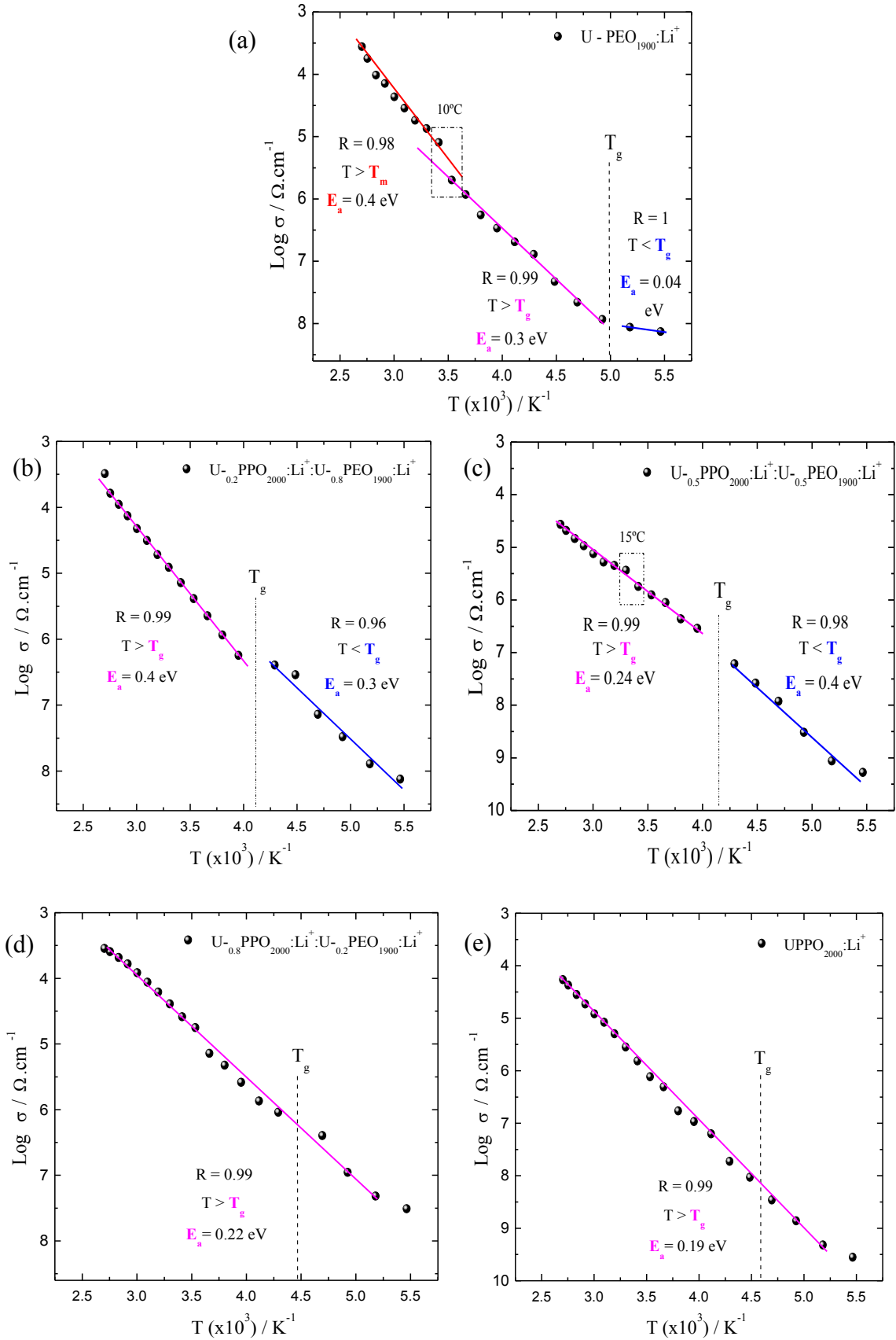


Figure 6.30: Temperature-dependent conductivities of (a) $\text{U-PEO}_{1900}:\text{Li}^+$, (b), (c) and (d) for $\text{U}_x\text{-PPO}_{2000}:\text{Li}^+:\text{U}_{1-x}\text{-PEO}_{1900}$ blending with PEO_{1900} fraction $x = 0.8, 0.5$ and 0.2 , respectively and (e) $\text{U-PPO}_{2000}:\text{Li}^+$.

The isothermal variation of the ionic conductivity with PPO₂₀₀₀ fraction in U-_xPPO₂₀₀₀:Li⁺:U-_{1-x}PEO₁₉₀₀:Li⁺ blends is presented in Fig. 6.31. The ionic conductivity of U-PEO₁₉₀₀:Li⁺ varies between $3 \times 10^{-8} \Omega \cdot \text{cm}^{-1}$ at -90 °C and $8.5 \times 10^{-4} \Omega \cdot \text{cm}^{-1}$ at approximately 100 °C (370 K). The ionic conductivity of blends with PPO₂₀₀₀ fraction higher than 0.5 shows an increasing trend with the fraction of PPO₂₀₀₀ over the temperature range of $-90 \text{ C} \leq T (\text{ C}) \leq +60 \text{ C}$. Comparing U-PEO₁₉₀₀:Li⁺ and the OIH blend with 0.8 PPO₂₀₀₀, it can be seen that the ionic conductivity increases by a factor of 4 times at -90 °C, and by a factor of 10 times at 80 °C. Thus, the incorporation of PPO₂₀₀₀ in the rubber U-_xPPO₂₀₀₀:Li⁺:U-_{1-x}PEO₁₉₀₀:Li⁺ blend significantly increases the electrolyte conductivity in a temperature range between $-90 \text{ C} \leq T \leq +10 \text{ C}$. Above 10 °C, it is observed that the U-PEO₁₉₀₀:Li⁺ specific conductivity becomes higher compared with all of the other OIH:Li⁺ monoliths studied. This intriguing phenomenon occurring near the Li⁺-unloaded PEO₁₉₀₀ melting phase transition is attributed to a nano-structural memory effect. Looking in the same temperature range, the SAXS curves show evidence of a decrease of intensity of the peak at the middle q-range, associated with the loss of memory of the PEO₁₉₀₀ semi-crystalline superstructure which leads to the increase of free volume, thus improving the charge transfer through the ether-type oxygens of PEO₁₉₀₀ chains.

The highest room temperature conductivity value ($\sigma_s \sim 5 \times 10^{-5} \Omega \cdot \text{cm}^{-1}$) was obtained U-PEO₁₉₀₀:Li⁺, while the lowest value of conductivity was found for the blend with PEO₁₉₀₀ $x = 0.8$ ($\sigma_s \sim 1 \times 10^{-5} \Omega \cdot \text{cm}^{-1}$). U-_{0.2}U-PPO₂₀₀₀:Li⁺:U-_{0.8}PEO₁₉₀₀:Li⁺ OIH blend has the highest value of T_g ($T_g = -54 \text{ C}$) among the OIH:Li⁺ monoliths studied by Impedance spectroscopy. As mentioned above, $\epsilon_{\text{PEO}} > \epsilon_{\text{PPO}}$, decreasing the U-PEO₁₉₀₀ active charge transfer concentration (polar oxygen ether-type) necessary for ionic motion. This result can tell us that the blend with $x = 0.2$ PPO₂₀₀₀ is not large enough to improve U-PEO₁₉₀₀:Li⁺ ionic conductivity. Otherwise, high PPO₂₀₀₀ fraction leads to lower conductivity values in a high temperature range of $T \geq 60 \text{ C}$, which implies that the ionic conductivity for OIH:Li⁺ blends with a high

plasticizer concentration is dominant for PPO₂₀₀₀ chain motion due to the steric hindrance caused by the presence of the methyl group present in the PPO₂₀₀₀ backbone (-CH-(CH₃)-CH₂-O-) and hence, the conductivity decreases.

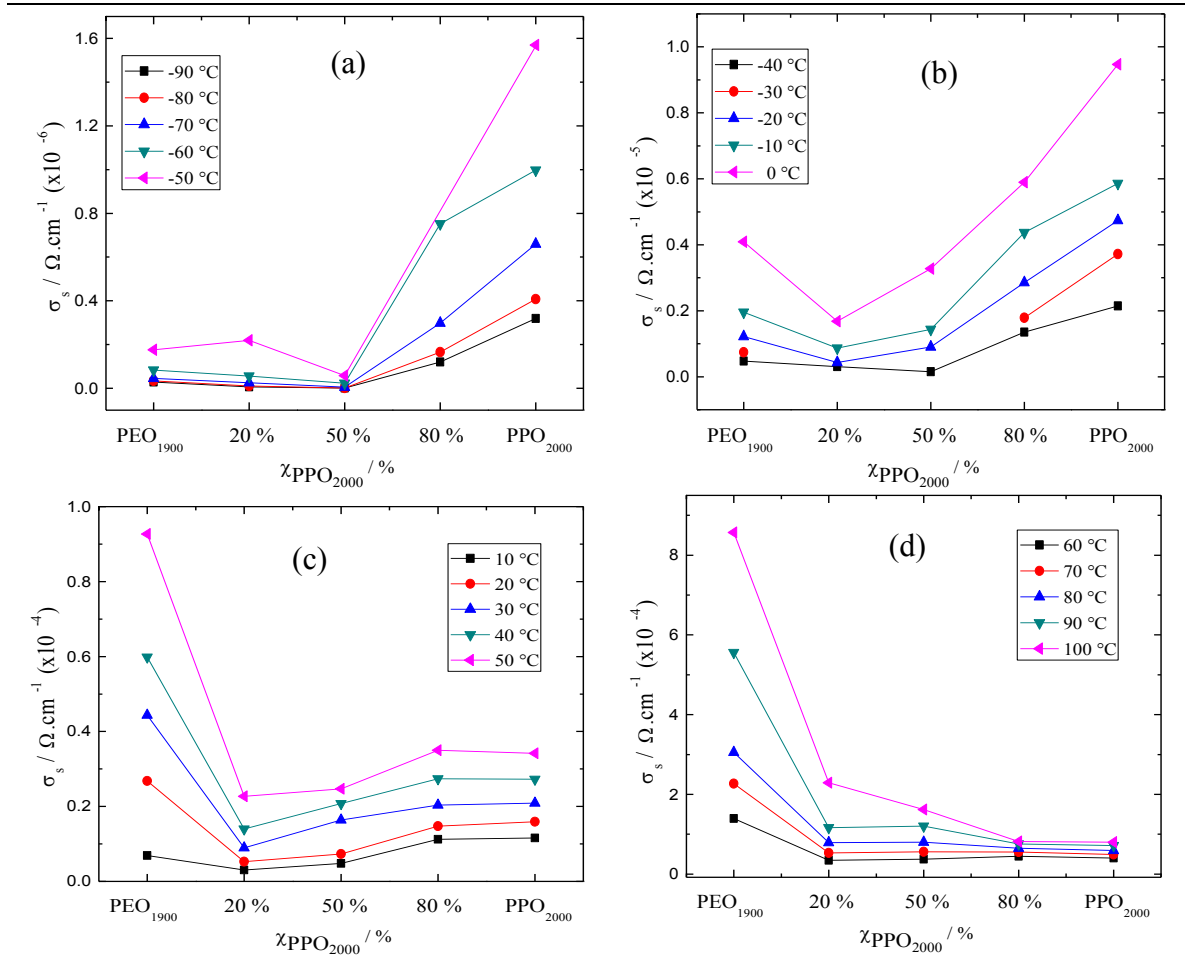


Figure 6.31: Isothermic evolution of the specific conductivity (σ_s) $U_xPPO_{2000}:Li^+:U_{1-x}PEO_{1900}:Li^+$ hybrid blend with different PPO₂₀₀₀ fraction (a) -90 to -50 °C (b) -0 to 0 °C (c) 10 to 50 °C and (d) +60 to +100 °C.

6.6: Partial Conclusions:

Homogeneous hybrid organic-inorganic solid electrolytes blends based on silica ethylene and propylene oxide network with $C_2F_5LiNO_4S_2$ were successfully synthesized by sol-gel method. The results of SAXS and DSC analyses indicated that the decrease in T_m of the crystalline segments of PEO₁₉₀₀ and the formation of an amorphous phase in the electrolyte has been observed by inclusion of PPO₂₀₀₀ in the blending system. The nanostructure of the hybrid blends could be described by the existence of homogeneous mixtures due to the

dilution effect. FTIR and Raman analysis confirmed the interactions of Li^+ cation with the $\text{O-CH}_2\text{-CH}_2\text{-O}$ backbone chains. Reduced chain mobility of polymeric chains is due to their complexation with Li^+ ions which resulted in an increase in the glass transition temperature. The overall crystallinity of PEO is reduced in the presence of salt ions. A crown-ether conformation, which favors the amorphous state of PEO_{1900} is considered to be the primary reason of suppressed its crystallinity. Ionic room temperature conductivity shows the highest value for the $\text{U-PEO}_{1900}:\text{Li}^+$ ($\sigma_s \sim 5 \times 10^{-5} \text{ } \Omega \cdot \text{cm}^{-1}$). The conductivity decreases for the $\text{PPO}_{2000} \times = 0.2$ blend, as a result of a decrease in the number of active carriers transfer, was attributed to an increase in the degree of lithium content at the PEO_{1900} fraction and an increase of its rigidity. It is found that the PPO_{2000} polymer is not a good candidate for plasticizers for lithium batteries in high values of temperature. On the other hand, PPO_{2000} addition results in a significant increase in the ionic conductivity of the electrolyte at lower temperatures. The best combination of ionic conductivity and mechanical properties, at low temperatures ($T < 0 \text{ } ^\circ\text{C}$) was obtained for the $\text{OIH}:\text{Li}^+$ blends monoliths with high PPO_{2000} fraction $x = 0.8$ and 1 $\text{U-PEO}_{1900}:\text{Li}^+$ showed a ECC model as $\text{RQ} - \text{RQ} - \text{RQ}$, ascribed to the PEO_{1900} helical conformation, amorphous conformation and electrode charge transfer, respectively, $\text{U-PPO}_{2000}:\text{Li}^+$ and the OIH blends showed a $\text{RQ} - \text{RQ}$ model, suppressing the PEO_{1900} helical conformation contribution. At $T > \text{PEO}_{1900} T_m$, the solids $\text{OIH}:\text{Li}^+$ monoliths behaves as ionic liquids, and the $\text{RQ} - \text{RQ}$ model is no longer anymore satisfactory to fit the Nyquist impedance patterns. The temperature-dependence conductivities of the $\text{OIH}:\text{Li}^+$ monoliths obey Arrhenius rule. The observed Arrhenius behavior in the blend is attributed to the lower mobility of PEO_{1900} segments in amorphous phase, which are restrained between crystalline regions, and the poor ionic mobility of PPO_{2000} . The enhancement of ionic conductivity with the increase of temperature ($T > 50 \text{ } ^\circ\text{C}$) is attributed to the fully amorphous structure.

Chapter 7:

General Conclusion and Future Perspectives

Sol-gel methods allowed for the synthesis of rubber, transparent, flexible and moldable OIH materials with different optical and ionic conductivity properties caused by the addition of Eu^{3+} and Li^+ , respectively.

From several spectroscopy techniques, we were able to prove that Eu^{3+} and Li^+ are coordinated by different polar sites of the OIH matrices, with the former interacting with the oxygen carbonyls of the urea linkage and the latter being solvated by ether type oxygens of the polyether. The Eu^{3+} dissociation into the matrix was confirmed by the narrow emission lines, ascribed to the $^5\text{D}_0 \rightarrow ^7\text{F}_j$ europium transition. The Eu^{3+} - $-\text{O}_{\text{carbonyl}}$ coordination leaves the PEO_{1900} *tgt* helical conformation ($\text{O}-\text{CH}_2-\text{CH}_2-\text{O}$ backbone chains) untouched, while the coexistent, amorphous and semi-crystalline phase led to the poor PL-QY values for this OIH: Eu^{3+} matrix, as compared to amorphous U-PPO₂₀₀₀: Eu^{3+} material.

Independent from the confirmation of Eu^{3+} - $\text{O}_{\text{carbonyl}}$ coordination from urea groups, we obtained the continuous recovery of the Amide I structure during Eu^{3+} decomplexation induced by exposure to intense UV-light. Formate and ester were considered the main photo-products formed by UV-light exposition, which were confirmed by the ammoniac chemical treatment of photo-degraded OIH materials. The visible red \rightarrow blue PL transition observed with the increase of UV-light exposure for OIH: Eu^{3+} materials based on PPO₂₀₀₀ and PPO₄₀₀₀ confirmed their quick loss of Eu^{3+} coordination. On the other hand, the properties of lanthanide-containing materials were found and their visible red \rightarrow blue PL transition allowed for the proposal of their application as UV-sensors and biological optical-markers, as well as optics markers and/or packaging monitoring of intense UV exposure.

In a different way, Li^+ cations show drastic changes in the polymer $\text{O}-\text{CH}_2-\text{CH}_2-\text{O}$ backbone chains, which confirm the solvation of Li^+ by ether-type oxygen atoms. This induces the reduction of PEO crystallinity, confirmed by DSC, Raman, and SAXS measurements. The evolution of nano-structure with temperature revealed the participation of

water molecules in the lamellae crystallite organization, leading to the increase of the electron density contrast between the crystalline lamellae and the amorphous phase as the temperature increases from T_g to 0°C . For OIH: Li^+ materials, the water molecule has the role of mediator in the $\text{Li}^+ \cdots \text{H}_2\text{O} \cdots \text{O}_{\text{ether}}$ interaction, and the *trans* crown-ether conformation (amorphous state of PEO_{1900}) was considered to be the primary reason for the loss of U- PEO_{1900} crystallinity. For OIH blends, DSC measurements reveal that the semi-crystalline PEO_{1900} is embedded by the amorphous fraction of the PPO_{2000} . However, the evolution of the nano-structure reveals that these materials do not obey a mixture law.

The best room temperature ionic conductivity was found for the U- $\text{PEO}_{1900}:\text{Li}^+$ ($\sigma_s \sim 5 \times 10^{-5} \Omega \cdot \text{cm}^{-1}$) sample. The best combination of ionic conductivity and mechanical properties at low temperatures ($T < 0^\circ\text{C}$) was obtained for OIH: Li^+ blend monoliths with high PPO_{2000} fraction $x = 0.8$ and 1. U- $\text{PEO}_{1900}:\text{Li}^+$ showed a form resembling the RQ – RQ – RQ ECC model, ascribed to the PEO_{1900} helical conformation, amorphous conformation and electrode charge transfer. U- $\text{PPO}_{2000}:\text{Li}^+$ and OIH blends showed a form resembling the RQ – RQ model, suppressing the contribution of PEO_{1900} helical conformation. The semi-crystalline PEO_{1900} melting has an important role in ionic conductivity because for $T > T_m$, the solid electrolyte behaves like ionic liquids and the RQ – RQ model is no longer satisfactory to fit the experimental results.

The distinct local coordination for the different metal cations in these OIH matrices reveal a new and interesting property of these OIH multifunctional materials, which is the possibility of combining the ionic conductivity of the polyelectrolyte with their photoluminescent properties. This finding can further increase the fields of application of OIH materials. However, some studies need to be carried out to better understand the role played by water molecules in structural properties of U-PEO materials.

Chapter 8:

References

-
- ¹ KARTHIK, P. et al. A visible-light active catechol-metal oxide carbonaceous polymeric material for enhanced photocatalytic activity. **Journal of Materials Chemistry A**, v. 5, n. 1, p. 384-396, 2017.
- ² KARIMI, M.; BADIEI, A.; ZIARANI, G.M. A click-derived dual organic-inorganic hybrid optical sensor based on SBA-15 for selective recognition of Zn^{2+} and CN^- in water. **Inorganica Chimica Acta**, v. 450, p. 346-352, 2016.
- ³ SCHMIDT, S. et al. Fe and Co methylene diphosphonates as conversion materials for Li-ion batteries. **Journal of Power Sources**, v. 342, p. 879-885, 2017.
- ⁴ GATFAOUI, S. et al. Synthesis, characterization, Hirshfeld surface analysis and antioxidant activity of a novel organic-inorganic hybrid material 1-methylpiperazine-1,4-dium bis(nitrate). **Journal of Molecular Structure**, v. 1139, p. 52-59, 2017.
- ⁵ LIU, F. et al. Green fabrication of ultraviolet curable epoxy acrylate-silica hybrid coatings. **Progress in Organic Coatings**, v. 109, p. 38-44, 2017.
- ⁶ KARTHIK, P. et al. A visible-light active catechol-metal oxide carbonaceous polymeric material for enhanced photocatalytic activity. **Journal of Materials Chemistry A**, v. 5, n. 1, p. 384-396, 2017.
- ⁷ KWON, J. et al. Two-terminal DSSC/silicon tandem solar cells exceeding 18% efficiency. **Energy and Environmental Science**, v. 9, n. 12, p. 3657-3665, 2016.
- ⁸ CHEN, C.; ZHANG, D. Cross-cascaded AWG-based wavelength selective switching integrated module using polymer optical waveguide circuits. **Frontiers of Optoelectronics**, v. 9, n. 3, p. 428-435, 2016.
- ⁹ CROISSANT, J. G. et al. Organosilica hybrid nanomaterials with a high organic content: syntheses and applications of silsesquioxanes. **Nanoscale**, v. 8, n. 48, p. 19945-19972, 2016.
- ¹⁰ CATAURO, M. et al. Modification of Ti_6Al_4V implant surfaces by biocompatible TiO_2/PCL hybrid layers prepared via sol-gel dip coating: Structural characterization, mechanical and corrosion behavior. **Materials Science and Engineering C**, v. 74, p. 501-507, 2017.
- ¹¹ YAO, H.-B.; GAO, M.-R.; YU, S.-H. Small organic molecule templating synthesis of organic-inorganic hybrid materials: their nanostructures and properties. **Nanoscale**, v. 2, p. 323-334, 2010.
- ¹² DAHMOUCHE, K. et al. Structural modelling of Eu^{3+} -based siloxane-poly(oxyethylene) nanohybrids. **Journal of Materials Chemistry**, v. 11, p. 3249-3257, 2001.
- ¹³ RIBEIRO, S. J. L. et al. Study of hybrid silica-polyethyleneglycol xerogels by Eu^{3+} luminescence spectroscopy. **Journal of Sol-Gel Science and Technology**, v. 13 p. 427-432, 1988.

-
- 14 BERMUDEZ, V. Z. et al. Coordination of Eu^{3+} ions in siliceous nanohybrids containing short polyether chains and bridging urea crosslinks. **Journal of Physical Chemistry B**. v. 105 p. 3378-3386, 2001
- 15 MOLINA, C. et al. Enhanced emission from Eu(III) b-diketone complex combined with ether-type oxygen atoms of di-ureasil organic-inorganic hybrids. **Journal of Luminescence**. v. 104 p. 93-101, 2003
- 16 LI, Y.; LUO, D.; YANG, M. Novel Nanocomposite of Poly(acrylonitrile-co-glycidyl methacrylate) Crosslinked with Jeffamine-Functionalized Multiwalled Carbon Nanotubes as Gel Polymer Electrolytes. **Journal of Applied Polymer Science**. 2012. doi: 10.1002/app.37936.
- 17 RAN, Y. et al. A polymer electrolyte based on poly(vinylidene fluoride-hexafluoropylene)/hydroxypropyl methyl cellulose blending for lithium-ion battery. **Ionics**. v. 19, p. 757-762, 2013.
- 18 LUO, D.; LI, Y.; YANG, M.; Preparation and characterization of novel crosslinked poly[glycidyl methacrylate-poly(ethylene glycol) methylether methacrylate] as gel polymer electrolytes; **J Journal of Applied Polymer Science**. v. 120, p. 2979-2984, 2011.
- 19 LUO, D.; LI, Y.; YANG, M.; Crosslinked poly(acrylonitrile-glycidyl methacrylate) as a novel gel polymer electrolyte. **Materials Chemistry and Physics**. v. 125, p. 231-235, 2011.
- 20 DAHMOUCHE, K. et al. Investigation of new ion-conducting ormolytes silica-polypropyleneglycol. **Journal of Sol-Gel Science and Technology**. v. 13 p. 909-913, 1998.
- 21 DAHMOUCHE, K. et al. New Li^+ ion-conducting ormolytes. **Solar Energy Materials and Solar Cell**, v. 54 p. 1-8, 1998.
- 22 DAHMOUCHE, K. et al. Silica-PEG hybrid ormolytes: structure and properties. **Journal of Non-Crystalline Solids**. v. 247 p. 108-113, 1999.
- 23 ESTEVES, A. C. C.; BARROS-TIMMONS, A.; TRINDADE, T. Nanocompósitos de matriz polimérica: estratégias de síntese de materiais híbridos. **Química Nova**, v. 27, n 5, p.798-806, 2004.
- 24 MYTHICAL CREATURES. **Griffin**. 2012. Disponível em: <mythortruth.com/griffin/>. Acesso em: 26 de maio 2017.
- 25 KIM, K.-H.; PARK, S.-Y. Enhancing light-extraction efficiency of OLEDs with high- and low-refractive-index organic-inorganic hybrid materials. **Organic Electronics: physics, materials, applications**, v. 36, p. 103-112, 2016.
- 26 KASHIF, M. K. et al. Cobalt polypyridyl complexes as transparent solution-processable solid-state charge transport materias. **Advanced Energy Materials**, v. 6, n. 24, 2016. doi: 10.1002/aenm.201600874.

-
- 27 AKRAM, D. et al. Castor and Linseed oil polyurethane/TEOS hybrids as protective coatings: a synergistic approach utilizing plant oil polyols, a sustainable resource. **Progress in Organic Coatings**, v. 108, p. 1-14, 2017.
- 28 PAN, Y. et al. Fabrication of highly hydrophobic organic-inorganic hybrid magnetic polysulfone microcapsules: a lab-scale feasibility study for removal of oil and organic dyes from environmental aqueous samples. **Journal of Hazardous Materials**, v. 309, p. 65-76, 2016.
- 29 LIANG, L. et al. Charge-tunable insertion process of carbon nanotubes into DNA nanotubes. **Journal of Molecular Graphics and Modelling**, v. 66, p. 20-25, 2016.
- 30 JIN, W. et al. Lanthanide-integrated supramolecular polymeric nanoassembly with multiple regulation characteristics for multidrug-resistant cancer therapy. **Biomaterials**, v. 129, p. 83-97, 2017.
- 31 WANG, H. et al. High-efficiency planar thin-film Si/PEDOT:PSS hybrid solar cell. **IEEE Journal of Photovoltaics**, v. 6, n. 1, p. 217-222, 2016.
- 32 FEI, F. et al. Syntheses, structures and catalytic properties of organic-inorganic hybrid materials constructed from Evans-Showell-type polyoxometalates and zinc-organic coordination units. **RSC Advances**, v. 6, n. 94, p. 92092-92103, 2016.
- 33 ZHAO, H. et al. Preparation of hydrophilic organic groups modified mesoporous silica materials and their humidity sensitive properties. **Sensors and Actuators B: Chemical**, v. 240, p. 681-688, 2017.
- 34 KITSCHKE, P. et al. Porous Ge@C materials via twin polymerization of germanium(II) salicyl alcoholates for Li-ion batteries. **Journal of Materials Chemistry A**, v. 4, n. 7, p. 2705-2719, 2016.
- 35 CHAKER, J. A. **Correlações entre estrutura e propriedades de condução iônica em materiais híbridos siloxanopoli(propileno óxido), dopados com sais de sódio e potássio**. 2004.164 f. Tese (Doutorado em Química) - Instituto de Química, Universidade Estadual Paulista, Araraquara, 2004.
- 36 SAMENTO, V. H. V. **Estrutura e propriedades de materiais híbridos siloxano-PMMA preparados pelo processo sol-gel**. 2005. 168 f. Tese (Doutorado em Química) - Instituto de Química, Universidade Estadual Paulista, Araraquara, 2005.
- 37 BENVENUTTI, E. V. et al. Materiais híbridos à base de sílica obtidos pelo método sol-gel. **Quimica Nova**, v. 32, n. 7, p. 1926-1933, 2009.
- 38 HALL, P. G. et al. Ion conductivity in polysiloxane comb polymers with ethylene glycol. **Polymer Communication**, v. 27, p. 98-100, Feb. 1986.
- 39 FISH, D.; KHAN, I. M.; SMID, J. Conductivity of solid complexes of lithium perchlorate with poly{[-methoxyhexa(oxyethylene)ethoxy]methylsiloxane}. **Macromolecular Chemistry Rapid Communication**, v. 7, p. 115-120, 1986.

-
- 40 MAMMERI, F. et al. Mechanical properties of hybrid organic–inorganic materials. **Journal of Materials Chemistry**, v. 15, p. 3787–3811, 2005.
- 41 MOLINA, E., F. et al. Fine-tuning of a nanostructure, swelling, and drug delivery profile by blending ureasil–PEO and ureasil–PPO hybrids. **Polymer Chemistry**, v. 5, p. 1897-1904, 2014.
- 42 MOURA, A. L. A. et al. Influence of the hydrophilic/hydrophobic nature of polyetheramines on the interaction between amine–alcohol–silicate hybrids and anionic dyes for effective water cleaning. **Journal of Materials Chemistry A**, v. 3, p. 16020 -16032, 2015.
- 43 GODOVSKY, Y. K.; SLONIMSKY, G. L.; GARBAR, N. M. Effect of molecular weight on the crystallization and morphology of poly(ethylene oxide) fractions. **Journal of Polymer Science**, v. 38, p. 1-21, 1972.
- 44 MARK, J. E.; LEE, C. Y-C.; BIANCINI, P. A. **Hybrid Organic-Inorganic Composites**. Washington, DC: American Chemical Society, 1995. 378 p.
- 45 CARLOS, L. D. et al. Full-color phosphors from amine-functionalized crosslinked hybrids lacking metal activator ions. **Advanced Functional Materials**, v. 11, p. 111-115, 2001.
- 46 LEE, K.-S.; KOBAYASHI, S. (Ed.). **Polymer Materials: block-copolymers, nanocomposites, organic/inorganic hybrids, polymethylenes**. Heidelberg: Springer, c2010. 235 p. (advances in polymer sciences, v. 231).
- 47 KLEMPNER, D.; SPERLING, L. H.; UTRACKI, L. A. **Interpenetration polymer networks**. Washington, DC: American Chemical Society, 1994. 638 p.
- 48 BEST, B. **Physical parameters of cooling in cryonics**. Disponível em: <<https://www.benbest.com/cryonics/cooling.html>>. Acesso em: 06 fev. 2017.
- 49 DUDA, J. L.; ZIELINKI, J. M. Free-volume theory. In: NEOGI, P. (Ed). **Diffusion in polymers**. New York: Marcel Dekker, c1996. p. 143-171.
- 50 CAMERON, G. G.; INGRAM, M. D.; SORRIE, G. A. Ionic conductivity in liquid polymeric electrolytes. **Journals of Electroanalytical Chemistry**, v. 198, p. 205-207, 1986.
- 51 MacCALLUM, J. R.; VINCENT, C. A. (Ed.), **Polymer electrolyte reviews**, London: Springer, c1987. 351 p.
- 52 CANGIALOSI, D. Dynamics and thermodynamics of polymer glasses. **Journal of Physics: Condensed Matter**, v. 26, 2014. doi: 10.1088/0953-8984/26/15/153101.
- 53 SCHMELZER, J. W. P.; GUTZOW, I. The Prigogine-Defay ratio revisited. **Journal of Chemical Physics**, v. 125, 2006. doi:10.1088/0953-8984/26/15/153101.

-
- 54 OTLES, S.; OTLES, S. Glass transition in food industry – characteristic properties of glass transition and determination techniques. **Electronic Journal Of Polish Agricultural Universities**. v. 8, n. 4, 2005. Disponível em: <<http://www.ejpau.media.pl/volume8/issue4/art-69.html>>. Acesso em: 05 fev. 2017.
- 55 FANG, Z. et al. Location of a nanoclay at the interface in an immiscible poly(ϵ -caprolactone)/ poly(ethylene oxide) blend and its effect on the compatibility of the components. **Journal of Applied Polymer Science**, v. 106, p. 3125-3135, 2007.
- 56 SI, M. et al. Compatibilizing bulk polymer blends by using organoclays. **Macromolecules**, v. 39, n. 14, p. 4793-4801, 2006.
- 57 KUO, C.-W. et al. Influence of lithium salt addition on ionic conductivity and transporting properties of lithium bis(trifluoromethanesulfonyl)imide-doped glycine-based ionic liquid electrolyte. **Journal of the Taiwan Institute of Chemical Engineers**, v. 45, p. 1270-1279, 2014.
- 58 PHILIPP, M. et al. Structure-property relationship and transport properties of structurally related silyl carbonate electrolytes. **Electrochimica Acta**, v. 173, p 687-697, 2015.
- 59 HAYAMIZU K. et al. Quaternary ammonium room-temperature ionic liquid including an oxygen atom in side chain/lithium salt binary electrolytes: ionic conductivity and ^1H , ^7Li , and ^{19}F NMR studies on diffusion coefficients and local motions. **Journal of Physical Chemistry B**, v. 112, p. 1189-1197, 2008.
- 60 BOWDEN, M. J.; TURNER, M., J. Polymers for electronic and photonic applications. In? BOWDEN, M. J.; TURNER, S. R. (Ed.). **Electronic and photonic applications of polymers**. Washington, DC: American Chemical Society, 1988. Chap. 1, p. 1-73. (Advances in chemistry, v. 218).
- 61 WRIGHT, P.V. Cyclization equilibrium constants and the conformations of polydimethylsiloxane chains. **Journal of Polymer Science Part A-2**. v. 11, p. 51-64, 1973.
- 62 ARMOND, R. A. S. Z. **Estudo de eletrólitos poliméricos a base de poliéter por espectroscopia raman, análise térmica e condutividade iônica**. 1999. 114 f. Tese (Doutorado em Física) - Instituto de Ciências Exatas, Universidade Federal de Minas Gerais, Belo Horizonte, 1999.
- 63 CARTER, F. L. (Ed.). **Molecular electronic devices**. New York: Marcel Dekker, c1982. 386 p.
- 64 CARTER, F. L. (Ed.). **Molecular electronic devices II**. New York: Marcel Dekker, c1987. 825 p.
- 65 PAINEL solar transparente promete revolucionar aplicações em energia solar. **Portal Energia: Energias Renováveis**, set 2014. Disponível em: <portal-energia.com/painel-solar-transparente-promete-revolucionar-aplicacoes-em-energia-solar>. Acesso em: 05 fev.2017.

66 SONG, S. Weirdest cell phones ever! **Dark Roasted Blend**. Disponível em: <<http://cotidianosuperficial.blogspot.com.br/2009/10/os-10-celulares-conceito-mais.html>>. Acesso em: 05 fev.2017.

67 MATA, D. da. Brasileiro cria conceito de celular com tela flexível. **Techguru**, ago. 2010. Disponível em: <<http://www.techguru.com.br/brasileiro-cria-conceito-de-celular-com-tela-flexivel/>>. Acesso em: 05 fev. 2017.

68 PROMETHEUS. Direção: Ridley Scott. Produção: Riddley Scott; Walter Hill; Tony Scott; David Giler. Los Angeles: 20th Century Fox, 2012. DVD.

69 WU, H.-Y. et al. Synthesis and characterization of highly conductive plasticized double core organiceinorganic hybrid electrolytes for lithium polymer batteries. **Journal of Power Sources**, v. 238, p. 265-273, 2013.

70 SCHANTZ, S. On the ion association at low salt concentrations in polymer electrolytes; a Raman study of NaCF₃SO₃ and LiClO₄ dissolved in polypropylene oxide. **Journal of Chemical Physics**, v. 94, p. 6296-6306, 1991.

71 ANILKUMARA, K. M. et al Poly(ethylene oxide) (PEO) – poly(vinyl pyrrolidone) (PVP) blend polymer based solid electrolyte membranes for developing solid state magnesium ion cells. **European Polymer Journal**, v. 89, p. 249-262, 2017.

72 SOO, P. P. et al. Rubbery block copolymer electrolytes for solid-state rechargeable lithium batteries. **Journal of Electrochemical Society**, v. 146, p. 32-37, 1999.

73 RUZETTE A. G. Melt-formable block copolymer electrolytes for lithium rechargeable batteries. **Journal of Electrochemical Society**, v. 148, p. A537-A543, 2001.

74 CHOI, J.-W. et al. Poly(ethylene oxide)-based polymer electrolyte incorporating room-temperature ionic liquid for lithium batteries. **Solid State Ionics**, v. 178 p. 1235-1241, 2007.

75 KUMAR K. K. et al. Investigations on the effect of complexation of NaF salt with polymer blend (PEO/PVP) electrolytes on ionic conductivity and optical energy band gaps. **Physica B**, v. 406, p. 1706-1712, 2011.

76 ALDALUR, I. et al. Jeffamine® based polymers as highly conductive polymer electrolytes and cathode binder materials for battery application. **Journal of Power Sources**, v. 347, p. 37-46, 2017.

77 CHAURASIA, S. K. et al. Electrical, mechanical, structural, and thermal behaviors of polymeric gel electrolyte membranes of poly(vinylidene fluoride-cohexafluoropropylene) with the ionic liquid 1-butyl-3-methylimidazolium tetrafluoroborate plus lithium tetrafluoroborate. **Journal of Applied Polymer Science**, v. 132, 2015. doi: 10.1002/app.41456.

78 GRÜNEBAUM, M. et al. Synthesis and electrochemistry of polymer based electrolytes for lithium batteries. **Progress in Solid State Chemistry**, v. 42, p. 85-105, 2014.

-
- 79 SHIN, J. H.; HENDERSON, W. A.; PASSERINI, S. PEO-based polymer electrolytes with ionic liquids and their use in lithium metal-polymer electrolyte batteries. **Electrochemical and Solid-State Letters**, v. 8, p. A125-A127, 2005. doi: 10.1149/1.1890701.
- 80 NOLLENBERGER, K.; ALBERS, J. Poly(meth)acrylate-based coatings. **International Journal of Pharmaceutics**, v. 457, p. 461-469, 2013.
- 81 SHIN, J. H.; HENDERSON, W. A.; PASSERINI, S. J. PEO-based polymer electrolytes with ionic liquids and their use in lithium metal-polymer electrolyte batteries. **Journal of Electrochemical Society**, v. 152 p. A978-A983 2005.
- 82 DENG, F. et al. Microporous polymer electrolyte based on PVDF/PEO star polymer blends for lithium ion batteries. **Journal of Membrane Science**, v. 491, p. 82-89, 2015.
- 83 NIMAH, Y. L. et al. Solid-state polymer nanocomposite electrolyte of TiO₂/PEO/NaClO₄ for sodium ion batteries. **Journal of Power Sources**, v. 278, p. 375-381, 2015.
- 84 JUNG, G. Y.; CHOI, J. H.; LEE, J. K. Thermal behavior and ion conductivity of polyethylene oxide/polyhedral oligomeric silsesquioxane nanocomposite electrolytes. **Advances in Polymer Technology**, v. 34, 2015. doi: 10.1002/adv.21499.
- 85 KUMAR K. K. et al. Investigations on PEO/PVP/NaBr complexed polymer blend electrolytes for electrochemical cell applications. **Journal of Membrane Science**, v. 454, p. 200-211, 2014.
- 86 KESAVAN, K.; MATHEW, C. M.; RAJENDRAN, S. Lithium ion conduction and ion-polymer interaction in poly(vinyl pyrrolidone) based electrolytes blended with different plasticizers. **Chinese Chemical Letters**, v. 25, p. 1428-1434, 2014.
- 87 VERMA, M. L. et al. Ab initio study of mechanical strength of solid polymer electrolyte (PEO)₅LiClO₄. **Ionics**, 2017. doi 10.1007/s11581-017-2025-x.
- 88 KUMAR, P. P.; YASHONATH, S. Ionic conduction in the solid state. **Journal of Chemical Science**, v. 118, n. 1, p. 135-154, 2006.
- 89 DAHMOUCHE, K. et al. Investigation of new Ion-Conducting Ormolytes: Structure and Properties. **Journal of Sol-Gel Science and Technology**, v. 8, p. 711-715, 1997.
- 90 POWELL, J. A.; VENKATAKRISHNAN, K.; TAN, B. Hybridized enhancement of the SERS detection of chemical and bio-marker molecules through Au nanosphere ornamentation of hybrid amorphous/crystalline Si nanoweb nanostructure biochip devices. **Journal of Materials Chemistry B**, v. 4, p. 5713-5728, 2016.
- 91 INTERNATIONAL UNION OF PURE AND APPLIED CHEMISTRY. **IUPAC compendium of chemical terminology – the Gold book**. 2nd ed. Oxford, [entre 2005 e 2017]. Disponível em: <<https://goldbook.iupac.org/html/L/L03641.html>>. Acesso em: 19 jun. 2017.

-
- 92 RODA, A. The discovery of luminescence: the bolognian stone. In: RODA, A.; PAZZAGLI, M.; KRICKA, L. J.; STANLEY, P. E. (Ed.). **Bioluminescence and chemiluminescence: perspectives for the 21st Century** (symposia on bioluminescence & chemiluminescence). Chichester: John Wiley & Sons, 1999. p. 3-12.
- 93 YEN, W. M.; WEBER, M. J. Inorganic phosphors: compositions, preparation and optical properties. Boca Raton. CRC Press, 2004. 496 p.
- 94 WIEDEMANN, E. Ueber Fluoreszenz und Phosphoreszenz I. Abhandlung. **Annalen der Physik**, v. 34, n. 7, 1888. doi:10.1002/andp.18882700703.
- 95 KHARE, A. et al. Optical properties of rare earth doped srs phosphor: a Review. **Journal of Electronic Materials**, v. 46, n. 2, p. 687-708, 2017.
- 96 WHITE, L. **The glow worms adaptations**. Disponível em: <tes.com/lessons/QkXkbudj2Ysajw/the-glow-worm-adaptations >. Acesso em: 02 jun. 2017.
- 97 THE 10 BEST places to stare in awe at the aurora borealis. **Raw Story**, jan. 2015. The aurora borealis (Shutterstock). Disponível em: <rawstory.com/2015/01/the-10-best-places-to-see-the-aurora-borealis>. Acesso em: 02 jun. 2017.
- 98 EXPLORE peixe de água salgada e muito mais! **Pinterest**. Disponível em: <pinterest.com/pin/498140408761060425>. Acesso em: 02 jun. 2017.
- 99 FABIAN'S TINY WORKSHOP. **Make a log slice wood art décor – woodworking**. 2014. Disponível em: <https://www.youtube.com/watch?v=A0IV7SLT7s4>. Acesso em: 02 jun. 2017.
- 100 LIU, H.-G. et al. Studies on composites formed by europium complex with different ligands and polyvinylpyrrolidone. **Materials Letters**, v. 58, p. 1677-1682, 2004.
- 101 MEZA-ROCHA, A. N. et al. Orange and reddish-orange light emitting phosphors: Sm³⁺ and Sm³⁺/Eu³⁺ doped zinc phosphate glasses. **Journal of Luminescence**, v. 167 p. 305-309, 2015.
- 102 XUA, H. et al. Electroluminescence from europium(III) complexes. **Coordination Chemistry Review**, v. 293, p. 228-249, 2015.
- 103 CARLOS, L. D. et al. White light emission of Eu³⁺-based hybrid xerogels. **Physical Review B**, v. 60, p. 10042-10053, 1999.
- 104 BINNEMANS, K. Interpretation of europium(III) spectra. **Coordination Chemistry Reviews**, v. 295, p. 1-45, 2015.
- 105 FU, Z. et al. Influence of doping concentration on valence states of europium in SrAl₂O₄:Eu phosphors. **Journal of Luminescence**, v. 143, p. 657-662, 2013.

-
- 106 GOBRECHT, H. Über die absorptions- und fluoreszenzspektren der ionen der seltenen erden in festen Körpern, insbesondere im ultrarot. **Annalen der Physik**, v. 28, p. 673-700, 1937.
- 107 BÜNZLI, J.-C. G.; ELISEEVA, S. V. Photophysics of lanthanoid coordination compounds. In: REEDIJK, J.; POEPELMEIER, K. (Ed.). **Comprehensive inorganic chemistry II: from elements to applications**. 2nd ed. Amsterdam: Elsevier, c2013. v. 8, p. 339-398. v. 8: Coordination and organometallic chemistry.
- 108 DOCHAIN, S. et al. Combining organocatalysis and lanthanide catalysis: a sequential one-pot quadruple reaction sequence/hetero-diels–alder asymmetric synthesis of functionalized tricycles. **Angewandte Chemie International Edition**, v. 55, p. 16153-16155, 2016.
- 109 NAM, M. et al. Multi-functional transparent luminescent configuration for advanced photovoltaics. **Advanced Energy Materials**, v. 6, 2016. doi:10.1002/aenm.201502404.
- 110 DU, P.-Y. et al. A multifunctional chemical sensor based on a three-dimensional lanthanide metal-organic framework. **Journal of Solid State Chemistry**, v. 244, p. 31-34, 2016.
- 111 WANG, J. et al. Fabrication of thermo-sensitive optical switches based on lanthanide-polyoxometalates and their “on-off” luminescence controlled by temperature. **Journal of Polymer Research**, v. 23, 2016. doi:10.1007/s10965-016-0968-7.
- 112 ZHANG, Y. et al. Synthesis and fluorescent pH sensing properties of nanoscale lanthanide metal-organic frameworks with silk fibroin powder as polymer ligands. **Dyes and Pigments**, v. 130, p. 129-137, 2016.
- 113 FIX, T. et al. Enhancement of silicon solar cells by downshifting with Eu and Tb coordination complexes. **Progress in Photovoltaics: Research and Applications**, v. 24, p. 1251-1260, 2016.
- 114 CHEN, C.; LI, C.; SHI, Z. Current advances in lanthanide-doped upconversion nanostructures for detection and bioapplication. **Advanced Science**, v. 3, n. 10, 2016. doi: 10.1002/advs.201600029.
- 115 ZHENG, W. et al. Tumor marker detection: ultrasensitive luminescent in vitro detection for tumor markers based on inorganic lanthanide nano-bioprobes. **Advanced Science**, v. 3, n. 11, 2016. doi:10.1002/advs.201600197
- 116 BINNEMANS, K. Lanthanide-Based Luminescent Hybrid Materials. **Chemical Reviews**, v. 109 p. 4283-4374, 2009.
- 117 HUSAIN, S. et al. Influence of cobalt doping on the structural, optical and luminescence properties of sol-gel derived TiO₂ nanoparticles. **Philosophical Magazine**, v. 7, n. 1, p. 17-27, 2017.

-
- 118 VUOJOLA, J.; SOUKKA, T. Luminescent lanthanide reporters: new concepts for use in bioanalytical applications. **Methods and Applications in Fluorescence**, v. 2, n. 1, 2014. doi:10.1088/2050-6120/2/1/012001.
- 119 ILLESCAS, J. et al. PEGDA-based luminescent polymers prepared by frontal polymerization. **Journal of Polymer Science, Part A: Polymer Chemistry**, v. 53 n. 24, p. 2890-2897, 2015.
- 120 KOVALCHUK, A. luminescent polymer composite films containing coal-derived graphene quantum dots. **ACS Applied Materials and Interfaces**, v. 7, n. 47, p. 26063-26068, 2015
- 121 ZHANG, A. Q. Syntheses and luminescent properties of a copolymer of terbium-p-aminobenzoic acid-methacrylic acid and styrene. **Luminescence**, v. 30, n. 7, p. 1020-1025, 2015.
- 122 ELSTS, E. et al. Rare earth doped glass–ceramics containing NaLaF₄ nanocrystals. **Optical Materials**, v. 59, p. 130-135, 2016.
- 123 KINDRAT, I. I. et al. Spectroscopic properties of the Ce-doped borate glasses. **Optical Materials**, v. 59, p. 20-27, 2016.
- 124 LIU, W. et al. A Multi-responsive regenerable europium–organic framework luminescent sensor for Fe³⁺, Cr^{VI} anions, and picric acid. **Chemistry - A European Journal**, v. 22, p. 18769-18776, 2016.
- 125 ZHOU, F. et al. Transparent and luminescent ionogels composed of Eu³⁺-coordinated ionic liquids and poly(methyl methacrylate). **Luminescence**, v. 30, n 8, p. 1303-1307, 2015.
- 126 RAMOS, T. J. de S. et al. Thermoreversible luminescent ionogels with white light emission: An experimental and theoretical approach. **Journal of Materials Chemistry C**, v. 3, n. 41, p. 10934-10942, 2015.
- 127 XIE, W. et al. An anionic interpenetrated zeolite-like metal–organic framework composite as a tunable dual-emission luminescent switch for detecting volatile organic molecules. **Chemistry - A European Journal**, v. 22, n. 48, p. 17298-17304, 2016.
- 128 LEE, C. W. et al. Encapsulating luminescent materials in zeolites. iii. crystal structure and scintillation properties of cs,na-lta treated with zirconium chloride vapor. **Journal of Physical Chemistry C**, v. 120, n. 33, p. 18682-18693, 2016.
- 129 VAN HEST, J. J. H. A. et al. In corporation of Ln-doped LaPO₄ nanocrystals as luminescent markers in silica nanoparticles. **Nanoscale Research Letters**, v. 11, p. 261-272, 2016.
- 130 HAO, X. Et al. Peculiar synergetic effect of MoS₂ quantum dots and graphene on metal-organic frameworks for photocatalytic hydrogen evolution. **Applied Catalysis B: Environmental**, v. 210, p. 45-56, 2017.

-
- 131 MAHATA, P. et al. Luminescent rare-earth-based MOFs as optical sensors. **Dalton Transactions**, v. 46, n. 2, p. 301-328, 2017.
- 132 CHOWDHURI, A.R. et al. Synthesis of multifunctional upconversion NMOFs for targeted antitumor drug delivery and imaging in triple negative breast cancer cells. **Chemical Engineering Journal**, v. 319, p. 200-211, 2017.
- 133 PETROVA, O. B. et al. Luminescent hybrid materials based on (8-hydroxyquinoline)-substituted metal-organic complexes and lead-borate glasses. **Optical Materials**, v. 69, p. 141-147, 2017.
- 134 VIANA, R. S. et al. Structural and spectroscopic investigation of new luminescent hybrid materials based on calixarene-tetracarboxylate and Ln^{3+} ions ($\text{Ln} = \text{Gd}, \text{Tb}$ or Eu). **Journal of Solid State Chemistry**, v. 251, p. 26-32, 2017.
- 135 SAS, S. et al. Highly luminescent hybrid materials based on smectites with polyethylene glycol modified with rhodamine fluorophore. **Applied Clay Science**, v. 138, p. 25-33, 2017.
- 136 PAROLA, S. et al. Optical properties of hybrid organic-inorganic materials and their applications. **Advanced Functional Materials**, v. 26, n. 36, p. 6506-6544, 2016.
- 137 JULIÁN, B. et al. Synthesis and optical properties of Eu^{3+} -doped inorganic-organic hybrid materials based on siloxane networks. **Journal of Materials Chemistry**, v. 14, p. 3337-3343, 2004.
- 138 SHIPWAY, A. N.; WILLNER, I. Nanoparticles as structural and functional units in surface-confined architectures. **Chemical Communications**, v. 20, p. 2035-2045, 2001.
- 139 FRANVILLE, A. C. Et. al. Molecular design of luminescent organic-inorganic hybrid materials activated by europium (III) ions. **Solid State Science**, v. 3, p. 211-222, 2001.
- 140 FRANVILLE, A. C. et al. Synthesis and optical features of an europium organic-inorganic silicate hybrid. **Journal of Alloys and Compounds**, v. 275, p. 831-834, 1998.
- 141 FRANVILLE, A. C. et al. Luminescence behavior of sol-gel-derived hybrid materials resulting from covalent grafting of a chromophore unit to different organically modified alkoxysilanes. **Chemical Materials**, v. 12, p. 428-435, 2000.
- 142 CARLOS, L., D. et al. Full-color phosphors from europium(III)-based organosilicates. **Advanced Materials**, v. 12, p. 594-598, 2000.
- 143 BÜNZLI, J.-C. Lanthanide luminescence for biomedical analyses and imaging. **Chemical Reviews**, v. 110, p. 2729-2755, 2010.
- 144 WEISSMAN, S. I. Intramolecular energy transfer the fluorescence of complexes of europium. **Journal of Chemical Physics**, v. 10, p. 214-217, 1942
- 145 JORGENSEN, C. K.; JUDD, B. R. Hypersensitive pseudoquadrupole transitions in lanthanides. **Molecular Physics**, v. 8, p. 281-290, 1964.

-
- 146 MOELLER, T.; ULRICH, W. F. J. Observations on the rare earths—LXVII: some observations on the absorption spectra of non-aqueous solutions of some acetylacetonate chelates. **Journal of Inorganic and Nuclear Chemistry**, v. 2, p. 164-175, 1956.
- 147 SINHA, S. P. (Ed.). **Systematics and the properties of the lanthanides**. Dordrecht: D. Reidel Publ., 1982. 653 p. (Serie C. Mathematical and physical sciences, n. 109).
- 148 JUDD, B. R. Hypersensitive transitions in rare-earth ions. **Journal of Chemical Physics**, v. 44, p. 839-840, 1966.
- 149 RUNOWSKI, M.; BALABHADRA, S.; LIS, S. Nanosized complex fluorides based on Eu^{3+} doped Sr_2LnF_7 (Ln=La, Gd). **Journal of Rare Earths**, v. 32, p. 242-247, 2014.
- 150 RUNOWSKI, M. Eu^{3+} and Tb^{3+} doped LaPO_4 nanorods, modified with a luminescent organic compound, exhibiting tunable multicolour emission. **RSC Advances**, v. 4, p. 46305-46312, 2014.
- 151 LONKAR, S. P.; LEUTERITZ, A.; HEINRICH, G. Antioxidant intercalated layered double hydroxides: A new multifunctional nanofiller for polymers. **RSC Advances**, v. 3, p. 1495-1501, 2013.
- 152 GORRASI, G. et al. Hybrid clay mineral-carbon nanotube-PLA nanocomposite films. Preparation and photodegradation effect on their mechanical, thermal and electrical properties. **Applied Clay Science**, v. 71, p. 49-54, 2013.
- 153 COELHO, C. et al. Inorganic-organic hybrid materials based on amino acid modified hydrotalcites used as UV-absorber fillers for polybutylene succinate. **European Journal of Inorganic Chemistry**, v. 32, p. 5252-5258, 2012.
- 154 DESHMUKH, P. P.; MAHANWAR, P. A.; SABHARWAL, S. S. Synthesis of urethane acrylate from PENTA based polyol and EB curing with varying ratio of TMTPA. **Pigment and Resin Technology**, v. 41, p. 284-295, 2012.
- 155 KATAOKA, H. Drastically improved durability and efficiency of silicon solar cells using hyper-stable lanthanide coordination polymer beads. **Bulletin of the Chemical Society of Japan**, v. 89, p. 103-109, 2016.
- 156 ABOHALKUMA, T.; TELEGDI, J. Corrosion protection of carbon steel by special phosphonic acid nano-layers. **Materials and Corrosion**, v. 66 p. 1382-1390, 2015.
- 157 DRUVARI, D. et al. Polymeric quaternary ammonium-containing coatings with potential dual contact-based and release-based antimicrobial activity. **Applied Materials & Interfaces**, v. 8, p. 35593-35605, 2016.
- 158 RANBY, B. Photodegradation and photo-oxidation of synthetic polymers. **Journal of Analytical and Applied Pyrolysis**, v. 15, p. 237-247, 1989.

-
- 159 PAPPAS, S. P. Weathering of coatings: formulation and evaluation. **Progress in Organic Coatings**, v. 17, p. 107-114, 1989.
- 160 GIESSE, R.; DE PAOLI, M.-A. Photo-degradable polymer films derived from low density polyethylene. **Polymer Degradation and Stability**, v. 23, p. 201-207, 1989.
- 161 BAUER, D. R. Photo-stabilization and photo-degradation in organic coatings containing a hindered amine light stabilizer: part V-infrared spectroscopic measurements of hindered amine effectiveness. **Polymer Degradation and Stability**, v. 28, p. 39-51, 1990.
- 163 KUBOTA, H.; TAKAHASHI, K.; OGIWARA, Y. Benzophenone-sensitized photodegradation of polyethylene. **Polymer Degradation and Stability**, v. 24, p. 201-211, 1989.
- 164 HAMID, S. H.; PRICHARD, W. H. Application of infrared spectroscopy in polymer degradation. **Polymer-Plastics Technology and Engineering**, v. 27 p. 303-334, 1988.
- 165 MORLAT, S. ; GARDETTE, J.-L. Phototransformation of water-soluble polymers. I: photo- and thermooxidation of poly(ethylene oxide) in solid state. **Polymer**, v. 42, p. 6071-6079, 2001.
- 166 MORLAT, S. et al. Mechanisms of photooxidation of polyglycerol. **Polymer Degradation and Stability**, v. 72, p. 199-208, 2001.
- 167 DECKER, C.; BIRY, S.; ZAHOULY, K. Photostabilisation of organic coatings. **Polymer Degradation and Stability**, v. 49, p. 111-119, 1995.
- 168 RIVATON, A.; LALANDE, D.; GARDETTE, J.-L. Influence of the structure on the γ -irradiation of polypropylene and on the post-irradiation effects. **Nuclear Instruments and Methods in Physics Research B**, v. 222, p. 187-200, 2004.
- 169 KONG, G. et al. Preparation conditions of inorganic–organic hybrid membranes synthesized from epoxyhexylethyltrimethoxysilane and 1-hydroxyethane-1,1-diphosphonic acid. **Journal of Sol-Gel Science Technology**, v. 66, p. 84-90, 2013.
- 170 HIRATSUKA, R. S.; SANTILLI, C. V.; PULCINELLI, S. H. Processo sol-gel: uma visão físico-química. **Química Nova**, v. 18, n. 2, p. 171-180, 1995.
- 171 BRINKER, C. J.; SCHERER, G. W. **Sol-gel science: the physics and chemistry of sol-gel processing**. San Diego: Academic Press, 1990. 462 p.
- 172 LIVAGE, J. et al. Sol-gel synthesis of oxide materials. **Acta Materialia**, v. 46, n. 3, p. 743-750, 1998.
- 173 GAWEL, B.; GAWEL, K.; OYE, G. Sol-gel synthesis of non-silica monolithic materials. **Materials**, v. 3, n. 4, p. 2815-2833, 2010.

-
- 174 KHELIFA, F. et al. Sol-gel incorporation of silica nanofillers for tuning the anti-corrosion protection of acrylate-based coatings. **Progress in Organic Coatings**, v. 76, p. 900-911, 2013.
- 175 NAKANISHI, K. Pore structure control of silica gels based on phase separation. **Journal of Porous Materials**, v. 4, n. 2, p. 67-112, 1997.
- 176 SANTILLI, C. V. et al. Controlled drug release from ureasil-polyether hybrid materials. **Chemical Materials**, v. 21, p. 463-467, 2009.
- 177 CAETANO, B. L. et al. Magnetic hyperthermia-induced drug release from ureasil-PEO- γ -Fe₂O₃ nanocomposites. **RSC Advances**, v. 6, p. 63291-63295, 2016.
- 178 MORLAT-THERIAS, S. et al. Polymer/carbon nanotube nanocomposites: Influence of carbon nanotubes on EVA photodegradation. **Polymer Degradation and Stability**, v. 92 p. 1873-1882, 2007.
- 179 HASSOUNA, F. et al. Influence of water on the photodegradation of poly(ethylene oxide). **Polymer Degradation and Stability**, v. 92, p. 2042-2050, 2007.
- 180 BRAZILIAN SYNCHROTRON LIGHT LABORATORY. [SAXS1 beam line instrumentation]. Campinas. Disponível em: <lnls.cnpem.br/en/linhas-de-luz/saxs1-en/overview/>. Acesso em: 05 dez. 2017.
- 181 ADUMEAU, P. et al. Two-photon absorption properties of Eu³⁺-DPA-triazolyl complexes and the derived silica nanoparticles embedding these complexes. **European Journal of Inorganic Chemistry**, v. 7, p. 1233-1242, 2015.
- 182 STRAWHECKER, K. E. MANIAS, E.; Crystallization behavior of poly(ethylene oxide) in the presence of Na⁺ montmorillonite fillers. **Chemical Materials**, v. 15, p. 844-849, 2003.
- 183 FERNANDES, M. et al. Di-ureasil hybrids doped with LiBF₄: spectroscopic study of the ionic interactions and hydrogen bonding. **Materials Chemistry and Physics**, v. 129, p. 385-393, 2011.
- 184 MATSURA, H.; MIYAZAWA, T. Vibrational analysis of molten poly(ethylene glycol). **Journal of Polymer Science**, v. 7, n. 10, p. 1735-1744, 1969.
- 185 BERMUDEZ, V. Z. et al. Coordination of Eu³⁺ ions in siliceous nanohybrids containing short polyether chains and bridging urea cross-links. **Journal of Physical Chemistry B**, v. 105 p. 3378-3386, 2001.
- 186 MIYAZAWA, T.; SHIMANOUCI, T.; MIZUSHIMA, S.-I. Characteristic infrared bands of monosubstituted amides. **Journal of Chemical Physics**, v. 24 p. 408-418, 1956.
- 187 ZHARKOV, V. V.; STRIKOVSKY A. G.; VERTELETSKAYA, T. E. Amide I absorption band: description of the urethane group association scheme in polyether urethane elastomers. **Polymer**, v. 34, p. 938-914, 1993.

-
- 188 SKROVANEK, D. J.; PAINTER, P. C.; COLEMAN, M. M. Hydrogen bonding in polymers. 2. Infrared temperature studies of nylon 11. **Macromolecules**, v. 19, p. 699-705, 1986.
- 189 CARLOS, L. D.; BERMUDEZ, V. Z.; FERREIRA, R. A. S. Multi-wavelength europium-based hybrid phosphors. **Journal of Non-Crystalline Solids**, v. 247, p. 203-208, 1999.
- 190 GONÇALVES, M. C. et al. Optically functional di-urethanesil nanohybrids containing Eu^{3+} ions. **Chemistry of Materials**, v. 16, p. 2530-2543, 2004.
- 191 GRENE, Y.; AVIGNON, M.; GARRKGOU-LAGRANGE, C. Molecular structure study of dipeptides isolated in an argon matrix by infrared spectroscopy. **Journal of Molecular Structure**, v. 24, p. 293-307, 1975.
- 192 SKROVANEK, D. J. et al. Hydrogen bonding in polymers: infrared temperature studies of an amorphous polyamide. **Macromolecules**, v. 18 p. 1676-1683, 1985.
- 193 GONÇALVES, M. C. et al. Cationic and anionic environments in mono-urethanesil hybrids doped with magnesium triflate. **Solid State Ionics**, v. 166, p. 103-114, 2004.
- 194 BERMUDEZ, V. Z.; CARLOS, L. D.; ALCÁCER, L. Sol-gel derived urea cross-linked organically modified silicates. 1. Room temperature mid-infrared spectra. **Chemistry of Materials**, v. 11, p. 569-580, 1999.
- 195 WANG, J. et al. Correlation of PEO conformations and solvation in PEO–NaSCN polymer electrolytes. **Chemical Physics**, v. 325, p. 538-544, 2006.
- 196 VAIA, R. A.; TEUKOLSKY, R. A.; GIANNELIS, E. P. Interlayer structure and molecular environment of alkylammonium layered silicates. **Chemistry of Materials**, v. 6, p 1017-10200, 1994.
- 197 HENDERSON, W. A.; BROOKS, N. R.; YOUNG, V. G. Jr. Single-crystal structures of polymer electrolytes. **Journal of the American Chemical Society**, v. 125, p. 12098-12099, 2003.
- 198 CHATANI, Y.; OKAMURA, S. Crystal structure of poly(ethylene oxide)-sodium iodide complex. **Polymer**, v. 28, p. 1815-1820, 1987.
- 199 CHATANI, Y. et al. Structures of two crystal forms of poly(ethylene oxide)-sodium thiocyanate complex with molar ratios of 3:1 and 1:1. **Polymer**, v. 31, p. 2238-2244, 1990.
- 200 LIGHTFOOT, P.; NOWINSKI, J. L.; BRUCE, P. G. Crystal structures of the polymer electrolytes poly(ethylene oxide)₄:MSCN (M = NH₄, K). **Journal of the American Chemical Society**, v. 116, p. 7469-7470, 1994.
- 201 STAUNTON, E. et al. The structure of poly(ethylene oxide)₈:NaBPh₄ from a single crystal oligomer and polycrystalline polymer. **Chemical Communication**, v. 10, p. 148-149, 2004.

-
- 202 CHRISPOPOULOU, K. et al. Crystallinity and chain conformation in PEO/layered silicate nanocomposites. **Macromolecules**, v. 44, p. 9710-9722, 2011.
- 203 MAXFIELD, J.; SHEPHERD, I., W. Conformational of poly(ethylene oxide) in the solid state, melt and solution measured by Raman scattering. **Polymer**, v. 16, p. 505-509, 1975.
- 204 DAHMOUCHE, K. et al. Small-angle X-ray scattering study of sol-gel-derived siloxane-PEG and siloxane-PPG hybrid materials. **Journal of Physical Chemistry B**, v. 103, p. 4937-4942, 1999.
- 205 GLATTER, O.; KRATKY, O. **Small-angle x-ray scattering**. New York: Academic Press, 1982. 515 p.
- 206 GIANCATERINA, S. et al. Photochemical evolution of poly(ether ether ketone). **Polymer Degradation and Stability**, v. 68, p. 133-144, 2000.
- 207 LI, L. et al. A series of exceptionally robust luminescent coordination polymers based on a bipyridyldicarboxylate ligand and rare-earth-metal ions. **European Journal of Inorganic Chemistry**, v. 36, p. 6111-6118, 2013.
- 208 NOBRE, S. S. et al. Eu³⁺-assisted short-range ordering of photoluminescent bridged silsesquioxanes. **Chemistry of Materials**, v. 22, n. 12, p. 3599-3609, 2010.
- 209 CARLOS, L. D. et al. Nanoscopic photoluminescence memory as a fingerprint of complexity in self-assembled alkyl/siloxane hybrids. **Advanced Materials**, v. 19, p. 341-348, 2007.
- 210 CARLOS, L. D. et al. White-light emission of amine-functionalized organic/inorganic hybrids: emitting centers and recombination mechanisms. **Journal of Physical Chemistry B**, v. 108, p. 14924-14932, 2004
- 211 NOBRE, S. S. et al. Energy transfer and emission quantum yields of organic-inorganic hybrids lacking metal activator centers. **Journal of Physical Chemistry C**, v. 111, p. 3275-3284, 2007.
- 212 FERNANDES, M. et al. Highly photostable luminescent poly(ϵ -caprolactone)siloxane biohybrids doped with europium complexes. **Chemistry of Materials**, v. 19, p. 3892 -3901, 2007.
- 213 NUNES, S. C. et al. Structure and photoluminescent features of di-amide cross-linked alkylene-siloxane hybrids. **Journal of Materials Chemistry**, v. 15, p. 3876-3886, 2005.
- 214 WANG, Y. et al. Luminescent organic-inorganic hybrid materials based on lanthanide containing ionic liquids and silylated β -diketone. **Journal of Sol-Gel Science and Technology**, v. 58, p. 711-715, 2011.
- 215 CARLOS, L. D. et al. Lanthanide-containing light-emitting organic-inorganic hybrids: A bet on the future. **Advanced Materials**, v. 21, p. 509-534, 2009.

-
- 216 SHAVALEEV, N. M. et al. N -aryl chromophore ligands for bright europium luminescence. **Inorganic Chemistry**, v. 49, p. 3927-3936, 2010.
- 217 CARLOS, L. D. et al. Local coordination of Eu(III) in organic/inorganic amine functionalized hybrids. **Journal of Alloys and Compounds**, v. 374, p. 50-55, 2004.
- 218 OFELT, G. S. Intensities of crystal spectra of rare-earths ions. **Journal of Chemical Physics**, v. 37, p. 511-520, 1962.
- 219 LAW, G.-L. et al. Structural characterization of shielded isomeric europium complexes with metal-metal contact. **Inorganic Chemistry**, v. 46, p. 9754-9759, 2007.
- 220 SU, S. et al. Lanthanide anionic metal-organic frameworks containing semirigid tetracarboxylate ligands: structure, photoluminescence, and magnetism. **Crystal Growth & Design**, v. 12, p. 1808-1815, 2012.
- 221 KAMINSKA, A.; KACZMAREK, H.; KOWALONEK, J. Cobalt(II) chloride catalysed oxidative degradation of poly(ethylene oxide) by a short wavelength UV-radiation. **Polymer**, v. 40, p. 5781-5791, 1999.
- 222 SHEN, Z.; SIMON, G. P.; CHENG, Y.-B. Comparison of solution intercalation and melt intercalation of polymer-clay nanocomposites. **Polymer**, v. 43, p. 425-4260, 2002.
- 223 LUNSTROOT, K. et al. Luminescent ionogels based on europium-doped ionic liquids confined within silica-derived networks. **Chemistry of Materials**, v. 18, p. 5711-5715, 2006.
- 224 RIVATON, A. et al. Basic aspects of polymer degradation. **Macromolecular Symposia**, v. 225, p. 129-146, 2005.
- 225 GARDETTE, M. et al. Photo- and thermal-oxidation of polyethylene: Comparison of mechanisms and influence of unsaturation content. **Polymer Degradation and Stability**, v. 98, p. 2383-2390, 2013.
- 226 ROUILLON, C. et al. Iscarbonyl index a quantitative probe to monitor polypropylene photodegradation. **Polymer Degradation and Stability**, v. 128, p. 200-208, 2016.
- 227 MORLAT-THERIAS, S. et al. P hotooxidation of ethylene-propylene-diene/montmorillonite nanocomposites. **Polymer Degradation and Stability**, v. 90, p. 78-85, 2005.
- 228 HASSOUNA, F. et al. Photochemical behaviour of poly(ethylene oxide) (PEO) in aqueous solution: influence of iron salts. **Journal of Photochemistry and Photobiology A: Chemistry**, v. 195, p. 167-174, 2008.
- 229 GONÇALVES, M. C. et al. Cationic and anionic environments in mono-urethanesil hybrids doped with magnesium triflate. **Solid State Ionics.**, v. 166, p. 103-114, 2004.

-
- 230 HIKOSAKA M. Y, et. al. Montmorillonite (MMT) effect on the structure of poly(oxyethylene) (PEO)–MMT nanocomposites and silica–PEO–MMT hybrid materials. **Journal of the Non-Crystalline Solids**, v. 352, p. 3705-3710, 2006.
- 231 EDMAN, L.; FERRY, A.; DOEFF, M. M. J. Slow recrystallization in the polymer electrolyte system poly(ethylene oxide)_n–LiN(CF₃SO₂)₂. **Materials Research**, v. 15, p. 1950-1954, 2000.
- 232 NISHI, T.; WANG, T. T. Melting point depression and kinetic effects of cooling on crystallization in poly(vinylidene fluoride)-poly (methyl methacrylate) mixtures. **Macromolecules**, v. 8, n. 6, p. 909-915, 1975.
- 233 MOLINA, E. F. et al. Ureasil–polyether hybrid blend with tuneable hydrophilic/hydrophobic features based on U-PEO1900 and U-PPO400 mixtures. **Journal of Sol-Gel Science and Technology**, v. 70, p. 317-328, 2014.
- 234 PAPKE, B. L.; RATNER, M. A.; SHRIVER, D. F.; Vibrational spectroscopy and structure of polymer electrolytes, poly(ethylene oxide) complexes of alkali metal salts. **Journal of Physics and Chemistry of Solids**, v. 42, p. 493-500, 1981.
- 235 DIDDENS, D.; HEUER, A.; BORODIN, O. Understanding the lithium transport within a rouse-based model for a PEO/LiTFSI polymer electrolyte. **Macromolecules**, v. 43, p. 2028–2036, 2010.
- 236 NUNES, S., C. et al. Cationic and anionic environments in LiTFSI-doped di-ureasils with application in solid-state electrochromic devices. **Chemical Physics**, v. 345, p. 32-40, 2008.
- 237 PAPKE, B., L.; RATNER, M., A.; SHRIVER, D., F. Vibrational spectroscopic determination of structure and ion pairing in complexes of poly(ethylene oxide) with lithium salts. **Journal of Electrochemical Society**, v. 129, p. 1434-1438, 1982.
- 238 SUZUKI, Y. et al. Suppression of poly(ethylene oxide) crystallization in diblock copolymers of poly(ethylene oxide)-b-poly(ϵ -caprolactone) confined to nanoporous alumina. **Macromolecules**, v. 47, p. 1793-1800, 2014.
- 239 TONAMI, K. et al. Excess X-ray scattering observed at low angles during melting of crystalline-amorphous diblock copolymers. **Polymer Journal**, v. 41, p. 1041-1048, 2009.
- 240 BEAUCAGE, G. approximations leading to a unified exponential/power-law approach to small-angle scattering. **Journal of Applied Crystallography**, v. 28, p. 717-728, 1995.
- 241 XI, J. et al. Composite polymer electrolyte doped with mesoporous silica SBA-15 for lithium polymer battery. **Solid State Ionics**, v. 176, p. 1249-1260, 2005.
- 242 LASINSKA, A., K. et al. Study of ageing effects in polymer-in-salt electrolytes based on poly (acrylonitrile-co-butyl acrylate) and lithium salts. **Electrochimica Acta**, v. 169, p. 61-72, 2015.

-
- 243 HERSTEDT, M. et al. Spectroscopic characterization of the conformational states of the bis(trifluoromethanesulfonyl)imide anion (TFSI-). **Journal of Raman Spectroscopy**, v. 36, p. 762-770, 2005.
- 244 SUBBA, R. C. V.; SHARMA, A. K.; NARASIMHA V. V. R. Conductivity and discharge characteristics of polyblend (PVP + PVA + KIO₃) electrolyte. **Journal of Power Sources**, v. 114, p. 338-345, 2003.
- 245 MICHAEL, M. et al. Enhanced lithium ion transport in PEO-based solid polymer electrolytes employing a novel class of plasticizers. **Solid State Ionics**, v. 98, p. 167-174, 1997.
- 246 LIANG, B. et al. Preparation and characterization of PEO-PMMA polymer composite electrolytes doped with nano-Al₂O₃. **Electrochimica Acta**, v. 169, p. 334-341, 2015.
- 247 KARAN, N. K. et al. Solid polymer electrolytes based on polyethylene oxide and lithium trifluoro- methane sulfonate (PEO-LiCF₃SO₃): Ionic conductivity and dielectric relaxation. **Solid State Ionics**, v. 179 p. 689-696, 2008.
- 248 MAO, G. et al. α -relaxation in PEO-litfsi polymer electrolytes. **Macromolecules**, v. 35, p. 415-419, 2002.
- 249 STEINHAUERA, M. et al. Investigation of the solid electrolyte interphase formation at graphite anodes in lithium-ion batteries with electrochemical impedance spectroscopy. **Electrochimica Acta**, v. 228, p. 652-658, 2017.
- 250 PELEG, M.; NORMAND, M., D.; CORRADINI, M., G. The Arrhenius equation revisited. **Critical Reviews in Food Science and Nutrition**, v. 52, n. 9, p. 830-851, 2012.

Chapter 9:

Annex

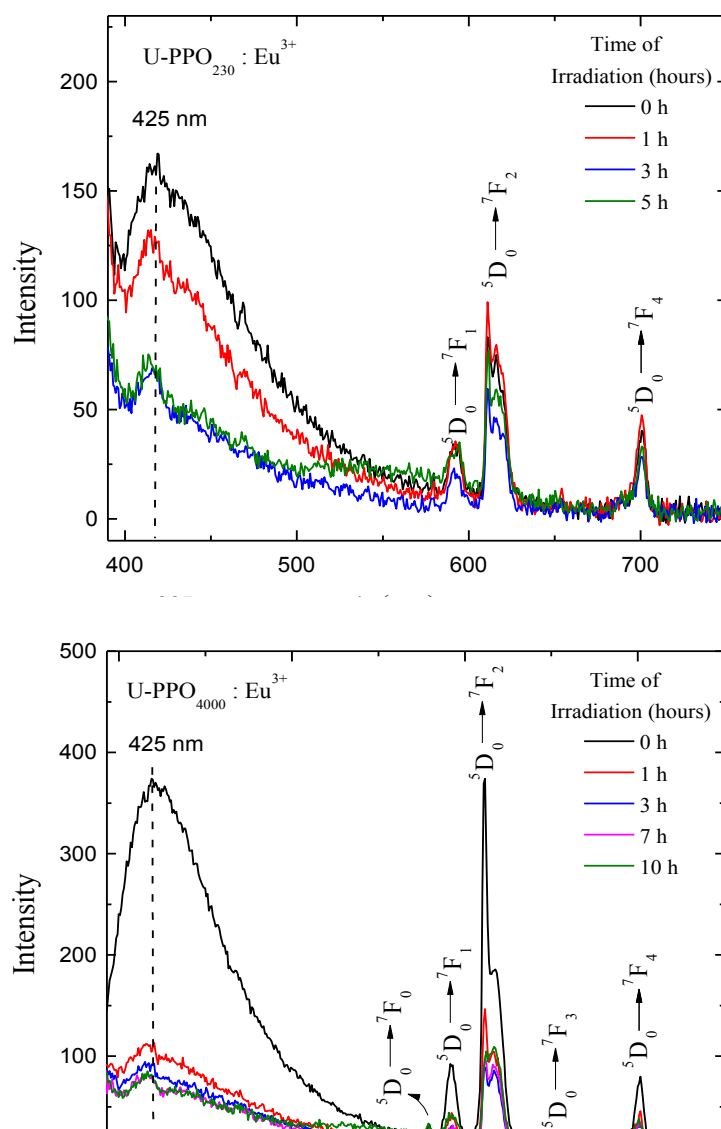


Figure A.1: Effect of UV-light exposure times on the emission spectra of the Eu³⁺- OIH complex, (left) U-PPO₂₃₀ and (right) U-PPO₄₀₀₀.

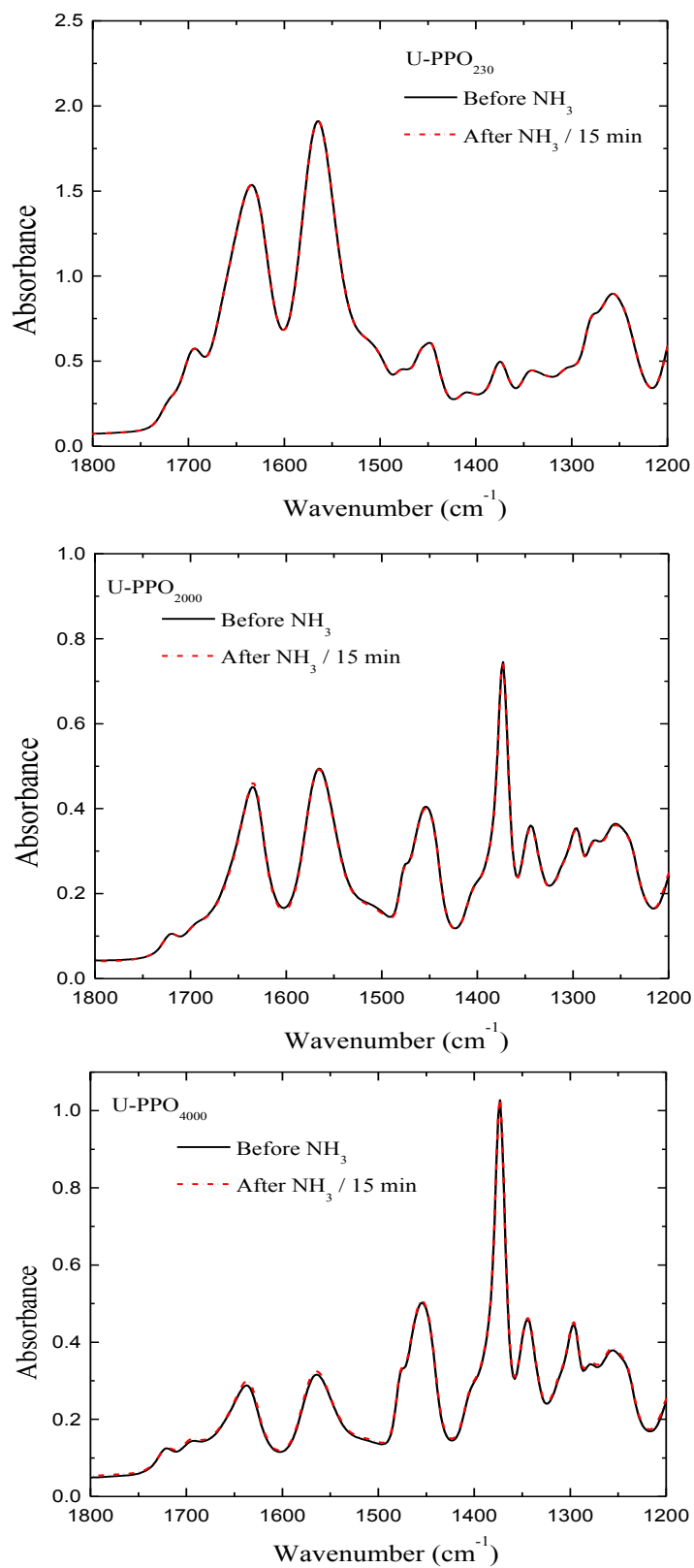


Figure A.2: NH₃ treatment of (top) U-PPO₂₃₀, (middle) U-PPO₂₀₀₀ and (bottom) U-PPO₄₀₀₀ films, in the carbonyl range (**black**) before NH₃ treatment and (**red**) after 15 min of NH₃ treatment.

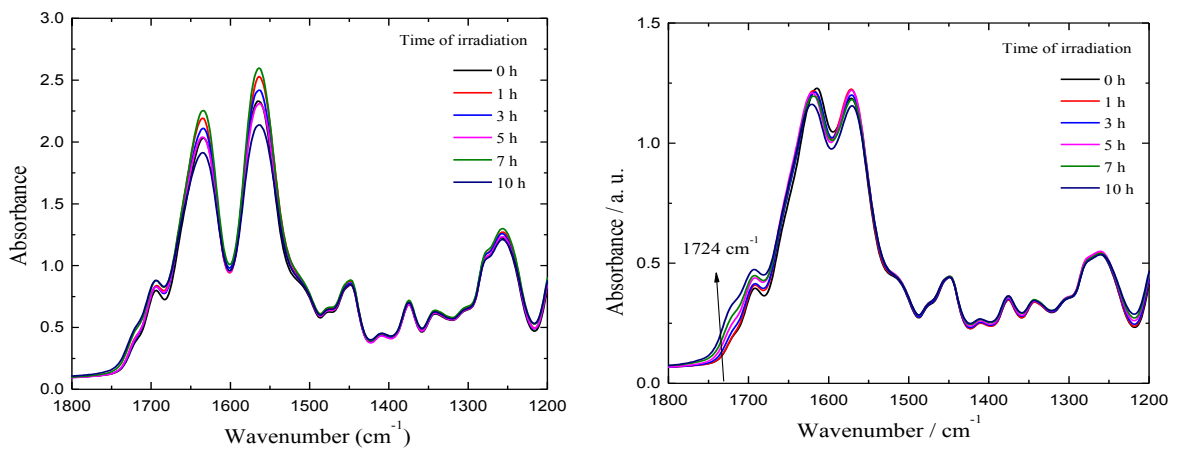


Figure A.3: FTIR spectra evolution during accelerated photo-aging assays (left) U-PPO₂₃₀ and (right) U-PPO₂₀₀₀:Eu³⁺ films (50 μm) in different UV-light exposure at $\lambda \geq 300$ nm and 60 °C.

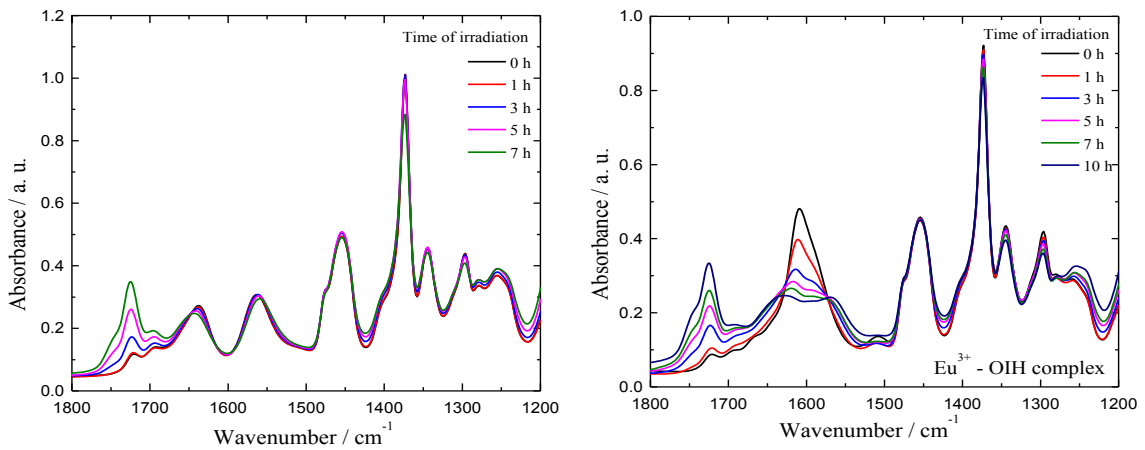


Figure A.4: FTIR spectra evolution during accelerated photo-aging assays (left) U-PPO₄₀₀₀ and (right) U-PPO₂₀₀₀:Eu³⁺ films (50 μm) in different UV-light exposure at $\lambda \geq 300$ nm and 60 °C.

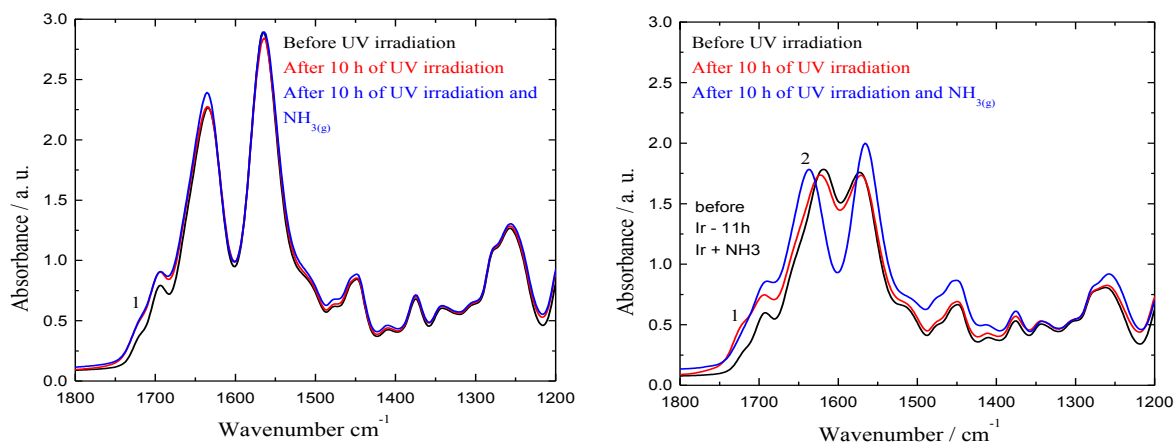


Figure A.5: NH_3 treatment of (left) U-PPO₂₃₀ and (right) U-PPO₂₃₀ : Eu^{3+} film photo-oxidised at 10 h of UV-light exposure ($\lambda \geq 300$ nm, 60 °C), in the carbonyl range.

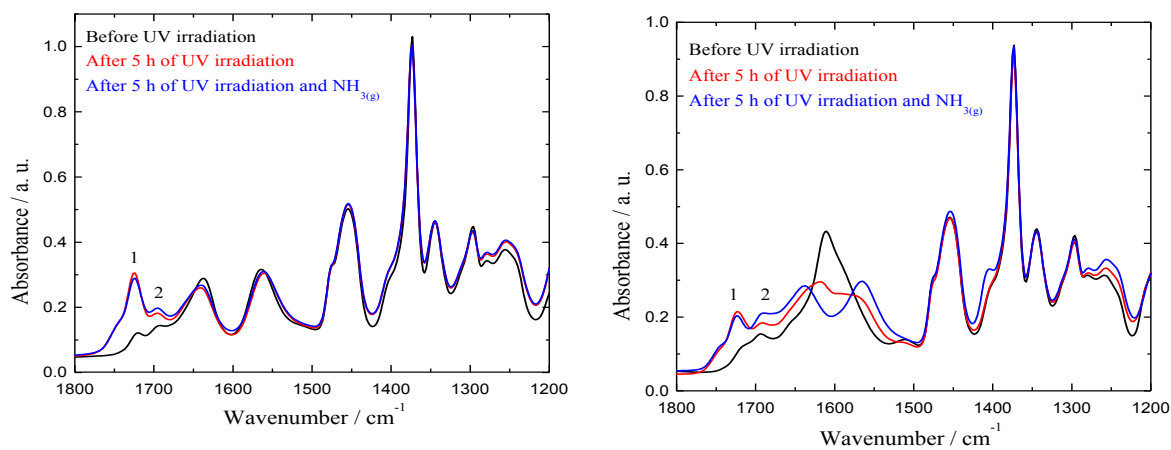


Figure A.6: NH_3 treatment of (left) U-PPO₄₀₀₀ and (right) U-PPO₄₀₀₀ : Eu^{3+} film photo-oxidised at 10 h of UV-light exposure ($\lambda \geq 300$ nm, 60 °C), in the carbonyl range.

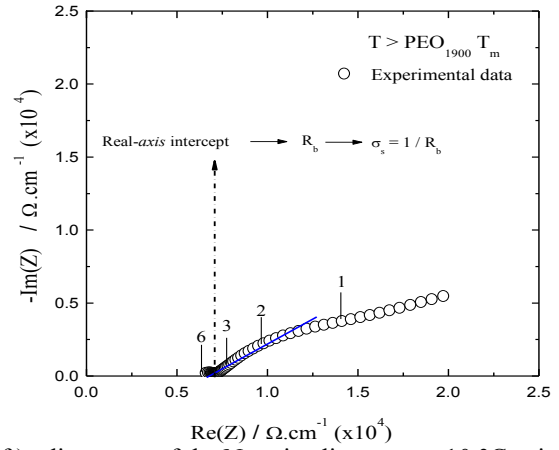
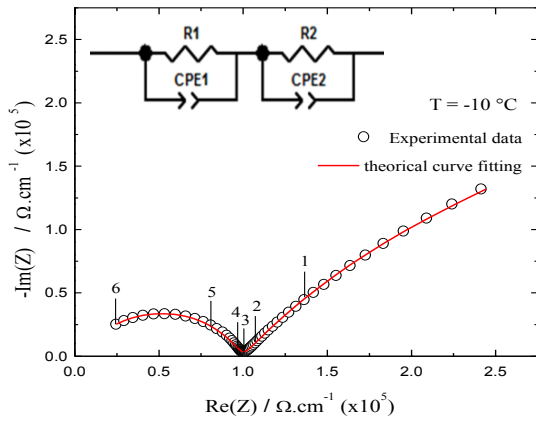


Figure A.7: $U_{-0.2}PPO_{2000}:U_{-0.8}PEO_{1900} -Li^+$ -loaded (Left) adjustment of the Nyquist diagram at $-10\text{ }^\circ\text{C}$ using a RQ – RQ model and (Right) Nyquist diagram at $+80\text{ }^\circ\text{C}$.

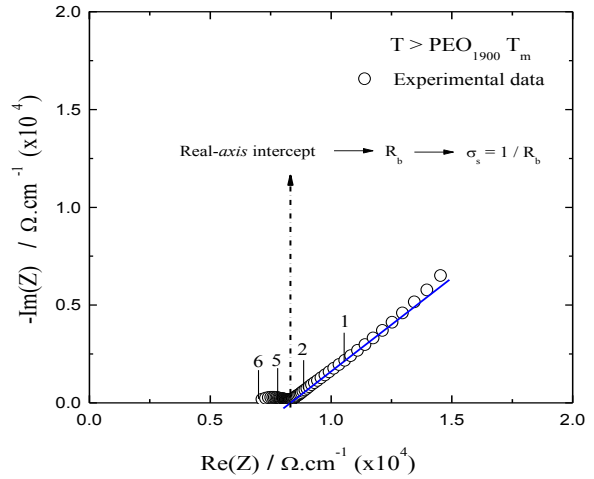
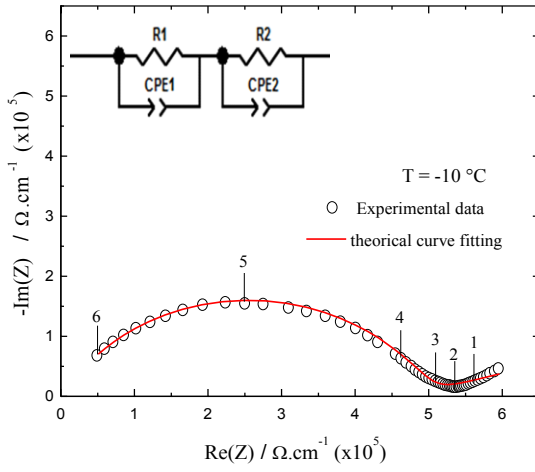


Figure A.8: $U_{-0.5}PPO_{2000}:U_{-0.5}PEO_{1900} -Li^+$ -loaded (Left) mathematical theoretical adjustment of the Nyquist diagram at $-10\text{ }^\circ\text{C}$ using a RQ – RQ model and (Right) Nyquist diagram at $+80\text{ }^\circ\text{C}$.

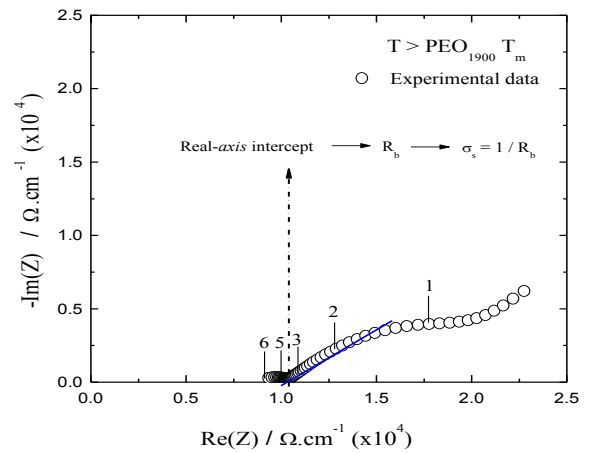
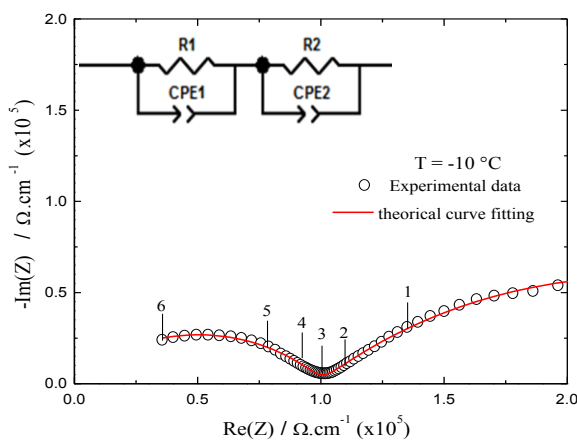


Figure A.9: $U_{-0.8}PPO_{2000}:U_{-0.2}PEO_{1900} -Li^+$ -loaded (Left) adjustment of the Nyquist diagram at $-10\text{ }^\circ\text{C}$ using a RQ – RQ model and (Right) Nyquist diagram at $+80\text{ }^\circ\text{C}$.